



HAL
open science

Analysis and modeling of crustal deformation using InSAR time series along selected active faults within the Africa-Eurasia convergence zone

Esra Cetin

► **To cite this version:**

Esra Cetin. Analysis and modeling of crustal deformation using InSAR time series along selected active faults within the Africa-Eurasia convergence zone. Geophysics [physics.geo-ph]. Université de Strasbourg; Yıldız Teknik Üniversitesi (Istanbul), 2015. English. NNT: 2015STRAH010. tel-01282011

HAL Id: tel-01282011

<https://theses.hal.science/tel-01282011v1>

Submitted on 3 Mar 2016

HAL is a multi-disciplinary open access archive for the deposit and dissemination of scientific research documents, whether they are published or not. The documents may come from teaching and research institutions in France or abroad, or from public or private research centers.

L'archive ouverte pluridisciplinaire **HAL**, est destinée au dépôt et à la diffusion de documents scientifiques de niveau recherche, publiés ou non, émanant des établissements d'enseignement et de recherche français ou étrangers, des laboratoires publics ou privés.

ÉCOLE DOCTORALE des SCIENCES de la TERRE
Institut de Physique du Globe de Strasbourg

THÈSE présentée par :
Esra CETIN

soutenue le : 2 juin 2015

pour obtenir le grade de : **Docteur de l'université de Strasbourg**

Discipline/ Spécialité : Géophysique

TITRE de la thèse

**Analysis and Modeling of Crustal Deformation
using InSAR Time Series Along Selected Active
Faults within the Africa-Eurasia Convergence
Zone**

THÈSE dirigée par :

Prof. MEGHRAOUI Mustapha
Assoc. Prof. ÇAKIR Ziyadin

Directeur de Thèse, Université de Strasbourg
Co-directeur de Thèse, Istanbul Technical University

RAPPORTEURS :

Prof. WRIGHT Tim J.
Prof. DOĞAN Uğur

Rapporteur Externe, University of Leeds
Rapporteur Externe, Yildiz Technical University

AUTRES MEMBRES DU JURY :

Prof. MASSON Frédéric
Assoc. Prof. OZEREN Sinan
Prof. AKYÜZ H. Serdar
Assoc. Prof. BALIK ŞANLI Fusun

Examineur, Université de Strasbourg
Examineur, Istanbul Technical University
Examineur, Istanbul Technical University
Examineur, Yildiz Technical University

ISTANBUL TECHNICAL UNIVERSITY ★ GRADUATE SCHOOL OF SCIENCE
ENGINEERING AND TECHNOLOGY

**ANALYSIS AND MODELING OF CRUSTAL DEFORMATION USING InSAR
TIME SERIES ALONG SELECTED ACTIVE FAULTS WITHIN THE AFRICA-
EURASIA CONVERGENCE ZONE**

Ph.D. THESIS

Esra ÇETİN

**Department of Geological Engineering
Geological Engineering Programme**

Thesis Advisor: Assoc. Prof. Dr. Ziyadin ÇAKIR

Co-advisor: Prof. Dr. Mustapha MEGHRAOUI

JUNE 2015

To my grandpa,

FOREWORD

First and foremost I would like to convey my sincere thanks to my advisors, Ziyadin akır and Mustapha Meghraoui, whose advices and mentorship have been tireless, fair and of top-notch standards. I am grateful to my advisor Ziyadin akır for teaching me InSAR and problem solving approaches, and sharing his past experiences and knowledge on active tectonics since my master's studies. Thanks to Mustapha Meghraoui, who provided me the privilege to study in Strasbourg, and guidance in my earthquake geology studies and field experience since the last four years. I am indebted to them for their wisdom, patience and continued assistance during my academic endeavors.

I am also grateful to my thesis committee, Frederic Masson, Tim Wright, Sinan zeren, Füsün Balık Şanlı, Gürsel Sunal, Uğur Doğan and H. Serdar Akyüz, whose constructive criticism significantly improved this study.

During this study I had well support and fruitful discussions with many of my colleagues. Especially, I am very grateful to Semih Ergintav and Ahmet Akođlu for for guiding me on modeling and computing problems; Gökhan Arslan for helping me on viscoelastic modeling; Tim Wright for useful advices during meetings and constructive comments that improved published papers from this study; Uğur Doğan for sharing with me GPS data at İsmetpaşa, and Pablo J. Gonzalez for sharing with me ascending InSAR data at Al Hoceima.

I would like to thank to my colleagues and friends in Istanbul, mainly Semih Can, Remziye, Nalan, Gönenç, Cemile, Fatma, Emir, Ersen, Gülsen, Burcu, Seden, Dođuşhan, Zümer and other members, with whom I have shared my graduate school years.

Furthermore, the enjoyment of my time in Strasbourg was catalyzed by a number of colleagues and friends; Romy, Abeer, Jean Remi, Karim, Juan, Yasser, Alice, Silke, Gülebru, Orkan, Semih, Marilyn, Cecile, Aline, Basile, Paul, Sheldon, Seyf, Satish, Jo, Nesma, Aurea and many more. I am pleased to know them all; merci beaucoup!

Outside of academic pursuit, great thanks go to Fadime, Evrim, Ferhat, Özgül, Onur Kılınççeker and Zia for their care and precious friendship throughout all these years that will never be forgotten. I am glad to have cheerful friends like you.

My special thanks go to Ülgen family who became my second family since many years. We have shared lifetime memories since undergraduate years; teşekkürler ikinci ailem!

I would like to acknowledge the Muđla Sıtkı Koçman University for the support of graduate school in Istanbul Technical University and University of Strasbourg. I would like to express them my gratitude for continuous encouragement and support to my studies. I am glad to be a part of the team in Faculty of Engineering.

This Ph.D. thesis is conducted in the frame of the “co-tutelle” scholarship (EOST-ITU) provided by French Embassy in Ankara. In addition, a 10-month scholarship « Bourse excellence Eiffel », and 8-month scholarship « TUBITAK 2214B - joint Ph.D. » were other sources of support for the preparation of this thesis. In addition, SAR images were obtained from the Category 1 projects 2532 and AOTR-2436 of the European Space Agency and the Geohazard Supersites program. I am obliged to acknowledge them for their generosity.

Last but not the least, my sincerest gratitude goes to my family; my father Mehmet, my mother Meral and my brother Cihan, have been an immense support through all these situations in my life to help me reach this place; bugüne kadar hep yanımda olduğunuz için teşekkür ederim!

April 2015

Esra ÇETİN

TABLE OF CONTENTS

	<u>Page</u>
FOREWORD	vii
TABLE OF CONTENTS	ix
ABBREVIATIONS	xi
LIST OF TABLES	xiii
LIST OF FIGURES	xv
SUMMARY	xxi
RESUME	xxv
1. INTRODUCTION	3
2. METHODOLOGY	9
2.1 Persistent Scatterer InSAR (PSI).....	10
2.1.1 Interferogram formation:.....	11
2.1.2 PS identification:.....	13
2.1.3 PS selection:.....	13
2.1.4 Displacement estimation:.....	15
2.2 Small Baseline Processing (SBI).....	16
2.2.1 Small Baseline interferograms.....	16
2.2.2 SDFP pixel selection.....	17
2.3 Concluding Remarks.....	17
3. POSTSEISMIC DEFORMATION FOLLOWING THE 21 MAY 2003 ZEMMOURI EARTHQUAKE (Mw 6.8) IN THE TELL ATLAS OF NORTHERN ALGERIA	23
3.1 Introduction.....	23
3.2 Seismotectonic Setting.....	24
3.3 InSAR Observations.....	26
3.4 Modeling.....	28
3.4.1 Afterslip.....	28
3.4.2 Visco-elastic.....	32
3.4.3 Poro-elastic.....	33
3.5 Discussion and Conclusion.....	34
4. COSEISMIC AND POSTSEISMIC DEFORMATION ASSOCIATED WITH THE Mw 6.4 FEBRUARY 24, 2004 AL HOCEIMA (MOROCCO) EARTHQUAKE	39
4.1 Introduction.....	39
4.2 Seismotectonic Settings.....	41
4.3 InSAR Observations.....	45
4.3.1 Coseismic InSAR data.....	45
4.3.2 Postseismic InSAR data.....	47
4.4 Modeling.....	51
4.4.1 Modeling of coseismic deformation.....	51
4.4.2 Modeling of postseismic deformation.....	54

4.5 Discussion and Conclusion	58
5. EXTENT AND DISTRIBUTION OF ASEISMIC SLIP ON İSMETPAŞA SEGMENT OF THE NORTH ANATOLIAN FAULT (TURKEY)	63
5.1 Introduction	63
5.2 InSAR Observations.....	65
5.2.1 Surface velocity.....	65
5.2.2 Estimation of creep rate and extent.....	67
5.3 Modeling	70
5.4 Discussion	74
5.5 Conclusions	75
6. CONCLUSIONS.....	81
APPENDICES	101
APPENDIX A	103
APPENDIX B	104
APPENDIX C	105
APPENDIX D	111
APPENDIX E.....	118
APPENDIX F	120
CURRICULUM VITAE.....	133

ABBREVIATIONS

CGPS	: Continuous GPS
DEM	: Digital Elevation Model
FFT	: Fast Fourier Transform
GARCH	: Generalized Autoregressive Conditional Heteroskedasticity
GIS	: Geographic Information Systems
GPS	: Global Positioning System
IGN	: Instituto Geografico Nacional
InSAR	: Interferometric Synthetic Aperture Radar
LOS	: Line of sight
NAF	: North Anatolian Fault
PS	: Persistent Scatterers
PSI	: Persistent Scatterer InSAR
SAR	: Synthetic Aperture Radar
SB	: Small Baseline
SBI	: Small Baseline InSAR
SDFP	: Slowly-Decorrelating Filtered Pixels
SNR	: Signal to Noise Ratio
SRTM	: Shuttle Radar Topography Mission
StaMPS	: Stanford Method of Persistent Scatterer

LIST OF TABLES

	<u>Page</u>
Table 3.1 : Large and moderate earthquakes with thrust mechanisms along the Tell Atlas.	24

LIST OF FIGURES

	<u>Page</u>
Figure 1.1 : Schematic of <i>Reid</i> [1910]'s <i>elastic rebound</i> model of the earthquake cycle (modified from <i>Wright</i> [2002]). a) Map view of area spanning a hypothetical fault, in the instant after the last earthquake. b) The same area, in 250 years. The profile A-A', straight at the beginning of the cycle, has become curved. This is known as interseismic strain accumulation. c) The same area, 20 s later, after an earthquake. A-A' is once more a straight line, but this time with a 5 m step at the fault. B-B', straight immediately before the earthquake, is now curved with an offset of 5 m at the fault, decaying with large distances from the fault.	4
Figure 2.1 : Phase simulations from <i>Hooper et al.</i> [2007] for (a) a distributed scatterer pixel and (b) a persistent scatterer pixel. The cartoons above represent the scatterers contributing to the phase of one pixel in an image and the plots below show simulations of the phase for 100 iterations, with the smaller scatterers moving randomly between each iteration. The brighter scatterer in (b) is three times brighter than the sum of the smaller scatterers.....	10
Figure 2.2 : Sketch of the interferometric data pairs (green lines) selection for a) single (PSI) and b) multiple master (SBI) image (red circles) configurations. The SAR dataset is relevant to the Envisat ASAR acquisitions carried out from 12-July-2003 to 18-September-2010 covering the 2003 Zemmouri earthquake region.	12
Figure 3.1 : Tectonics and seismicity of the Zemmouri-Boumerdes region shown with SRTM shaded topography. Focal mechanisms are from Global CMT project. Two destructive earthquakes and related aftershocks (Tipaza 1989 and Zemmouri 2003, green and yellow circles, respectively) limit the Mitidja-Algiers active zone (black lines are thrust faults [<i>Maouche et al.</i> , 2011]). Dashed box is the Envisat images frame (Track 65). Black box in inset map shows the study region.....	25
Figure 3.2 : The baseline plot showing the interferogram pairs (green lines) between radar images (red circles).	26
Figure 3.3 : Seven-year postseismic cumulative LOS range change following the 2003 Zemmouri earthquake. Movements away from the satellite are shown with yellow to red colors and, those towards the satellite with yellow to blue. The black arrows with 95% confidence ellipses are 2.5-year cumulative postseismic GPS displacements from <i>Mahsas et al.</i> [2008]. Red line is the trace of the modeled fault on the sea floor. Numbers show the locations of time series plotted in Figure 1.4.	27
Figure 3.4 : Time series of InSAR data (red circles) and groundwater table measurements (blue squares [<i>Mimouni</i> , 2010]) in the study area. Note the strong correlation between water level fluctuations and InSAR phase	

	changes in the Mitidja basin (plots 1 to 3). Postseismic deformation in the earthquake region (plot 4 and 5) is manifested by logarithmic decay in the InSAR time series.....	28
Figure 3.5 :	The smoothing operator used in the InSAR and GPS data inversion. An optimum solution can be obtained with a 0.4 smoothing factor.....	30
Figure 3.6 :	Color-coded postseismic afterslip distribution on the Zemmouri earthquake rupture. Black dashed lines show the coseismic slip distribution inferred by <i>Belabbes et al.</i> [2009]. The afterslip distribution inverted from InSAR and GPS data shows two patches of maximum slip (40 to 65 cm) along the upper sections of the fault (<5-km-depth) complementing the coseismic slip at deeper fault sections.....	31
Figure 3.7 :	Model of 7 year cumulative LOS surface deformation and GPS displacements predicted by the modeled slip distribution shown in Figure 3.6. The fault rupture projected to the surface is illustrated by the triangulated network; parallel and perpendicular profiles to the fault are located by number 1 and 2. Inset shows LOS change of modeled (red lines) and observed (blue dots) postseismic surface deformation, together with coseismic model (green lines [<i>Belabbes et al.</i> , 2009]). Pink lines show vertical component of the LOS change predicted by the model.....	31
Figure 3.8 :	Residual LOS velocity field.....	32
Figure 3.9 :	Model of 7-year cumulative LOS surface deformation and GPS displacements predicted by visco-elastic relaxation. Red line shows the modeled fault rupture.....	33
Figure 3.10 :	Model of 7-year cumulative LOS surface deformation and GPS displacements predicted by poro-elastic rebound. Red line shows the modeled fault rupture.....	34
Figure 4.1 :	Al Hoceima region of Morocco with shaded relief (SRTM 90m). Large beach balls are focal mechanism solutions of the 26 May 1994 and 24 February 2004 Al Hoceima earthquakes [<i>Calvert et al.</i> , 1997; <i>Bezzeghoud and Buforn</i> , 1999], whose epicenters are indicated by gray and black stars, respectively. Small black circles are $M > 4$ aftershocks from IGN with focal mechanism solutions from <i>Buforn et al.</i> [2004] and <i>Stich et al.</i> [2005]. Dashed rectangles are the frames of the Envisat radar images with arrows showing the flight direction of the satellite. The convergent plate boundary between Africa and Eurasia is depicted with a thick gray line in the inset map with arrows illustrating the direction and estimated rate (min. and max.) of convergence [<i>Nocquet and Calais</i> , 2004]. Red arrows indicate the recent GPS measurements [<i>Koulali et al.</i> , 2011].....	40
Figure 4.2 :	Tectonic map of the Al Hoceima region (compiled from <i>Calvert et al.</i> , 1997; <i>Ait Brahim, Tadili, et al.</i> , 2004) with surface cracks and fissures observed after the 2004 event (redrawn from <i>Ait Brahim, Nakhcha, et al.</i> , 2004). Thick white line is the surface trace of the modeled fault plane.....	43
Figure 4.3 :	Aftershocks distribution of the 2004 earthquake obtained from <i>Tahayt et al.</i> [2009] and <i>van der Woerd et al.</i> [2014] in the Al Hoceima region. Blue lines show the mapped thrust and nappe structures in the mountains and normal faults that limit the Al Hoceima Quaternary Basin. Thick white line is the surface projection of our modeled	

coseismic fault. Dashed lines show the perpendicular profiles to the fault (see profiles on the right). Cross sections of the aftershocks are shown on the right panel with profile numbers at the right bottom. Topographic profiles are shown as black lines on the top of sections. Blue arrows indicate the tip of our modeled coseismic blind fault location. 44

- Figure 4.4 :** Coseismic interferograms of the February 24, 2004 Al Hoceima earthquake. Each fringe shows 2.83 cm of surface displacement along the radar line-of-sight. Dashed lines are digitized fringes used in modeling of the interferograms. Blue line is the best model fault. Inactive thrust faults are shown to facilitate comparison of the interferograms. The gray and black arrows indicate the satellite flight direction and line-of-sight direction (right looking), respectively. 46
- Figure 4.5 :** Baseline plot showing the interferogram pairs (green lines) between descending (T280) and ascending (T230) radar images (red circles). .. 48
- Figure 4.6 :** Cumulative LOS range change **(a)** between 2004 and 2010 deduced from SBI time series on descending track and **(b)** between 2004 and mid-2007 deduced from StaMPS/MTI time series on the ascending track in the Al Hoceima region. Movements away from the satellite are shown with warm colors and those towards the satellite with cool colors, which is consistent with right-lateral sense of motion. Thick black line is the best model fault. The gray and black arrows indicate the satellite flight direction and line-of-sight direction (right looking), respectively. Numbers show the locations of time series plotted in Figure 4.7. 49
- Figure 4.7 :** Time series of InSAR data (blue circles for descending and red circles for ascending). Postseismic deformation in the earthquake region is manifested by linear change in descending time series due to lack of four months data just after the earthquake and similarly linear change in ascending time series after sudden change due to the earthquake. 50
- Figure 4.8 :** **a, b)** Synthetic interferograms predicted by a right-lateral strike-slip **c, d)** residual interferograms obtained after subtracting the synthetic interferograms from the observed data (shown in Figure 4.4). Dashed lines are digitized fringes used in modeling of the interferograms. Blue line is the best model fault. 52
- Figure 4.9 :** Color-coded postseismic strike-slip distribution (right-lateral) on the 2004 Al Hoceima earthquake rupture with a reverse slip component (black dashed lines), which coincides with the step or/and bend of the earthquake rupture, and a normal slip component located on the main branches of the fault. 53
- Figure 4.10 :** **a)** Ascending and **b)** descending cumulative LOS data sets during ~3.3 years used in inversions. Thick black line is modeled coseismic fault. The pink line shows the model fault tested to improve the model fit to LOS data change. The blue line indicates a fault suggested by the NE-SW trending aftershocks distribution. 55
- Figure 4.11 :** Color-coded postseismic right-lateral strike-slip afterslip distribution on the Al Hoceima earthquake rupture. The afterslip distributions inverted from ascending data show patches of slip (up to 35 cm) along mostly the upper sections of the fault (<5-km-depth) complementing the coseismic slip (black dashed lines) at deeper fault sections. Descending

	data on the other hand predicts a deep slip on the southern side of the fault similar to the coseismic model.	57
Figure 4.12 :	Residual maps obtained after subtracting the synthetic InSAR data (Figure D.2) from the observed data (shown in Figure 4.10). Residuals after inversion of (a) the ascending and (b) the descending data alone, and (c, d) jointly with a lower weighting for the descending data. Black line is the top of the coseismic model fault, and the dashed black line is the bottom of the coseismic model fault.	58
Figure 5.1 :	a) Tectonic map of Turkey and surrounding regions with GPS vectors in a Eurasia fixed reference frame [Reilinger <i>et al.</i> , 2006]. Rectangle shows the location of Figure 5.1b. b) Shaded SRTM topography map along the North Anatolian fault zone in northwestern Turkey with the recent rupture segments of large earthquakes [Barka and Kadinsky-Cade, 1988; Şaroğlu <i>et al.</i> , 1992]. The dashed rectangles are the Envisat image frames with track numbers used in this study.	64
Figure 5.2 :	Baseline versus time plot of synthetic aperture radar orbits from two Envisat tracks used to calculate the deformation field and the time series. Empty circles denote the SAR images with stars indicating the master orbits chosen for the PSI analyses.	66
Figure 5.3 :	Velocity field in the region of Ismetpaşa deduced from PSI time series. a, b) Fault-parallel horizontal velocity field (identical color scale for both tracks) between 2003 and 2010 on a SRTM shaded relief image with known active faults (black lines). The gray and black arrows to the bottom right corner show the satellite flight direction (descending) and the line-of-sight direction (right looking), respectively. Thick dashed lines with numbers are locations of profiles as shown in Figure 5.4. Red star shows the location of the PSI and GPS time series plotted in Figure 5.7. White boxes show the neighboring Envisat track used in this study.	67
Figure 5.4 :	Some of the observed and modeled fault-parallel velocity profiles perpendicular to the fault. Red curves show the best fitting model to PSI data with the creep rate and depth given above. The blue curves represent an interseismic model for a locked fault at 15 km of depth. Dashed line represents the topographic elevation along the profiles. Arrows indicate the mapped active fault location. Profile-1 crosses the location of the offset wall and the geodetic network that have been used to measure the creep rate at Ismetpaşa over the last 40 years.	68
Figure 5.5 :	Estimation procedure for the creep rate using best-fitting lines to InSAR velocity profiles that extend for 3 km on both sides of the fault (pink and blue colors). Creep rate is calculated from the offset of the two lines at the fault trace (e.g., the length of black line).	69
Figure 5.6 :	Rate and extent of aseismic surface creep along the Ismetpaşa section of the North Anatolian Fault. a) A mosaicked map of fault-parallel horizontal velocity field on SAR image tracks T479 and T207. Red line shows the creeping section of the NAF and the blue pentagon indicates the location of the micro-GPS network. White star represents the location of the wall where creep was discovered by Ambraseys [1970]. White arrows show the extents previously found by Cakir <i>et al.</i> [2005] and Kaneko <i>et al.</i> [2013]. b) Creep rates with error bars along the fault	

	are estimated from the InSAR velocities on track T479 (pink color) and track T207 (green color).....	69
Figure 5.7 :	Time series of line-of-sight InSAR (blue circles) and GPS (red squares) velocities (blue pentagon shown in Figure 5.6). The LOS velocities represent the mean of all pixels in a circle of ~600 m diameter to the north and south of the fault around the GPS network. The general trend and decay of creeping rate from InSAR time series are in good agreement with GPS time series.....	70
Figure 5.8 :	Modeling of aseismic slip distribution. a) Residual LOS velocities, obtained by the removal of the long-term signal due to interseismic loading and unwrapping, atmospheric and orbital errors, are used to model the aseismic slip on the fault. The blue circular anomaly located around the town of Orta is most likely due to the postseismic deformation of the 6 June 2000 Orta earthquake (Mw=6.0). Red arrows on the fault (white lines) indicate the tips of the modeled fault shown in Figure 5.9. Dashed lines show the profiles in Figure 5.8b. b) Observed (green and purple points) and modeled residual velocities (red lines) along the profiles perpendicular to the fault.....	71
Figure 5.9 :	(a) Variation of surface creep rate along the fault, (b) depth distribution of the variable aseismic slip on the Ismetpaşa creeping segment. Red arrow indicates the position of the geodetic network located 3.5 km east of the train station near Hamamlı village at Ismetpaşa. Slip is heterogeneously distributed along the fault and confined mostly to uppermost 5 km of the seismogenic crust with a maximum slip of $\sim 20 \pm 2$ mm/yr 20 km west of Ismetpaşa. (c) Uncertainty of the slip distribution with depth obtained from inversions of 200 InSAR data sets perturbed with synthetic noise.....	73
Figure 5.10 :	a) Geology map of the study region simplified from <i>Herece and Akay</i> [2003] with surface creep rates along the North Anatolian Fault obtained in this study. Geological units presumably involved in creeping are shown in colors and the others are labeled in white with abbreviations. Black and red lines represent the active fault and the creeping segment, respectively. The eastern end of the creeping section can be clearly seen in the inset rectangle. b) Creep rates and error ranges for two individual tracks are indicated in purple and green colors as in Figure 6.	76
Figure 5.11 :	Time history of surface creep at Ismetpaşa as reported by various studies following the 1944 earthquake (after <i>Cakir et al.</i> , [2005]). Horizontal and vertical bars are the time window and error range of measurements, respectively. The question mark corresponds to the unknown effect of the 1951 earthquake on creep rate. Curve shows the fit of the exponential relaxation function to the change of the creep rate with time [<i>Savage</i> , 2005].	77
Figure A.1 :	Resolution test using check-box approach with 0.10 m slip at different depths for each cell.	103
Figure B.1 :	Coseismic slip distribution used as an input file for PSCMP, which is simulated on a planar fault by enforcing the slip distribution deduced by <i>Belabbes et al.</i> [2009], is 55-km-long and 20-km-wide offshore thrust fault striking N60°, and dipping 42° SE.	104

Figure D.1 :	(a-b) Since InSAR measures surface change in 1-D (i.e. between surface and the radar) the surface deformation due to a right-lateral strike-slip fault on the ground will be recorded differently from ascending and descending orbits. The model fault used in the figure trends approximately NE-SW and has a dip of about 80° to the NE. The uniform slip observed on the fault surface is 50 cm. (c) The sum of the two phases of ascending and descending interferograms is largely vertical motion, and (d) the difference between two phases (descending minus ascending) is approximately east-west motion.	111
Figure D.2 :	Time series of ascending LOS for Al Hoceima region between 2003 and 2007. Each image represents the incremental displacement towards the satellite since the time of the previous image, relative to pixels in the northwest corner.	112
Figure D.3 :	Model of 3.3-year cumulative LOS postseismic surface deformation predicted by the modeled slip distribution shown in Figure 4.11. Black lines show the top of the modeled fault. White dashed lines show the bottom of the modeled fault.	113
Figure D.4 :	Model of 3.3-year cumulative LOS postseismic surface deformation predicted by the two fault rupture inversions according to aftershocks distribution. Black line shows the main modeled fault. Blue line indicates the fault branch obtained using aftershocks distribution.....	114
Figure D.5 :	Residual maps obtained after subtracting the synthetic InSAR data (Figure D.3) from the observed data (shown in Figure 4.10). Residuals after inversion of (a) the ascending and (b) the descending data alone, and (c, d) jointly with a lower weighting for the descending data. Black line shows the main coseismic model fault, and blue line is the secondary fault branch.....	115
Figure D.6 :	Model of 3.3-year cumulative LOS postseismic surface deformation predicted by the two fault rupture inversions according to PS LOS change in the southern section of the fault. Black line shows the main modeled fault. Pink line indicates the fault branch obtained using PS LOS displacement fields.....	116
Figure D.7 :	Residual maps obtained after subtracting the synthetic InSAR data (Figure D.5) from the observed data (shown in Figure 4.10). Residuals after inversion of (a) the ascending and (b) the descending data alone, and (c, d) jointly with a lower weighting for the descending data. Black line shows the main coseismic model fault, and pink line is the secondary fault branch.....	117
Figure D.8 :	Resolution test using checker-box approach with 0.10 m slip at different depths for each cell.	117
Figure E.1 :	Velocity standard deviation maps calculated by StaMPS using bootstrapping.....	118
Figure E.2 :	Variable interseismic slip model using multiple fault patches to flatten the far field velocity field.	118
Figure E.3 :	Residual LOS velocity field.....	119
Figure E.4 :	Resolution test using checker-box approach with 0.10 m slip at different depths for each cell.	119

**ANALYSIS AND MODELING OF CRUSTAL DEFORMATION USING
InSAR TIME SERIES ALONG SELECTED ACTIVE FAULTS WITHIN THE
AFRICA-EURASIA CONVERGENCE ZONE**

SUMMARY

The convergence between African and Eurasian plates is at the origin of active tectonic structures that generate large and destructive earthquakes. This thesis aims to improve our understanding of fault behavior and the earthquake cycle by analyzing surface deformation along selected active faults during the periods of co-, post-and inter-seismic deformation within the Africa-Eurasia convergence zone. In this context, slow deformation observed at the surface and associated with the earthquake cycle is analyzed using Synthetic Aperture Radar Interferometry (InSAR) time series technique, and modeled with elastic dislocation methods.

This thesis has VI Chapters and presents the application of InSAR, Persistent Scatterers (PSI) and Small Baseline (SBI) methods with the analysis of active deformation and related seismic cycle of earthquake areas. The core chapters focus on the postseismic deformation following the May 21, 2003 Zemmouri (Mw 6.8, Algeria) and February 24, 2004 Al Hoceima (Mw 6.4, Morocco) earthquakes, and creeping along the Ismetpaşa section of the North Anatolian Fault (Turkey).

The introduction (Chapter I) presents the InSAR technique in space geodesy, involved in active tectonics research about 20 years ago when it was utilized for the first time to study the surface displacement field of the 1992 Landers earthquake (Mw 7.4 in California). InSAR is a powerful technique for measuring surface deformation with centimeter-to-millimeter accuracy due to high spatial resolution and ability to acquire the data remotely. Advanced multi-temporal InSAR time series methods such as PSI and/or SBI approaches, are capable of simultaneous processing of multiple SAR acquisitions over time; this will increase the number of locations where a subtle deformation signal can be extracted by reducing the associated errors. The advanced InSAR techniques are able to reduce the noise effects and signal

decorrelation due to atmospheric effects, digital elevation (DEM) errors, and orbital inaccuracies. Compared to conventional InSAR, the PSI and/or SBI analysis generates time series of ground deformation for individual targets using multi-temporal stacks of SAR images (with regard to these targets that have a constant echo over the time) also called persistent scatterers.

Chapter II briefly describes the basic principles of InSAR time series analysis such as Persistent Scatterer and Small Baseline, applied in this thesis to study the postseismic and creep rupture mechanisms. Monitoring and investigating surface displacements associated with active faulting may contribute to improve our understanding of the driving mechanisms behind earthquakes and the interaction between them. The study of crustal tectonics using InSAR techniques is added with GPS data, regional seismotectonics and geology that help constraining the co-and post-seismic, and surface creep motions. Hence, the knowledge of earthquake cycle is an important step not only for the seismic hazard assessment but also for the understanding of the short and long-term Earth deformation and its potential for the future earthquake generation.

Chapter III depicts the postseismic deformation following the 2003 Zemmouri earthquake studied using the SBI technique. InSAR time series calculated from 31 Envisat ASAR images from 2003 to 2010 reveal subtle (sub-cm) ground movements in the earthquake area. The results show that two regions display subsidence along the shoreline, where the maximum coseismic uplifts was observed with InSAR and field measurements. The inverse modeling using dislocations on triangular faults in an elastic and homogeneous half-space suggest that subsidence in the area of high coseismic uplift can be explained by afterslip on the shallow sections (< 5 km) of the fault above the areas of coseismic slip, in agreement with previous estimates based on GPS observations. The impact of earthquake sequence on soft sediments and ground water table southwest of the earthquake area, allow us to characterize a ground deformation of non-tectonic origin. The cumulative postseismic moment due to afterslip during 7 years following the 2003 main shock is equivalent to an Mw 6.3 earthquake. Therefore, the postseismic deformation and stress buildup has significant implications on the earthquake cycle models and recurrence intervals of large earthquakes in the Algiers area.

Chapter IV presents the coseismic and postseismic surface deformation associated with the 2004 Al Hoceima earthquake deduced from the SBI technique. The earthquake rupture location is poorly known since the absence of clear coseismic faulting and related features. The postseismic surface displacement fields are mapped using Envisat ASAR data acquired in ascending (15 images) and descending modes (15 images). The coseismic fault rupture is however required a revision in light of postseismic deformation field to refine the suggested best fault model in the southern tip of the fault. InSAR analysis and modeling suggest that the earthquake is associated with a NW-SE trending right-lateral, apparently blind strike-slip fault with a left bend or step, and reveal remarkable postseismic surface displacement in the region of coseismic surface deformation. Although, thrust-and-fold structures of the Rif Mountains evolved during the Tertiary tectonic episodes, the recent significant seismic events and late-Quaternary deformation indicates E-W extension with N-S trending normal and NW-SE and NE-SW trending conjugate strike-slip faults. The Africa-Iberia collision and west-southwestward escape tectonics lead to the fragmentation of the Rif Mountain range.

Chapter V describes the study of creeping along the North Anatolian Fault (NAF). The PSI technique with elastic dislocation models and geology along the creeping section of the NAF at Ismetpaşa has been utilized to map and deduce the velocity field and the aseismic slip distribution. Revealing the spatiotemporal characteristics of the creep helped us associate the creep with potential lithological controls, hence providing a new perspective to better understand the underlying causes and mechanisms. The PSI analysis of Envisat ASAR images between 2003 and 2010 (55 images) reveals a clear picture of surface creep along the fault and a new interseismic velocity field transitioning gradually between the creeping and the locked fault sections. The creep rate is found to fluctuate along a 100-km long section of the fault in a manner similar to that along the Hayward fault (a branch of the San Andreas fault in California), reaching a maximum of $\sim 20 \pm 2$ mm/yr, close to the far field plate velocity ($\sim 25 \pm 1.5$ mm/yr). At Ismetpaşa, it is in the range of 8 ± 2 mm/yr, consistent with the previous geodetic observations. Modeling of the PSI data reveals a heterogeneous creep distribution at depth with two main patches confined mostly to the uppermost 5 km portion of the seismogenic crust, releasing annually 6.2×10^{16} Nm ($M_w = 5.1$) geodetic moment. There is a correlation between aseismic

surface creep and the geology along the fault as it is in major part associated to rocks with low frictional strength such as the andesitic-basaltic, limestone and serpentine bodies within the fault zone.

The conclusion (Chapter VI) resumes the main results and show how slow surface displacements associated with postseismic deformation of blind or hidden faults and aseismic creep of major active faults are successfully identified and characterized from InSAR time series. The results obtained for the Zemmouri earthquake emphasize the existence of a hidden offshore fault with a shallow afterslip on a complex coseismic rupture and confirm coastal subsidence following the earthquake where the coastal uplift was measured. The contribution of the postseismic surface deformation to the study of moderate sized Al Hoceima earthquake is noteworthy since it considerably improves the determination of the earthquake location, and identification of co- and post-seismic slip on a blind fault system. The fault creep parameters along the North Anatolian fault at Ismetpaşa section is also successfully deduced from InSAR time series and show the shallow rupture properties of creeping with the influence of geological background on the slow slip along the fault.

In perspective, this thesis emphasizes the contribution of InSAR time series to the study of slow surface deformation along selected active faults within the Africa-Eurasia convergence zone. Improving our understanding of the crustal deformation and the earthquake cycle requires detailed analysis of slow deformation related with active faulting. In order to buildup reliable and accurate models of the earthquake cycle, it is important to develop further the study of small surface displacements also linked to moderate or large sized events on Earth with new tools and techniques. These techniques should see more development with the use of the new generation SAR images (Sentinel, TerraSAR-X). The analysis of every significant seismic event may reveal new characterizations on the physics of earthquakes.

**ANALYSE ET MODELISATION DE LA DEFORMATION CRUSTALE PAR
TRAITEMENT DES SERIES TEMPORELLES InSAR SUR UNE
SELECTION DE FAILLES ACTIVES DE LA ZONE DE CONVERGENCE
AFRIQUE-EURASIE**

RESUME

Les travaux de cette thèse de Doctorat ont été menés dans le cadre de l'accord en co-tutelle entre l'Université de Strasbourg (EOST) et Istanbul Technical University (Dept. of Geology), avec l'octroi d'une bourse d'étude annuelle de l'Ambassade de France à Ankara, une bourse d'excellence EIFFEL de 10 mois, et un support financier de 8 mois de « TUBITAK 2214B - joint Ph.D. ».

La zone de convergence de plaques Afrique – Eurasie comporte des failles capables de générer de forts séismes destructeurs. L'objectif de cette thèse est une meilleure compréhension du comportement de ces failles, et du cycle sismique associé, par l'analyse des déformations co-, post- et inter-sismiques enregistrées en surface, dans la zone de convergence. Une attention particulière est portée aux déformations lentes et à leur part dans le cycle sismique, mesurées en surface et analysées à l'aide des techniques InSAR (Synthetic Aperture Radar Interferometry), et modélisées par les méthodes de la dislocation élastique.

Cette thèse comporte VI chapitres centrés sur l'application des méthodes InSAR et multi-temporelles InSAR (PSI et SBI), avec analyse des déformations en surface et en profondeur des zones sismiques. Les principaux chapitres traitent notamment des déformations postsismiques liées aux séismes du 21 mai 2003 à Zemmouri (Mw6.8, Algérie), du 24 février 2004 à Al Hoceima (Mw 6.4, Maroc), et aux déplacements lents le long du segment Ismetpaşa de la faille nord-Anatolienne (Turquie). Les images SAR ont été obtenues par les projets Category-1 2532 et AOTR-2436 de l'Agence Spatiale Européenne, et du programme « Geohazard Supersites ».

Un Chapitre I d'introduction présente les éléments fondamentaux de la technique InSAR en géodésie spatiale et sa relation aux travaux de tectonique active initiés depuis 20 ans, suite au séisme de Landers en 1992 (Mw 7.4 en Californie). L'InSAR est une méthode robuste pour la mesure des déformations de surface dont la précision peut atteindre le millimètre par une résolution spatiale réalisée à l'aide de la télédétection (imagerie spatiale). Les méthodes ASAR (Advanced multi-temporal InSAR time series) des séries multi-temporelles appelées « Persistent Scatterer (PSI) » et « Small Baseline (SBI) » offrent l'avantage d'un traitement simultané des images SAR multiples, acquises par séries temporelles, augmentant ainsi la couverture spatiale et la résolution (avec calcul des incertitudes) du signal des zones à faible déformation. En effet, les calculs sur le signal en surface tiennent compte de la réduction du bruit d'acquisition, du délai d'enregistrement due aux caractéristiques de l'atmosphère, des erreurs de résolution sur la topographie, et des incertitudes sur la position orbitales du satellite lors de l'acquisition de l'image SAR. Comparé à la méthode InSAR désormais classique, les approches PSI et SBI permettent l'analyse simultanée de la déformation de surface par pixel (ou parcelle d'image) et empilement d'images SAR par séries temporelles.

Le Chapitre II décrit les principes des séries temporelles PSI et SBI et leur application à l'étude des déplacements postsismiques et lents le long des failles actives. L'analyse de ces déplacements par des investigations détaillées le long des failles peut contribuer à une meilleure compréhension des processus sismogènes et fonctionnement des ruptures sismiques. L'étude de la déformation crustale par les techniques InSAR est consolidée par une comparaison aux résultats des données GPS, l'analyse sismotectonique et les caractéristiques géologiques locales, afin de mettre en évidence les déplacements co- et post-sismiques, lents ou rapides, en surface. Cette contribution à la connaissance du cycle sismique aux abords des failles actives devrait permettre une meilleure évaluation du cycle sismique, du comportement à court et long terme de la déformation crustale et du potentiel pour l'occurrence des séismes futurs.

Le Chapitre III montre les détails de la technique SBI appliquée à l'étude des déformations postsismiques liées au séisme du 21 mai 2003 à Zemmouri (Mw6.8, Atlas du Tell, nord Algérie). Les séries temporelles InSAR obtenues à partir de 31 images Envisat ASAR acquises de 2003 à 2010, révèlent des déplacements de l'ordre

sub-centimétriques dans la zone épiscoptrale. Les résultats montrent l'existence de deux zones de déformation postsismiques en subsidence le long de la côte, localisées aux mêmes emplacements des soulèvements cosismiques obtenus par l'InSAR. La modélisation des déformations postsismiques par inversion des données de surface, utilisant les dislocations élastiques en demi-espace homogène sur des ruptures triangulaires, suggère une déformation en « afterslip » sur une portion superficielle (< 5 km) de la faille cosismique, ceci en accord avec les résultats GPS. La répartition en surface des déformations postsismiques comparée à celle des sédiments meubles et à la fluctuation de la nappe phréatique (par pompage agricole local) indique l'existence d'une déformation d'origine non-tectonique (par compaction). La déformation postsismique (sur ~7 ans) rapportée au moment sismique cumulé équivaut à l'occurrence d'un séisme de magnitude Mw 6.3. Par conséquent, la déformation postsismique cumulée et les contraintes associées peuvent avoir des implications notables sur le modèle de cycle sismique et de la récurrence des forts séismes dans la région d'Alger.

Le Chapitre IV présente une analyse des déformations cosismique et postsismique, liées au séisme du 24 février 2004 à Al Hoceïma (Mw 6.4, Rif, nord Maroc), obtenues par un traitement des images SAR utilisant la technique SBI. A noter que pour cet exemple, la localisation de la faille cosismique était très imprécise étant donné l'absence de ruptures bien identifiées en surface. Le déplacement en surface postsismique a été cartographiée en utilisant des images Envisat ASAR acquises en mode ascendant (15 images) et descendant (15 images). La faute coseismique est cependant nécessaire une révision à la lumière de déformation postseismique d'affiner le meilleur modèle de défaut suggéré dans la pointe sud de la faille. L'analyse et la modélisation des données de surface impliquent l'existence d'une rupture décrochante « aveugle », dextre, de direction NW-SE, avec courbure ou zone de relais sur la gauche liée à la déformation postsismique, sur la zone de déformation cosismique. Bien-que la tectonique crustale du Rif est constituée de chevauchements et pli-failles inverses d'âge tertiaire, la tectonique fini-Quaternaire (Pleistocène supérieur) indique des épisodes extensifs de direction E-W liés à des failles normales de direction N-S, associés à des failles en décrochement conjuguées de direction NW-SE et NE-SW. Dans ce secteur de limite des plaques Afrique-

Eurasie (Ibérie), la collision implique une tectonique avec échappement des blocs et la fragmentation du Rif.

Le Chapitre V est consacré à l'étude des mouvements lents le long de la faille nord Anatolienne en Turquie. L'utilisation de la méthode PSI associée à la modélisation de la déformation de surface en dislocation élastique, combinée aux caractéristiques géologiques observées le long de la faille dans la localité de Ismetpaşa nous a permis de déduire le champ de vitesse et l'étendue de la zone de déformation lente (par opposition à la zone de faille bloquée). Les caractéristiques spatio-temporelles de cette déformation montrent un contrôle lithologique potentiel possible le long de la zone de faille, ce qui ouvre une perspective nouvelle sur les causes des mécanismes des ruptures sismiques. L'analyse des 55 images Envisat ASAR acquises entre 2003 et 2010, illustre clairement la zone de déformation lente et montre un champ de vitesse intersismique graduel entre la zone en « creep » et la partie bloquée de la faille. Le taux de déformation lent varie le long des 100 km de faille d'une façon comparable à la zone de « creep » de la faille de Hayward (branche de la faille de San Andreas en Californie), et atteint un maximum de $\sim 20 \pm 2$ mm/an, proche de la vitesse des plaques ($\sim 25 \pm 1.5$ mm/an). A Ismetpaşa, la vitesse du déplacement lent qui est de 8 ± 2 mm/an, est comparable aux valeurs géodésiques des études précédentes. La modélisation des données PSI révèle une répartition hétérogène des mouvements lents dans la couche sismogène (en profondeur), avec l'apparition de deux zones de rupture principales, limitées aux premiers 5 km depuis la surface, et relâchant 6.2×10^{16} N.m ($M_w = 5.1$) de moment géodésique. Nous reconnaissons ici une corrélation entre des déplacements lents asismiques et les caractéristiques principales des roches environnantes (andésite basaltique, calcaire et serpentinites) montrant des valeurs de friction interne et de résistance au cisaillement relativement basses le long de la faille.

La conclusion générale (Chapitre VI) résume les principaux résultats de la thèse et montre comment les déplacements lents en surface associés à la déformation postsismique sur des failles aveugles ou cachées, et aux déplacements asismiques, peuvent être identifiés et caractérisés à partir des analyses multi-temporelles InSAR. Pour le séisme de Zemmouri (Atlas du Tell, Algérie), notre étude confirme l'existence d'une rupture cachée au large dans la zone en mer, avec un « afterslip » superficiel lié à une rupture complexe avec subsidence côtière co-localisée aux

soulèvements cosismiques. La mise en évidence des déformations postsismiques liées au séisme d'Al Hoceima (Rif, Maroc) contribue à la localisation précise du séisme de 2004, et à l'identification des déplacements co- et postsismiques sur une faille « aveugle ». Les caractéristiques des déplacements lents près de la localité de Ismetpaşa montrent le rôle d'une rupture superficielle lente par rapport aux aspérités bloquées, et l'influence de l'environnement géologique sur les propriétés mécaniques de la faille nord Anatolienne.

Pour les trois cas d'étude présentés dans cette thèse, l'analyse des séries temporelles InSAR donne des informations décisives sur les déformations postsismiques. Deux types de faille active, l'une en mécanisme inverse et l'autre en décrochement, ont été sélectionnés pour illustrer la déformation postsismique. Des signaux significatifs et remarquables ont été observés pour les deux types de faille et dans le cas de séismes modérés ou forts. L'analyse InSAR révèle l'existence de divers signaux sur les processus de déplacement visible en surface. Dans le cas de la faille inverse, les signaux cosismiques et postsismiques sont en opposition, alors que dans le cas de la faille en décrochement dextre les signaux cosismiques et postsismiques de la déformation sont comparables (même mécanisme de faille dextre). Le troisième exemple étudié montre un cas de déformation asismique lente (en creep) qui suggère une initiation des déplacements postsismiques depuis environ 70 ans, en liaison avec les deux séismes majeurs de M_w 7.3 (1944) et de M_w 6.9 (1951). Bien-que la répétition de l'acquisition des images radar nécessite 35 jours, l'utilisation des images Envisat SAR a permis l'étude des déformation cosismique et postsismique pour des séismes modérés à forts. La perspective de l'utilisation de nouvelles générations d'images SAR (TerraSAR-X, et Sentinel qui permettent une acquisition tous les 3 à 12 jours) offrent la possibilité d'augmenter la résolution des images, et une réduction importante des effets de la décorrélation temporelle. Par conséquent, les nouvelles générations de constellations et capteurs d'image SAR en multi-fréquences avec réduction des temps d'acquisition, semblent très prometteurs pour l'étude spatio-temporelle de la déformation crustale.

Au cours de cette thèse, nous avons distingué quatre mécanismes de déformation possibles (visco-élastique, poro-élastique, « afterslip » et zone de faille en effondrement ou bien zone de faille scellée) liés aux déplacements en surface, aux abords de la rupture et mesurables par les techniques géodésiques. La prépondérance

des mécanismes de déformation postsismique suggère le développement d'un système analytique dédié aux mécanismes de déformation postsismique. L'apport de chaque mécanisme au modèle de déformation observé peut-être déduit de la longueur d'onde et du temps écoulé de l'amplitude des déplacements. Par conséquent, le mécanisme de « l'afterslip » apparaît comme dominant pour les déformations postsismiques liées aux séismes modérés ou forts, aux processus visco-élastique profonds et/ou à la relaxation poro-élastiques, pouvant parfois contribuer aux déformations de surface cumulées. Cependant, on ne peut ignorer l'aspect complexe de la combinaison des méthodes d'analyse des mécanismes de déformation qui requièrent des traitements robustes pour éviter les résultats peut fiables. Par exemple, malgré l'apport des processus visco-élastiques et poro-élastiques à la relaxation postsismique dans le cas du séisme de Zemmouri, les résultats InSAR ne permettent pas la caractérisation des déplacements horizontaux, car restreints à la déformation suivant le LOS. Le moment cumulé des déplacements postsismiques en « afterslip » peuvent atteindre 30% de la déformation totale cosismique liée à un fort séisme ($M \geq 6$) ; les séismes faibles à modérés ($M < 6$) peuvent exceptionnellement montrer de forts déplacements en « afterslip » qui peuvent atteindre 70% du moment cosismique. Par ailleurs, les déplacements lents asismiques (creep) peuvent s'initier lors des déplacements en « afterslip » et se continuer durant plusieurs années tels qu'illustrés par l'exemple d'Ismetpaşa le long de la faille nord anatolienne.

La modélisation en problème inverse utilisant la dislocation élastique sur des failles triangulaires avec une procédure de minimisation non-linéaire basée sur des algorithmes de simulation, a été utilisée pour obtenir la répartition des déplacements liée à une surface de rupture. Les résultats de la modélisation obtenus lors des différents cas d'étude de notre thèse indiquent que « l'afterslip » ou la déformation asismique sont le plus souvent confinés dans la partie superficielle de la croûte supérieure (< 5 km), ce qui est en bon accord avec d'autres études de zones de faille actives. Les profondeurs superficielles de « l'afterslip » et des mouvements asismiques le long des zones de rupture sont cohérents avec les caractéristiques physiques de la déformation (velocity-strengthening behavior) et des roches fragiles par rapport à un substratum plus solides. Par ailleurs, notre étude confirme encore une fois que les déplacements « afterslip » sont complémentaires et entourent généralement les zones de rupture cosismique avec de grands déplacements, comme

c'est le cas pour le séisme de Zemmouri (chapitre III) et dans une moindre mesure pour le séisme de Al Hoceima (chapitre IV).

En perspective, et pour pouvoir développer des évaluations fiables de l'aléa sismique, il est important de mieux comprendre les caractéristiques du cycle sismique, des comportements de faille, des mécanismes générant les séismes et de leur interaction. Le cycle sismique est ici conceptualisé par le biais de l'accumulation et du relâchement des déformations élastiques sur les failles, en complément de la déformation transitoire. Une analyse réaliste de l'aléa sismique doit explorer les nombreuses possibilités de percevoir le mode de cycle sismique, en incluant l'accumulation des déformations liées au mouvement des plaques tectoniques, des changements de contrainte dynamiques durant les ruptures et de la déformation postsismique transitoire. Cette analyse de l'aléa sismique doit pouvoir expliquer la relation entre les déplacements sismiques et asismiques, la segmentation des failles et les variations spatiales importantes de l'intensité des vibrations sismiques. Le développement de l'évaluation de l'aléa sismique nécessite des observations détaillées en champ proche, associées à des données complémentaires « in-situ » de la déformation de la croûte terrestre. Par conséquent, les études géodésiques par satellite en général, et de l'InSAR en particulier, contribuent significativement à une meilleure compréhension du cycle sismique et au développement d'une évaluation réaliste de l'aléa sismique d'une zone sismogène.

Notre étude montre l'utilité et le rendement des méthodes InSAR pour l'identification et la caractérisation de la déformation crustale liée aux séismes, ainsi qu'à la déformation asismique, ou bien à la déformation lente en profondeur associée aux mouvements des plaques tectoniques. Nous montrons par ce travail la contribution des séries temporelles à l'étude des déformations lentes de surface liée à la tectonique active. Nous démontrons également qu'en l'absence de la rupture en surface, la contribution des déplacements cosismiques combinée aux répliques des séismes aide à une meilleure définition de la géométrie d'une faille sismique (e.g. voir le cas du séisme de 2004 à Al Hoceima, chapitre IV). Il est également utile de noter l'importance de l'utilisation des deux modes d'acquisition ascendantes et descendantes des images radar satellite afin de contraindre la déformation cosismique et postsismique. Par ailleurs, les données GPS sont souvent bien utiles et complémentaires aux données InSAR pour déterminer les paramètres de la

déformation cosismique et postsismique (e.g., le cas du séisme de Zemmouri et la déformation postseismique en 2003), et la corrélation des taux de mouvements lents (voir le cas des mouvements asismiques à Ismetpaşa). En parallèle, un mouvement non-tectonique lié aux fluctuations de la nappe phréatique a été identifié dans le bassin de la Mitidja, lors de l'étude des mouvements postsismiques liée au séisme de Zemmouri de 2003. Enfin, nous pensons que l'application de la méthode InSAR, seule, peut ne pas être suffisante pour contraindre les paramètres de la déformation cosismique et postsismique, ou bien asismique, et qu'il est nécessaire d'associer les mesures de terrain en tectonique et géodésie (conventionnelle, GPS), et l'analyse géologique pour une meilleure estimation de la tectonique crustale.

Chapter I :
INTRODUCTION

1. INTRODUCTION

Understanding the mechanics of active faults is important for building reliable seismic hazard evaluations and better understanding of the earthquake physics and earthquake deformation cycle. The simplest form of the earthquake cycle was conceptualized by Reid [1910] and is referred to as elastic rebound theory (Figure 1.1), which was the first attempt on the earthquake surface deformation based on observations and field measurements. The idea was based on the cyclic buildup and release of elastic strain around faults, which is complemented by transient deformation at the Earth's surface. The earthquake cycle is typically split into three phases: rapid displacement that occurs during an earthquake is referred to as coseismic; it is followed by postseismic transient movements for years to decades, which is finally decays to a steady-state interseismic deformation for typically hundreds to thousands of years [e.g. Thatcher and Rundle, 1979; Wright, 2002; Feigl and Thatcher, 2006]. In order to understand the fault behaviors and driving mechanisms behind the earthquakes and the interaction between them, it is necessary to examine the spatial and temporal evolution of the crustal deformation along active faults. Although, we do not have deformation observations with modern instruments spanning a complete earthquake cycle because of the long interseismic-event time in many fault zones, we can observe deformation around faults at different stages of the cycle by looking globally [Wright et al., 2013].

Crustal deformation observations by satellite geodesy have contributed significantly to our understanding of tectonics and earthquakes. Measurements of surface deformation are routinely used to constrain the subsurface geometry of active faults and the spatial distribution of coseismic, postseismic and aseismic slip. Recent advances in satellite geodesy, particularly in InSAR, have led to a dramatic improvement in the quantity and quality of deformation measurements of the earthquake cycle [e.g. Wright, 2002; Akoglu et al., 2006; Peyret et al., 2011; Cakir et al., 2012]. Since its application to the 1992 Landers earthquake [Massonet et al., 1993], the InSAR technique has been widely used for measuring the coseismic

displacements associated with continental earthquakes [e.g. Cakir et al., 2003; Sudhaus and Jónsson, 2011], but also particularly valuable for examining and constraining postseismic [e.g. Ryder et al., 2007; Biggs et al., 2009], interseismic [e.g. Wang et al., 2009; Cavalie et al., 2012] and aseismic slip [e.g. Cakir et al., 2005, 2012; Champenois et al., 2012] deformation in several cases.

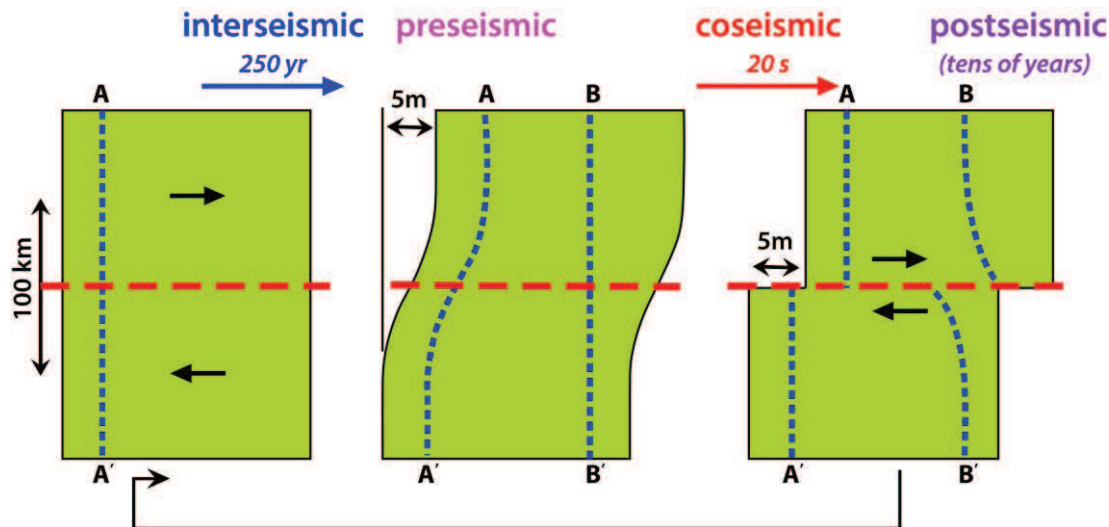


Figure 1.1 : Schematic of Reid [1910]’s *elastic rebound* model of the earthquake cycle (modified from Wright [2002]). **a)** Map view of area spanning a hypothetical fault, in the instant after the last earthquake. **b)** The same area, in 250 years. The profile A-A’, straight at the beginning of the cycle, has become curved. This is known as interseismic strain accumulation. **c)** The same area, 20 s later, after an earthquake. A-A’ is once more a straight line, but this time with a 5 m step at the fault. B-B’, straight immediately before the earthquake, is now curved with an offset of 5 m at the fault, decaying with large distances from the fault.

The surface deformation associated with moderate-to-large size earthquakes ($M > 6$) is, however, very often hardly visible in the field since deformation occur on blind faults that do not produce a visible rupture on the earth surface (e.g., Al Hoceima 2004, M_w 6.4 [Cakir et al., 2006]; Ain Temouchent 1999, M_w 5.7 [Belabbes et al., 2009b]) or hidden faults beneath Quaternary deposits or offshore faults along the coastlines (e.g., Zemmouri 2003; M_w 6.8 [Belabbes et al., 2009], Bam 2003, M_w 6.6 [Funning et al., 2005]). One of the utmost advantages of InSAR is its capability to monitor such tectonically complex zones and provide the surface field displacement (to the subtle scale) and related seismic rupture parameters. Recent advanced InSAR techniques that can measure displacements with millimeter-level accuracy reveal transient signals in the deformation fields produced by both moderate and large earthquakes.

Postseismic transient signals exhibit characteristic time scales ranging from weeks to decades and distance scales from hundreds of meters to hundreds of kilometers. Geodetic measurements following numerous large earthquakes show that amplitudes of postseismic deformation are in general an order of magnitude smaller than coseismic deformation and decreases exponentially with time over a period of years to decades [Schwartz and Rokosky, 2007]. However, the postseismic contribution following moderate sized earthquakes has been inferred to exceed in some cases the coseismic deformation (e.g. M 6.0, 2004 Parkfield earthquake [Freed, 2007]). There are three mechanisms that have been proposed and widely used to explain postseismic deformation, which are (1) afterslip on the coseismic rupture plane [Smith and Wyss, 1968], (2) visco-elastic relaxation in the lower crust/upper mantle [Pollitz *et al.*, 2000], and (3) poro-elastic rebound [Peltzer *et al.*, 1998]. While in some cases only one mechanism is claimed to have operated [Freed, 2007], several mechanisms are thought to contribute to postseismic deformation in others [Hearn *et al.*, 2009].

Fault creep, or aseismic slip on a fault plane, is thought to be an important component of the earthquake cycle [e.g. Tse and Rice, 1986]. Although, the majority of active faults may be locked, accumulating strain over a long period of time (e.g., up to 300 years along a single segment of the North Anatolian fault; Barka, [1996]) and releasing it abruptly during moderate-to-large earthquakes ($M_w > 6$), some faults slip freely, accumulating little or no strain and generating no significant earthquakes [Steinbrugge, *et al.*, 1960; Thatcher, 1979; Burford and Harsh, 1980; Bürgmann *et al.*, 2000]. Faults that exhibit surface creep can appear to be locked at shallow or mid crustal depths, but nevertheless episodically produce moderate earthquakes. Examples of such partially locked faults include the Hayward fault [Savage and Lisowski, 1993; Schmidt *et al.*, 2005], the Superstition Hills fault [Bilham, 1989; Wei *et al.*, 2009], the Longitudinal Valley fault [Champenois *et al.*, 2012; Thomas *et al.*, 2014] and the Ismetpaşa segment of the North Anatolian Fault [Ambraseys, 1970; Cakir *et al.*, 2005]. Knowledge of the extent and rate of aseismic creep on the fault plane is therefore critical for reliable assessment of seismic hazard as it effectively reduces the fault surface area capable of rupture in earthquakes. Its spatiotemporal variation along faults has also important implications for forecasting the timing,

locations, and potential sizes of future earthquakes and for understanding the fault behavior [Bürgmann *et al.*, 2000].

The possibility to study the spatial and temporal evolution of these slow crustal motions is a key issue with important implications in the understanding of the dynamics of the deformation phenomena. An effective way to study the temporal behavior is the generation of deformation time series. Recent InSAR time series approaches [e.g. Ferretti *et al.*, 2000; Hooper, 2008] are capable of mapping slow surface deformation, such as postseismic and aseismic slip, over time. These approaches have been successfully used to reveal slow crustal motions in several cases; for instance, postseismic deformation following the L'Aquila 2009, M_w 6.3, earthquake (Italy) [Lanari *et al.*, 2010], interseismic strain accumulation across the Gazikoy-Saros segment of the NAF (Turkey) [Motagh *et al.*, 2007], and slow surface creep on NAF faults [Cakir *et al.*, 2014].

Due to aforementioned reasons throughout this dissertation study, the InSAR time series techniques are applied to selected active faults within the Africa-Eurasia convergence zone to reveal typically slow surface deformation characteristics. After a presentation on the fundamentals of InSAR techniques, I present the postseismic deformation following the 2003 Zemmouri (M_w 6.8, Algeria) earthquake (Chapter 3), the coseismic and postseismic deformation associated with the 2004 Al Hoceima (M_w 6.4, Morocco) earthquake (Chapter 4), and the aseismic slip on the Ismetpaşa segment of the NAF (Chapter 5). Finally, a general conclusion provides with the main results and perspectives of this contribution.

Chapter II :
METHODOLOGY

2. METHODOLOGY

InSAR is a powerful technique for measuring surface deformation because of the high spatial resolution achieved and the ability to acquire the data remotely. While ground displacement due to many geophysical processes are now routinely calculated with conventional InSAR, mapping the subtle and slow surface deformation such as aseismic processes requires more sophisticated approaches than the classical differential InSAR method which is often limited by atmospheric errors and signal decorrelation. Advanced techniques increase the number of locations where a deformation signal can be extracted and reduce the associated error with regard to involve the simultaneous processing of multiple SAR acquisitions in time [Ferretti et al., 2000, 2001]. Such advanced techniques are able to reduce the effects of noise and signal decorrelation due to atmospheric effects, digital elevation model (DEM) errors, and orbital inaccuracies [Hooper et al., 2007]. Compared to conventional InSAR, the advanced techniques generate time series of ground deformations for individual targets using multi-temporal stacks of SAR images with regard to these targets that have a constant echo over the time and that are called persistent scatterers (PS) [Ferretti et al., 2000; Hooper et al., 2004; Kampes, 2005].

Currently there are two broad categories of algorithms for processing multiple acquisitions, persistent scatterer and small baseline approaches, which are optimized for different models of scattering. In this dissertation, ground displacements have been calculated using the StaMPS (Stanford Method for Persistent Scatterers) [Hooper et al., 2007; Hooper, 2008] software package. The StaMPS uses ROI_pac software [Rosen et al., 2004] for focusing the raw images, and DORIS software [Kampes and Usai, 1999] for calculating interferograms. The topographic phase contribution in the interferograms is removed using the SRTM 90-m DEM data [Farr et al, 2007]. In this chapter, persistent scatterer (PSI) and small baseline (SBI) algorithms that have been applied in this dissertation will be generally described.

2.1 Persistent Scatterer InSAR (PSI)

The PSI method is an extension to the conventional InSAR techniques, which addresses both decorrelation and atmospheric problems. The decorrelation degree of radar signals depends on the distribution of scattering centers on the ground that contributes to a pixel. In a radar image, the reflected wave from a resolution element is the coherent sum of individual wavelets scattered by many discrete scatterers on the ground (Figure 2.1). If these scatterers move with respect to each other between satellite passes, the phase of the returning radar echo will vary in a random manner which leads to decorrelation (Figure 2.1a). In contrast, if one of the scatterers contributing to the pixel is much brighter than the background scatterers, the variance in the phase of the radar echo due to relative movement of the background scatterers will be reduced, and may be small enough to enable extraction of the underlying deformation signal (Figure 2.1b).

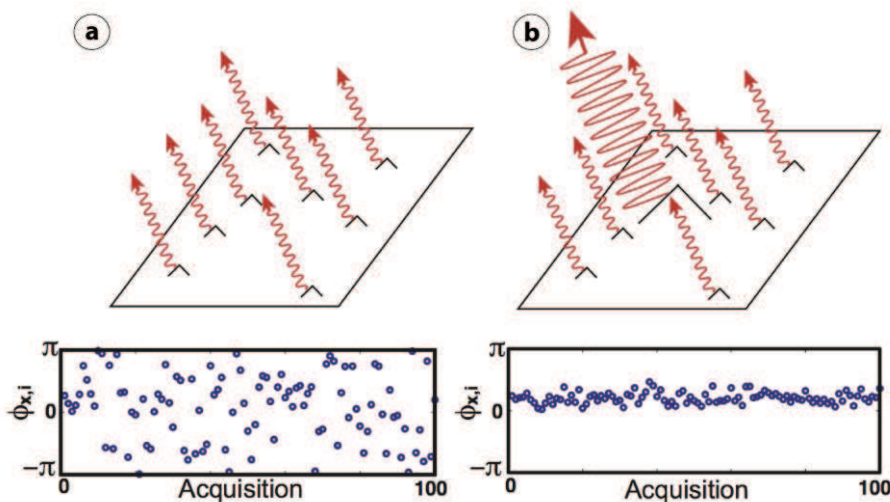


Figure 2.1 : Phase simulations from *Hooper et al.* [2007] for **(a)** a distributed scatterer pixel and **(b)** a persistent scatterer pixel. The cartoons above represent the scatterers contributing to the phase of one pixel in an image and the plots below show simulations of the phase for 100 iterations, with the smaller scatterers moving randomly between each iteration. The brighter scatterer in (b) is three times brighter than the sum of the smaller scatterers.

The approach in which these pixels are identified and isolated, was first achieved for InSAR applications by *Ferretti et al.* [2000, 2001], with further improvements by *Colesanti et al.* [2003], and is referred to as Permanent Scatterers Technique™ in their patented method. There are various PSI approaches that have

since been developed [e.g., *Adam et al.*, 2003; *Crosetto et al.*, 2003; *Lyons and Sandwell*, 2003; *Werner et al.*, 2003; *Kampes*, 2005; *Hooper et al.*, 2007; *Ketelaar et al.*, 2008]. In comparison, PS selection algorithms and deformation estimation methods are different in between these approaches. For many of these algorithms, initial sets of PS pixels are identified by analysis of their amplitude scintillations in a series of interferograms. Furthermore, these methods consider not only a PS pixel is characterized by a certain phase stability over time, but also its phase history must match an assumed model of how displacement varies with time [*Ferretti et al.*, 2000, 2001; *Adam et al.*, 2003; *Lyons and Sandwell*, 2003; *Werner et al.*, 2003; *Kampes*, 2005]. These algorithms have been very successful for urban areas that contain large numbers of man-made structures that tend to produce very efficient reflectors that dominate background scattering. Since these methods use a functional temporal model to identify PS pixels, approximate knowledge of how the deformation varies with time is required a priori. Commonly, deformation is assumed to be steady-state or periodic in nature, whereas the temporal nature of the deformation is usually one of the phenomena that we wish to detect. In comparison to these approaches, the StaMPS persistent scatterer approach is applicable in areas undergoing non-steady deformation, such as most volcanoes and aseismic slip, with no prior knowledge of the variations in deformation rate since it does not use any temporal deformation model in the PS identification step [*Hooper et al.*, 2007]. It has been successfully used to reveal slow surface creep along the Longitudinal Valley (Eastern Taiwan) [*Champenois et al.*, 2012], and along the North Anatolian Fault (Turkey) at Izmit [*Cakir et al.*, 2012] and Ismetpaşa [*Cetin et al.*, 2014a].

There are four parts in StaMPS; interferogram formation, PS identification, PS selection and displacement estimation.

2.1.1 Interferogram formation:

In order to select PS pixels with StaMPS, 12 interferograms are usually sufficient instead of the least 25 interferograms relying on functional temporal model algorithms [*Colesanti et al.*, 2003]. Suppose we form N single-look interferograms from $N+1$ images, all with respect to one “master” image (Figure 2.2a), which minimizes the sum decorrelation that is a product of four terms, dependent on temporal baseline (T), spatial perpendicular baseline (B_{\perp}), Doppler centroid baseline

(F_{DC}) and thermal noise [Zebker and Villasenor, 1992]. The critical values are dependent on the data set, but typical values for the ERS satellites acquired in arid regions are $T^c = 5$ years, $B_{\perp}^c = 1100$ m and $F_{DC}^c = 1380$ Hz. We choose the master that maximizes total correlation, assuming a constant value for thermal correlation. PS identification algorithm does not actually require that all interferograms are formed with respect to one master, only that all are coregistered to one master [Hooper et al., 2007].

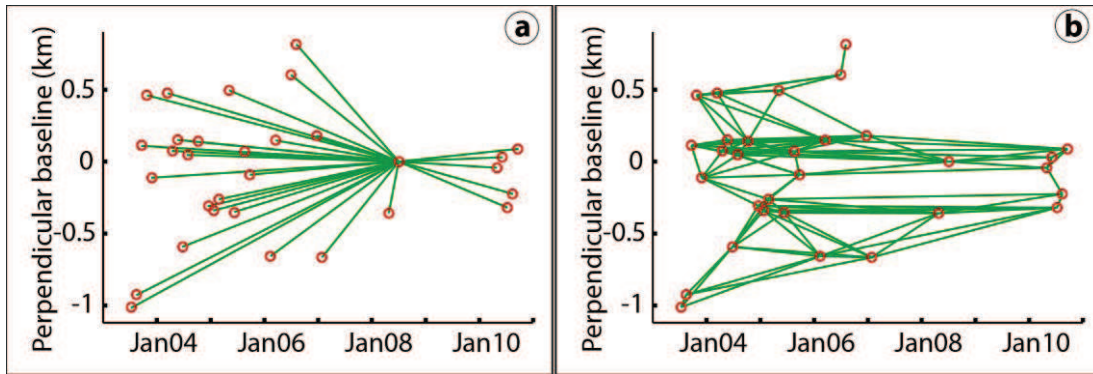


Figure 2.2 : Sketch of the interferometric data pairs (green lines) selection for **a)** single (PSI) and **b)** multiple master (SBI) image (red circles) configurations. The SAR dataset is relevant to the Envisat ASAR acquisitions carried out from 12-July-2003 to 18-September-2010 covering the 2003 Zemmouri earthquake region.

In order to avoid high decorrelation due to larger temporal separation, perpendicular baseline and Doppler separation that cause standard coregistration routines fail, Hooper et al. [2007] have developed a coregistration algorithm, which uses an amplitude-based algorithm to estimate offsets in position between pairs of images with good correlation. As in conventional InSAR, the geometric phase is corrected as first flattening the interferograms and then estimating the phase due to deviation of the real surface from the reference ellipsoid by transforming a DEM (Digital Elevation Model) into the radar coordinate system. Two error terms arise in this processing, look angle error and squint angle error. The look angle error is due almost entirely to error in the DEM, and is commonly referred to as DEM error. Squint angle error is commonly avoided in conventional InSAR by processing both images to a common squint angle [Hooper et al., 2007].

Eventually, the position of every pixel is estimated in a geocoded reference frame using the orbital parameters and the DEM. Theoretically, our estimates of

position could be improved using various parameters estimated during processing, but positional accuracy to within several meters is usually sufficient for the most deformation modeling purposes [Hooper *et al.*, 2007].

2.1.2 PS identification:

We use both amplitude and phase analysis to estimate the PS probability for each pixel in the series of interferograms that we have formed. Although a PS pixel is defined by phase stability, there is a statistical relationship between amplitude stability and phase stability. For phase analysis, an initial selection of candidate pixels is made based on amplitude analysis using amplitude dispersion, D_A , which is the ratio of the standard deviation of the amplitude over its mean defined by *Ferretti et al.* [2001]. For StaMPS, the threshold value of $D_A \leq 0.4$ reduces the data by an order of magnitude and includes most of the PS. Then the PS probability is refined using phase analysis in an iterative process. Finally, the PS probability is estimated for those PS pixels not included in the initial selection [Hooper *et al.*, 2007].

2.1.3 PS selection:

We select PS candidates on the basis of their phase characteristics since PS are defined by phase stability. Current methods for selecting PS candidates rely on thresholding pixel amplitude dispersion with time [Ferretti *et al.*, 2001]. If signal to noise ratio (SNR) is high (>10), amplitude dispersion is an accurate proxy for phase standard deviation, which leads to pick bright PS, e.g., certain man-made structures. However, the simple relationship between amplitude dispersion and phase stability breaks down for low SNR scatterers, and the method is no longer successful.

The StaMPS approach is to form interferograms and remove most of the topographic phase signature using a digital elevation model (DEM). The residual phase, ϕ , of the x th pixel in the i th topographically corrected interferogram can be written as the sum of 5 terms,

$$\phi_{x,i} = \phi_{def,x,i} + \phi_{\alpha,x,i} + \phi_{orb,x,i} + \phi_{\epsilon,x,i} + n_{x,i} \quad (2.1)$$

where ϕ_{def} is the phase change due to movement of the pixel in the satellite line-of-sight (LOS) direction, ϕ_{α} is the phase equivalent of the difference in atmospheric retardation between passes, ϕ_{orb} is the phase due to orbit inaccuracies, ϕ_{ϵ} is the residual topographic phase due to error in the DEM and n is the noise term due to

variability in scattering from the pixel, thermal noise and coregistration errors. PS is defined as pixels where n is small enough that it does not completely obscure the signal [Hooper *et al.*, 2004].

Variation in the first four terms of equation (2.1) can dominate the noise term making it difficult to identify which scatterers are persistent. ϕ_{def} , ϕ_α and ϕ_{orb} are assumed to be spatially correlated over distances of a specified length scale, L , and that ϕ_ε and n are uncorrelated over the same distance, with a mean of zero. If the positions of other PS are already known, averaging the phase of all those within a circular patch centered on pixel x with radius L implies

$$\bar{\phi}_{x,i} = \bar{\phi}_{def,x,i} + \bar{\phi}_{\alpha,x,i} + \bar{\phi}_{orb,x,i} + \bar{n}_{x,i} \quad (2.2)$$

where the bar denotes the sample mean of the patch and \bar{n} is the sum of the sample means of $n + \phi_\varepsilon$ and is assumed small. Subtracting equation (2.2) from equation (2.1) leaves

$$\phi_{x,i} - \bar{\phi}_{x,i} = \phi_{\varepsilon,x,i} + n_{x,i} - \bar{n}'_{x,i} \quad (2.3)$$

where $\bar{n}' = \bar{n} + (\bar{\phi}_{def} - \phi_{def}) + (\bar{\phi}_\alpha - \phi_\alpha) + (\bar{\phi}_{orb} - \phi_{orb})$.

The phase error from uncertainty in the DEM is proportional to the perpendicular component of the baseline, B_\perp , so $\phi_{\varepsilon,x,i} = B_{\perp,x,i} K_{\varepsilon,x}$ where K_ε is a proportionality constant. Substituting this expression into equation (2.3) we are able to estimate for K_ε pixel x in a least square sense, as this is the only term that would correlate with baseline. A measure is defined based on the temporal coherence of pixel x as

$$\gamma_x = \frac{1}{N} \left| \sum_{i=1}^N \exp \{ j (\phi_{x,i} - \bar{\phi}_{x,i} - \hat{\phi}_{\varepsilon,x,i}) \} \right| \quad (2.4)$$

where N is the number of available interferograms and $\hat{\phi}_{\varepsilon,x,i}$ is our estimate of $\phi_{\varepsilon,x,i}$. Assuming $\bar{n}'_{x,i}$ values are small, γ_x is a measure of the phase stability of the pixel and hence an indicator of whether the pixel is a PS. Statistically, however, pixels with higher γ_x are more likely to be PS.

The final step is to select PS based on the calculated values of γ_x (2.4). Any pixel with random phase has a finite chance of having high γ_x and therefore we can only select in a probabilistic fashion. Therefore, Hooper *et al.* [2004] described a

threshold value γ^{thresh} that maximizes the number of real PS selected while keeping the fraction of random phase pixels selected (false positives) below a specified value, q . The probability density function (PDF) of γ_x for the data, $p(\gamma_x)$, is a weighted sum of the PDF for the random phase pixels, $p_r(\gamma_x)$, and the PDF for the non-random phase (PS) pixels, $p_{ps}(\gamma_x)$ i.e.,

$$p(\gamma_x) = (1 - \alpha)p_r(\gamma_x) + \alpha p_{ps}(\gamma_x). \quad (2.5)$$

We want to find γ^{thresh} such that

$$\frac{(1 - \alpha) \int_{\gamma^{thresh}}^1 p_r(\gamma_x) d\gamma_x}{\int_{\gamma^{thresh}}^1 p(\gamma_x) d\gamma_x} \quad (2.6)$$

where $p_r(\gamma_x)$, and α are unknown. For low γ_x values (< 0.3), $p_{ps}(\gamma_x) \approx 0$. Assuming then that

$$\int_0^{0.3} p(\gamma_x) d\gamma_x = (1 - \alpha) \int_0^{0.3} p_r(\gamma_x) d\gamma_x \quad (2.7)$$

allows a conservative value of α to be estimated and hence we can calculate γ^{thresh} .

Since the risk of false positives increases with increasing amplitude dispersion, the number of PS selected further by calculating γ^{thresh} is refined as a function of amplitude dispersion. For each PS candidate, the value of γ^{thresh} is used that corresponds to the amplitude dispersion of the candidate as the threshold value. In order to exclude sideslopes, adjacent selected pixels are assumed to be dominated by the same scatterer, and discard all but the pixel with the highest γ_x value [Hooper *et al.*, 2007].

2.1.4 Displacement estimation:

Once the most likely PS pixels are selected, their phase is corrected for DEM error by subtracting the estimated values of $\phi_{\epsilon,x,i}$,

$$\phi_{x,i} - \hat{\phi}_{\epsilon,x,i} = \phi_{def,x,i} + \phi_{\alpha,x,i} + \phi_{orb,x,i} + \phi'_{\epsilon,x,i} + n_{x,i} \quad (2.8)$$

where $\phi'_{\epsilon,x,i}$ is the residual DEM error term due to uncertainty in our estimate of $K_{\epsilon,x}$, including any spatially correlated DEM error.

In order to retrieve the phase due to deformation, $\phi_{def,x,i}$, the phase must be unwrapped. In this analysis, the three-dimensional unwrapping algorithm described

by *Hooper and Zebker* [2007], two in space and one in time, is used to have more reliable results.

After unwrapping, several terms remain in equation (2.8), which mask ϕ_{def} . Unlike ϕ_{def} , the spatially correlated portion of these terms is assumed to be uncorrelated temporally. Thus, by high-pass filtering the unwrapped data in time then low-pass filtering in space, we are able to estimate the spatially correlated error (similar to *Ferretti et al.* [2001]). Subtracting this signal from the equation (2.8) leaves just ϕ_{def} and spatially uncorrelated error terms that can be modeled as noise.

The detailed processing procedure of PSI can be found at *Hooper et al.* [2004, and 2007].

2.2 Small Baseline Processing (SBI)

The targets of SB methods are those pixels whose phases when filtered decorrelate little over short time intervals, referring to as slowly-decorrelating filtered phase (SDFP) pixels by *Hooper* [2008]. Standard SB approaches [*Berardino et al.*, 2002; *Schmidt and Bürgmann*, 2003] work with multi-looked and individually phase-unwrapped interferograms, which does not take advantage of two potential benefits provided by processing multiple acquisitions together. The first is the potential to process the data at the highest possible resolution, which enable identification of isolated SDFP pixels surrounded by completely decorrelated pixels. The second is the ability to unwrap the phase more robustly in three dimensions. StaMPS SBI approach operates on single-look images to identify single-look SDFP pixels directly, and uses a new statistical algorithm proposed by *Hooper* [2010] for three-dimensional unwrapping that is applicable to single- or multiple-master time series.

2.2.1 Small Baseline interferograms

In order to maximize the correlation of the produced interferograms, small baseline methods seek to minimize the perpendicular, temporal and Doppler baselines, which will limit spatial decorrelation effects and increase the number of observable ground points [*Berardino et al.*, 2002; *Hooper*, 2008]. The data pairs used to produce interferograms are characterized by a small perpendicular baseline, while

ensuring that no isolated clusters are present in the network of image pairs (Figure 2.2b). In SBI analysis minimum 5 images are required, however, in practice typically more are necessary to provide the minimum correlation requirements. The recombination of the resampled SLC images from the PS processing are used to generate the interferograms by filtering in azimuth to exclude non-overlapping Doppler spectrum, and in range to reduce the effects of geometric decorrelation. Geometric phase is estimated by orbital ephemerides and a DEM, and subtracted [Hooper, 2008].

2.2.2 SDFP pixel selection

An initial subset of pixels expecting to include almost all SDFP pixels is selected through amplitudes analysis. For Gaussian scatterer pixels, an indication of the phase stability is given by the amplitude difference dispersion, $\widehat{D}_{\Delta A} \equiv \sigma_{\Delta A}/\mu_A$, which is the ratio of the standard deviation of the difference in amplitude between master and slave over the mean amplitude. This is similar to the amplitude dispersion index derived by *Ferretti et al.* [2001] for point scatterers. However, $D_{\Delta A}$ is a better estimate of phase stability in the case where spectral filtering has been applied. Note that although the same algorithm [Hooper et al., 2007] is used to select both PS and SDFP pixels, different sets of pixels are chosen as the algorithm is applied to different sets of interferograms i.e. single master with no spectral filtering vs. multiple masters with spectral filtering. Details of processing procedure of SBI technique can be found at Hooper [2008].

2.3 Concluding Remarks

The advanced InSAR time series algorithms offer many advantages with respect to conventional InSAR regardless of the selected approach. First of all, atmospheric artifacts can be detected and filtered out due to their different space-time behavior with respect to the deformation signal [Ferretti et al., 2000; Berardino et al., 2002]. Second, topographic artifacts and unwrapping errors can be diminished using space-time data redundancy [Pepe and Lanari, 2006; Hooper and Zebker, 2007]. Moreover, possible orbital errors can be effectively compensated using the measurements of a limited number of GPS stations [Gourmelen et al., 2010; and references therein]. All these characteristics contribute to improve the measurement

final precision up to about 1 mm/yr and 5 mm for determination of velocity maps and time series displacements, respectively [*Casu et al.*, 2006; *Lanari et al.*, 2007].

On the other hand, there are limitations to the PSI method. StaMPS approach is the improved version of the method, which addresses these limitations and includes other minor adjustments to the method. The first limitation is the step to estimate spatially correlated terms depends on the assumed length scale of the correlation, which is fixed with a band-pass filtering method that adapts to any phase gradient present in the data itself. The second limitation is the phase unwrapping is implemented as a series of two-dimensional (2-D) problems, leading to artifacts in the unwrapped phase. Two algorithms are developed to solve the problem, the first being a true three-dimensional (3-D) algorithm and the second being a pseudo-3-D algorithm. The 3-D algorithm is only applicable where there are no multiple-cycle phase discontinuities and no 2-D closed-loop discontinuities. For other cases, the pseudo-3-D algorithm is applicable [*Hooper et al.*, 2007; *Hooper*, 2010].

Regarding the main limitations of the SBI technique, the unwrapping errors and the unfiltered atmospheric artifacts characterize the main error sources in the deformation retrieval process. Indeed, they may affect the accuracy and the coherent pixel density of the obtained results. In addition, there are limitations related to the InSAR technology that is essentially based on SAR sensors operating at C-band. In this case, the coherence is essentially maintained only in urbanized and rocky areas. The next generation sensors such as the ALOS-PALSAR system that operate at lower frequencies of the electromagnetic spectrum and in particular within the L-band (1.27 GHz frequency corresponding to a 23.6 cm wavelength) can play a key role in this context. Although, a sensitivity reduction in the displacement detection will be caused by the wavelength increase, a significant improvement of the coherence characteristics is also expected in the generated differential InSAR interferograms [*Lanari et al.*, 2007]. Furthermore, another promising element is the development of SAR sensor constellations such as the COSMO-SKYMED, TerraSAR-X and Sentinel that should allow a significant reduction in the SAR sensor revisit time with a drastic and positive impact on the temporal decorrelation phenomena.

In the following, through the analysis of a number of selected case studies within the African-Eurasian convergence zone, we use these advanced InSAR

techniques to monitor and characterize the field displacements associated with the small-scale deformation along seismogenic faults.

Chapter III :
**Postseismic Deformation Following The 21 May 2003
Zemmouri Earthquake (Mw 6.8) In The Tell Atlas
Of Northern Algeria**

3. POSTSEISMIC DEFORMATION FOLLOWING THE 21 MAY 2003 ZEMMOURI EARTHQUAKE (M_w 6.8) IN THE TELL ATLAS OF NORTHERN ALGERIA

3.1 Introduction

Improving our understanding of the crustal deformation and the earthquake cycle requires detailed analysis of postseismic deformation, a transient response of the lithosphere to the stresses changes caused by moderate to large earthquakes. The 21 May 2003 Zemmouri earthquake and related coseismic rupture (M_w 6.8) provides a noteworthy case study for postseismic deformation associated with thrust slip events. This seismic event is the largest continental thrust-slip earthquake of the last decade that can be studied with space geodesy in the Tell Atlas of northern Algeria. Coseismic studies using InSAR, teleseismic data, coastal uplift and GPS measurements, combined with the mainshock and aftershock seismicity distribution revealed a N60°-65° trending fault rupture, dipping 40° to 50° SE and located offshore about 8-13 km from the coastline [Delouis *et al.*, 2004; Meghraoui *et al.*, 2004; Ayadi *et al.*, 2008; Mahsas *et al.*, 2008; Belabbes *et al.*, 2009].

Following the 2003 Zemmouri earthquake, the study of continuous GPS (CGPS) measurements at 6 benchmarks gave evidence of < 1 cm/yr postseismic deformation during 2.5 years [Mahsas *et al.*, 2008]. The CGPS data can be best explained with shallow rupture patches (<7.5-km-depth) with up to 30 cm afterslip, inferring Mw 6.3 cumulative seismic moment. In this study, in order to obtain a better picture of the postseismic surface deformation during a longer period of time (7 years), SBI technique has been used with Envisat SAR data acquired by the European Space Agency. The mean velocity field deduced from the SBI reveals surface deformation of both tectonic and non-tectonic origin. The ground deformation along the coastal region has been modeled with afterslip on the coseismic fault of Belabbes *et al.* [2009], has been discussed the coseismic/postseismic deformation, the signification of water level fluctuations in the Mitidja Basin and the role of poro-elastic/visco-elastic deformation.

3.2 Seismotectonic Setting

The Tell Atlas of northern Algeria is the source of frequent large and moderate seismic events mostly with thrust fault mechanisms (Table 3.1), including Zemmouri earthquake of 2003 revealed a comparable pattern of active deformation in agreement with the NNW-SSE to NW-SE convergence and transpressive tectonics along the Africa-Eurasia plate boundary [Morel and Meghraoui, 1996; Meghraoui and Pondrelli, 2012]. These seismogenic structures described with the E-W to NE-SW trending folds and en-echelon thrust faults results from 2 to 3 mm/yr shortening across the Tell Atlas during the late Quaternary [Meghraoui and Doumaz, 1996], which is comparable to the 4 to 6 mm/yr present day rate of convergence between Africa and Eurasia obtained from NUVEL-1A and global GPS solutions [Nocquet and Calais, 2004; Serpelloni et al., 2007]. In north-central Algeria, the dominant active tectonic structures are NE-SW to E-W trending Blida thrust and fold system to the south and ENE-WSW trending Sahel anticline to the north, which form the edges of the Mitidja Basin (Figure 3.1) [Maouche et al., 2011].

Table 3.1 : Large and moderate earthquakes with thrust mechanisms along the Tell Atlas.

Location	Date	Longitude (deg)	Latitude (deg)	Mw
Orleansville	9 Sep 1954	1.47	36.28	6.7
El Asnam	10 Oct 1980	1.36	36.18	7.3
Tipaza	29 Oct 1989	2.92	36.84	5.9
Mascara	18 Aug 1994	-0.03	35.40	5.7
Ain Temouchent	22 Dec 1999	-1.45	35.34	5.7
Beni Ourtilane	10 Nov 2000	4.69	36.71	5.7
Zemmouri	21 May 2003	3.65	36.83	6.8

As illustrated by the mainshock rupture and aftershocks, the Zemmouri earthquake affected ~55 km-long shoreline and ~15 km-thick upper crustal structure of the eastern part of the Mitidja Basin and related Blida thrust and fold system [Ayadi et al., 2008]. A detailed study of the mainshock relocation [Bounif et al., 2004] and aftershock distribution using the tomography analysis reveals a NE-SW trending and 40° SE dipping fault rupture with two seismicity patches [Ayadi et al., 2008]. Analysis of body and surface waves of teleseismic records denotes 2.86×10^{19}

N m seismic moment and a ~15 s fault rupture with ~1 m surface slip, and 2.1 m maximum slip at depth with bilateral rupture propagation along two patches [Delouis *et al.*, 2004]. Also, the source models from body wave inversion suggest similar results pointing out the bilateral rupture propagation on a 60-km-long fault with two patches and 2.3 m maximum slip at depth [Yagi, 2003]. The geodetic studies (coastal uplift, GPS and InSAR) also point out two patches with up to 1 m of surface slip at SW of the earthquake rupture [Semmane *et al.*, 2005; Mahsas *et al.*, 2008; Belabbes *et al.*, 2009]. Seismic moment, mainshock location at depth and field observations suggest that the earthquake rupture did not reach to the surface along the coastline but likely offshore at the seafloor.

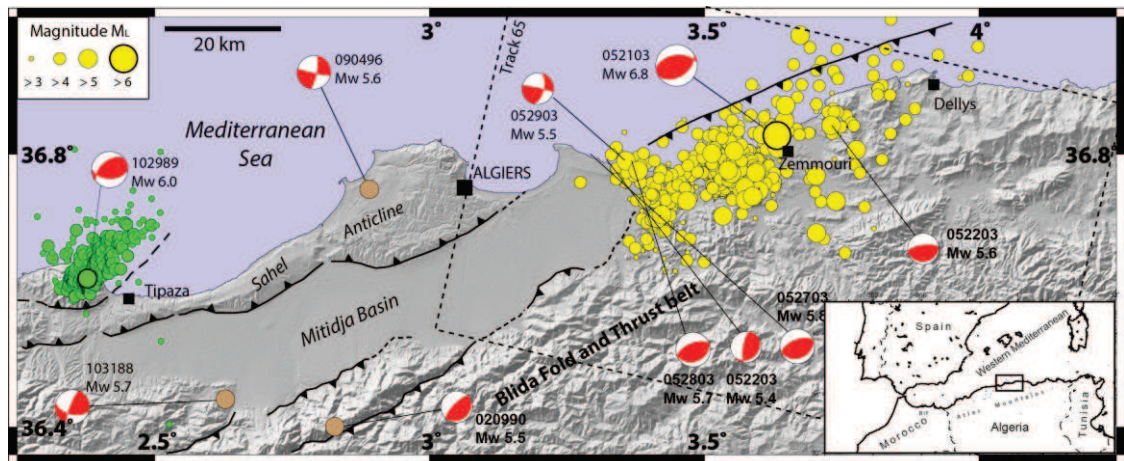


Figure 3.1 : Tectonics and seismicity of the Zemmouri-Boumerdes region shown with SRTM shaded topography. Focal mechanisms are from Global CMT project. Two destructive earthquakes and related aftershocks (Tipaza 1989 and Zemmouri 2003, green and yellow circles, respectively) limit the Mitidja-Algiers active zone (black lines are thrust faults [Maouche *et al.*, 2011]). Dashed box is the Envisat images frame (Track 65). Black box in inset map shows the study region.

Measurements of uplifted marine terraces along a 55-km-long coastline reveal an average ~0.5 m uplift with a max 0.75 m east of Boumerdes and a minimum of almost zero near Cap Djenet [Meghraoui *et al.*, 2004; Maouche *et al.*, 2011]. The coastal deformation and rupture history associated with the aftershock distribution (Figure 3.1), representing a clear concentration on the SW patch suggest, however, a complex fault rupture likely resulting from several asperities along fault strike. Initial geodetic and seismicity studies [Bounif *et al.*, 2004; Meghraoui *et al.*, 2004; Delouis *et al.*, 2004; Yelles *et al.*, 2004; Semmane *et al.*, 2005; Alasset *et al.*, 2006] imply the existence of a N54°– N70° striking and 40° to 50° SE dipping fault

rupture with surface slip at 5 to 15 km offshore. The high-resolution swath bathymetry and seismic profiles of the continental slope offshore the 2003 earthquake area identify outcropping thrust fault and scarps located at ~20 and 32 km from the shoreline and infer a flat and ramp rupture geometry [Devercheres *et al.*, 2005]. The moment tensor analysis obtained from broadband seismic records indicates a 25° SE dipping rupture suggesting a fault surface trace at 15 to 20 km offshore limited to the SW by a NNE trending transform fault and forms a step over with the Blida thrust system [Braunmiller and Bernardi, 2005].

3.3 InSAR Observations

A map of cumulative line-of-sight (LOS) deformation between 12-July-2003 and 18-September-2010 is obtained from a mean LOS velocity field calculated from 31 descending ENVISAT images covering the earthquake region and the Bay of Algiers (Figure 3.2, and 3.3) using SBI technique (see Chapter 2.2 for processing details). The map reveals LOS range increase largely in three regions reaching to 12 mm/yr in the Mitidja basin, 3.5 mm/yr around Boumerdes-Zemmouri area, and 2 mm/yr around Cap Djenet (Figure 3.3).

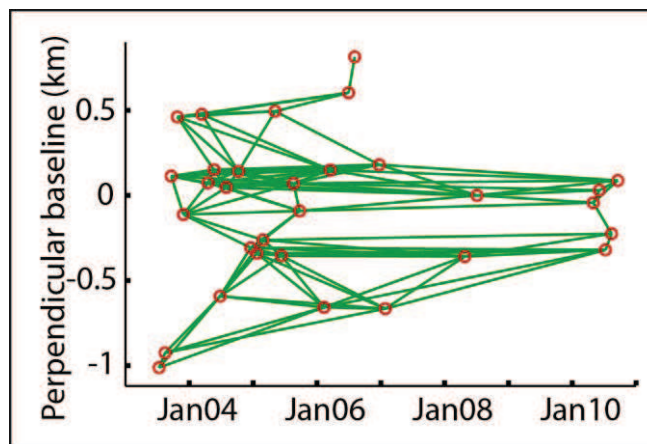


Figure 3.2 : The baseline plot showing the interferogram pairs (green lines) between radar images (red circles).

LOS range increase in the descending imaging geometry can be due to either ground subsidence or westerly horizontal motion of the ground. While the high rate of LOS range increase in the Mitidja basin SW of Cap Matifou can be attributed to subsidence due to excess ground water extraction in Holocene fine-grained alluvial deposits [Mimouni, 2010], those observed in the earthquake region along the coast

are likely due to both horizontal and vertical (subsidence) displacements associated with the postseismic deformation because the basements of these regions are formed by solid rocks (e.g., granitic, volcanic and metamorphic units). Although the LOS increase in the Boumerdes-Zemmouri is consistent with the CGPS measurements that show both subsidence and northwestward horizontal displacements, the CGPS displacements with large component of uplift in Cap Djenet contradicts InSAR results as it predicts decrease in LOS range instead of increase. It must be noted that the vertical components of the CGPS measurements are crudely constrained (see Fig. 3 of *Mahsas et al.*, [2008]). As for the coseismic uplift, the postseismic ground deformation in the Boumerdes-Zemmouri and Cap Djenet must therefore be the result of crustal deformation, an inference being also supported by the logarithmic decay in InSAR time series (Figure 3.4). The evidence for subsidence in the Mitidja basin being due to seasonal water level fluctuation and ground water extraction comes from the remarkable correlations observed between InSAR time series and water level piezometric changes (Figure 1.4; [*Mimouni*, 2010]).

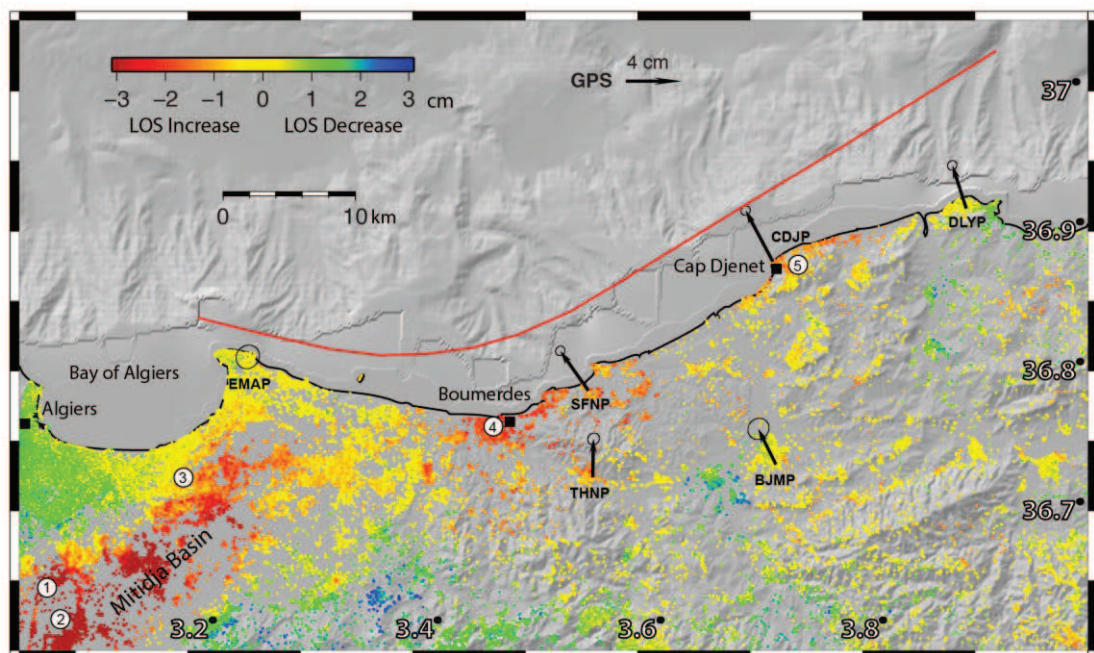


Figure 3.3 : Seven-year postseismic cumulative LOS range change following the 2003 Zemmouri earthquake. Movements away from the satellite are shown with yellow to red colors and, those towards the satellite with yellow to blue. The black arrows with 95% confidence ellipses are 2.5-year cumulative postseismic GPS displacements from *Mahsas et al.* [2008]. Red line is the trace of the modeled fault on the sea floor. Numbers show the locations of time series plotted in Figure 1.4.

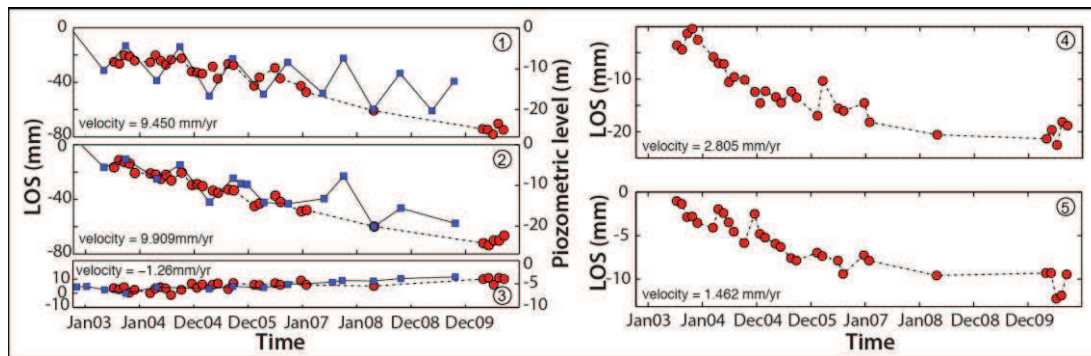


Figure 3.4 : Time series of InSAR data (red circles) and groundwater table measurements (blue squares [Mimouni, 2010]) in the study area. Note the strong correlation between water level fluctuations and InSAR phase changes in the Mitidja basin (plots 1 to 3). Postseismic deformation in the earthquake region (plot 4 and 5) is manifested by logarithmic decay in the InSAR time series.

Although much smaller, the sense of postseismic vertical motion in the Zemmouri-Boumerdes and Cap Djenet is remarkably opposite to the uplift (i.e. LOS range decrease) observed during the coseismic deformation (see *Belabbès et al.*, [2009]). Part of the signal can be explained by postseismic reverse slip on the N60 to 65E-striking and southeast dipping main rupture since it produces NW directed horizontal motion and thus LOS range increase. However, InSAR can detect only 20-25% of these horizontal displacements in the descending imaging geometry. Because InSAR captures about 90% of the vertical displacements, the LOS velocity field most probably largely be made up of vertical movement taking into account 40°-50° SE dipping fault rupture. Therefore, the LOS increase can be explained by subsidence due to visco-elastic relaxation or afterslip above or below the coseismic slip at depth, consistent with the shallow afterslip model proposed by *Mahsas et al.* [2008]. Afterslip taking place on the sections of high coseismic slip would otherwise produce uplift, and thus LOS range decrease, instead of LOS range increase observed in the earthquake region.

3.4 Modeling

3.4.1 Afterslip

In order to investigate to what extent a model of afterslip can explain the InSAR LOS velocity field together with the CGPS measurements of *Mahsas et al.* [2008], inverse modeling has been performed utilizing the boundary element

software, Poly3Dinv [Thomas, 1993; Maerten *et al.*, 2005] that predicts surface displacements due to angular dislocations on triangular faults buried in a linear-elastic and homogeneous, isotropic half-space with a damped least square minimization. Triangular boundary elements allows to reconstruct of a surface of any desired tipline shape fault models that better approximate 3D planar surfaces, avoiding gaps and overlaps that are inevitably encountered when modeling curved or segmented faults of varying strike with rectangular planes commonly used to model geodetic observations [Maerten *et al.*, 2002].

In our inversions, we use the model fault deduced by *Belabbes et al.* [2009] from coseismic SAR, GPS data, and coastal uplift measurements. It is a curved surface dipping $\sim 45^\circ$ towards the south and trending $N60^\circ-65^\circ E$ along the coast between Boumerdes and Dellys (Figure 3.3). The fault surface is discretized into triangular elements from surface down to the depth of 20 km using MATLAB[®]. The distribution of reverse slip on the triangular elements was then inverted with the scale-dependent smoothing operator of Poly3Dinv to avoid unphysical oscillatory slip, using the cumulative LOS change along the shoreline and re-estimated horizontal GPS displacements during ~ 7 years. We use the time series provided by *Mahsas et al.* [2008] to recalculate the horizontal GPS velocities taking into account the total displacements recorded in between the acquisition of the first Envisat image used in the InSAR time series (i.e., July 2003) and the end of CGPS measurements in October 2005. Although, the rates decrease logarithmically, in the inversion we assume for simplicity a linear rate for GPS displacements for the next five years till the acquisition of the last Envisat image used (September, 2010). Several inversions have been run weighting the GPS and LOS data equally with a smoothing factor changing between 0 (i.e. rough) to 1 (i.e. smooth) to explore its effects on the location, magnitude (hence the seismic moment) of slip and misfit. Although the fit improves almost linearly for LOS data with decreasing smoothing factor, at a certain point GPS data exhibit a higher misfit as the slip localizes further reaching a maximum 2 m (Figure 3.5). The preferred model of slip distribution shown in Figure 3.6 is obtained with an optimum 0.4 smoothing factor for both data sets with 0.57 cm RMS misfit. As for all the other models with different smoothing factors, the preferred model predicts shallow afterslip of up to 65 cm localized mostly between 5-km-depth and surface. Although weakly pronounced, the afterslip is distributed on

two patches above the lobes of high coseismic slip. The coseismic slip deficit at the uppermost sections of the fault appears to be filled by the postseismic afterslip, indicating a complementary coseismic and postseismic slip as commonly observed for other large earthquakes [Reilinger *et al.*, 2000]. The resolution tests shown in Figure A.1 in the appendix indicates that the InSAR data have an adequate resolution in constraining the shallow slip on the fault.

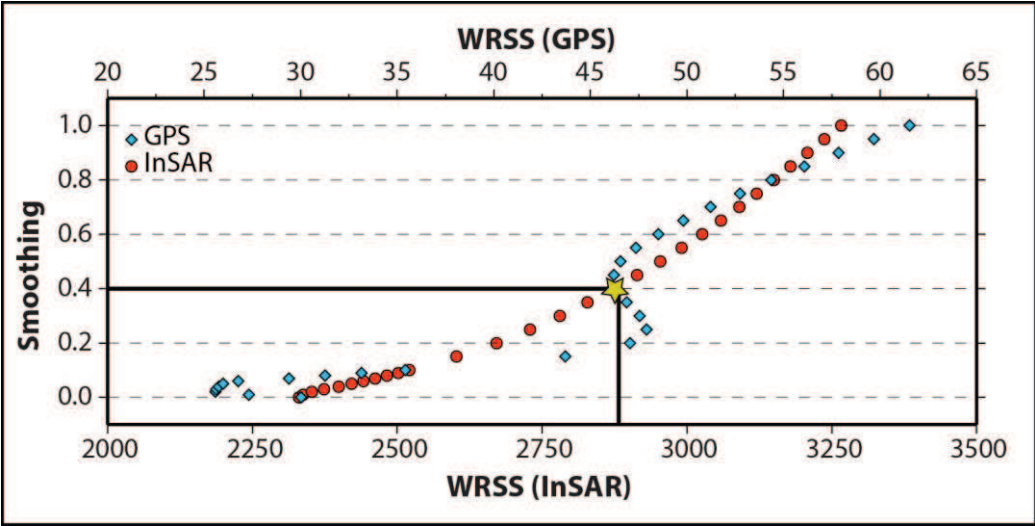


Figure 3.5 : The smoothing operator used in the InSAR and GPS data inversion. An optimum solution can be obtained with a 0.4 smoothing factor.

The modeling results are overall in good agreement with the observed postseismic SBI and GPS data. As illustrated with the in Figure 3.7 and 3.8, the fit between the model and InSAR data can be reasonably accepted. In contrast, the GPS fit in the south and east is poor and requires deeper slip on fault although the model predicts the overall northward displacements observed by GPS. The discrepancy between the modeled and observed GPS velocities and the InSAR data is probably partly due to much faster decays of the afterslip on the deeper sections of the fault. The estimated moment released for 7 years (2003 – 2010) is 4.1×10^{18} Nm ($M_w = 6.34$), ~28% higher than that estimated during the first 2.5 years [Mahsas *et al.*, 2008]. It increases to 4.6×10^{18} Nm ($M_w = 6.38$), in the case of 0.3 smoothing factor. These estimates suggest that the cumulative postseismic moment release during 7 years is around 15 to 25% of the coseismic moment release estimated from seismology and geodesy [Delouis *et al.*, 2004; Belabbes *et al.*, 2009].

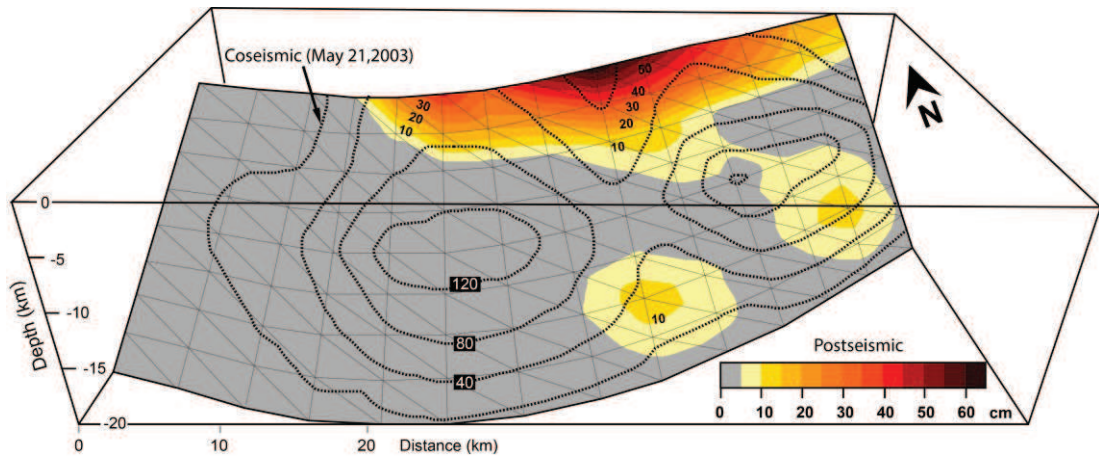


Figure 3.6 : Color-coded postseismic afterslip distribution on the Zemmouri earthquake rupture. Black dashed lines show the coseismic slip distribution inferred by *Belabbes et al.* [2009]. The afterslip distribution inverted from InSAR and GPS data shows two patches of maximum slip (40 to 65 cm) along the upper sections of the fault (<5-km-depth) complementing the coseismic slip at deeper fault sections.

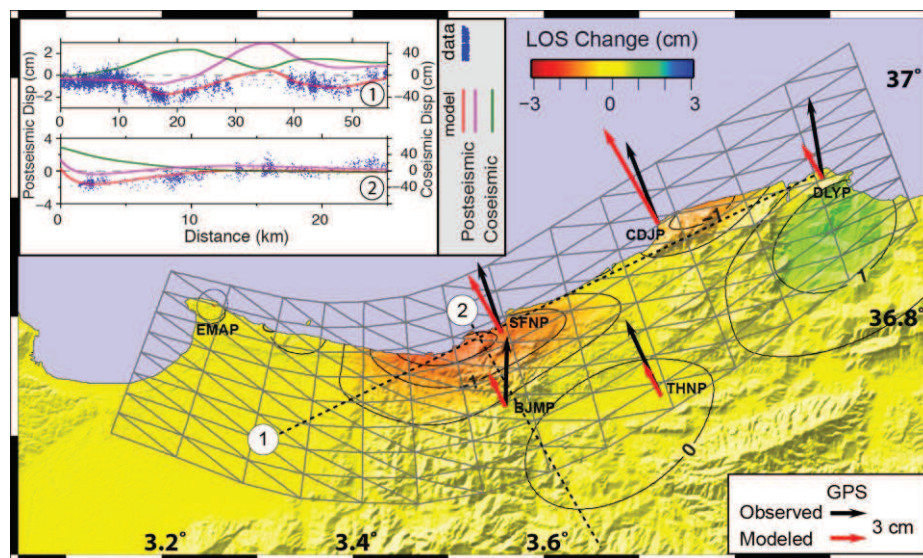


Figure 3.7 : Model of 7 year cumulative LOS surface deformation and GPS displacements predicted by the modeled slip distribution shown in Figure 3.6. The fault rupture projected to the surface is illustrated by the triangulated network; parallel and perpendicular profiles to the fault are located by number 1 and 2. Inset shows LOS change of modeled (red lines) and observed (blue dots) postseismic surface deformation, together with coseismic model (green lines [*Belabbes et al.*, 2009]). Pink lines show vertical component of the LOS change predicted by the model.

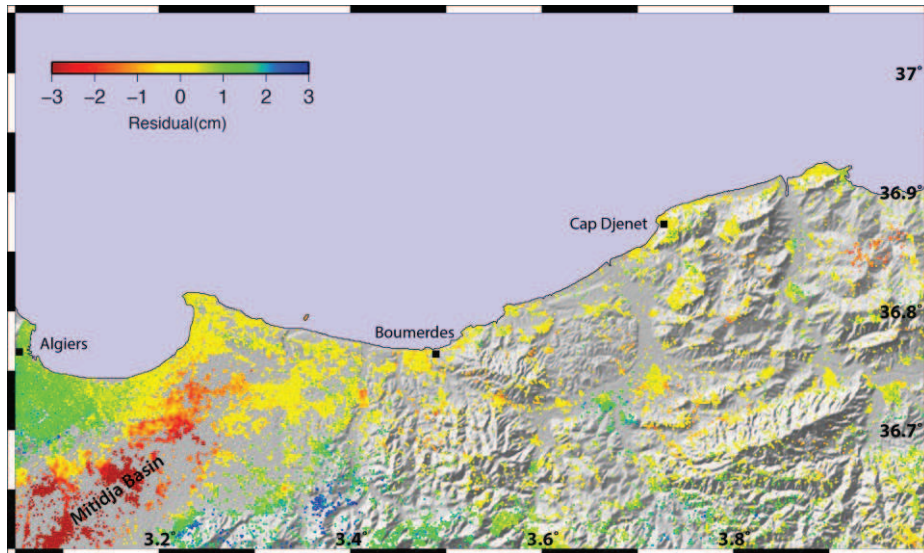


Figure 3.8 : Residual LOS velocity field.

3.4.2 Visco-elastic

A possibly noteworthy controlling factor of the postseismic deformation transients is the inelastic response of the Earth by time, since it consists of an elastic brittle upper crust and ductile visco-elastic lower crust and upper mantle. The theory of viscoelasticity assumes that the deformation initiates in elastic upper crust and expands to ductile lower crust up to upper mantle [Nur and Mavko, 1974; Savage, 1990]. In order to compute the visco-elastic relaxation, we used the numerical code developed by Wang *et al.* [2006] which models the Earth as a multilayered elastic to visco-elastic half-space from surface up to upper mantle. It is split into two programs, namely PSGRN and PSCMP (see Appendix B). PSGRN is used to calculate the time-dependents Green's functions required to describe the response of the model, which contains the rheology parameters. Fault geometry and slip distribution of earthquake rupture were described in PSCMP (Figure B.1).

To explore possible contributions of visco-elastic relaxation following the 2003 Zemmouri earthquake, we test the possible configurations of the multi-layered half-space (see Appendix B). We built a two-layer rheological model, made up of an elastic half-space layer on a visco-elastic half-space layer (Maxwell rheology). For each configuration, different depths of the elastic half-space (12-30 km-depths) and viscosity of the lower visco-elastic half-space (10^{17} - 10^{19} Pa.s) has been tested and searched for the viscosity leads to the minimum misfit with respect to GPS observed horizontal and InSAR LOS surface displacements. We estimate that the best-fit

viscosity of lower visco-elastic half-space (> 12 km depth) is 5×10^{19} Pa.s, respectively. Each calculation was conducted by applying the coseismic slip distribution, then allowing the viscoelastic region to relax for 7 years. Coseismic slip is simulated on a planar fault by enforcing the slip distribution deduced by *Belabbes et al.* [2009]. The simulated fault model located at ~ 13 km offshore from the epicenter with 55-km-long and 20-km-wide offshore thrust fault striking $N60^\circ$, and dipping 42° SE (Figure 3.9, and B.1). We find that the visco-elastic relaxation models predict successfully the subsidence observed in the InSAR results, but fail to explain large horizontal displacements at GPS sites (Figure 3.9).

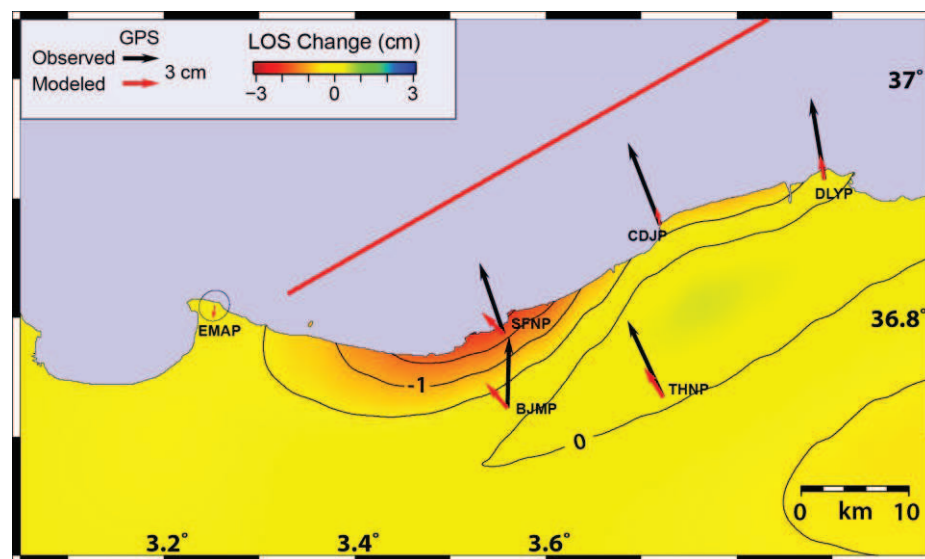


Figure 3.9 : Model of 7-year cumulative LOS surface deformation and GPS displacements predicted by visco-elastic relaxation. Red line shows the modeled fault rupture.

3.4.3 Poro-elastic

Poro-elastic approaches estimate the near field pore pressure change that earthquake loads. In order to evaluate poro-elastic deformation, we computed the poro-elastic rebound signal by calculating the difference between the elastic deformation induced by the earthquake in undrained and drained crustal rocks. We used the coseismic model of the *Belabbes et al.*, [2009] with the Poisson's ratio values for undrained (0.31) and drained (0.27) elastic parameters as suggested by *Peltzer et al.*, [1998] for the 1992 Landers earthquake. The observed two-lobe pattern has been successfully reproduced by the poro-elastic model but with a much lower value of subsidence (i.e., maximum 5 mm) on the coastline. In the attempt of

maximizing the poro-elastic response, we have chosen extreme values of Poisson's ratio (i.e., 0.33 and 0.25) as in the case of the 1997 Umbri-Marche earthquake sequence (i.e., 0.35 and 0.20 chosen by *Riva et al.* [2007]). Even though the poro-elastic model may explain most of the signal, it fails again to reproduce the horizontal motions observed by GPS (Figure 3.10).

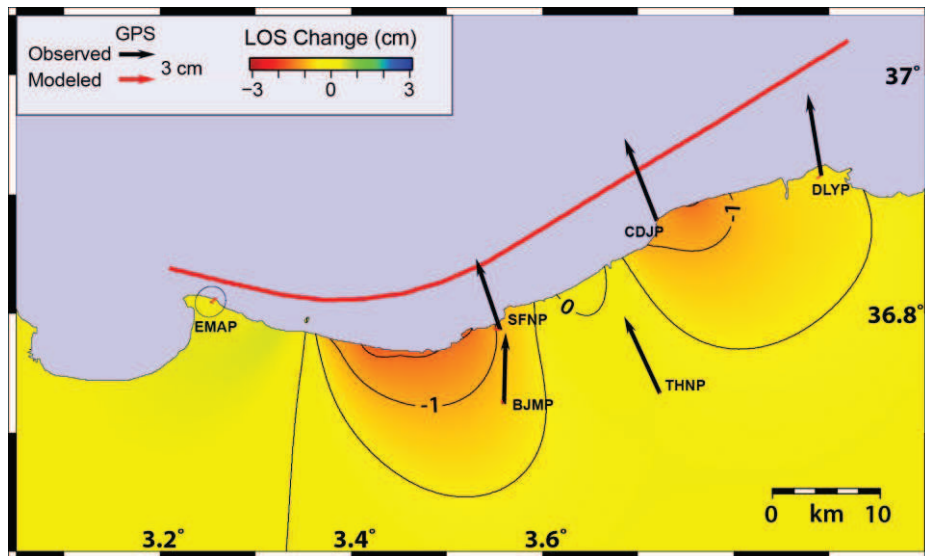


Figure 3.10 : Model of 7-year cumulative LOS surface deformation and GPS displacements predicted by poro-elastic rebound. Red line shows the modeled fault rupture.

3.5 Discussion and Conclusion

Postseismic deformation associated with the 2003 Zemmouri earthquake during the period between 2003 and 2010 is documented using Envisat ASAR data combined with 2.5-year GPS data. The broad spatial coverage and seven years of high-resolution SBI data provide a powerful constraint on the characteristics of postseismic deformation. The results reveal two lobes of relatively higher rate of subsidence with 3.5 to 2 mm/yr LOS displacement in Zemmouri-Boumerdes and Cap Djenet, respectively, as opposed to the coseismic uplift. Elastic dislocation modeling shows that these lobes can be adequately explained by shallow (< 5 km) afterslip with up to 0.65 m displacement above the coseismic slip with 4.1×10^{18} Nm (M_w 6.34) cumulative moment release. The coseismic and postseismic slip distributions are shown to be complementary implying that both types of surface deformation with the same fault model suggest well-constrained fault rupture parameters. The large amount of afterslip gives rise to additional static stress transfer onto the neighboring

faults and affects previous Coulomb stress modeling [Lin *et al.*, 2011]. This also changes our perception of the seismic cycle characterization and suggests longer recurrence intervals for large earthquakes in the Algiers region.

The afterslip distribution is well constrained and appears to be the most significant mechanism of the postseismic deformation following the 2003 Zemmouri thrust earthquake since all the models with different factors of smoothing and weighting predict afterslip mostly at shallow depths. On the other hand, part of the postseismic deformation can be due to poro-elastic and/or visco-elastic relaxation in the lithosphere. Postseismic deformation of the Chi-Chi thrust earthquake (M_w 7.7) obtained from GPS measurements over a 15-month period are better explained by afterslip than viscoelastic relaxation [Hsu *et al.*, 2007]. In the Zemmouri earthquake, the visco-elastic relaxation model predicts the subsidence observed in the InSAR results. The model however fails to explain the horizontal motions observed with GPS and the two-lobe pattern observed by SBI. The visco-elastic contribution to the observed surface deformation remains unclear (Figure 3.9). On the other hand, the poro-elastic rebound is a fairly rapid response [Riva *et al.*, 2007], and its contribution is likely to be small since the first SAR image was taken ~6 weeks after the earthquake (Figure 3.10).

Comparing the high-resolution of SBI time series and water level change measurements in the Mitidja basin shows that both are consistently decreasing with time, suggesting the subsidence is controlled by water level changes (Figure 3.4). Although, the subsidence may be partly due to tectonic ground movements, their distinction is difficult due to the resolution and error range of the water level fluctuations. While the postseismic deformation in the Mitidja basin should be trivial since coseismic surface deformation was absent or negligible there [Belabbes *et al.*, 2009], strong shaking during the coseismic activity may cause pre-existing fractures to open and rock sediments to dilate leading to a step like decrease in water level [Wang and Manga, 2010]. Moreover, precipitation, stream flows or human activities may add to the postseismic ground deformation in the alluvial basin.

Published paper from this chapter can be found in Appendix C.

Chapter IV :
**Coseismic And Postseismic Deformation Associated
With The Mw 6.4 February 24, 2004 Al Hoceima
(Morocco) Earthquake**

4. COSEISMIC AND POSTSEISMIC DEFORMATION ASSOCIATED WITH THE M_w 6.4 FEBRUARY 24, 2004 AL HOCEIMA (MOROCCO) EARTHQUAKE

4.1 Introduction

The Al Hoceima region of Northern Morocco is located within the east-west trending imbricated thrust-and-fold system of the Rif Mountain range that results from collision between the African and Eurasian plates. The Rif mountain range has experienced several moderate-to-large earthquakes of mainly strike-slip mechanisms consistent with a NNW-SSE to NW-SE direction of plate convergence [*DeMets et al.*, 1990; *Meghraoui and Pondrelli*, 2012]. The Al Hoceima earthquakes of the May 26, 1994 (M_w 6.0) and February 24, 2004 (M_w 6.4) are the largest seismic events in the last century that occurred on conjugate strike-slip faults trending approximately NNE-SSW and NW-SE on the Rif Mountain range (Figure 4.1) [*Bezzeghoud and Buforn*, 1999; *Akoglu et al.*, 2006]. Although, several geophysical and geodetic studies have been performed since the earthquake [*Buforn et al.*, 2004; *Stich et al.*, 2005; *Cakir et al.*, 2006; *Akoglu et al.*, 2006; *Biggs et al.*, 2006; *Tahayt et al.*, 2009; *van der Woerd et al.*, 2014], the source of the 2004 earthquake remains debated including key parameters such as fault geometry (e.g. number and location of broken fault segments), maximum slip and depth. Models of the 2004 earthquake based on InSAR data suggest different fault ruptures with mainly NW-SE trending planar or curved shaped right-lateral strike-slip fault [*Cakir et al.*, 2006; *Biggs et al.*, 2006; *Tahayt et al.*, 2009], consistent with the aftershocks distribution on surface and at depth [*Tahayt et al.*, 2009; *van der Woerd et al.*, 2014].

In this study, we analyze both the co-and post-seismic deformation associated with the 2004 earthquake on the Al Hoceima region using the InSAR technique. InSAR time series calculated from Envisat ASAR images using small baseline approach by means of the Stanford Method of Persistent Scatterers (StaMPS) [*Hooper*, 2008] reveal the subtle ground movements between 2004 and 2010 in the

same area where we observe the remarkable coseismic displacements. The SBI analysis shows up to 4 cm cumulative line-of-sight movement, towards and away from the satellite, in the same region of coseismic surface deformation, which is in good agreement with the right-lateral strike-slip motion. The spatial pattern of the postseismic deformation suggests that a revision of the coseismic fault model of *Akoglu et al.* [2006] is necessary in the southern tip of the fault. On the basis of these new observations the coseismic model has been revised using the same data set (one ascending and one descending interferogram) used by *Akoglu et al.*, [2006]. We calculate various models to better understand the relationships between the coseismic and postseismic deformation, and to constrain the earthquake rupture geometry and related slip at depth.

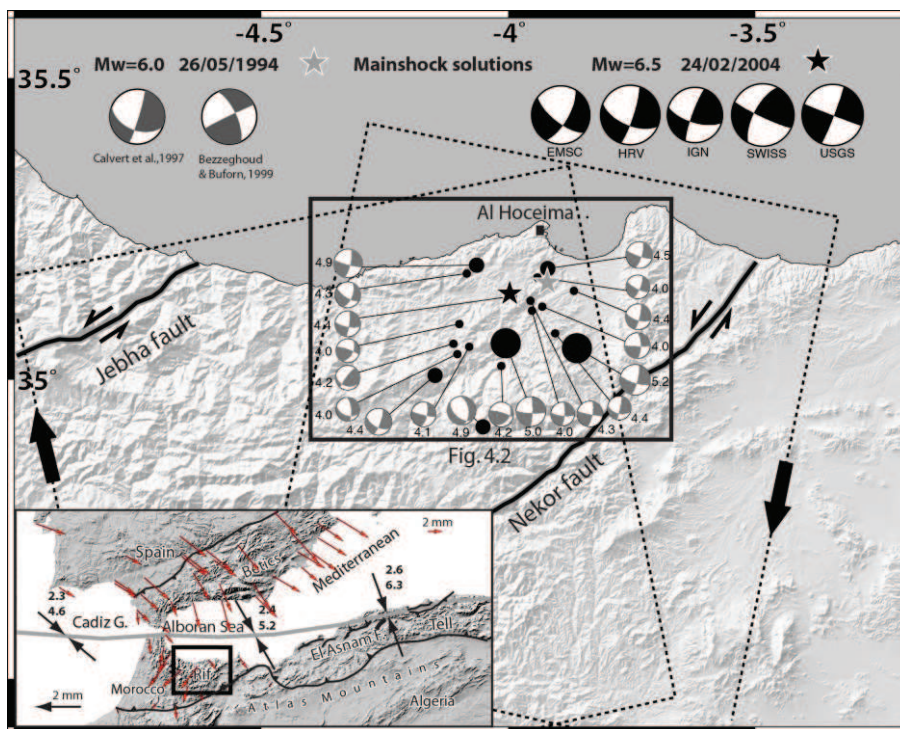


Figure 4.1 : Al Hoceima region of Morocco with shaded relief (SRTM 90m). Large beach balls are focal mechanism solutions of the 26 May 1994 and 24 February 2004 Al Hoceima earthquakes [*Calvert et al.*, 1997; *Bezzeghoud and Buforn*, 1999], whose epicenters are indicated by gray and black stars, respectively. Small black circles are $M > 4$ aftershocks from IGN with focal mechanism solutions from *Buforn et al.* [2004] and *Stich et al.* [2005]. Dashed rectangles are the frames of the Envisat radar images with arrows showing the flight direction of the satellite. The convergent plate boundary between Africa and Eurasia is depicted with a thick gray line in the inset map with arrows illustrating the direction and estimated rate (min. and max.) of convergence [*Nocquet and Calais*, 2004]. Red arrows indicate the recent GPS measurements [*Koulali et al.*, 2011].

4.2 Seismotectonic Settings

The Rif Mountain range belongs to the E-W trending thrust-and-fold system of North Africa that results mainly from the convergent movements of Africa toward Eurasia (Iberia) during the Tertiary [Morel and Meghraoui, 1996]. The African-Eurasian plate boundary forms a collision tectonics strip including the Alboran Sea, Tell Atlas Mountain ranges of Algeria and Tunisia along the Mediterranean coast to the east. The Quaternary counter-clockwise rotation of Africa with respect to Eurasia based on the global models of plate tectonics indicates an oblique convergence along the western section of North Africa, and shows a decreasing westward rate of shortening with a range of 6 mm/yr to 3 mm/yr (Figure 4.1) [DeMets *et al.*, 1994; Nocquet and Calais, 2004]. Besides, recent GPS observations confirm the WNW-ESE oblique convergence between Africa and Iberia and associated rate in the Strait of Gibraltar (4.3 ± 0.5 mm/yr along the $N116^\circ E \pm 6^\circ$ direction) [Mc Clusky *et al.*, 2003; Fernandes *et al.*, 2007; Serpelloni *et al.*, 2010; Vernant *et al.*, 2010]. This oblique convergence is the driving force for the active deformation along the plate boundary; however, the seismicity is considerably complex and varies significantly from east to west. Although the rate of seismicity might be correlated with the long-term rate (several ka) of convergence along the plate boundary, it is not evident to determine this rate only with short period of instrumental seismic records. While the 1994-2004 Al Hoceima seismic sequence and the recent seismicity imply that the Rif Mountain range is being deformed under a strike-slip tectonic regime [Bezzeghoud and Buforn, 1999], adjacent regions in Gulf of Cadiz to the west and northern Algeria to the east are subject to thrust faulting deformation [Grimison and Cheng, 1986; Morel and Meghraoui, 1996]. According to the kinematic model of transpression and block rotation in North Africa, the discrepancy between the shortening and convergence directions might reflect the oblique tectonics with interactions between thrust-related folding and strike-slip faulting along the plate boundary [Meghraoui and Pondrelli, 2012]. Local and regional seismotectonic studies in North Africa have suggested that the active thrusts and strike-slip faulting are coeval, and that contractional tectonics are accompanied by right-lateral en echelon fold axes, basal decollements and dip-slip geometries with imbricated structures in the upper crust [Yielding *et al.*, 1989; Meghraoui *et al.*, 1996; Meghraoui and Pondrelli, 2012]. Although trending clearly in NW-SE direction between Iberia and the Tell Atlas of Algeria, the recent GPS

velocities (Figure 4.1 inset) illustrate a southwestward motion of the Rif and Betic domains relative to Nubia and Eurasia respectively [Fernandes *et al.*, 2007; Serpelloni *et al.*, 2010; Pérouse *et al.*, 2010; Koulali *et al.*, 2011]. They hypothesize that the unexpected velocity field in the Rif-Betic zone is the result of the combined effects of long-term northwest-southeast oblique convergence between the Eurasian and the Nubian plates; low rigidity of the Alboran Sea domain [Ammar *et al.*, 2007]; and a south-southwest-directed horizontal traction applied beneath the External Rif which is due to the rollback of the delaminated African continental lithospheric mantle pulled by the sinking oceanic Western Mediterranean slab [Fadil *et al.*, 2006].

Neotectonic features of the Rif consist of the major NE-SW trending Nekor and Jebha left-lateral strike-slip faults (Figure 4.1), accompanied by N-S trending normal faults that form a graben-like structure east of Al Hoceima city and a conjugated network of relatively small (10 to 20-km-long) NW-SE and NE-SW strike-slip faults (Figure 4.2). The transpressive tectonics and existence of a complex fault network with thrust, normal and strike-slip faulting in the Rif probably reflect the rapidly changing local tectonic regime with block rotations during the Neogene and Quaternary [Meghraoui *et al.*, 1996]. Typical prominent geomorphological features of late Pleistocene and Holocene seismogenic faulting are undocumented along the Rif neotectonic faults.

The source mechanisms of the 2004 earthquake rupture, based on different observations (i.e. aftershock distribution, waveform inversion, InSAR, field observations) made by various investigators, propose a NW-SE trending right-lateral and/or a NNE-SSW trending left-lateral strike-slip faulting. However, there are inconsistencies in the literature regarding the source, location and geometry of the rupture. While based on apparent source time functions and seismic wave modeling, Stich *et al.* [2005] and Buforn *et al.* [2004] deduce NNE-SSW trending left-lateral rupture south of Al Hoceima, van der Woerd *et al.* [2014] based on aftershock distribution (Figure 4.3) infer two possible fault ruptures striking NW-SE with right-lateral and/or NE-SW with left-lateral mechanism. InSAR studies predict NW-SE trending planar or curved shaped right-lateral strike-slip fault [Akoglu *et al.*, 2006; Cakir *et al.*, 2006; Biggs *et al.*, 2006]. On the contrary, Tahayt *et al.* [2009] infer a complex rupture with two sub-events initiated on the N10°E left-lateral strike-slip

fault and transferred to the N132°E right-lateral strike-slip fault. The absence of coseismic surface ruptures and the complex thrust and nappe tectonic context clearly require the contribution of new methods of investigations such as InSAR to characterize blind or hidden faults.

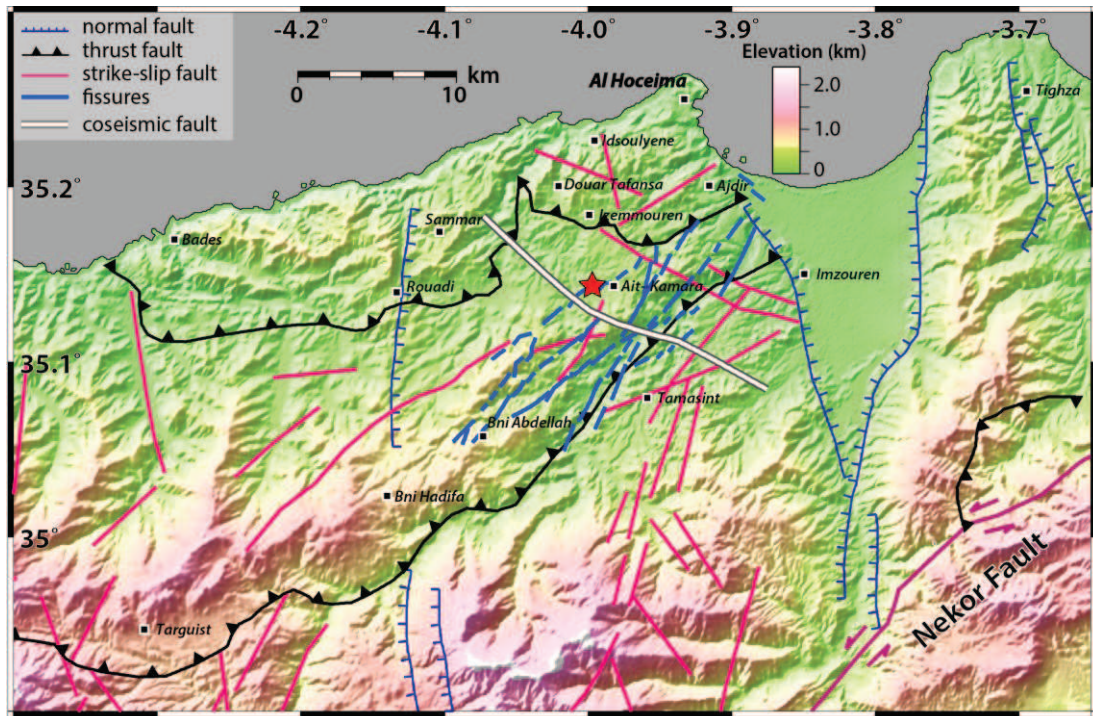


Figure 4.2 : Tectonic map of the Al Hoceima region (compiled from *Calvert et al.*, 1997; *Ait Brahim, Tadili, et al.*, 2004) with surface cracks and fissures observed after the 2004 event (redrawn from *Ait Brahim, Nakhcha, et al.*, 2004). Thick white line is the surface trace of the modeled fault plane.

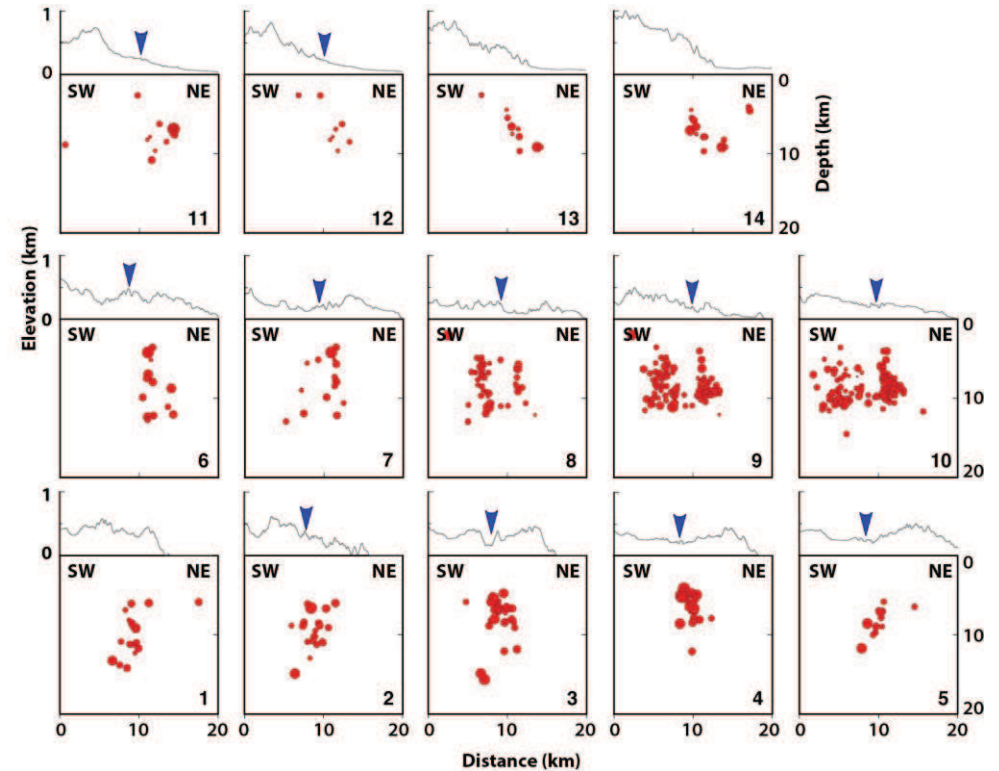
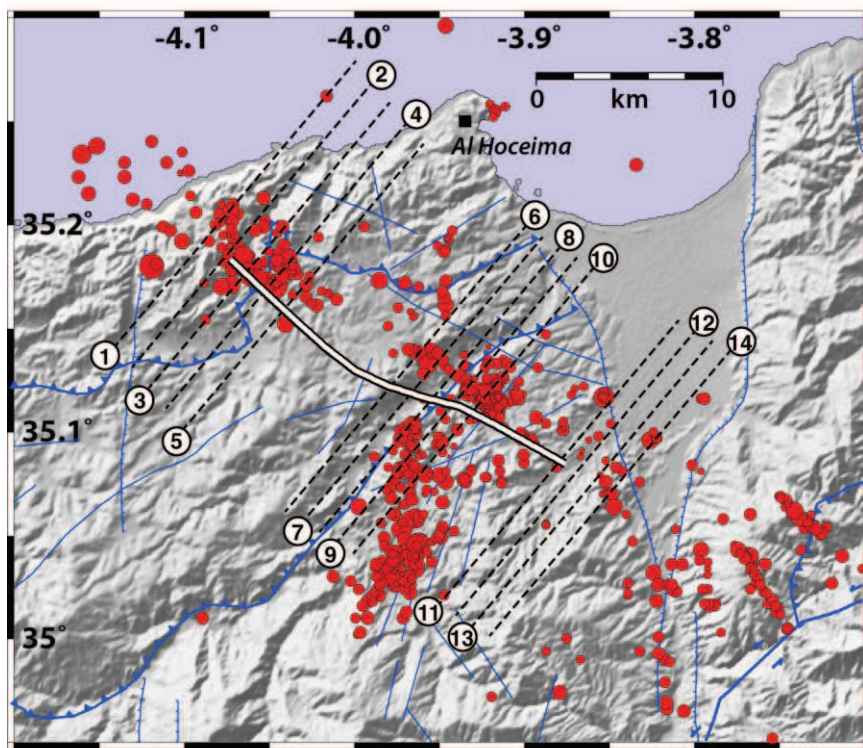


Figure 4.3 : Aftershocks distribution of the 2004 earthquake obtained from *Tahayt et al.* [2009] and *van der Woerd et al.* [2014] in the Al Hoceima region. Blue lines show the mapped thrust and nappe structures in the mountains and normal faults that limit the Al Hoceima Quaternary Basin. Thick white line is the surface projection of our modeled coseismic fault. Dashed lines show the perpendicular profiles to the fault (see profiles on the right). Cross sections of the aftershocks are shown on the right panel with profile numbers at the right bottom. Topographic profiles are shown as black lines on the top of sections. Blue arrows indicate the tip of our modeled coseismic blind fault location.

4.3 InSAR Observations

In order to examine and model the surface deformation associated with the 2004 Al Hoceima earthquake, the coseismic and postseismic surface displacement fields have been mapped using InSAR technique.

4.3.1 Coseismic InSAR data

We use the ASAR data of Envisat satellite's to examine the coseismic surface displacement of the earthquake on both ascending and descending geometry (Figure 4.1). Interferograms have been calculated using DORIS InSAR processing software [Kampes *et al.*, 2003] and precise satellite orbits from Delft University [Scharoo and Visser, 1998]. Topographical effects have been removed from the interferograms using the SRTM 3-arcsec (~90 m) posting digital elevation model [Farr and Kobrick, 2000]. The interferograms have been filtered using a weighted power spectrum technique [Goldstein and Werner, 1998].

The interferograms are shown in Figure 4.4 with wrapped fringes, each representing half a wavelength (i.e. 2.83 cm) range change along the radar line-of-sight (LOS). Having the shortest temporal (7 months) and spatial (16 m) baseline, the ascending interferogram experienced minimum decorrelation (Figure 4.4); which occurs due to large baselines, agricultural activities within the time span between image pairs (mainly descending pair), and steep slopes in the ragged terrain. On the contrary, both the ascending and the descending interferograms though include postseismic deformation, which should be considered, since they cover all of the recorded aftershocks. The descending interferogram shows three lobes of deformation with a maximum of five fringes (~12 cm) in the eastern lobe, whereas two lobes of deformation can be seen in ascending interferogram with a peak-to-peak line-of-sight displacement of about 23 cm (eight fringes). Although the two lobes in the coastal regions are clearly visible in the both interferograms, the southern lobe is rather obscured due to the poor coherence. The only common lobe in both interferograms is the one located immediately southwest of Al Hoceima city (Figure 4.4). The continuity of the fringes across the north portion of the fault in the ascending interferogram implies that the earthquake rupture did not reach the surface, which is also confirmed by the absence of the aftershocks above 3 km of depth (Figure 4.3) [van der Woerd *et al.*, 2014].

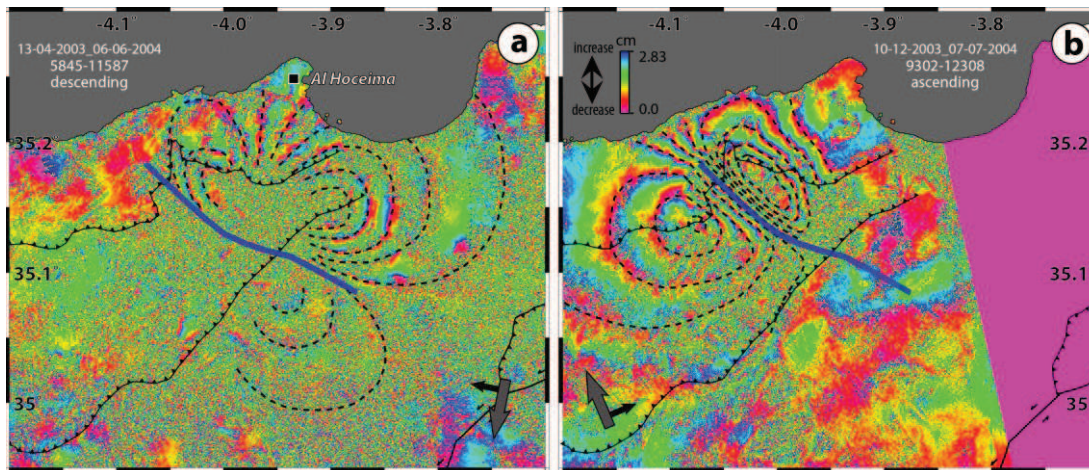


Figure 4.4 : Coseismic interferograms of the February 24, 2004 Al Hoceima earthquake. Each fringe shows 2.83 cm of surface displacement along the radar line-of-sight. Dashed lines are digitized fringes used in modeling of the interferograms. Blue line is the best model fault. Inactive thrust faults are shown to facilitate comparison of the interferograms. The gray and black arrows indicate the satellite flight direction and line-of-sight direction (right looking), respectively.

Synthetic Aperture Radar (SAR) of Envisat satellite can measure approximately 90% of vertical and 40% of east-west changes with a steep look angle ($\sim 23^\circ$ in the image center), while horizontal motion along the satellite direction, which is approximately north-south but varies with latitude, cannot be detected. Furthermore, the combination of horizontal and vertical displacement may lead to signal cancellation. Therefore, the change in the viewing geometry and the nature of surface deformation associated with a strike-slip fault trending oblique to the satellite flight direction are mostly the source of the striking difference in the fringe pattern between the ascending and descending interferograms. Earth surface is scanned from nearly opposite directions in the ascending and descending geometry, and any changes in shape of the deformation reflect differences in the vertical versus horizontal deformation. The sum of the two phases of ascending and descending interferograms is largely vertical motion, with about 10% of north-south motion (Figure D.1c), and the difference between two phases (descending minus ascending) is approximately east-west motion (Figure D.1d). These simple components are not exact because the incidence angle varies across the swath, but the changes are gradual and have little effect on the short wavelength [Fielding *et al.*, 2005]. Consequently, the surface displacement in the Al Hoceima region where there is a

common lobe between the ascending and descending interferograms must be overwhelmingly vertical (i.e., subsidence as is it shows range increase).

4.3.2 Postseismic InSAR data

Two sets of SAR data were used to analyze postseismic surface deformation using a time series approach, as applied to reveal slow surface creep along the North Anatolian Fault at Izmit (Turkey) faults [Cakir *et al.*, 2012], postseismic deformation following the May 21, 2003 Zemmouri (Algeria) earthquake [Cetin *et al.*, 2012], and interseismic surface deformation along the North Tabriz Fault [Karimzadeh *et al.*, 2013]. InSAR time series calculated from Envisat ASAR images acquired in the ascending and descending modes using StaMPS software [Hooper, 2008], which reveal the subtle surface deformation in the Al Hoceima region associated with the 2004 earthquake. Orbital errors are estimated and removed from the mean line-of-sight velocity field with a best-fit bilinear ramp instead of using the StaMPS orbital error estimations. The detailed processing procedure for SBI technique can be found in Chapter 2.2.

We have analyzed 15 Envisat ASAR images on descending track (T280) between 06-June-2004 and 31-January-2010 covering the earthquake region (Figure 4.5). A map of cumulative line-of-sight deformation is obtained from a mean LOS velocity field calculated from 33 interferograms using SBI technique (Figure 4.5). The time series of displacements on ascending track (T230) were calculated by Gonzalez *et al.* [2010], using 33 differential interferograms from 15 Envisat ASAR images between 01-October-2003 and 01-August-2007 (Figure 4.5). The analysis of time series displacements on ascending track is based on adopted approach to Atzori *et al.* [2008] to minimize the effect of temporal smoothing and also the erroneous propagation of the coseismic signal over the pre- and post-seismic periods. Firstly, all SAR images have been co-registered to a common reference image (master image), and then all possible interferograms with small baselines (less than 300 meters) have been generated. Then, StaMPS/MTI [Hooper, 2008] has been run to solve for the unwrapped differential phases and to invert for the time series displacements (Figure D.1). Prior to that point, all parameters related to temporal smoothing have been selected below the maximum temporal sampling rate (typically, 35 days for Envisat and ERS). Once the time series of displacements has

been generated, temporal filtering has been applied by splitting the time series into two subsets (pre- and post-earthquake), and temporally low-pass filtering with the same Gaussian type ($\sigma = 0.75$ yr). No coseismic signal is allowed to propagate to pre- and post-seismic periods through this approach.

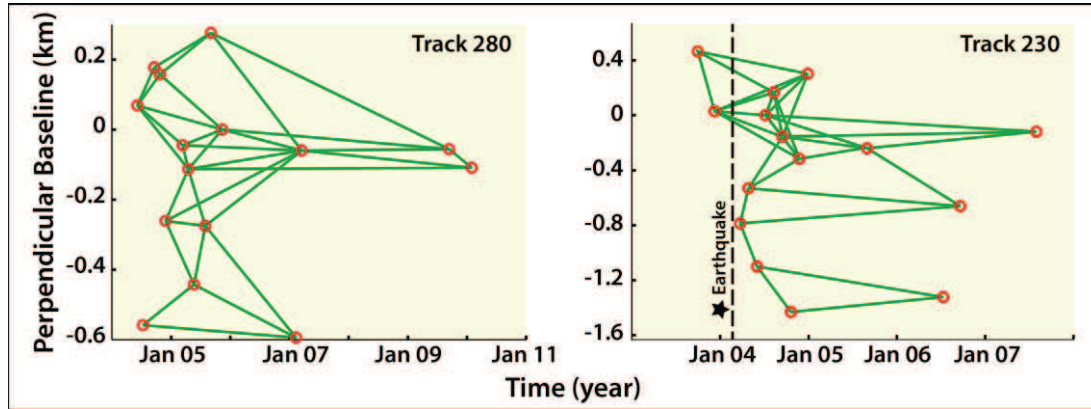


Figure 4.5 : Baseline plot showing the interferogram pairs (green lines) between descending (T280) and ascending (T230) radar images (red circles).

The cumulative LOS change maps shown in Figure 4.6 reveals a clear postseismic signal in the earthquake region. Warm colors (i.e., negative values) indicate motion away from the satellite and cool colors (i.e., positive values) indicate the motion toward the satellite, consistent with a right-lateral sense of motion across the fault. The spatial pattern of postseismic surface deformation shows considerably similar pattern as coseismic surface deformation with some exceptions on the ascending and descending data sets. On the descending track, the map reveals LOS range largely decrease in the southeastern part of the fault reaching up to 4 cm east of the basin, particularly where it shows a step or bend, which may probably be related with the dip-slip component due to the geometry of the fault. Furthermore, the time series shown in Figure 4.7 imply mainly linear change with time, since the SAR images do not cover the first few months after the earthquake. On the ascending track, the map reveals LOS range largely increase in the northern part of the fault reaching up to 3 cm where the maximum coseismic line-of-sight increase was observed (5 fringes). Also, the ascending time series show sudden change that signifies the earthquake and then this is followed by linear change after the earthquake (Figure 4.7). Furthermore, peak-to-peak cumulative line-of-sight displacement is about 5 cm during 3 years and 5 months, which is the magnitude of around 20% of the coseismic deformation (~ 23 cm, see Figure 4.4).

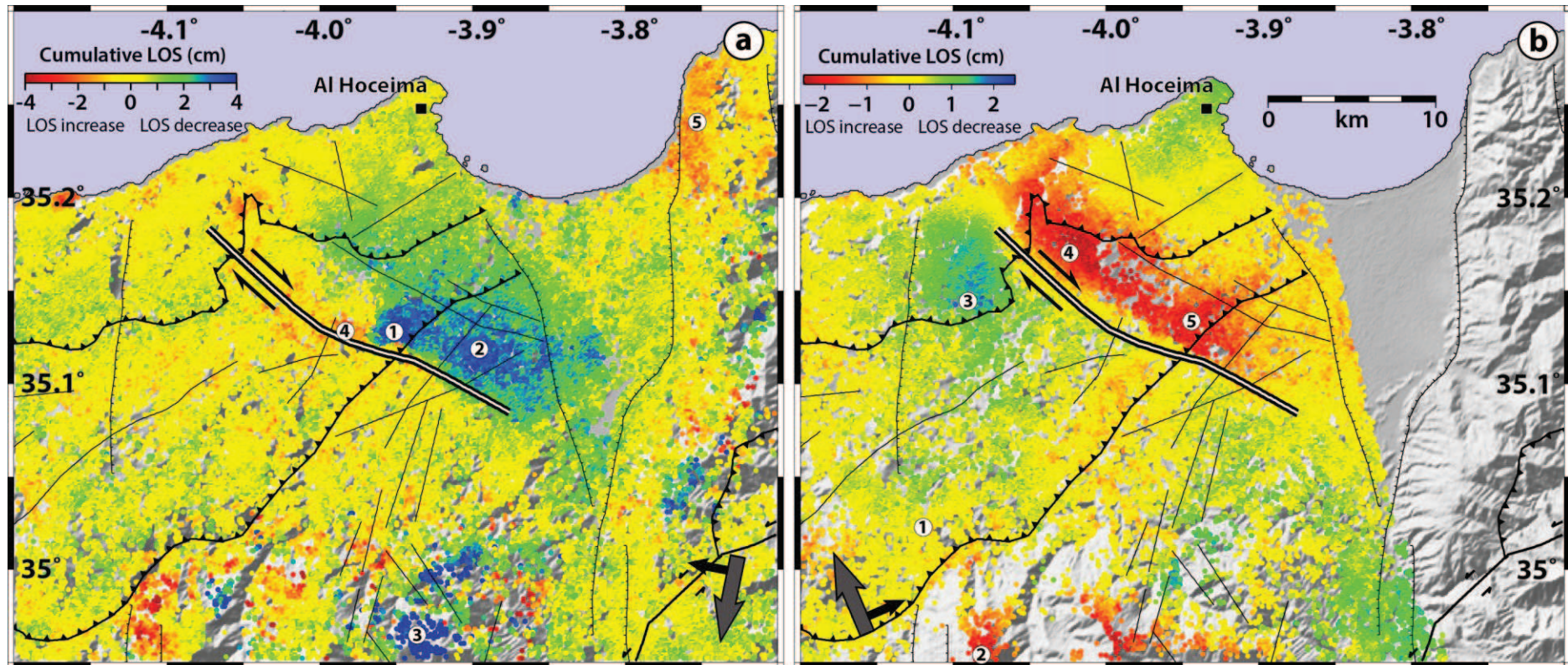


Figure 4.6 : Cumulative LOS range change **(a)** between 2004 and 2010 deduced from SBI time series on descending track and **(b)** between 2004 and mid-2007 deduced from StaMPS/MTI time series on the ascending track in the Al Hoceima region. Movements away from the satellite are shown with warm colors and those towards the satellite with cool colors, which is consistent with right-lateral sense of motion. Thick black line is the best model fault. The gray and black arrows indicate the satellite flight direction and line-of-sight direction (right looking), respectively. Numbers show the locations of time series plotted in Figure 4.7.

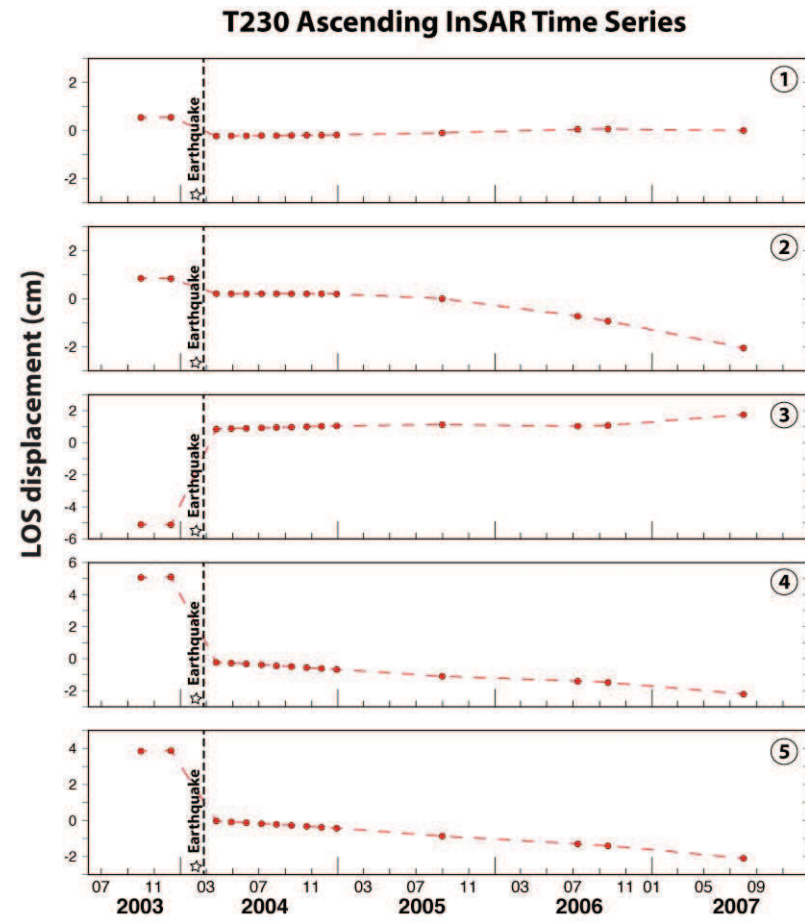
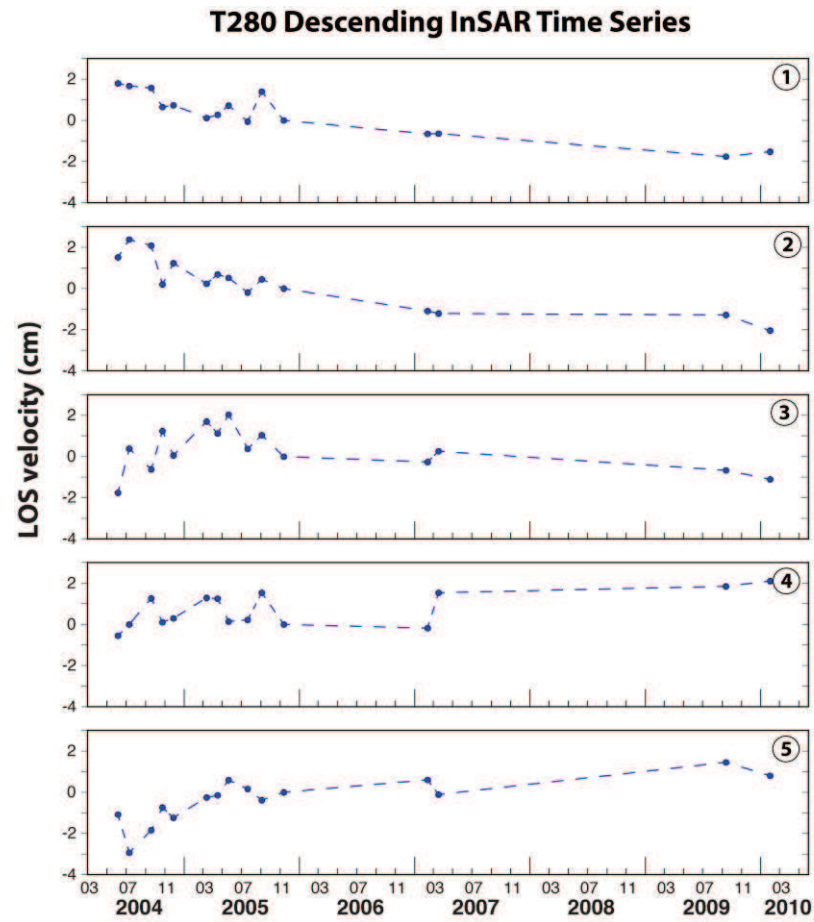


Figure 4.7 : Time series of InSAR data (blue circles for descending and red circles for ascending). Postseismic deformation in the earthquake region is manifested by linear change in descending time series due to lack of four months data just after the earthquake and similarly linear change in ascending time series after sudden change due to the earthquake.

4.4 Modeling

In order to estimate what kind of fault geometry and slip distribution can explain both the co- and post-seismic LOS velocity fields, inverse modeling has been performed utilizing the boundary element software Poly3Dinv [Thomas, 1993; Maerten *et al.*, 2005].

4.4.1 Modeling of coseismic deformation

The analysis of coseismic interferograms, benefiting from aftershocks and postseismic InSAR time series, provides significant information on the main characteristics and location of the 2004 earthquake rupture, which requires a revision in the southern tip of the fault according to these new observations. Since the modeled main fault must not crosscut the visible fringes [Cakir *et al.*, 2006], northeast-southwest-trending right-lateral strike-slip faults are placed along the fringes of zero LOS deformation in between the two lobes of the ascending interferogram to the north of the earthquake area, similar to Akoglu *et al.* [2006] fault model. Postseismic LOS deformation data (Figure 4.6) and aftershocks distribution (Figure 4.3) are utilized to detect the fault location and geometry since the fault rupture did not reach to surface and the coseismic LOS deformation captured by SAR interferometry is not quite unambiguous in the south of earthquake area. Fault surfaces meshed with triangles were constructed using MATLAB[®]. While the length of the triangular elements is kept approximately the same (1.7-2.1 km) along the fault, their sizes are gradually increased from 1 km to 2.5 km along the dip direction down to 20 km of depth because the resolution of inverted slip decreases with increasing depth. The digitized fringes of coseismic interferograms are used instead of unwrapped data in the inversion because most of the fringes that readily are visible could not be properly unwrapped due to poor coherence to the south of earthquake area (Figure 4.4). The slip distribution on the triangular elements was then inverted with a negativity constraint on the strike-slip component (i.e., right-lateral for the modeled fault). The scale-dependent umbrella-smoothing operator of Poly3Dinv is applied to the inverted slip distribution (with a factor of 0.3) to avoid unphysical oscillatory slip. The smoothing operator with a zero slip constraint on the fault edges, including the topmost patches, prevents deducing high slip peaks where the inverted data are insufficient or absent due to using digitized contours.

After testing faults with varying dip direction and angles, the best model is determined by a N50°W-trending right-lateral strike-slip fault of about 21 km that dips 78°-79° eastward with a restraining bend or step to the left around 2 km (Figure 4.8 and 4.9). The location and the azimuth of the north section of the fault is well constrained, as we are forced to place the fault between the two lobes of the ascending interferogram (Figure 4.4b). This fault geometry is the same as that of *Akoglu et al.* [2006] in the northern section, except its southernmost section where the postseismic surface deformation and aftershocks distribution require a bend or step to the left and NW-SE trending planar fault after the bend. However, the presence of the poor coherence does not allow us to better constrain the location or connection of the bend or step. We assume a continuous fault rupture with a bend to the left, as it is a common feature along strike-slip faults.

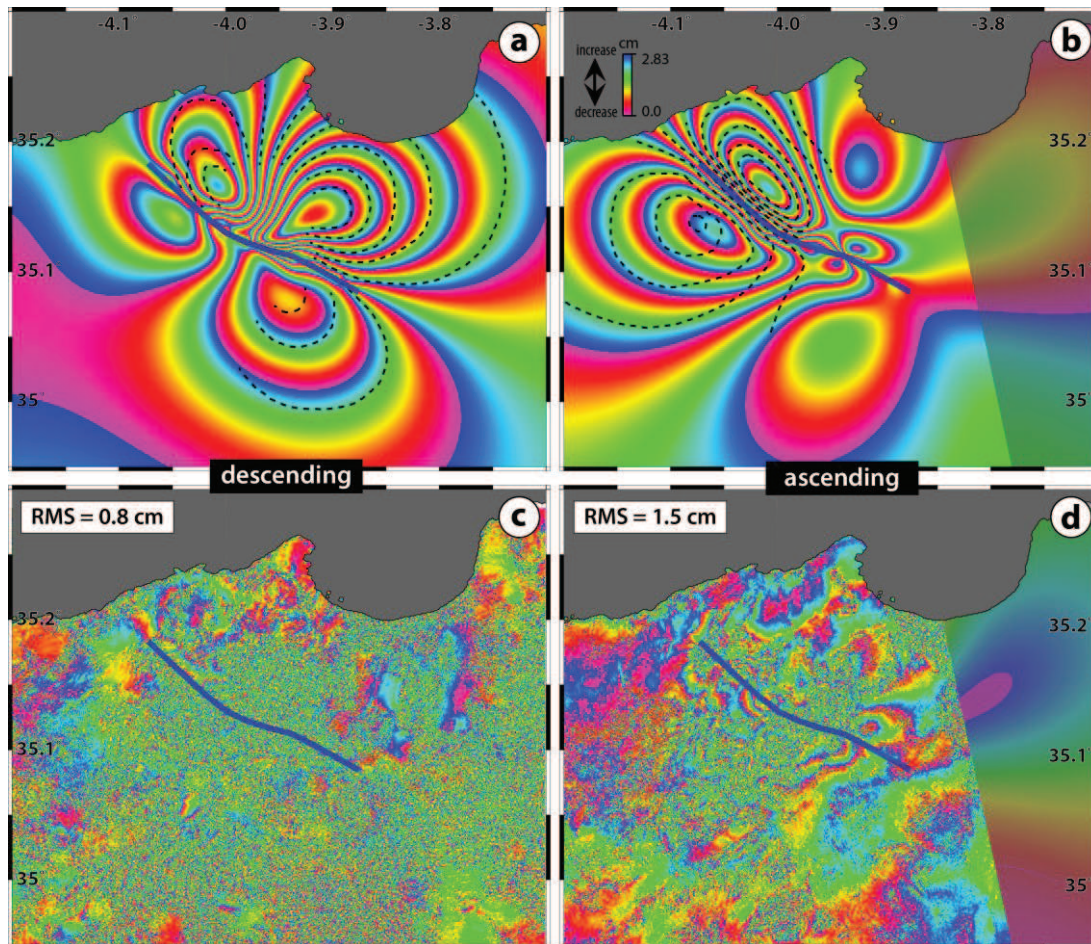


Figure 4.8 : a, b) Synthetic interferograms predicted by a right-lateral strike-slip c, d) residual interferograms obtained after subtracting the synthetic interferograms from the observed data (shown in Figure 4.4). Dashed lines are digitized fringes used in modeling of the interferograms. Blue line is the best model fault.

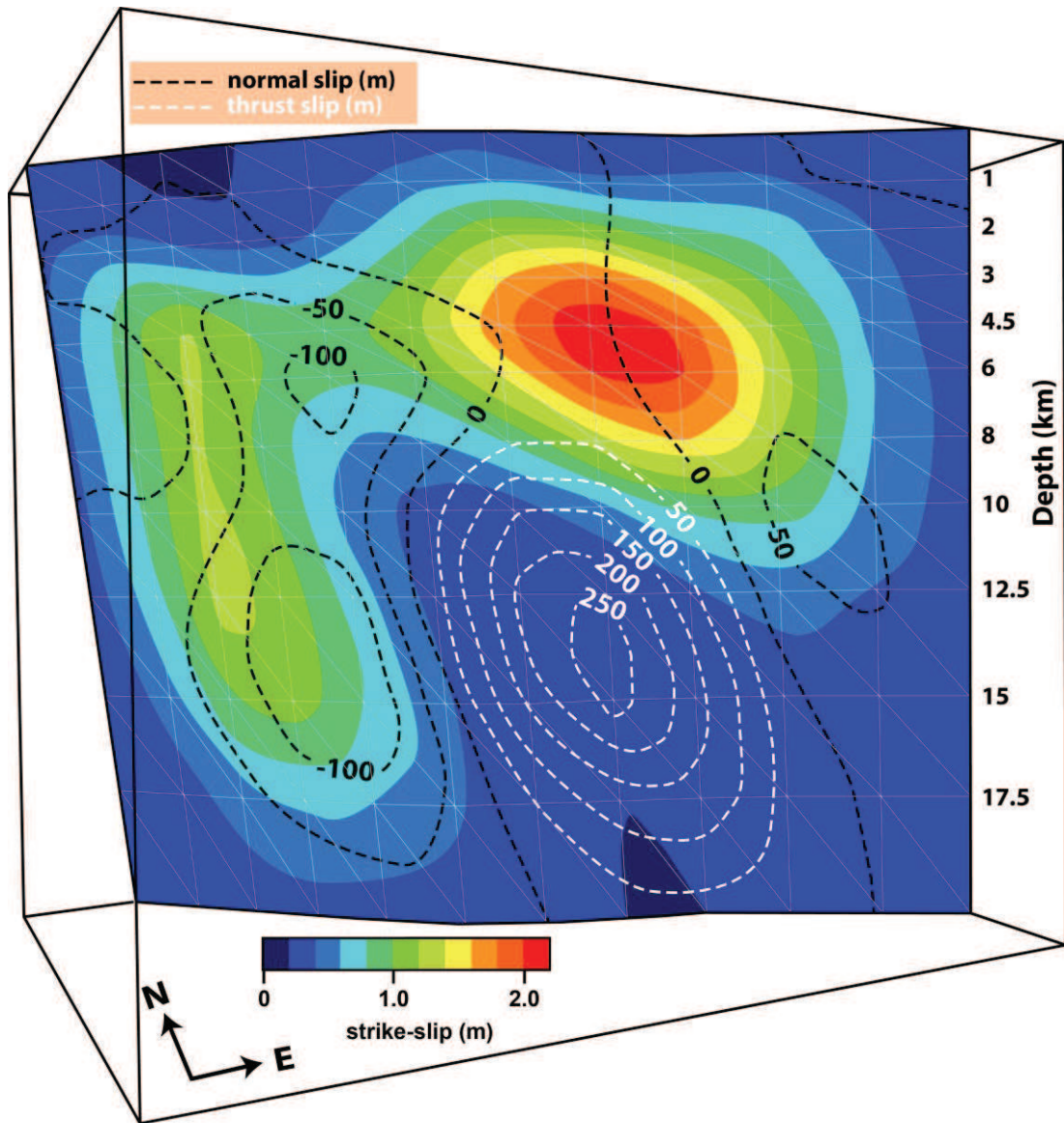


Figure 4.9 : Color-coded postseismic strike-slip distribution (right-lateral) on the 2004 Al Hoceima earthquake rupture with a reverse slip component (black dashed lines), which coincides with the step or/and bend of the earthquake rupture, and a normal slip component located on the main branches of the fault.

The slip distribution predicted by the model with a right-lateral slip is shown in Figure 4.9. It shows predominantly right-lateral displacements up to 2.2 m localized mostly at depths between 4 and 7 km on the southern section around the fault bend, similar to that of *Akoglu et al.* [2006]. The southern section of the fault rupture is supplemented by reverse slip due to the restraining bend on the fault. Furthermore, northern section of the fault suggests right-lateral slip with normal faulting, which is in good agreement with extensional faults seen in the region and aftershocks focal mechanisms. The inferred 5×10^{18} Nm (equivalent of M_w 6.4)

geodetic moment determined from modeling is also in good agreement with those obtained from seismological observations [Ait Brahim *et al.*, 2004; Stich *et al.*, 2005], and InSAR studies [Akoglu *et al.*, 2006; Biggs *et al.*, 2006; Cakir *et al.*, 2006]. As shown in Figure 4.8, the slip model successfully reproduces the main features of the observed interferograms with RMS (root mean square) misfits well below an individual fringe (2.83 cm).

While the descending residual interferograms show no clear remaining fringes, the ascending residual interferograms contain some residuals in the near field after inversions. Furthermore, the depth of the coseismic slip along the south section could not be well constrained due to the poor coherence and absence of aftershocks in this region, where some residual fringes are present. The presence of deep coseismic slip with large amplitudes suggests that the earthquake probably nucleated at depths below 8 km (Figure 4.9), which may explain why the rupture did not break the surface. Consequently, some of the remaining fringes in the residual interferograms are most probably due to atmospheric artifacts, unmodeled fault complexity in the near field and/or contribution of the aftershocks ($M > 5$) to the interferograms.

4.4.2 Modeling of postseismic deformation

In order to estimate to what extent a model of afterslip can explain the SAR data, we utilize the fault model deduced from coseismic interferograms with cumulative postseismic LOS displacements during ~3.3 years (Figure 4.10). While the ascending SAR data set spans about 3.3 years after the earthquake, the descending data set covers a postseismic period of about 5.6 years. Therefore, we recalculate a cumulative displacement for the descending track for 3.3 years, assuming a linear deformation as suggested by the time series obtained from SBI analysis (Figure 4.7). Before modeling the data, we mask the southeastern part of the ascending data to avoid unrealistic slip due to far field LOS change in mountainous region that is not associated with the 2004 earthquake (Figure 4.10) and displays comparable pattern with high elevation (Figure 4.6b). In order to avoid heavy calculation during the inversion due to over hundreds of thousands data points, we reduce the data points by applying the near-neighbor algorithm of the Generic Mapping Tools (GMT) [Wessel *et al.*, 1998, 2013] with a 1-km search radius. Then

we contour the data every 0.2 cm taking into account the sampling interval for each contour length to avoid the unrealistic weighting of the longer contours.

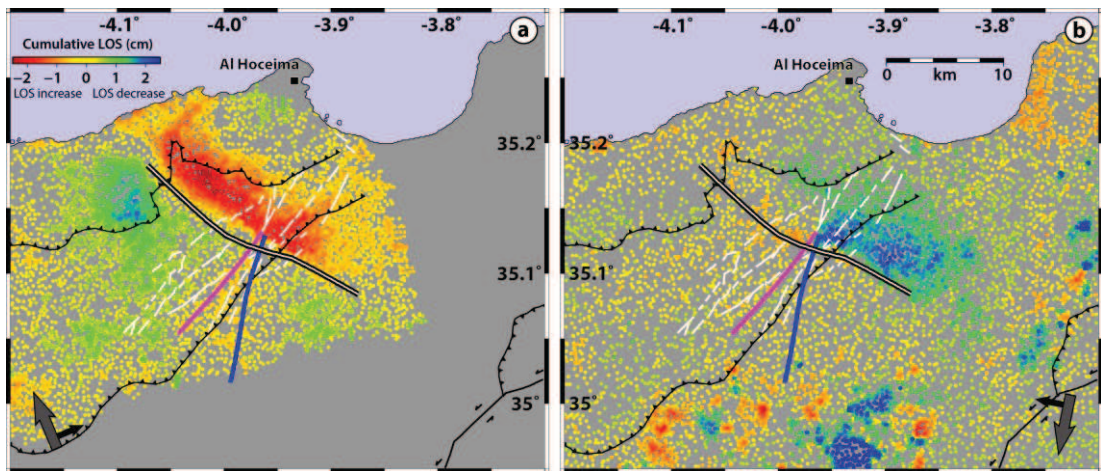


Figure 4.10 : **a)** Ascending and **b)** descending cumulative LOS data sets during ~ 3.3 years used in inversions. Thick black line is modeled coseismic fault. The pink line shows the model fault tested to improve the model fit to LOS data change. The blue line indicates a fault suggested by the NE-SW trending aftershocks distribution.

Several inversions have been run with a single or multiple faults geometry using the coseismic model as a main fault with a postseismic-triggered branch based on the NE-SW trending aftershocks distribution and postseismic LOS change crossing the main earthquake rupture (Figure 4.10). We invert for the optimal slip distribution and seek models that minimize the misfit, while preserving smoothness of the model afterslip distribution. Smoothing (i.e., 0.3) and right-lateral strike-slip constraints are applied to avoid models with oscillating slip patterns that are favored by a free inversion without such additional constraints. We do not apply any dip-slip constraint for the postseismic models with regard to diminishing the inversion parameters and maintaining the simplicity. We apply a zero slip constraint on the fault edges, except the topmost patches where the inverted data are sufficient to obtain a reasonable slip.

In our modeling, we invert the ascending and descending data sets separately and jointly to see similarities and differences they predict (Figure 4.11 and 4.12). As can be seen from Figure 4.11, the two data sets predict rather different slip distributions. While descending data set predicts deep (5-12 km) slip on the northern side of the fault opposite to the coseismic model, the ascending data suggest fairly shallow afterslip mainly from surface down to 5 km depth. In addition, joint

inversion also presents shallow afterslip mainly from 1-8 km depth complementing the coseismic slip. Figure 4.12 illustrates the residuals obtained after these inversions. Although models after inverting two data sets separately explain the main features of the postseismic displacement fields, the predicted slip distribution is rather different in the earthquake region. Furthermore, these models do not show a satisfactory fit to the data as they result in significant residuals in near field along the fault rupture, which might be probably due to triggered postseismic splay fault on the northern section of the fault as suggested previously by *Cetin et al.* [2014b] that is connected to the main rupture around the fault bend. Consequently, inversions with joint data sets show quite deteriorated residuals. Therefore, the two data sets are rather inconsistent with each other, which is evident in the velocity maps shown in Figure 4.10. As expected, the lobes of LOS decrease (blue) and increase (red) are separated by the coseismic fault in the ascending data. However, in the descending data, the fault runs through the red lobe along its northern section, which makes it difficult to explain it with a coseismic model. Therefore, we consider that the descending data contains significant errors possibly resulting from atmospheric interference and unwrapping. Consequently, we give less weighting to the descending data in the joint inversions (models shown in Figure D.2). The estimated moment released for the joint inversion is 5.0×10^{17} Nm (M_w 5.73) for 3.3 years. It increases to 5.77×10^{17} Nm (M_w 5.77), in the case of individual ascending data inversion. These estimates suggest that the cumulative postseismic moment release during 3.3 years is around 8 to 15% of the coseismic moment release estimated from seismology and geodesy [*Stich et al.*, 2005; *Akoglu et al.*, 2006]. The multiple faults inversion results given in Appendix D (Figure D.2-D.6) show no significant improvement. The resolution tests shown in Figure D.7 indicate that the InSAR data sets have an adequate resolution in constraining the shallow slip on the fault.

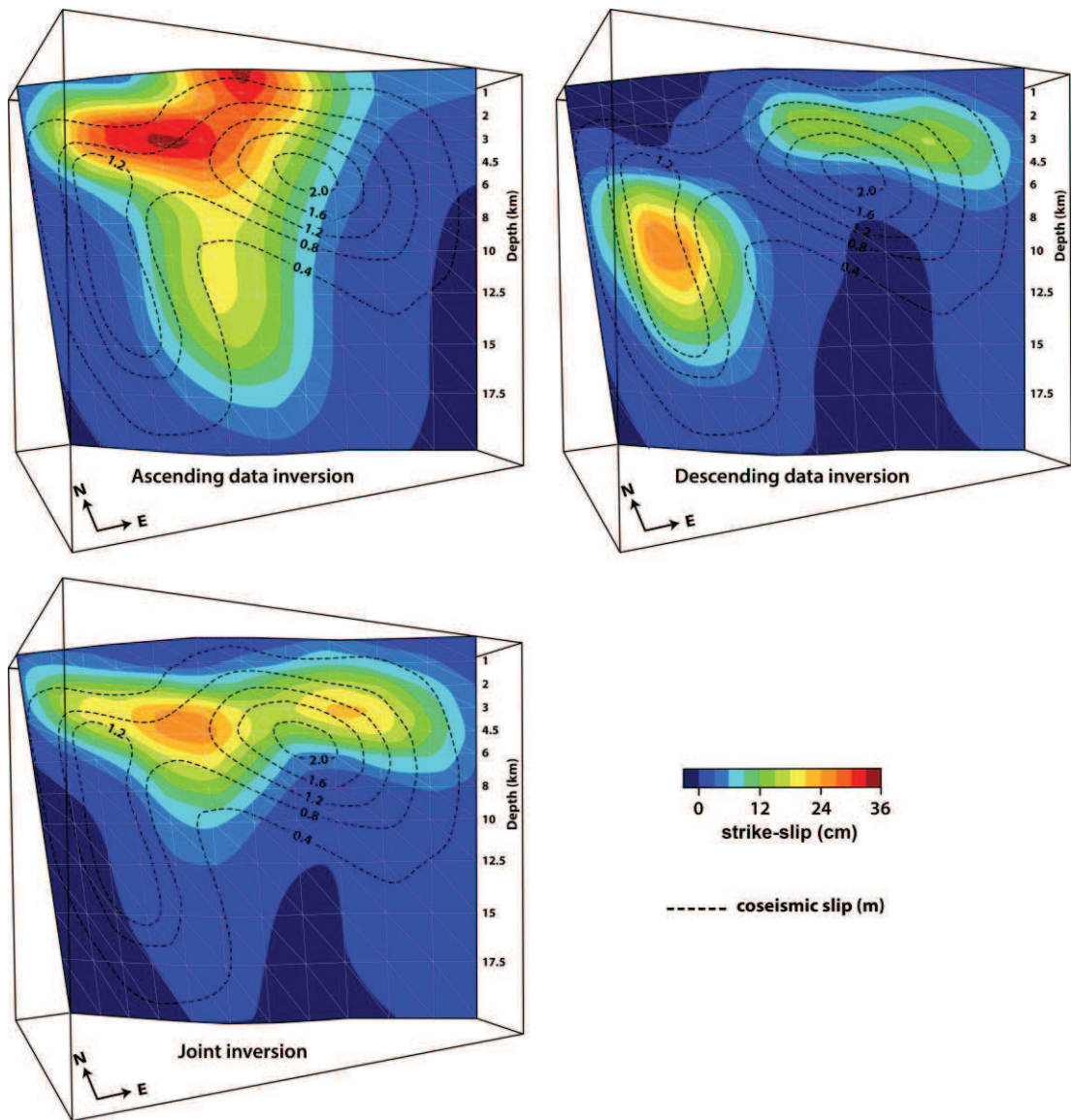


Figure 4.11 : Color-coded postseismic right-lateral strike-slip afterslip distribution on the Al Hoceima earthquake rupture. The afterslip distributions inverted from ascending data show patches of slip (up to 35 cm) along mostly the upper sections of the fault (<5-km-depth) complementing the coseismic slip (black dashed lines) at deeper fault sections. Descending data on the other hand predicts a deep slip on the southern side of the fault similar to the coseismic model.

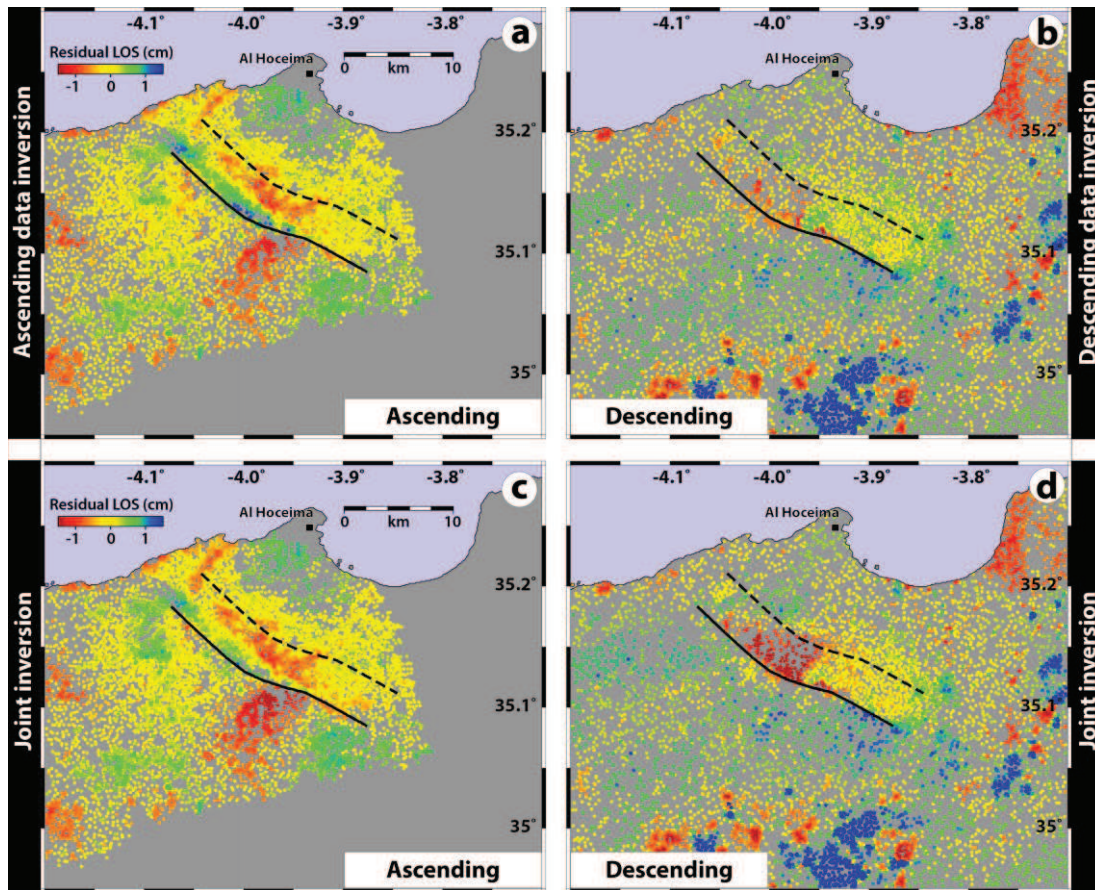


Figure 4.12 : Residual maps obtained after subtracting the synthetic InSAR data (Figure D.2) from the observed data (shown in Figure 4.10). Residuals after inversion of **(a)** the ascending and **(b)** the descending data alone, and **(c, d)** jointly with a lower weighting for the descending data. Black line is the top of the coseismic model fault, and the dashed black line is the bottom of the coseismic model fault.

4.5 Discussion and Conclusion

Postseismic deformation associated with the 2004 Al Hoceima earthquake is documented using Envisat ASAR data from 2004 to 2010 in descending geometry and from 2004 to 2007 in ascending geometry. InSAR time series analysis has revealed postseismic LOS displacements up to 4 cm uplift and subsidence where a remarkable coseismic displacement was observed after the earthquake. The spatial pattern of the postseismic displacement fields and aftershocks distribution however required a revision in the southern tip of the fault of the coseismic fault rupture models proposed by previous studies [*Cakir et al.*, 2006; *Akoglu et al.*, 2006; *Biggs et al.*, 2006; *Gonzalez et al.*, 2010]. The coseismic fault model has been revised using the same data set (one ascending and one descending interferogram) used in *Cakir et al.* [2006]. Remodeling of the coseismic interferograms suggests a fault geometry

same as that of *Akoglu et al.* [2006] in the northern section that is well constrained according to ascending interferogram, except its southernmost section where the postseismic surface deformation and aftershocks distribution require a bend or step to the left and a NW-SE trending planar segment after the bend. The model is predominated by right-lateral slip with normal faulting on main branches of the fault that is similar to that of *Akoglu et al.* [2006], which is in good agreement with extensional faults seen in the region and aftershocks focal mechanisms [i.e., *van der Woerd et al.*, 2014], and reverse faulting around the fault bend that is consistent with the restraining bend. Remodeling of the coseismic interferograms indicates a geodetic moment of 5×10^{18} Nm (equivalent of M_w 6.4), which is in good agreement with those obtained from seismological observations [*Ait Brahim et al.*, 2004a; *Stich et al.*, 2005], and InSAR studies [*Akoglu et al.*, 2006; *Biggs et al.*, 2006; *Cakir et al.*, 2006].

The elastic dislocation modeling of the postseismic LOS displacements indicates that postseismic deformation can be explained by shallow (< 8 km) afterslip with up to 0.3 m displacement mainly above the high slip patches of the coseismic slip as with 5.0×10^{17} Nm (M_w 5.73) cumulative moment release. Afterslip can occur either up-dip or down-dip of the ruptured zone [*Smith and Wyss*, 1968; *Marone et al.*, 1991; *Zweck et al.*, 2002; *Hsu et al.*, 2006]. The coseismic slip deficit at the uppermost sections of the fault appears to be filled by the postseismic afterslip, inferring a complementary coseismic and postseismic slip as commonly observed for other moderate-large earthquakes [*Reilinger et al.*, 2000; *Cetin et al.*, 2012]. Additionally, the postseismic deformation requires further studies to explain the remaining residuals in the near field by the afterslip modeling, which might possibly be related with a triggered postseismic splay fault. Shallow moderate-to-large earthquakes in the Rif Mountain of northern Morocco expose postseismic deformation that may constitute a significant part in the earthquake cycle.

Aftershocks and postseismic deformation are the most common manifestations of stress relaxation following moderate-large earthquakes. Identifying the relation between aftershocks and postseismic deformation remains unclear. In some cases of large thrust earthquakes, it has been observed that the aftershocks and geodetic deformation follow the same temporal evolution [*Perfettini and Avouac*, 2004; *Perfettini et al.*, 2005; *Hsu et al.*, 2006]. This observation seems to hold also

for the M_w 6.4, 2004 Al Hoceima earthquake (Figure 4.3). The Rif is subject to distributed strike-slip deformation via northeast-southwest and northwest-southeast-trending conjugate faults that is supported by strike-slip earthquakes and related aftershocks with left- and right-lateral kinematics. These conjugate faults including the 1994-2004 earthquake ruptures crosscut the thrust faults of the Rif illustrate that Quaternary strike-slip tectonics superimposed on Tertiary thrust- and -fold tectonics [Meghraoui *et al.*, 1996]. That active tectonics and related geomorphological features associated with strike-slip faults are not well developed on the landscape suggests that the Rif neotectonic regime is probably on its early stages, which can be interpreted as fragmentation of the Rif Mountain range result from a westward escape tectonics in the frame of the Africa-Eurasia (Iberia) collision tectonics.

Chapter V :
**Extent And Distribution Of Aseismic Slip On
Ismetpaşa Segment Of The North Anatolian Fault
(Turkey)**

5. EXTENT AND DISTRIBUTION OF ASEISMIC SLIP ON İSMETPAŞA SEGMENT OF THE NORTH ANATOLIAN FAULT (TURKEY)

5.1 Introduction

Understanding the mechanics of major active faults is important for better understanding of the earthquake physics and reliable seismic hazard evaluations [Carpenter *et al.*, 2011]. The majority of active faults may be locked, accumulating strain over a long period of time and releasing it abruptly by producing earthquakes, some faults freely slip over time, accumulating little or no strain and generating no significant earthquakes [Thatcher, 1979; Burford and Harsh, 1980]. Knowledge of the extent and rate of aseismic slip on the fault plane is therefore important parameters for reliable assessment of seismic hazard as it effectively reduces the fault surface area capable of rupture in earthquakes. Its spatiotemporal variation along faults has also important implications for forecasting the timing, locations, and potential sizes of future earthquakes and for understanding the fault behavior [Bürgmann *et al.*, 2000].

The İsmetpaşa creeping segment was ruptured by the 1944 Bolu-Gerede (M=7.3), and 1951 Kurşunlu (M=6.9) earthquakes, part of the westward migrating earthquake sequence of the NAF during the 20th century (Figure 5.1) [Barka and Kadinsky-Cade, 1988; Barka, 1996; Stein *et al.*, 1997]. Based on the railway maintenance reports, Ambraseys [1970] estimated a rapid right-lateral surface creep of 50 mm/yr following the 1944 earthquake until the 1951 event. The spatiotemporal evolution of the surface creep at İsmetpaşa remained, however, unknown until the mid 2000s despite its discovery in the late sixties [Ambraseys, 1970]. Offset measurements on the walls of the railway station at İsmetpaşa town suggested that the creep rate had decreased to 20 mm/yr between 1957 and 1969 [Ambraseys, 1970]. A micro-geodetic network installed across the fault at İsmetpaşa in 1972, added with other geodetic measurements (LIDAR and InSAR) along the creeping segment show an exponential or logarithmic decrease of creep rate reaching a steady

slip rate of about 9 mm/yr over the last decade [Aytun, 1982; Eren, 1984; Deniz et al., 1993; Cakir et al., 2005; Kutoglu and Akcin, 2006; Karabacak et al., 2011; Ozener et al., 2012; Kaneko et al., 2013]. Using the conventional InSAR method, Cakir et al. [2005] identified, for the first time, a 70 km-long lateral extent of the creeping section, which is roughly confirmed later on by Kaneko et al. [2013] using stacking of independent InSAR data (ALOS).

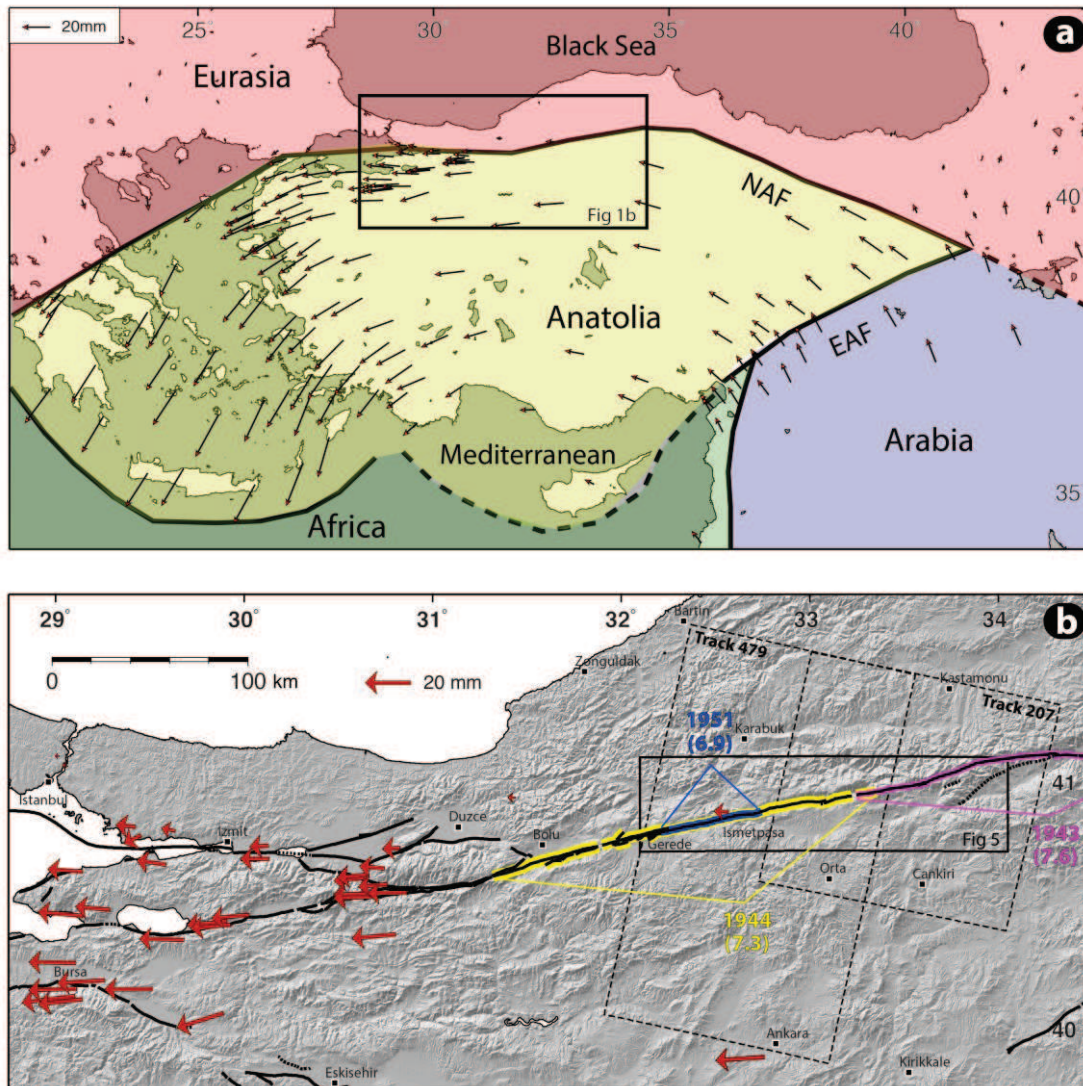


Figure 5.1 : a) Tectonic map of Turkey and surrounding regions with GPS vectors in a Eurasia fixed reference frame [Reilinger et al., 2006]. Rectangle shows the location of Figure 5.1b. b) Shaded SRTM topography map along the North Anatolian fault zone in northwestern Turkey with the recent rupture segments of large earthquakes [Barka and Kadinsky-Cade, 1988; Şaroğlu et al., 1992]. The dashed rectangles are the Envisat image frames with track numbers used in this study.

In this study we present an interseismic velocity field mapped using the PSI time series technique [Ferretti *et al.*, 2001; Hooper *et al.*, 2004] between 2003 and 2010 on two overlapping descending tracks of Envisat ASAR (C-band) satellite covering the NAF between 32.1°E and 34.3°E (Figure 5.1). We use the surface velocity field and provide for the first time a model of aseismic slip distribution on the fault using elastic half-space dislocations. Finally, we discuss the mechanism of aseismic creep, its initiation and the potential causes for its along-strike variation on the basis of creep rate variation and lithology along the fault.

5.2 InSAR Observations

We present interseismic velocity fields obtained from PSI analysis [Hooper *et al.*, 2004], which has been successfully used to reveal slow surface creep along the Longitudinal Valley (Eastern Taiwan) [Champenois *et al.*, 2012] and the NAF faults [Cakir *et al.*, 2014]. Orbital errors are estimated and removed from the mean line-of-sight velocity field with a best-fit bilinear ramp. Velocity standard deviation maps, calculated by StaMPS using bootstrapping, reach a maximum of 2.4 mm/yr for two individual overlapping tracks (Figure E.1). The detailed processing procedure can be found in Chapter 2.1.

5.2.1 Surface velocity

We have analyzed 55 Envisat ASAR images on two descending and overlapping tracks (T479 and T207; Fig.1b) between 2003 and 2010 (Figure 5.2). Images acquired on May 6, 2007 on T479 and August 8, 2008 on T207 are chosen as the master scenes of all the interferometric pairs in each track to minimize the spatial and temporal decorrelation, and atmospheric effects. A mean radar line-of-sight (LOS) velocity field for each track is obtained and then projected to fault-parallel horizontal velocities assuming that the radar LOS displacements are due to purely horizontal motion on a N76°E trending strike-slip fault, parallel to the strike of the İsmetpaşa segment taking into account the local incidence angles that vary across the range. The fault-parallel velocity field shown in Figure 5.3 reveals very clearly the surface creep as well as the interseismic strain accumulation across the NAF. Warm colors on the southern side of the fault indicate motion away from the satellite (i.e., westward), and cool colors on the northern side of the fault indicate motion towards

the satellite (i.e., eastward), consistent with a right-lateral sense of plate motion across the NAF. Surface creep is characterized by steep fault-parallel velocity gradients, and by a sharp color contrast across the fault trace along a distance of more than 100 km (Figure 5.3). In contrast, locked segments are clearly shown by gradual changes in the velocity field across the fault, particularly between Gerece and Ismetpaşa. Besides, to the south of the NAF the interseismic signal is strongly disturbed by a circular deformation pattern attributed to the postseismic displacements after the June 6, 2000 Orta earthquake [Taymaz *et al.*, 2007; Cakir and Akoglu, 2008].

Fault-parallel velocities along four different profiles are shown in Figure 5.4 together with best-fit models for creeping and locked faults obtained with elastic dislocations. The velocity profiles of locked faults (at 15 km-depth) show a classic arctangent shape predicted by elastic screw dislocations across a strike-slip fault [Savage and Burford, 1973]. Conversely, the steps in the velocity profiles at the fault indicate surface creep. The shape and height of these steps are controlled by the locking depth and creep rate; abrupt vertical changes indicating creep reaching to the surface, and gradual changes showing deeper locking depths. It is worthwhile noting that fault-parallel velocities in Figure 5.4 do not correlate with topography.

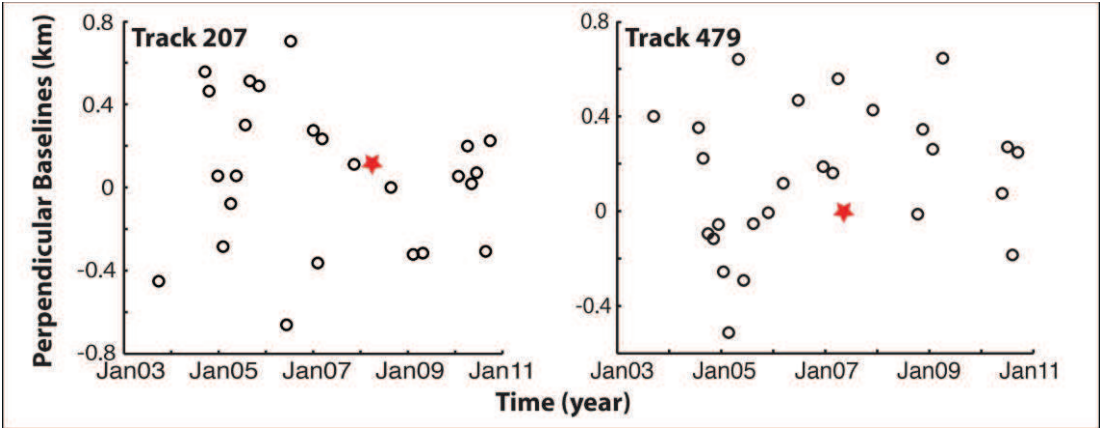


Figure 5.2 : Baseline versus time plot of synthetic aperture radar orbits from two Envisat tracks used to calculate the deformation field and the time series. Empty circles denote the SAR images with stars indicating the master orbits chosen for the PSI analyses.

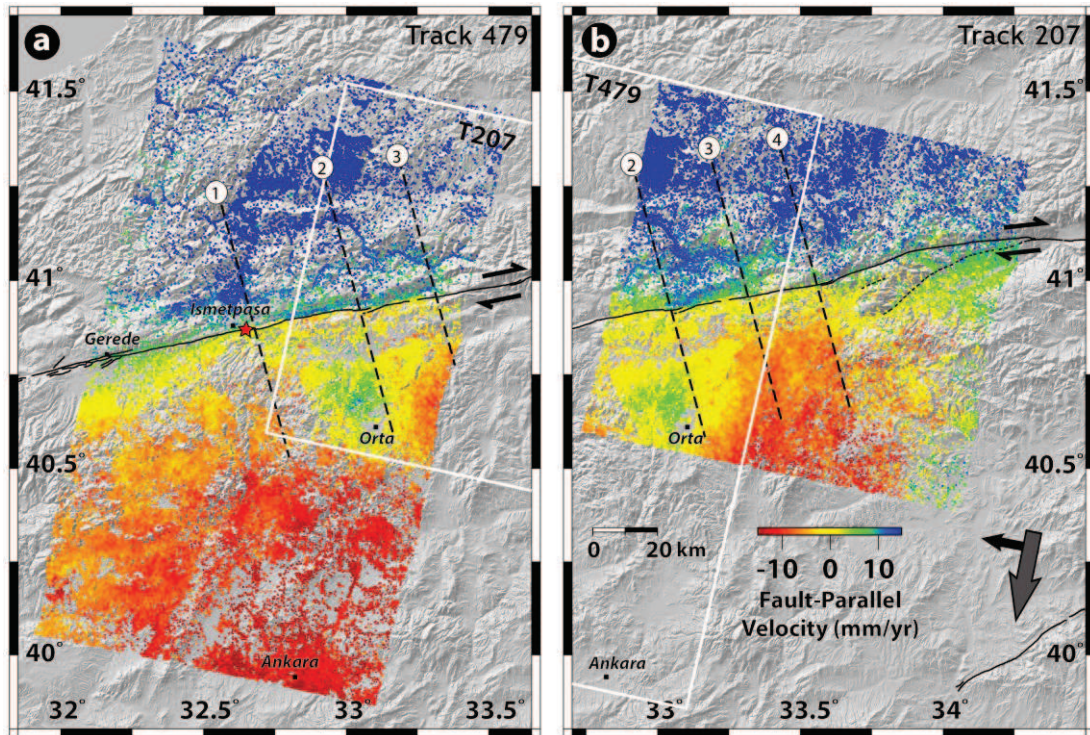


Figure 5.3 : Velocity field in the region of Ismetpaşa deduced from PSI time series. **a, b)** Fault-parallel horizontal velocity field (identical color scale for both tracks) between 2003 and 2010 on a SRTM shaded relief image with known active faults (black lines). The gray and black arrows to the bottom right corner show the satellite flight direction (descending) and the line-of-sight direction (right looking), respectively. Thick dashed lines with numbers are locations of profiles as shown in Figure 5.4. Red star shows the location of the PSI and GPS time series plotted in Figure 5.7. White boxes show the neighboring Envisat track used in this study.

5.2.2 Estimation of creep rate and extent

In order to determine the surface creep rate and its variations along the fault, we first subtract from the velocity field an interseismic model as explained in the modeling section below. Subsequently, profiles of residual velocities perpendicular to the fault are extracted at every ~ 1 km along the fault. Along 3 km on each side of the fault, we find a best-fitting line to the profiles, and compute the creep rate as an offset of the intercepts of these two lines at the fault trace (Figure 5.5) [Burford and Harsh, 1980]. Using standard deviations of PS pixels predicted by StaMPS, weighted means are calculated at every 50 m using a bin width of 100 m along these fault perpendicular profiles. The error bars of creep rates for individual profiles are estimated from the root-mean-square residuals of the line fitting using weighted means. The results reveal a ~ 120 -km long creeping section with a creep rate varying

in an oscillating manner along the fault and reaching a maximum of 20 ± 2 mm/yr around 20 km east of Ismetpaşa (Figure 5.6). At its eastern end, it overlaps with the western part of the 1943, and the eastern part of the 1944 and 1951 earthquake ruptures (Figure 5.6a). Oscillation of creep to the east might result from atmospheric errors and hence inferred creep east of 32.5°E (~ 80 km east of Ismetpaşa) requires confirmation. Note that despite some discrepancies, creep rate estimates from two different InSAR datasets in the central section of the fault are overall in good agreement. The creep rate is 8 ± 2 mm/yr at Ismetpaşa, consistent with most previous studies [Deniz *et al.*, 1993; Cakir *et al.*, 2005; Karabacak *et al.*, 2011; Ozener *et al.*, 2012; Kaneko *et al.*, 2013]. The InSAR LOS time series are in good agreement with LOS-projected GPS time series at Ismetpaşa and show linear decays with time (Figure 5.7).

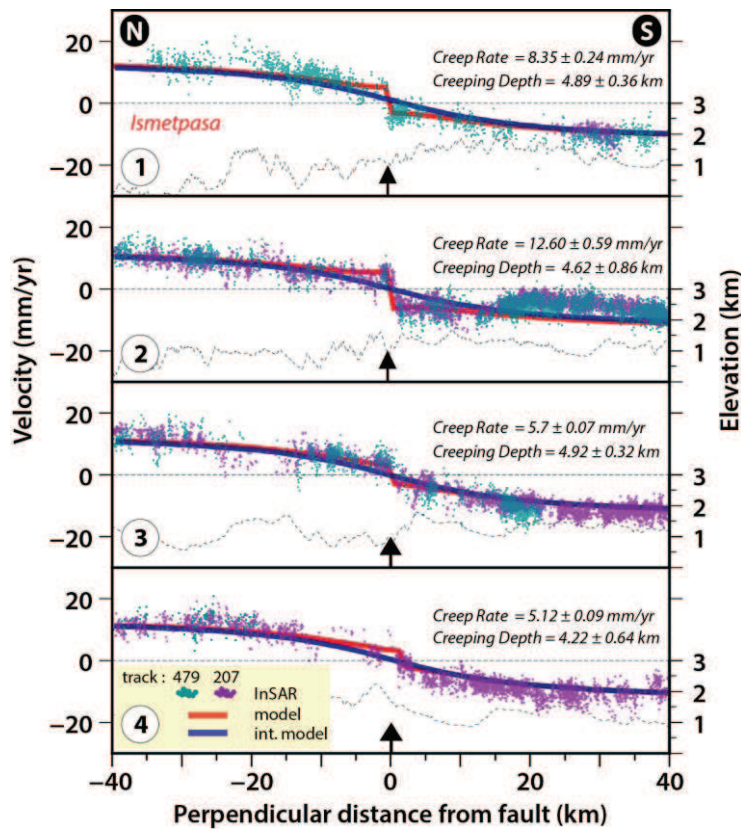


Figure 5.4 : Some of the observed and modeled fault-parallel velocity profiles perpendicular to the fault. Red curves show the best fitting model to PSI data with the creep rate and depth given above. The blue curves represent an interseismic model for a locked fault at 15 km of depth. Dashed line represents the topographic elevation along the profiles. Arrows indicate the mapped active fault location. Profile-1 crosses the location of the offset wall and the geodetic network that have been used to measure the creep rate at Ismetpaşa over the last 40 years.

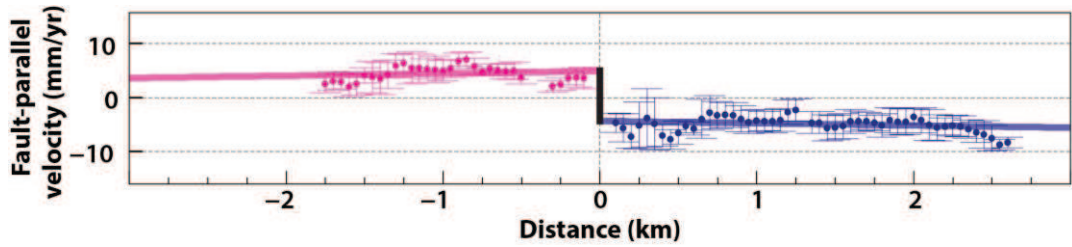


Figure 5.5 : Estimation procedure for the creep rate using best-fitting lines to InSAR velocity profiles that extend for 3 km on both sides of the fault (pink and blue colors). Creep rate is calculated from the offset of the two lines at the fault trace (e.g., the length of black line).

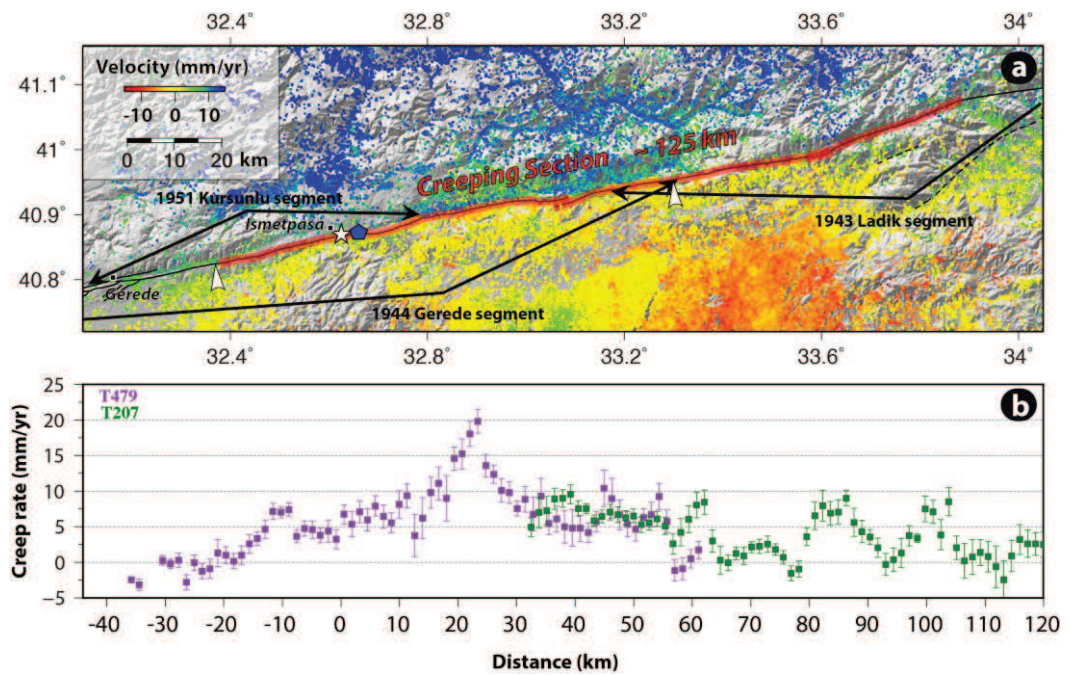


Figure 5.6 : Rate and extent of aseismic surface creep along the Ismetpaşa section of the North Anatolian Fault. **a)** A mosaicked map of fault-parallel horizontal velocity field on SAR image tracks T479 and T207. Red line shows the creeping section of the NAF and the blue pentagon indicates the location of the micro-GPS network. White star represents the location of the wall where creep was discovered by *Ambraseys* [1970]. White arrows show the extents previously found by *Cakir et al.* [2005] and *Kaneko et al.* [2013]. **b)** Creep rates with error bars along the fault are estimated from the InSAR velocities on track T479 (pink color) and track T207 (green color).

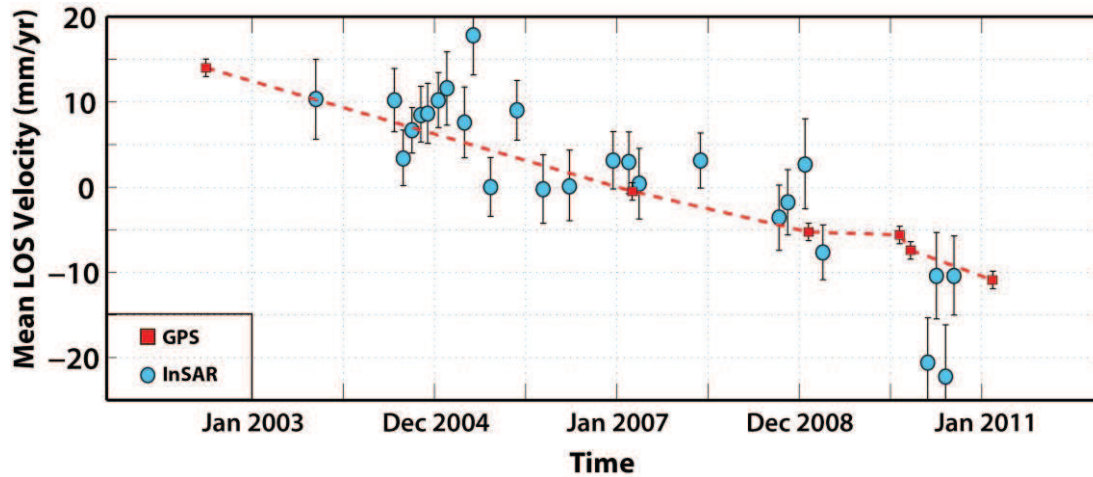


Figure 5.7 : Time series of line-of-sight InSAR (blue circles) and GPS (red squares) velocities (blue pentagon shown in Figure 5.6). The LOS velocities represent the mean of all pixels in a circle of ~ 600 m diameter to the north and south of the fault around the GPS network. The general trend and decay of creeping rate from InSAR time series are in good agreement with GPS time series.

5.3 Modeling

To estimate the aseismic slip distribution on the Ismetpaşa segment, we model the LOS displacements using the Poly3Dinv software [Maerten *et al.*, 2005] that uses the boundary element approach (see details in Chapter 3.4.1). To infer the aseismic slip distribution on the fault, we first model and remove from the LOS velocity field the long wavelength signal due to the interseismic strain assuming that the regional deformation due to the secular loading arises from buried displacement below the NAF. To model this secular loading, we use the far field (> 20 km away from the fault) LOS velocity field data (with the Orta earthquake region being masked). We invert for a right-lateral sense of slip on a single fault patch buried below 10 km to infinity (900 km) and obtain ~ 25 mm/yr of interseismic slip rate. However, the model does not entirely account for the long wavelength signal in the velocity field, implying the presence of unwrapping and unmodeled atmospheric errors, and orbital residuals in the data. We therefore obtain a variable interseismic slip model using multiple fault patches (12 triangles) to flatten the far field velocity field required for modeling the distribution of shallow creep on the fault (Figure E.2). We subtract this inverted interseismic model from the LOS velocity field and obtain a residual LOS velocity field that is considered as a creep signal in vicinity of the fault (Figure 5.8). The residual LOS velocities show a sharp color contrast across

the fault that can also be seen in the profiles shown in Figure 5.8b. Some of the remaining velocities, which are on the corner of the tracks with $\pm 2-3$ mm/yr, in the velocity field are, however, most probably due to atmospheric artifacts or unmodeled orbital errors but these don't affect offset at fault. In addition, the postseismic surface deformation associated with the 2000 Orta earthquake [Cakir and Akoglu, 2008] becomes more prominent and appears as circular area of range decrease ~ 30 km across anomaly with a blue color.

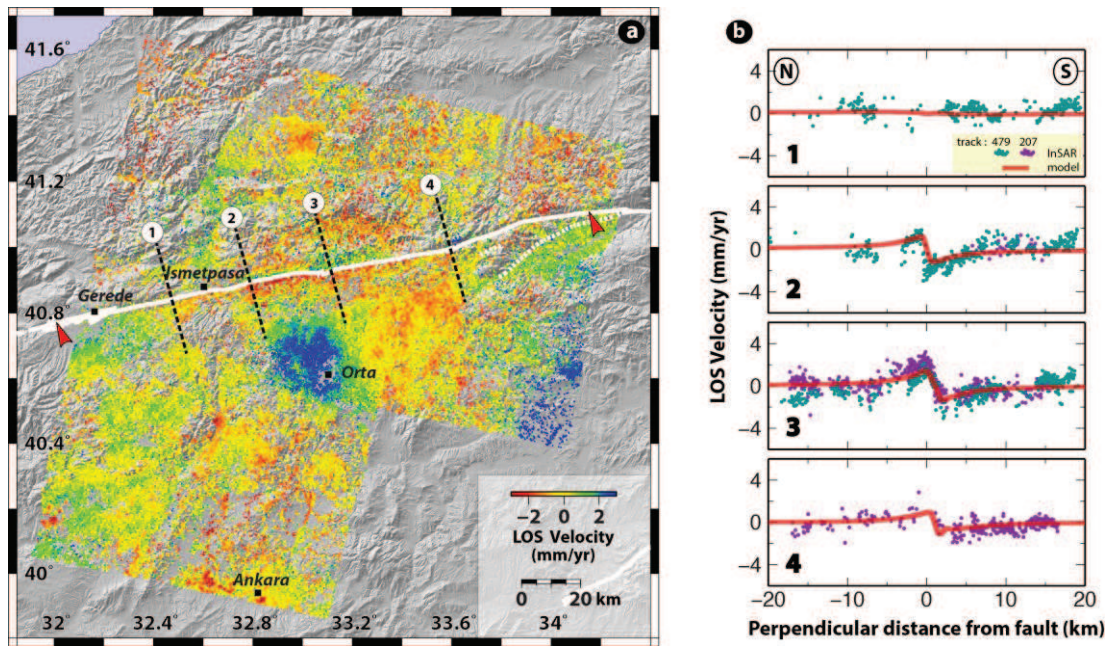


Figure 5.8 : Modeling of aseismic slip distribution. **a)** Residual LOS velocities, obtained by the removal of the long-term signal due to interseismic loading and unwrapping, atmospheric and orbital errors, are used to model the aseismic slip on the fault. The blue circular anomaly located around the town of Orta is most likely due to the postseismic deformation of the 6 June 2000 Orta earthquake ($M_w=6.0$). Red arrows on the fault (white lines) indicate the tips of the modeled fault shown in Figure 5.9. Dashed lines show the profiles in Figure 5.8b. **b)** Observed (green and purple points) and modeled residual velocities (red lines) along the profiles perpendicular to the fault.

To model the creep on the fault surface, we formed a vertical fault from surface to a depth of 10 km, using quadrangles of about 5 km long along the fault strike. The width of the quadrangles increases from 1 to 3 km in the down dip direction (Figures 5.8 and 5.9). To evaluate the uncertainty of slip distribution, we first estimate a 1-D covariance function for each data set by radially averaging a 2-D autocorrelation function calculated using the power spectrum of the data in the far field where there are no orbital ramps or deformation signal due to aseismic creep

[Hanssen, 2001]. We then fit a colored noise model [Lennon, 2000] to the 1-D covariance function. Using the procedures in Fukushima *et al.* [2003], for each data set on the two tracks we construct 200 simulations of spatially correlated random noise that matches the colored noise model. We use them to perturb each of our original data sets [Funning *et al.*, 2005], which are then inverted for pure right-lateral strike slip (locked on the fault edges, except at its top) using a scale-dependent umbrella-smoothing operator to avoid any unphysical oscillatory slip distribution. A smoothing factor of 0.5 is used since lower values predict slip rates much higher than the interseismic slip rates estimated from the GPS measurements (24.2 ± 0.2 mm/yr) by Reilinger *et al.* [2006] and from InSAR (25 ± 1.5 mm/yr) in this study. After calculating the mean slip, we estimate 95% confidence intervals from its distribution on each triangular patch. The results show a shallow creeping depth (mostly above 5 km) and an intermittent slip distribution with a highest rate of 20 ± 2 mm/yr on several patches along the fault, similar to that inferred along the Hayward fault [Schmidt *et al.*, 2005] (Figure 5.9). Although the surface creep deduced from offsets of best-fitting lines correlates to some extent with the creep inferred with Poly3Dinv modeling at depth, the largest patch located ~ 40 km east of Ismetpaşa is not obvious in the surface creep rate curves. Figure 5.8b illustrates that the model explains the LOS data reasonably well (~ 1.25 mm/yr RMS, Figure E.3). As expected, checker-box tests show that slip resolution decreases with increasing depth, but as shown in supplementary Figure E.4 the InSAR data have an adequate resolution in constraining the shallow slip (< 5 km) on the fault.

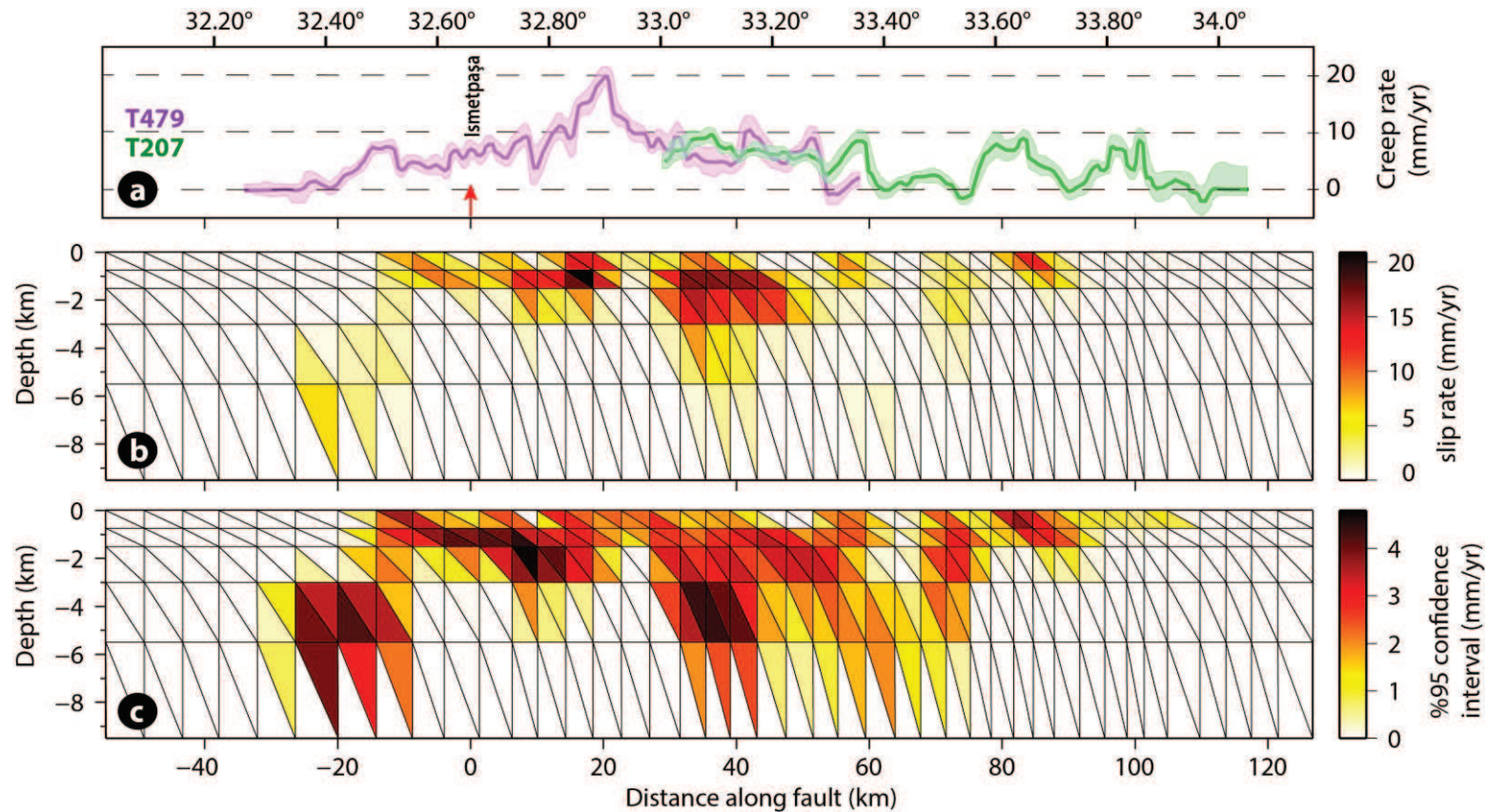


Figure 5.9 : (a) Variation of surface creep rate along the fault, (b) depth distribution of the variable aseismic slip on the Ismetpaşa creeping segment. Red arrow indicates the position of the geodetic network located 3.5 km east of the train station near Hamamlı village at Ismetpaşa. Slip is heterogeneously distributed along the fault and confined mostly to uppermost 5 km of the seismogenic crust with a maximum slip of $\sim 20 \pm 2$ mm/yr 20 km west of Ismetpaşa. (c) Uncertainty of the slip distribution with depth obtained from inversions of 200 InSAR data sets perturbed with synthetic noise.

5.4 Discussion

The mechanical behavior of active fault zones can vary from continuous aseismic creep to sudden rupture during earthquakes, and the same fault zone may evolve either laterally or at depth from seismic to aseismic deformation [Freed, 2007; Gratier *et al.*, 2013]. It is therefore important to determine whether this transition is geologically and tectonically controlled since some types of rocks are more prone to seismic failure while the others are more likely to exhibit aseismic creep [Gratier *et al.*, 2013]. If the fault zone rocks are weaker than the surrounding rocks and do not heal after the rupture, they may exhibit stable sliding friction behavior, so called velocity-strengthening conditions [Carpenter *et al.*, 2011]. Inherited tectonic structures, the presence of weak rocks or the thickness of the gouge zone may control the distribution of surface creep. Serpentine [Allen, 1968] and clay rich lithology [Warr and Cox, 2001] have long been identified as zones of structural characteristics with phyllosilicate foliations resulting into fault weakening [Collettini *et al.*, 2009]. Similarly, calcareous rocks with phyllosilicates are able to creep in the upper crust by pressure solution [Gratier *et al.*, 2013].

The analysis of geological maps reveals that the aseismic surface creep can be, to some extent, correlated with the geology along the North Anatolian Fault (Figure 5.10). The major surface creep in the shallow depths of the western part of the creeping segment, overlapping with 1944 earthquake rupture is correlated with the Upper Jurassic-Lower Cretaceous limestone unit, probably due to pressure solution. In the eastern part of the creeping segment, which overlaps with the 1943 earthquake rupture, aseismic slip is possibly related to the serpentinite bodies marked in the geology map as Mesozoic ophiolitic mélangé along the fault zone (Figure 5.10a). There appears to be no correlation, however, between the variation of creep rate and surface lithology along the fault (Figure 5.10).

The downward-circulation of meteoric fluids may also contribute to the creep in the weaker upper crust as shown by the numerous hot springs along the Alpine active fault zone in New Zealand [Allis and Shi, 1995], and in particular in the western and central-western segments of the North Anatolian fault zone. In fact, Paleozoic metamorphic rocks, along with Mesozoic limestone and flysch, comprise the basement rocks in the geothermal fields along the North Anatolian fault zone

[Erisen *et al.*, 1996]. Therefore both the geology and the downward circulation of meteoric fluids might have a control on the aseismic slip of the Ismetpaşa segment.

Although it is not known whether or not the fault was creeping before the 1944 earthquake, postseismic measurements at Ismetpaşa reveals an exponential decay in creep rate that appears to have graded into a steady-state slip over the last decades or so (Figure 5.11). This suggests that aseismic slip may continue for decades, and plausibly during the entire earthquake cycle (~200-300 yr). Change in the creep rate with time is fitted to an exponential relaxation function that suggests Newtonian behavior of creep in a ductile shear zone [Savage, 2005]. Using fully dynamic models of earthquake cycles, Kaneko *et al.* [2013] inferred that the friction behavior of Ismetpaşa creeping segment is velocity strengthening at shallow depths, changing to velocity weakening at 3 to 6 km-depth. Our models suggest that these properties may vary in space along the fault.

5.5 Conclusions

We have studied the spatial distribution of aseismic creep on the Ismetpaşa segment of the NAF using Envisat ASAR data between 2003 and 2010. The surface velocity field obtained with the PSI technique provides a tighter constraint on the characteristics of surface creep compared to conventional InSAR techniques. The results reveal a surface creep rate of 8 ± 2 mm/yr at Ismetpaşa, which reaches a maximum of 20 ± 2 mm/yr 20 km to the east. Aseismic slip releases every year a moment of 6.2×10^{16} Nm, which is equivalent of an earthquake of $M_w = 5.1$. It implies that a significant portion of the fault is locked and accumulates interseismic strain to be released coseismically as demonstrated with the 1943, 1944 and 1951 earthquakes. High creep rates coincide mostly with the 1951 and eastern part of the 1944 earthquake ruptures. Measurements over the last 60 years show that creep on the Ismetpaşa segment has graded with time into a steady-state rate after the 1944 and/or 1951 earthquakes (Figure 5.11), suggesting that it was probably triggered as postseismic afterslip following the 1944 earthquake as was found with the surface deformation following the 1999 Izmit earthquake [Cakir *et al.*, 2012].

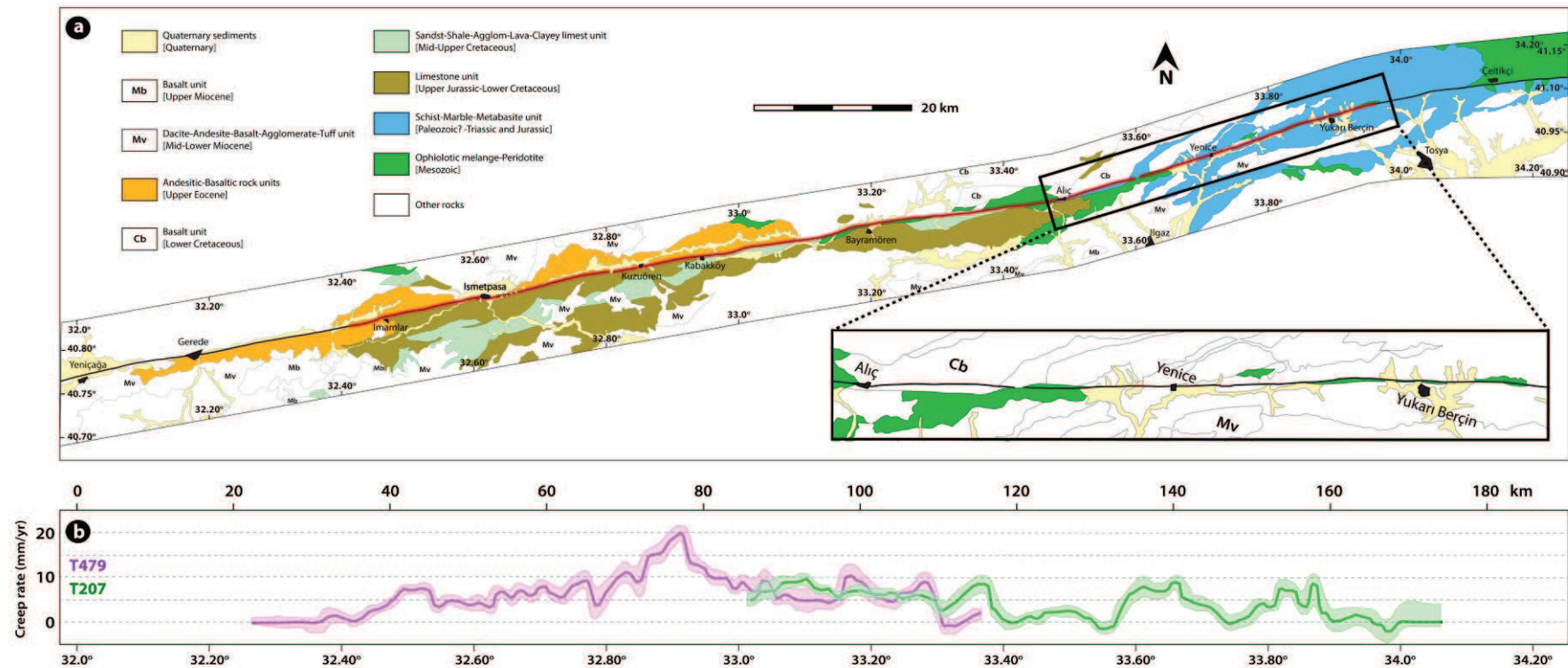


Figure 5.10 : a) Geology map of the study region simplified from *Herece and Akay* [2003] with surface creep rates along the North Anatolian Fault obtained in this study. Geological units presumably involved in creeping are shown in colors and the others are labeled in white with abbreviations. Black and red lines represent the active fault and the creeping segment, respectively. The eastern end of the creeping section can be clearly seen in the inset rectangle. b) Creep rates and error ranges for two individual tracks are indicated in purple and green colors as in Figure 6.

The three-dimensional elastic dislocation modeling suggests that surface creep occurs along a 100-km long section since the easternmost 20 km creeping section estimated with best fitting linear approximations (Figure 5.6b) is not detected with the 3-D elastic dislocation modeling (Figure 5.9) probably due to high level of noise in this section. The creeping section extends at least 30 km further east compared to the previous studies [Cakir *et al.*, 2005; Kaneko *et al.*, 2013]. Modeling results indicate a shallow creeping depth, mostly less than 5 km, in good agreement with the velocity-strengthening at shallow depths deduced from dynamic models by Kaneko *et al.* [2013] and elastic dislocation models by Cakir *et al.* [2005]. Thus, the Ismetpaşa segment appears to be locked with a higher stressing rate at the lower seismogenic crust, which is able to generate strain release during moderate-large earthquakes such as those that occurred in the 1943, 1944 and 1951 earthquakes. An analysis of the geological structures suggests that aseismic slip along the Ismetpaşa creeping segment is mainly controlled by the limestone and serpentine bodies.

Published paper from this chapter can be found in Appendix F.

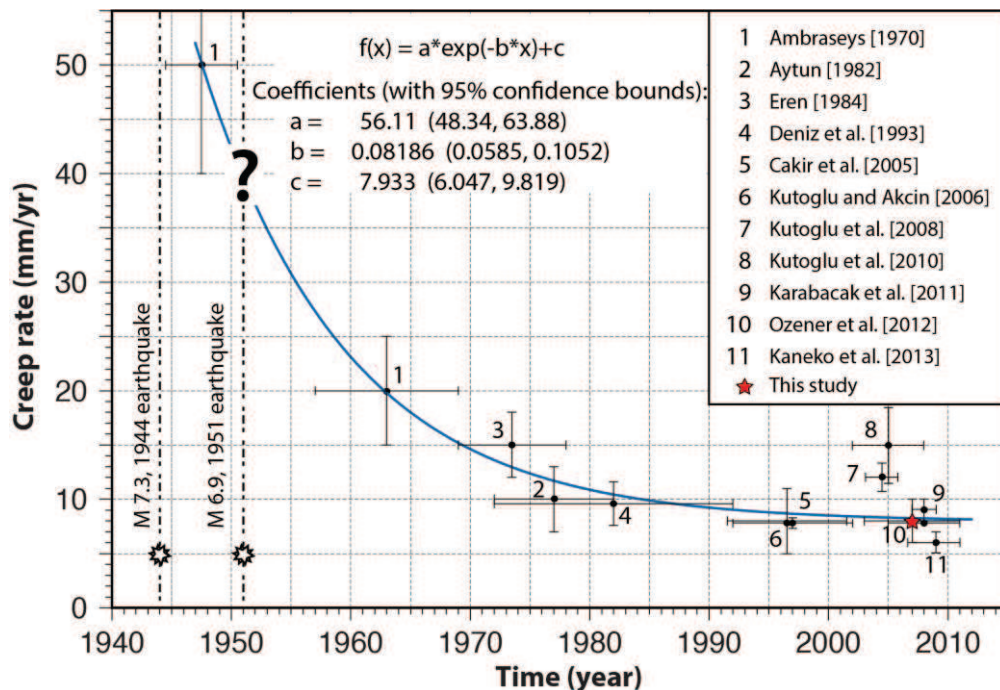


Figure 5.11 : Time history of surface creep at Ismetpaşa as reported by various studies following the 1944 earthquake (after Cakir *et al.*, [2005]). Horizontal and vertical bars are the time window and error range of measurements, respectively. The question mark corresponds to the unknown effect of the 1951 earthquake on creep rate. Curve shows the fit of the exponential relaxation function to the change of the creep rate with time [Savage, 2005].

Chapter VI :
CONCLUSIONS

6. CONCLUSIONS

Improving our understanding of the fault behaviors and the earthquake cycle requires detailed analysis of slow deformation related with active faulting. In this thesis we have used the advanced multi-temporal InSAR time series techniques such as PSI and SBI approaches, which are capable of simultaneous processing of multiple SAR acquisitions over time, to map the surface deformation as a result of slow crustal motions (postseismic relaxation, afterslip and surface creep) along selected active faults within the African-Eurasian convergence zone. Compared to conventional InSAR, the advanced InSAR time series techniques are able to reduce the noise effects and signal decorrelation due to atmospheric effects, DEM errors, and orbital inaccuracies. The PSI and/or SBI analysis generates time series of ground deformation, which is an effective way to study spatial and temporal behavior of slow surface deformations. We analyze and model the postseismic deformation following the 2003 Zemmouri (M_w 6.8, Algeria) earthquake, coseismic and postseismic deformation associated with the 2004 Al Hoceima (M_w 6.4, Morocco) earthquake, and aseismic slip on the Ismetpaşa segment of the NAF.

The postseismic surface deformation of the M_w 6.8, 2003 Zemmouri earthquake has been studied using the SBI technique. InSAR time series obtained from 31 Envisat ASAR images from 2003 to 2010 reveal subtle (sub-cm) ground movements along the shoreline between Cap Matifou and Dellys. The results show that two regions display subsidence at a maximum rate of 2.0 mm/yr in Cap Djenet and 3.5 mm/yr in Zemmouri-Boumerdes. These regions correlate well with the areas of maximum coseismic uplifts obtained from InSAR and field measurements, supporting the previous inferences that the earthquake was associated with two rupture segments. Inverse modeling using dislocations on triangular faults in an elastic and homogeneous half-space suggest that subsidence in the area of high coseismic uplift can be explained by afterslip on the shallow sections (< 5 km) of the fault above the areas of coseismic slip, in agreement with previous estimates based on GPS observations. The impact of earthquake sequence on soft sediments and

ground water table southwest of the earthquake area, allow us to characterize a ground deformation of non-tectonic origin. The cumulative postseismic moment due to afterslip during 7 years following the 2003 mainshock is equivalent to an M_w 6.3 earthquake. Therefore, the postseismic deformation and stress buildup has significant implications on the earthquake cycle models and recurrence intervals of large earthquakes in the Algiers area.

The coseismic and postseismic surface deformation associated with the February 24, 2004 Al Hoceima earthquake (M_w 6.4) in the Rif Mountains of Northern Morocco has been analyzed using Envisat ASAR data acquired in both ascending and descending modes. Due the absence of clear coseismic faulting and related features in the field, the exact location of the earthquake rupture location was not known before the previous InSAR studies [Cakir *et al.*, 2006; Akoglu *et al.*, 2006; Biggs *et al.*, 2006]. These studies showed that the earthquake must be associated with a NW-SE trending right-lateral, apparently blind strike-slip fault. In this study we remodel the coseismic interferograms in light of postseismic deformation field to refine the coseismic model of Akoglu *et al.* [2006]. The InSAR time series of postseismic deformation and aftershocks distribution allow us to better constrain the southeastern end of the earthquake rupture. This fault geometry is similar to that of Akoglu *et al.* [2006] in the northern section, which is well constrained due to narrow distance in between the fringes of zero LOS deformation in the ascending interferograms. To the south, the rupture displays a left bend or step, instead of a curvature proposed by Cakir *et al.* [2006], and a planar and parallel fault plane after the bend. Postseismic displacement field is remarkably prominent and quite high considering the size of the main shock (M_w 6.4). Modeling of 3.3-year postseismic deformation suggests that it is most likely due to shallow (< 8 km) afterslip on the coseismic fault mainly above the high slip patches of the coseismic slip as with 5.0×10^{17} Nm (M_w 5.73) cumulative moment release. Modeling results suggest a complementary coseismic and postseismic slip as commonly observed for other moderate-large earthquakes [Reilinger *et al.*, 2000; Cetin *et al.*, 2012]. Shallow moderate-large earthquakes in the Rif Mountain of northern Morocco expose postseismic deformation that may constitute a significant part in the earthquake cycle.

We use the PSI technique with elastic dislocation models and geology along the creeping section of the NAF at Ismetpaşa, to map and deduce the velocity field and the aseismic slip distribution. Revealing the spatiotemporal nature of the creep helps us associate the creep with potential lithological controls, hence providing a new perspective to better understand the underlying causes and mechanisms. The PSI analysis of Envisat ASAR images between 2003 and 2010 reveals a clear picture of the surface creep along the fault and a new interseismic velocity field transitioning gradually between the creeping and the locked fault sections. The creep rate is found to fluctuate along a 100-km long section of the fault in a manner similar to that along the Hayward fault, reaching a maximum of $\sim 20 \pm 2$ mm/yr, close to the far field plate velocity ($\sim 25 \pm 1.5$ mm/yr). At Ismetpaşa, it is in the range of 8 ± 2 mm/yr, consistent with the previous geodetic observations. The creeping section appears to extend 30 km further east than those previously reported. Modeling of the PSI data reveals a heterogeneous creep distribution at depth with two main patches confined mostly to the uppermost 5 km portion of the seismogenic crust, releasing annually 6.2×10^{16} Nm (M_w 5.1) geodetic moment. Our analysis combined with previous studies suggests that creep might have commenced as postseismic deformation following the 1944 earthquake, and has evolved to stable fault creep with time. There is a correlation between aseismic surface creep and the geology along the fault as it is in major part associated to rocks with low frictional strength such as the andesitic-basaltic, limestone and serpentine bodies within the fault zone.

In the three individual case studies presented in this thesis, InSAR time series provide valuable information about subtle postseismic deformations. Two different types of active fault have been chosen to study postseismic deformation; a thrust fault and a right-lateral strike-slip fault. Remarkable signals of postseismic displacements have been observed in both cases following moderate to large-sized earthquakes. The InSAR analysis reveals diverse indications for two individual postseismic case studies. While the thrust fault mechanism shows opposite sign for coseismic and postseismic surface displacements, the right-lateral strike-slip shows similar sign in both coseismic and postseismic surface displacements. The third case study reveals a clear picture of surface creep, and suggests that it might have commenced as postseismic deformation about 70 years ago after two large earthquakes (M_w 7.3 – 6.9). Although with relatively large time acquisition (35

days), the use of Envisat SAR images allowed the study of coseismic and postseismic deformation for moderate and large earthquakes. The perspective of using new generations of SAR images from TerraSAR-X and Sentinel (12 to 3 days image acquisition) may increase the resolution of interferograms and provide a significant reduction on temporal decorrelation phenomena. Hence, the new generation SAR sensor constellations involving multi-frequency coupled with reduced revisit time options seem extremely promising for the understanding of spatiotemporal behavior of the crustal deformation.

The four possible mechanisms for postseismic deformation that could cause significant displacements near the rupture measurable by geodetic techniques are visco-elastic, poro-elastic, afterslip, and fault zone collapse or strengthening. The prominence of postseismic deformation mechanisms suggests a systems analysis of the postseismic deformation phenomena. The contribution of each of these phenomena to the observed displacement pattern can be inferred from the wavelength, pattern, and temporal decay of the displacement amplitudes. Consequently, afterslip however appears to be a dominant postseismic deformation mechanism produced by both moderate and large earthquakes, deep visco-elastic and/or poro-elastic relaxation might contribute to cumulative surface deformation in some cases. Yet, this is rather puzzling to apply the precise approach to combine them together and requires more detailed analysis to avoid unreliable results. For instance, visco-elastic and poro-elastic contributions to the postseismic relaxation were however analyzed in the Zemmouri postseismic deformation; InSAR data did not provide adequate horizontal motions information since it captures line-of-sight displacements. Furthermore, the cumulative moment release of postseismic afterslip may commonly reach to 30% of a moderate or large-sized earthquake moment release. On the other hand, smaller earthquakes ($M < 6$) may exceptionally have a higher postseismic afterslip relative to coseismic moment release that reach to 70% of coseismic moment release, which is observed following the 2007 Ghazaband (M 5.5, Balochistan, Pakistan) fault earthquake [Fattahi *et al.*, 2015]. Besides, surface creep may initiate as a postseismic afterslip and continue for a long time as shown in the Işmetpaşa case.

The inverse modeling using elastic dislocations on triangular faults with a nonlinear minimization procedure based on simulating algorithm has been utilized to

obtain slip distribution associated with the surface deformation. Modeling results indicate that afterslip and/or aseismic slip is mostly confined to superficial depths (< 5km) as shown in the three case studies, which is in good agreement with several locales worldwide. The shallower depth of afterslip and aseismic slip is consistent with inferred velocity-strengthening behavior along the shallow parts of faults related to zone of weaker rocks than the surrounding rocks. In addition, this study confirms again that afterslip generally surrounds the high-slip patches of the coseismic rupture as shown in the Zemmouri and Al Hoceima cases.

In perspective, in order to build reliable seismic hazard evaluations, it is important to understand the earthquake cycle, fault behaviors, driving mechanisms behind the earthquakes and interaction between them. The earthquake cycle is simply conceptualized on cyclic build up and release of elastic strain around faults, which is complemented by transient deformation. Realistic seismic hazard analysis must accurately explore numerous seismic cycles and include the strain build-up via plate motions, dynamic stress changes during rupture, and postseismic transient deformation. Such seismic hazard analysis must be able to explain the interaction of aseismic and seismic slip, the segmentation of faults, and the strong spatial variations in the intensity of strong shaking [Bakun *et al.*, 2005]. Consequently, improved seismic hazard assessments require up-close and detailed observations, and complementary data from in situ studies of the Earth's crust. Therefore, satellite geodesy observations, particularly InSAR, have contributed significantly to our understanding of earthquake cycle and build reliable hazard assessments.

This study shows once again that InSAR is a remarkably useful and powerful tool in detecting crustal deformation due to earthquakes and aseismic surface or deep fault creep as a result of plate motions. We show here that the InSAR time series contribution to analyze slow surface deformations is satisfactory for active tectonic studies. This work also demonstrates that the contribution of postseismic displacement maps combined with aftershocks distribution is useful to determine the fault geometry if there is no clear surface faulting (e.g. the case of 2004 Al Hoceima earthquake). Also, it is noteworthy using both ascending and descending acquisition modes of satellite to estimate the reliable slip distributions associated with the coseismic and postseismic deformations. Besides, GPS data were beneficial as a supplementary data to determine the related parameters with the deformation (e.g.

the case of 2003 Zemmouri postseismic deformation) and correlate the estimated creep rates obtained from InSAR analysis and modeling (e.g. the case of Ismetpaşa aseismic slip). Furthermore, ground water level changes data was critical to detect the non-tectonic origin subsidence in the Mitidja Basin for the Zemmouri study. Consequently, InSAR alone may not be sufficient enough to constrain the needed parameters for postseismic or aseismic slip, so as to field observations, additional measurements and/or geological analysis may be necessary for better estimations in some cases.

REFERENCES

- Adam, N., B. Kampes, M. Eineder, J. Worawattanamateekul, and M. Kircher** (2003). The development of a scientific permanent scatterer system, paper presented at *ISPRS Hannover Workshop, Inst. for Photogramm. and Geoinf.*, Hannover, Germany.
- Ait Brahim, L., C. Nakhcha, B. Tadili, A. El Mrabet, and N. Jabour** (2004a). Structural analysis and interpretation of the surface deformations of the February 24th, 2004 Al Hoceima earthquake, *EMSC-Newsletter*, **21**, 10-12.
- Ait Brahim, L., B. Tadili, C. Nakhcha, I. Mouayn, M. Ramdani, M. Limouri, A. El Qadi, F. Sossey Alaoui, and M. Benhalima** (2004b). Modeling in the eastern Rif (northern Morocco) using active faults and seismicity for the strong motion, *Pure Appl. Geophys.*, **161**, 1081-1091.
- Akoglu, A.M., Z. Cakir, M. Meghraoui, S. Belabbes, S.O. El Alami, S. Ergintav, and H.S. Akyuz** (2006). The 1994-2004 Al Hoceima (Morocco) earthquake sequence: Conjugate fault ruptures deduced from InSAR, *Earth and Plan. Sci. Lett.*, **252**, 467-480.
- Alasset, P.J., H. Hebert, S. Maouche, V. Calbini, and M. Meghraoui** (2006). The tsunami induced by the 2003 Zemmouri earthquake (Mw 6.9, Algeria); modeling and results, *Geophys. J. Int.*, **166**, 213-226.
- Allen, C.R.** (1968). The tectonic environments of seismically active and inactive areas along the San Andreas fault system, *Stanford University Publications, Geological Sciences*, **11**, 70-80.
- Allis, R.G., and Y. Shi** (1995). New insights to temperature and pressure beneath the central Southern Alps, New Zealand, *New Zealand Journal of Geology and Geophysics*, **38**, 585-592.
- Ambraseys, N.N.** (1970). Some characteristic features of the Anatolian fault zone, *Tectonophysics*, **9**, 143-165.
- Ammar, A., A. Mauffret, C. Gorini, and H. Jabour** (2007). The tectonic structure of the Alboran Margin of Morocco, *Revista de la Sociedad Geológica de España*, **20(3-4)**, 247-271.
- Atzori, S., M. Manunta, G. Fornaro, A. Ganas, and S. Salvi** (2008). Postseismic displacement of the 1999 Athens earthquake retrieved by the Differential Interferometry by Synthetic Aperture Radar time series, *J. Geophys. Res.: Solid Earth*, **113**, B09309.
- Ayadi, A., C. Dorbath, F. Ousadou, S. Maouche, M. Chikh, M. Bounif, and M. Meghraoui** (2008). Zemmouri earthquake rupture zone (Mw 6.8, Algeria): Aftershocks sequence relocation and 3D velocity model, *J. Geophys. Res.: Solid Earth*, **113**, B09301.

- Aytun, A.** (1982). Creep measurements in the Ismetpaşa region of the North Anatolian Fault Zone, in: *Multidisciplinary approach to earthquake prediction*, edited by: Isikara, A.M. and Vogel, A., **2**, 279-292, Vieweg & Braunschweig.
- Bakun, W.H., B. Aagaard, B. Dost, W.L. Ellsworth, J.L. Hardebeck, R.A. Harris,** and et al. (2005). Implications for prediction and hazard assessment from the 2004 Parkfield earthquake, *Nature*, **437(7061)**, 969-974.
- Barka, A.A.** (1996). Slip distribution along the North Anatolian fault associated with the large earthquakes of the period 1939-1967, *Bull. Seismol. Soc. Am.*, **86**, 1238-1254.
- Barka, A.A., and K. Kadinsky-Cade** (1988). Strike-slip fault geometry in Turkey and its influence on earthquake activity, *Tectonics*, **7(3)**, 663-684.
- Belabbes, S., C. Wicks, Z. Cakir, and M. Meghraoui** (2009). Rupture parameters of the 2003 Zemmouri (Mw 6.8). Algeria, earthquake from joint inversion of interferometric synthetic aperture radar, coastal uplift, and GPS, *J. Geophys. Res.*, **114**, B03406.
- Belabbes, S., M. Meghraoui, Z. Çakir, and Y. Bouhadad** (2009b). InSAR analysis of a blind thrust rupture and related active folding: the 1999 Ain Temouchent earthquake (M w 5.7, Algeria) case study, *J of Seismology*, **13(4)**, 421-432.
- Berardino, P., G. Fornaro, R. Lanari, and E. Sansosti** (2002). A new algorithm for surface deformation monitoring based on small baseline differential SAR interferograms, *Geosci. and Remote Sensing, IEEE Trans. on*, **40**, 2375-2383.
- Bezzeghoud, M., and E. Buforn** (1999). Source parameters of the 1992 Melilla (Spain, Mw 4.8). 1994 Al Hoceima (Morocco, Mw 5.8) and 1994 Mascara (Algeria, Mw 5.7) earthquakes and seismotectonic implications, *Bull. Seismol. Soc. Am.*, **89**, 359-372.
- Biggs, J., E. Bergman, B. Emmerson, G.J. Funning, J. Jackson, B. Parsons, and T.J. Wright** (2006). Fault identification for buried strike-slip earthquakes using InSAR: The 1994 and 2004 Al Hoceima, Morocco earthquakes, *Geophys. J. Int.*, **166(3)**, 1347-1362.
- Biggs, J., R. Bürgmann, J. Freymueller, Z. Lu, B. Parsons, I. Ryder, G. Schmalzle, and T. Wright** (2009). The postseismic response to the 2002 M 7.9 Denali Fault earthquake: constraints from InSAR 2003–2005, *Geophys. J. Int.*, **176**, 353-367.
- Bilham, R.** (1989). Surface slip subsequent to the 24 November 1987 Superstition Hills, California, earthquake monitored by digital creepmeters, *Bull. Seismol. Soc. Am.*, **79**, 424-450.
- Bounif, A., C. Dorbath, A. Ayadi, M. Meghraoui,** and et al. (2004). The 21 May 2003 Zemmouri (Algeria) earthquake Mw 6.8; relocation and aftershock sequence analysis, *Geophys. Res. Lett.*, **31**, L19606.
- Braunmiller, J., and F. Berardini** (2005). The 2003 Boumerdes, Algeria, earthquake; regional moment tensor analysis, *Geophys. Res. Lett.*, **32**, L06305.

- Bufo**, E., **M. Bezzeghoud**, **A. Udias**, and **C. Pro** (2004). Seismic sources on the Iberia-African plate boundary and their tectonic implications, *Pure Appl. Geophys.*, **161**(3), 623-646.
- Burford**, R.O., and **P.W. Harsh** (1980). Slip on the San Andreas fault in central California from alignment array surveys, *Bull. Seismol. Soc. Am.*, **70**, 1223-1261.
- Bürgmann**, R., **P. Rosen**, and **E. Fielding** (2000). Synthetic aperture radar interferometry to measure Earth's surface topography and its deformation, *Ann. Rev. Earth Planet Sci.*, **28**, 169-209.
- Bürgmann**, R., **D. Schmidt**, **R. Nadeau**, **M. d'Alessio**, **E. Fielding**, **D. Manaker**, **T. McEvelly**, and **M.H. Murray** (2000). Earthquake potential along the northern Hayward fault, *Science*, **289**, 1178-1182.
- Cakir**, Z., **J.B. de Chabali**, **R. Armijo**, **B. Meyer**, **A. Barka**, and **G. Peltzer** (2003). Coseismic and early post-seismic slip associated with the 1999 Izmit earthquake (Turkey). from SAR interferometry and tectonic field observations, *Geophys. J Int.*, **155**, 93-110.
- Cakir**, Z., **A.M. Akoglu**, **S. Belabbes**, **S. Ergintav**, and **M. Meghraoui** (2005). Creeping along the Ismetpaşa section of the North Anatolian Fault (Western Turkey): Rate and extent from InSAR, *Earth Planet Sc. Lett.*, **238**, 225-234.
- Cakir**, Z., **M. Meghraoui**, **A.M. Akoglu**, **N. Jabour**, **S. Belabbes**, and **L. Ait-Brahim** (2006). Surface deformation associated with the Mw 6.4, 24 February 2004 Al Hoceima, Morocco, earthquake deduced from InSAR: implications for the active tectonics along North Africa, *Bull. Seismol. Soc. Am.*, **96**(1), 59-68.
- Cakir**, Z., and **A.M. Akoglu** (2008). Synthetic aperture radar interferometry observations of the M=6.0 Orta earthquake of 6 June 2000 (NW Turkey): Reactivation of a listric fault, *Geochem. Geophys. Geosyst.*, **9**, Q080009.
- Cakir**, Z., **S. Ergintav**, **H. Ozener**, **U. Dogan**, **A.M. Akoglu**, **M. Meghraoui**, and **R. Reilinger** (2012). Onset of aseismic creep on major strike-slip faults, *Geology*, **40**(12), 1115-1118.
- Cakir**, Z., **S. Ergintav**, **A.M. Akoğlu**, **R. Çakmak**, **O. Tatar**, and **M. Meghraoui** (2014). InSAR velocity field across the North Anatolian Fault (eastern Turkey): Implications for the loading and release of interseismic strain accumulation, *J. Geophys. Res.*, **119**, 7934-7943.
- Calvert**, A., **F. Gomez**, **D. Seber**, **M. Barazangi**, **N. Jabour**, **A. Ibenbrahim**, and **A. Demnati** (1997). An integrated geophysical investigation of recent seismicity in the Al-Hoceima region of North Morocco, *Bull. Seismol. Soc. Am.*, **87**(3), 637-651.
- Carpenter**, B.M., **C. Marone**, and **D.M. Saffer** (2011). Weakness of the San Andreas Fault revealed by samples from the active fault zone, *Nature Geoscience*, **4**, 251-254.
- Casu**, F., **M. Manzo**, and **R. Lanari** (2006). A quantitative assessment of the SBAS algorithm performance for surface deformation retrieval from DInSAR data, *Remote Sens. Environ.*, **102**(3), 195-210.

- Cavalié, O., C. Lasserre, M.P. Doin, G. Peltzer, J. Sun, X. Xu, and Z.K. Shen** (2008). Measurement of interseismic strain across the Haiyuan fault (Gansu, China) by InSAR, *Earth and Planet Sc. Lett.*, **275**, 246-257.
- Cetin, E., M. Meghraoui, Z. Cakir, A.M. Akoglu, O. Mimouni, and M. Chebbah** (2012). Seven years of postseismic deformation following the 2003 Mw=6.8 Zemmouri earthquake (Algeria) from InSAR Time Series, *Geophys. Res. Lett.*, **39**, L10307.
- Cetin, E., Z. Cakir, M. Meghraoui, S. Ergintav, and A.M. Akoglu** (2014a). Extent and distribution of aseismic slip on the Ismetpaşa segment of the North Anatolian Fault (Turkey) from Persistent Scatterer InSAR, *Geochem. Geophys. Geosyst.*, **15**, 2883-2894.
- Cetin, E., Z. Cakir, M. Meghraoui, A.M. Akoglu, A. Tahayt, and P.J. Gonzalez** (2014b). Coseismic and postseismic deformation associated with the Mw=6.4 February 24, 2004 Al Hoceima earthquake (Morocco) from InSAR: Evidence for triggered postseismic slip on neighboring faults, *AGU Fall Meeting 2014*, San Francisco, California, USA, 15-18 December.
- Champenois, J., B. Fruneau, E. Pathier, B. Deffontaines, K.-C. Lin, and J.-C. Hu** (2012). Monitoring of active tectonic deformations in the Longitudinal Valley (Eastern Taiwan) using Persistent Scatterer InSAR method with ALOS PALSAR data, *Earth Planet Sc. Lett.*, **337**, 144-155.
- Colesanti, C., A. Ferretti, F. Novali, C. Prati, and F. Rocca** (2003). SAR monitoring of progressive and seasonal ground deformation using the permanent scatterers technique, *IEEE Trans. Geosci. Remote Sens.*, **41**, 1685-1701.
- Collettini, C., A. Niemeijer, C. Viti, and C. Marone** (2009). Fault zone fabric and fault weakness, *Nature*, **462**, 907-910.
- Crosetto, M., A. Arnaud, J. Duro, E. Biescas, and M. Agudo** (2003). Deformation monitoring using remotely sensed radar interferometric data, paper presented at *11th FIG Symposium on Deformation Measurements*, Patras Univ., Santorini, Greece.
- Delouis, B., M. Vallee, M. Meghraoui, E. Calais, S. Maouche, K. Lammali, A. Mahsas, P. Briole, F. Benhamouda, and K. Yelles** (2004). Slip distribution of the 2003 Boumerdes-Zemmouri earthquake, Algeria, from teleseismic, GPS, and coastal uplift data, *Geophys. Res. Lett.*, **31**, L18607.
- DeMets, C., R.G. Gordon, D.F. Argus, and S. Stein** (1990). Current plate motions, *Geophys. J. Int.*, **101**, 425-478.
- DeMets, C., R.G. Gordon, D.F. Argus, and S. Stein** (1994). Effects of recent revisions to the geomagnetic reversal time scale on estimates of current plate motions, *Geophys. Res. Lett.*, **21**, 2191-2194.
- Deniz, R., A. Aksoy, D. Yalin, H. Seeger, and O. Hirsch** (1993). Determination of crustal movement in Turkey by terrestrial geodetic methods, *J. Geodyn.*, **18**, 13-22.
- Déverchère, K. Yelles, A. Domzig, B. Mercier de Lépinay, and J.-P. Bouillin, et al.** (2005). Active thrust faulting offshore Boumerdes, Algeria, and its relations to the 2003 Mw 6.9 earthquake, *Geophys. Res. Lett.*, **32**, L04311.

- Eren, K.** (1984). Strain analysis along the North Anatolian fault by using geodetic surveys, *Bull. Geodesique*, **58**, 137-149.
- Erisen, B., I. Akkus, N. Uygur, and A. Kocak** (1996). Türkiye jeotermal envanteri, General Directorate of Mineral Research and Exploration (MTA). Ankara, Turkey.
- Fadil, A., P. Vernant, S. McClusky, R. Reilinger, F. Gomez, D.B. Sari, T. Mourabit, K. Feigl, and M. Barazangi** (2006). Active tectonics of the western Mediterranean: Geodetic evidence for rollback of a delaminated subcontinental lithospheric slab beneath the Rif Mountains, Morocco. *Geology*, **34**(7), 529-532.
- Farr, T., and M. Kobrick** (2000). Shuttle radar topography mission produces a wealth of data, *EOS Trans. AGU*, **81**, 583-585.
- Farr, T.G., et al.** (2007). The Shuttle Radar Topography Mission, *Rev. Geophys.*, **45**, RG2004.
- Fattahi, H., F. Amelung, E. Chaussard, and S. Wdowinski** (2015). Coseismic and postseismic deformation due to the 2007 M5. 5 Ghazaband fault earthquake, Balochistan, Pakistan, *Geophys. Res. Lett.*, **42**, 3305–3312.
- Feigl, K.L., and W. Thatcher** (2006). Geodetic observations of post-seismic transients in the context of the earthquake deformation cycle, *Comptes Rendus Geoscience*, **338**(14), 1012-1028.
- Fernandes, R.M.S., J.M. Miranda, B.M.L. Meijninger, M.S. Bos, R. Noomen, L. Bastos, B.A.C. Ambrosius, and R.E.M. Riva** (2007). Surface velocity field of the Ibero-Magrebian segment of the Eurasia-Nubia Plate boundary, *Geophys. J. Int.*, **169**(1), 315-324.
- Ferretti, A., C. Prati, and F. Rocca** (2000). Nonlinear subsidence rate estimation using Permanent Scatterers in Differential SAR Interferometry, *IEEE Trans. Geosci. Remote Sens.*, **38**, 2202-2212.
- Ferretti, A., C. Prati, and F. Rocca** (2001). Permanent scatterers in SAR interferometry, *IEEE Trans Geosci. Remote Sens.*, **39**, 8-20.
- Fialko, Y.** (2006). Interseismic strain accumulation and the earthquake potential on the southern San Andreas fault system, *Nature*, **441**, 968-971.
- Fielding, E.J., M. Talebian, P.A. Rosen, H. Nazari, J.A. Jackson, M. Ghorashi, and R. Walker** (2005). Surface ruptures and building damage of the 2003 Bam, Iran, earthquake mapped by satellite synthetic aperture radar interferometric correlation, *J. Geophys. Res.*, **110**, B03302.
- Freed, A.M.** (2007). Afterslip (and only afterslip) following the 2004 Parkfield, California, earthquake. *Geophys. Res. Lett.*, **34**, L06312.
- Fukushima, Y., O. Nishizawa, H. Sato, and M. Ohtake** (2003). Laboratory study on scattering characteristics in rock samples, *Bull. Seismol. Soc. Am.*, **93**, 253-263.
- Funning, G.J., B. Parsons, T.J. Wright, J. A. Jackson, and E. J. Fielding** (2005). Surface displacements and source parameters of the 2003 Bam (Iran) earthquake from Envisat advanced synthetic aperture radar imagery, *J. Geophys. Res.*, **110**, B09406.

- Goldstein, R., and C. Werner** (1998). Radar interferogram filtering for geophysical applications, *Geophys. Res. Lett.*, **25**, 4035-4038.
- Gonzalez, P.J., M. Palano, and J. Fernandez** (2010). Study of the present-day tectonics and seismogenic sources of the Al-Hoceima region (Morocco) using GPS and MTInSAR, *Proceedings of FRINGE 2009 Workshop*, Frascati, Italy, 30 Nov.-4 December.
- Gourmelen, N., F. Amelung, and R. Lanari** (2010). Interferometric synthetic aperture radar–GPS integration: Interseismic strain accumulation across the Hunter Mountain fault in the eastern California shear zone, *J Geophys. Res.: Solid Earth*, **115(B9)**, B09408.
- Gratier, J.-P., F. Thouvenot, L. Jenatton, A. Tourette, M.-L. Doan, and F. Renard** (2013). Geological control of the partitioning between seismic and aseismic sliding behaviours in active faults: Evidence from the Western Alps, France, *Tectonophysics*, **600**, 226-242.
- Grimison, N., and W. Cheng** (1986). The Azores-Gibraltar plate boundary: focal mechanisms, depths of earthquakes and their tectonic implications, *J. Geophys. Res.*, **91**, 2029-2047.
- Hanssen, R. F.** (2001). *Radar interferometry: data interpretation and error analysis, (Vol. 2)*, Springer.
- Hearn, E. H., S. McClusky, S. Ergintav, and R. E. Reilinger** (2009). Izmit earthquake postseismic deformation and dynamics of the North Anatolian Fault Zone, *J. Geophys. Res.*, **114**, B08405.
- Herece, E., and E. Akay** (2003). Atlas of North Anatolian Fault, *Special Publication Series-2*, MTA, Ankara, Turkey.
- Hooper, A.** (2008). A multi-temporal InSAR method incorporating both persistent scatterer and small baseline approaches, *Geophys. Res. Lett.*, **35**, 16.
- Hooper, A.** (2010). A statistical-cost approach to unwrapping the phase of InSAR time series, *Proceedings of FRINGE 2009 Workshop*, Frascati, Italy, 30 Nov.-4 December.
- Hooper, A., H. Zebker, P. Segall, and B. Kampes** (2004). A new method for measuring deformation on volcanoes and other natural terrains using InSAR persistent scatterers, *Geophys. Res. Lett.*, **31(23)**, L23611.
- Hooper, A., P. Segall, and A. Zebker** (2007). Persistent scatterer interferometric synthetic aperture radar for crustal deformation analysis, with application to Volcan Alcedo, Galapagos, *J. Geophys. Res.*, **112**, B07407.
- Hsu, Y.-J., M. Simons, J.-P. Avouac, J. Galetzka, K. Sieh, M. Chlieh, D. Natawidjaja, L. Prawirodirdjo, and Y. Bock** (2006). Frictional afterslip following the 2005 Nias-Simeulue earthquake, Sumatra, *Science*, **312**, 1921-1926.
- Hsu, Y., P. Segall, S. Yu, L. Kuo, and C. Williams** (2007). Temporal and spatial variations of post-seismic deformation following the 1999 Chi-Chi, Taiwan earthquake, *Geophys. J. Int.*, **169**, 367-379.

- Kampes, B.M.** (2005). *Displacement parameter estimation using permanent scatterer interferometry*, Ph.D thesis, TU Delft, Delft University of Technology.
- Kampes, B.M., and S. Usai** (1999). Doris: the delft object-oriented radar interferometric software, paper presented at *ITC 2nd ORS Symposium, Int. Inst. For Geoinf. Sci. and Earth Obs.*, Enchede, Netherlands.
- Kampes, B., R. Hanssen, and Z. Perski** (2003). Radar interferometry with public domain tools, *Proceedings of FRINGE 2003 Workshop*, Frascati, Italy, 1-3 December.
- Kaneko, Y., Y. Fialko, D.T. Sandwell, X. Tong, and M. Furuya** (2013). Interseismic deformation and creep along the central section of the North Anatolian fault (Turkey): InSAR observations and implications for rate-and-state friction properties, *J. Geophys. Res.*, **118**, 316-331.
- Karabacak, V., E. Altunel, and Z. Cakir** (2011). Monitoring aseismic creep along the North Anatolian Fault (Turkey) using ground-based LIDAR, *Earth and Planet Sci. Lett.*, **304**, 64-70.
- Karimzadeh, S., Z. Cakir, B. Osmanoglu, G. Schmalzle, M. Miyajima, R. Amiraslanzadeh, and Y. Djamour** (2013). Interseismic strain accumulation across the North Tabriz Fault (NW Iran) deduced from InSAR time series, *J. Geodyn.*, **66**, 53-58.
- Ketelaar, K.** (2009). *Satellite Radar Interferometry, Subsidence Monitoring Techniques, (Vol. 14)*, Springer Science & Business Media.
- Koulali, A., D. Ouazar, A. Tahayt, R. W. King, Philippe Vernant, R. E. Reilinger, S. McClusky, T. Mourabit, J. M. Davila, and N. Amraoui** (2011). New GPS constraints on active deformation along the Africa-Iberia plate boundary, *Earth and Planet. Sci. Lett.*, **308(1)**, 211-217.
- Kutoglu, H.S., and H. Akcin** (2006). Determination of 30-year Creep on the Ismetpaşa segment of the North Anatolian Fault using an old geodetic network, *Earth Planets Space*, **58**, 937-942.
- Kutoglu, H.S., H. Akcin, H. Kemaldere, and K.S. Gormus** (2008). Triggered creep rate on the Ismetpasa segment of the North Anatolian Fault, *Nat. Hazards Earth Syst. Sci.*, **8**, 1369-1373.
- Kutoglu, H.S., H. Akcin, O. Gundogdu, K.S. Gormus, and E. Koksal** (2010). Relaxation on the Ismetpasa segment of the North Anatolian Fault after Golcuk Mw=7.4 and Duzce Mw=7.2 shocks, *Nat. Hazards Earth Syst. Sci.*, **10**, 2653-2657.
- Lanari, R., F. Casu, M. Manzo, and P. Lundgren** (2007). Application of the SBAS-DInSAR technique to fault creep: A case study of the Hayward fault, California, *Remote Sens. Environ.*, **109(1)**, 20-28.
- Lanari, R., P. Berardino, M. Bonano, F. Casu, A. Manconi, M. Manunta, M. Manzo, A. Pepe, S. Pepe, E. Sansosti, G. Solaro, P. Tizzani, and G. Zeni** (2010). Surface displacements associated with the L'Aquila 2009 Mw 6.3 earthquake (central Italy): New evidence from SBAS-DInSAR time series analysis, *Geophys. Res. Lett.*, **37**, L20309.

- Lennon, J.J.** (2000). Red-shifts and red herrings in geographical ecology, *Ecography*, **23**, 101-113.
- Li, Y.G., J.E. Vidale, K. Aki, F. Xu, and T. Burdette** (1998). Evidence of shallow fault zone strengthening after the 1992 M7.5 Landers, California, earthquake, *Science*, **279(5348)**, 217-219.
- Lin, J., R. Stein, M. Meghraoui, S. Toda, A. Ayadi, C. Dorbath, and S. Belabbes** (2011). Stress transfer among en echelon and opposing thrusts and tear faults: Triggering caused by the 2003 Mw=6.9 Zemmouri, Algeria, earthquake, *J. Geophys. Res.*, **116**, B03305.
- Lyons, S., and D. Sandwell** (2003). Fault creep along the southern San Andreas from interferometric synthetic aperture radar, permanent scatterers, and stacking, *J. Geophys. Res.*, **108(B1)**, 2047.
- Maerten, L., P. Gillespie, and D.D. Pollard** (2002). Effects of local stress perturbation on secondary fault development, *J. Structural Geology*, **24**, 145-153.
- Maerten, F., P. Resor, D. Pollard, and L. Maerten** (2005). Inverting for slip on three dimensional fault surfaces using angular dislocations, *Bull. Seismol. Soc. Am.*, **95(5)**, 1654-1665.
- Mahsas, A., K. Lammali, K. Yelles, E. Calais, A. Freed, and P. Briole** (2008). Shallow afterslip following the 2003 May 21, Mw= 6.9 Boumerdes earthquake, Algeria, *Geophys. J. Int.*, **172**, 155-166.
- Maouche, S., M. Meghraoui, C. Morhange, S. Belabbes, Y. Bouhadad, and H. Haddoum** (2011). Active coastal thrusting and folding, and uplift rate of the Sahel Anticline and Zemmouri earthquake area (Tell Atlas, Algeria), *Tectonophysics*, **509(1)**, 69-80.
- Marone, C.J., C.H. Scholz, and R. Bilham** (1991). On the mechanics of earthquake afterslip, *J. Geophys. Res.*, **96**, 8441-8452.
- Massonet, D., M. Rossi, C. Carmona, F. Adragna, G. Peltzer, K. Feigl, and T. Rabaute** (1993). The displacement field of the Landers earthquake mapped by radar interferometry, *Nature*, **364**, 138-142.
- Massonnet, D., W. Thatcher, and H. Vadon** (1996). Detection of postseismic fault-zone collapse following the Landers earthquake, *Nature*, **382**, 612-616.
- McClusky, S., R. Reilinger, S. Mahmoud, D. Ben Sari, and A. Tealeb** (2003). GPS constraints on Africa (Nubia) and Arabia plate motions, *Geophys. J. Int.*, **155**, 126-138.
- Meghraoui, M., and F. Doumaz** (1996). Earthquake-induced flooding and paleoseismicity of the El Asnam, Algeria, fault-related fold, *J. Geophys. Res.*, **101**, 17617-17644.
- Meghraoui, M., S. Maouche, B. Chema, Z. Cakir, A. Aoudia, A. Harbi, P. Alasset, A. Ayadi, Y. Bouhadad, and F. Benhamouda** (2004). Coastal uplift and thrust faulting associated with the Mw= 6.8 Zemmouri (Algeria) earthquake of 21 May, 2003, *Geophys. Res. Lett.*, **31**, L19605.

- Meghraoui, M., and S. Pondrelli** (2012). Active faulting and transpression tectonics along the plate boundary in North Africa, *Annals of Geophysics*, **55**(5).
- Mimouni, O.** (2010). *Pollutions des eaux de la région d'Alger, leurs impacts sur l'environnement et les risques majeurs*, (Ph.D. thesis), USTHB - FSTGAT, Algiers.
- Morel, J.L., and M. Meghraoui** (1996). Goringe-Alboran-Tell tectonic zone: A transpression system along the Africa-Eurasia plate boundary, *Geology*, **24**, 755.
- Motagh, M., J. Hoffmann, B. Kampes, M. Baes, and J. Zschau** (2007). Strain accumulation across the Gazikoy-Saros segment of the North Anatolian Fault inferred from Persistent Scatterer Interferometry and GPS measurements, *Earth Planet Sci. Lett.*, **255**, 432-444.
- Nocquet, J.M., and E. Calais** (2004). Geodetic measurements of crustal deformation in the Western Mediterranean and Europe, *Pure Appl. Geophys.*, **161**, 661-681.
- Nur, A., and G. Mavko** (1974). Postseismic viscoelastic rebound, *Science*, **183**(4121), 204-206.
- Ozener, H., A. Dogru, and B. Turgut** (2012). Quantifying aseismic creep on the Ismetpaşa segment of the North Anatolian Fault Zone (Turkey) by 6 years of GPS observations, *J. Geodyn.*, **67**(7), 72-77.
- Peltzer, G., P. Rosen, F. Rogez, and K. Hudnut** (1998). Poro-elastic rebound along the Landers 1992 earthquake surface rupture, *J. Geophys. Res.*, **103**(B12), 30131-30145.
- Pepe, A., and R. Lanari** (2006). On the extension of the minimum cost flow algorithm for phase unwrapping of multitemporal differential SAR interferograms, *IEEE Trans. Geosci. Remote Sens.*, **44**(9), 2374-2383.
- Perfettini, H., and J.-P. Avouac** (2004). Postseismic relaxation driven by brittle creep: A possible mechanism to reconcile geodetic measurements and the decay rate of aftershocks, application to the Chi-Chi earthquake, Taiwan, *J. Geophys. Res.*, **109**, B02304.
- Perfettini, H., J.-P. Avouac, and J.-C. Ruegg** (2005). Geodetic displacements and aftershocks following the 2001 Mw = 8.4 Peru earthquake: Implications for the mechanics of the earthquake cycle along subduction zones, *J. Geophys. Res.*, **110**, B09404.
- Pérouse, E., P. Vernant, J. Chéry, R. Reilinger, and S. McClusky** (2010). Active surface deformation and sub-lithospheric processes in the western Mediterranean constrained by numerical models, *Geology*, **38**(9), 823-826.
- Peyret, M., S. Dominguez, R. Cattin, J. Champenois, M. Leroy, A. Zajac** (2011). Present-day interseismic surface deformation along the Longitudinal Valley, eastern Taiwan, from a PS-InSAR analysis of the ERS satellite archives, *J. Geophys. Res.*, **116**, B03402.
- Pollitz, F. F., G. Peltzer, and R. Bürgmann** (2000). Mobility of continental mantle: Evidence from postseismic geodetic observations following the 1992 Landers earthquake, *J. Geophys. Res.*, **105**, 8035-8054.

- Reid, H. F.** (1910). The mechanics of the earthquake: the California earthquake of 18 April, 1906, Report of *the State Earthquake Investigation Commission*, no. 2, Washington: Carnegie Institution, USA.
- Reilinger, R.E, S. Ergintav, R. Bürgmann, S. McClusky, O. Lenk, A. Barka,** and et al. (2000). Coseismic and Postseismic Fault Slip for the 17 August 1999, M=7.5, Izmit, Turkey Earthquake, *Science*, **289 (5484)**, 1519-1524.
- Reilinger, R.E.,** and et al. (2006). GPS constraints on continental deformation in the Africa-Arabia- Eurasia continental collision zone and implications for the dynamics of plate interactions, *J. Geophys. Res.*, **111**, V05411.
- Riva, R. E. M., A. Borghi, A. Aoudia, R. Barzaghi, R. Sabadini, and G. F. Panza** (2007). Viscoelastic relaxation and long-lasting after-slip following the 1997 Umbria-Marche (Central Italy) earthquakes, *Geophys. J. Int.*, **169**, 534-546.
- Rosen, P., S. Hensley, G. Peltzer, G., and M. Simons** (2004). Updated repeat orbit interferometry package released, *Eos Trans. AGU*, **85**, 47.
- Ryder, I., B. Parsons, T. Wright, and G. Funning** (2007). Post-seismic motion following the 1997 Manyi (Tibet) earthquake: InSAR observations and modeling, *Geophys. J. Int.*, **169**, 1009-1027.
- Savage, J.C.** (1990). Equivalent strike-slip earthquake cycles in half-space and lithosphere-asthenosphere earth models, *J. Geophys. Res.*, **95(B4)**, 4873-4879.
- Savage, J.C., and R.O. Burford** (1973). Geodetic determination of relative plate motion in central California, *J. Geophys. Res.*, **78**, 832-845.
- Savage, J.C., and M. Lisowski** (1993). Inferred depth of creep on the Hayward fault, central California, *J. Geophys. Res.*, **98**, 787-793.
- Savage, J.C., J. L. Svarc, and S.-B. Yu** (2005). Postseismic relaxation and transient creep, *J. Geophys. Res.*, **110**, B11402.
- Scharoo, R., and P. Visser** (1998). Precise orbit determination and gravity field improvement for the ERS satellites, *J. Geophys. Res.*, **103**, 8113-8127.
- Schmidt, D. A., and R. Bürgmann** (2003). Time-dependent land uplift and subsidence in the Santa Clara valley, California, from a large interferometric synthetic aperture radar data set, *J Geophys. Res.*, **108(B9)**, 2416.
- Schmidt, D.A., R. Bürgmann, R.M. Nadeau, and M.A. d’Alessio** (2005). Distribution of aseismic slip-rate on the Hayward fault inferred from seismic and geodetic data, *J. Geophys. Res.*, **110**, B08406.
- Schwartz, S. Y., and J. M. Rokosky** (2007). Slow slip events and seismic tremor at Circum-Pacific subduction zones, *Rev. Geophys.*, **45**, RG3004.
- Semmane, F., M. Campillo, and F. Cotton** (2005). Fault location and source process of the Boumerdes, Algeria, earthquake inferred from geodetic and strong motion data, *Geophys. Res. Lett.*, **32**, L01305.
- Serpelloni, E., G. Vannucci, S. Pondrelli, A. Argnani, G. Casula, M. Anzidei, P. Baldi, and P. Gasperini** (2007). Kinematics of the western Africa-Eurasia plate boundary from focal mechanisms and GPS data, *Geophys. J. Int.*, **169(3)**, 1180-1200.

- Serpelloni, E., R. Bürgmann, M. Anzidei, P. Baldi, B.M. Ventura, and E. Boschi** (2010). Strain accumulation across the Messina Straits and kinematics of Sicily and Calabria from GPS data and dislocation modeling, *Earth Planet Sci. Lett.*, **298(3)**, 347-360.
- Smith, S. W., M. and Wyss** (1968), Displacement on the San Andreas fault subsequent to the 1966 Parkfield earthquake, *Bull. Seismol. Soc. Am.*, **58(6)**, 1955-1973.
- Stein, R.S., A. Barka, and J.H. Dieterich** (1997). Progressive failure on the North Anatolian fault since 1939 by earthquake stress triggering, *Geophys. J. Int.*, **128**, 594-604.
- Steinbrugge, K.V., E.G. Zacher, D. Tocher, C.A. Whitten, and C.N. Claire** (1960). Creep on the San Andreas fault, *Bull. Seismol. Soc. Am.*, **50(3)**, 389-415.
- Stich, D., F. de Lis Mancilla, D. Baumont, and J. Morales** (2005). Source analysis of the Mw 6.3 2004 Al Hoceima earthquake (Morocco) using regional apparent source time functions, *J. Geophys. Res.: Solid Earth*, **110**, B06306.
- Sudhaus, H., S. Jónsson** (2011). Source model for the 1997 Zirkuh earthquake (MW=7.2) in Iran derived from JERS and ERS InSAR observations, *Geophys. J. Int.*, **185**, 676-692.
- Şaroğlu, F., Ö. Emre, and I. Kuşçu** (1992). *Active Fault Map of Turkey*, General Directorate of Mineral Research and Exploration (MTA), Ankara, Turkey.
- Tahayt, A., K. L. Feigl, T. Mourabit, A. Rigo, R. Reilinger, S. McClusky, and et al.** (2009). The Al Hoceima (Morocco) earthquake of 24 February 2004, analysis and interpretation of data from ENVISAT ASAR and SPOT5 validated by ground-based observations, *Remote Sens. Environ.*, **113**, 306-316.
- Taymaz, T., T.J. Wright, S. Yolsal, O. Tan, E. Fielding, and G. Seyitoglu** (2007). Source characteristics of the 6 June 2000 Orta, Cankiri (central Turkey) earthquake: A synthesis of seismological, geological and geodetic (InSAR) observations, and internal deformation of the Anatolian plate, in *The Geodynamics of the Aegean and Anatolia*, edited by T. Taymaz et al., *Geol. Soc. Spec. Publ.*, **291**, 259-290.
- Thatcher, W.** (1979). Systematic inversion of geodetic data in central California, *J. Geophys. Res.*, **84**, 2283-2297.
- Thatcher, W., and J. Rundle** (1979). A model for the earthquake cycle in underthrust zones, *J Geophys. Res.*, **84**, 5540-5556.
- Thomas, A. L.** (1993). *Poly3D: A three-dimensional, polygonal element, displacement discontinuity boundary element computer program with applications to fractures, faults, and cavities in the Earth's crust*, Ph.D thesis, Stanford Univ., Stanford, California, USA.
- Thomas, M. Y., Avouac, J. P., Champenois, J., Lee, J. C., and Kuo, L. C.** (2014). Spatio-temporal evolution of seismic and aseismic slip on the Longitudinal Valley Fault, Taiwan. *J. Geophys. Res.*, **119(6)**, 5114-5139.

- Tse, S.T., and J.R. Rice** (1986). Crustal earthquake instability in relation to the depth variation of frictional slip properties, *J Geophys. Res.*, **91(B9)**, 9452-9472.
- van der Woerd, J., C. Dorbath, F. Ousadou, L. Dorbath, B. Delouis, and et al.** (2014). The Al Hoceima Mw 6.4 earthquake of 24 February 2004 and its aftershocks sequence, *J. Geodyn.*, **77**, 89-109.
- Vernant, Ph., A. Fadil, T. Mourabit, D. Ouazar, A. Koulali, J.M. Davilla, J. Garate, S. McClusky, and R. Reilinger** (2010). Geodetic constraints on active tectonics of the Western Mediterranean: Implications for the kinematics and dynamics of the Nubia-Eurasia plate boundary zone, *J. Geodyn.*, **49**, 123-129.
- Wang, C., and M. Manga** (2010). *Earthquakes and Water, Vol. 114*, Springer.
- Wang, R., F. Lorenzo-Martín, and F. Roth** (2006). PSGRN/PSCMP—a new code for calculating co-and post-seismic deformation, geoid and gravity changes based on the viscoelastic-gravitational dislocation theory, *Computers and Geosciences*, **32(4)**, 527-541.
- Wang, H., T.J. Wright, and J. Biggs** (2009). Interseismic slip rate of the northwestern Xianshuihe fault from InSAR data, *Geophys. Res. Lett.*, **36**, L03302.
- Warr, L.N., and S. Cox** (2001). Clay mineral transformations and weakening mechanisms along the Alpine Fault, New Zealand, *Geological Society, London, Special Publications*, **186(1)**, 85-101.
- Wei, M., D. Sandwell, and Y. Fialko** (2009). A silent M4.8 event of October 3-6, 2006, on the Superstition Hills Fault, Southern California, *J. Geophys. Res.*, **114**, B07402.
- Werner, C., U. Wegmüller, T. Strozzi, and A. Wiesmann** (2003). Interferometric point target analysis for deformation mapping, paper presented at *Int. Geosci. and Remote Sens. Symposium, Geosci. and Remote Sens. Soc.*, Toulouse, France.
- Wessel, P., and W.H.F. Smith** (1998). New improved version of Generic Mapping Tools released, *Eos Trans. AGU*, **79 (47)**, 579.
- Wessel, P., W. H. F. Smith, R. Scharroo, J. F. Luis, and F. Wobbe** (2013). Generic Mapping Tools: Improved version released, *EOS Trans. AGU*, **94**, 409-410.
- Wright, T.** (2002). Remote monitoring of the earthquake cycle using satellite radar interferometry, *Philosophical transactions of the Royal Society of London, Series A: Mathematical Physical and Engineering Sciences*, **360**, 2873-2888.
- Wright, T., B. Parsons, and E. Fielding** (2001). Measurement of interseismic strain accumulation across the North Anatolian Fault by satellite radar interferometry, *Geophys. Res. Lett.*, **28**, 2117-2120.
- Wright, T., J.R. Elliott, H. Wang, and I. Ryder** (2013). Earthquake cycle deformation and the Moho: Implications for the rheology of continental lithosphere, *Tectonophysics*, **609**, 504-523.

- Yagi, Y.** (2003). Source process of large and significant earthquakes in 2003, *Bull. Int. Inst. Seismol. Earthquake Eng.*, special volume, 145-153.
- Yelles, K., K. Lammali, A. Mahsas, E. Calais, and P. Briole** (2004). Coseismic deformation of the Algerian Atlas mountains-Evidence from aftershocks of the 1980 El Asnam earthquake, *Geophys. Res. Lett.*, **31**, L13610.
- Yielding, G., M. Ouyed, G. King, and D. Hatzfield** (1989). Active tectonics of the Algerian Atlas Mountains, evidence from aftershocks of the 1980 El Asnam earthquake, *Geophys. J. Int.*, **99**, 761-788.
- Zebker, H. A., and J. Villasenor** (1992). Decorrelation in interferometric radar echoes, *IEEE Trans. Geosci. Remote Sens.*, **30(5)**, 950-959.
- Zweck, C., J.T. Freymueller, and S.C. Cohen** (2002). Three-dimensional elastic dislocation modeling of the postseismic response to the 1964 Alaska earthquake, *J. Geophys. Res.*, **107(B4)**, 2064.

APPENDICES

APPENDIX A: Supplementary documents of the postseismic deformation following the 2003 Zemmouri earthquake (Chapter 3)

APPENDIX B: Supplementary documents of the viscoelastic modeling (Chapter 3.4.2)

APPENDIX C: Cetin et al. [2012], GRL paper about the 2003 Zemmouri postseismic deformation (Chapter 3)

APPENDIX D: Supplementary documents of the coseismic and postseismic deformation following the 2004 Al Hoceima earthquake (Chapter 4)

APPENDIX E: Supplementary documents of the creeping section at Ismetpaşa of the North Anatolian Fault (Chapter 5)

APPENDIX F: Cetin et al. [2014], G-cubed paper about the Ismetpaşa creeping section (Chapter 5)

APPENDIX A

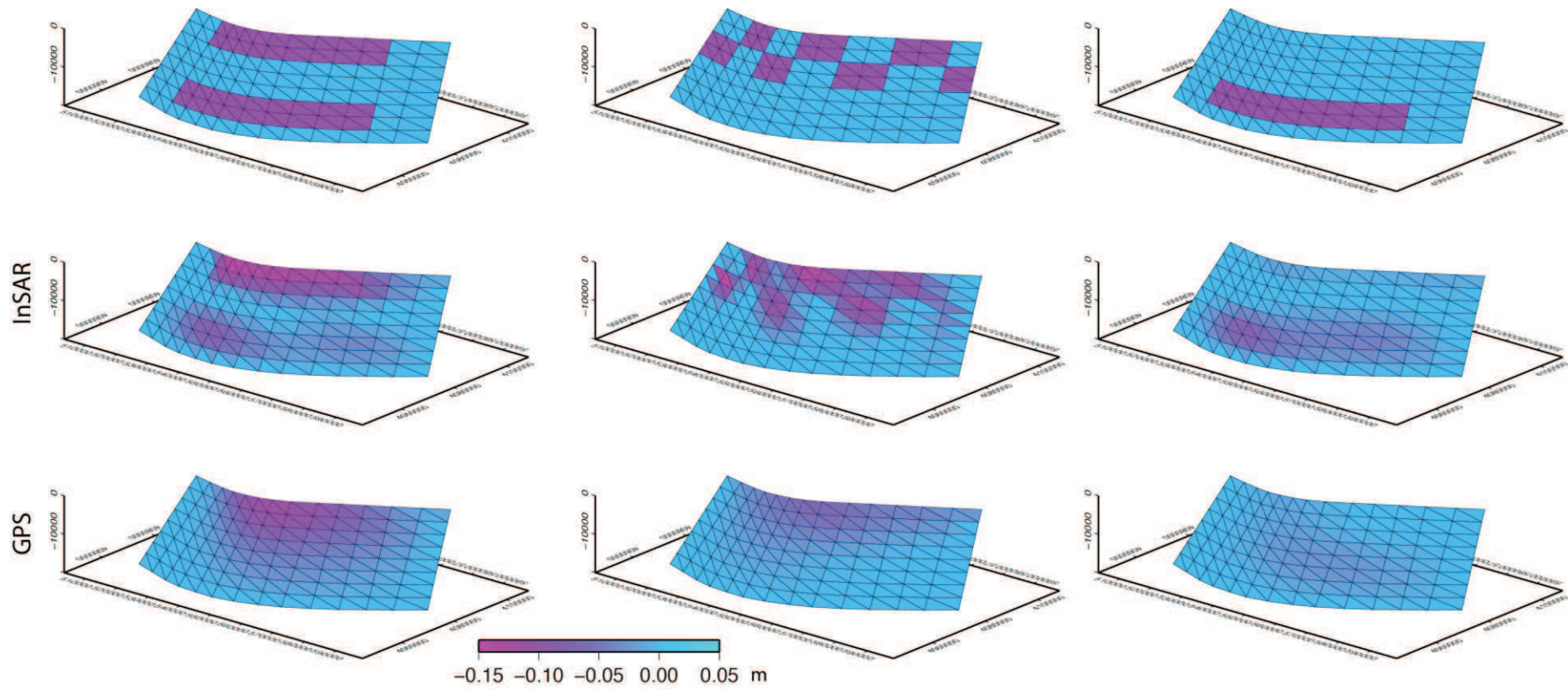


Figure A.1 : Resolution test using check-box approach with 0.10 m slip at different depths for each cell.

APPENDIX B

APPENDIX B1: PSGRN-PSCMP viscoelastic modeling code

PSGRN which is based on the Riemann-Mellin contour integral in combination with the fast Fourier transform technique to produce not only surface and subsurface deformation, but and also geoid and gravity changes. The numerical code models the Earth as a multi-layered visco-elastic gravitational half-space. The viscoelasticity is described by the Maxwell rheology. Although the PSGRN code is computationally intensive, once the Green's functions have been calculated they can be used for any fault model if the Earth model remained the same. PSCMP calculates the deformation transients (i.e., surface displacements, stress, geo-potential components) from a fault using the Green's functions computed by PSGRN. The user defined rectangular fault plane(s) is discretized into point dislocations at the center of each patch. The deformation is then calculated at any observation points by integrating the deformation due to each point source on the fault planes. The detailed numerical solution can be found in *Wang et al.* [2006].

APPENDIX B2:

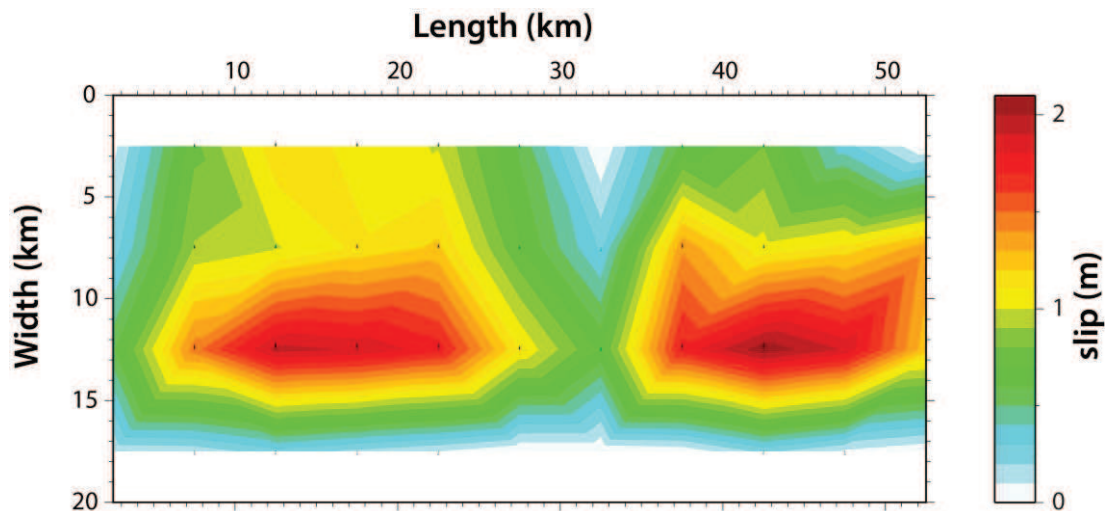


Figure B.1 : Coseismic slip distribution used as an input file for PSCMP, which is simulated on a planar fault by enforcing the slip distribution deduced by *Belabbes et al.* [2009], is 55-km-long and 20-km-wide offshore thrust fault striking N60°, and dipping 42° SE.

Seven years of postseismic deformation following the 2003 Mw = 6.8 Zemmouri earthquake (Algeria) from InSAR time series

Esra Cetin,^{1,2} Mustapha Meghraoui,² Ziyadin Cakir,¹ Ahmet M. Akoglu,³ Omar Mimouni,⁴ and Mouloud Chebbah⁵

Received 13 February 2012; revised 18 April 2012; accepted 21 April 2012; published 24 May 2012.

[1] We study the postseismic surface deformation of the Mw 6.8, 2003 Zemmouri earthquake (northern Algeria) using the Multi-Temporal Small Baseline InSAR technique. InSAR time series obtained from 31 Envisat ASAR images from 2003 to 2010 reveal sub-cm coastline ground movements between Cap Matifou and Dellys. Two regions display subsidence at a maximum rate of 2 mm/yr in Cap Djenet and 3.5 mm/yr in Boumerdes. These regions correlate well with areas of maximum coseismic uplifts, and their association with two rupture segments. Inverse modeling suggest that subsidence in the areas of high coseismic uplift can be explained by afterslip on shallow sections (<5 km) of the fault above the areas of coseismic slip, in agreement with previous GPS observations. The earthquake impact on soft sediments and the ground water table southwest of the earthquake area, characterizes ground deformation of non-tectonic origin. The cumulative postseismic moment due to 7 years afterslip is equivalent to an Mw 6.3 earthquake. Therefore, the postseismic deformation and stress buildup has significant implications on the earthquake cycle models and recurrence intervals of large earthquakes in the Algiers area. **Citation:** Cetin, E., M. Meghraoui, Z. Cakir, A. M. Akoglu, O. Mimouni, and M. Chebbah (2012), Seven years of postseismic deformation following the 2003 Mw = 6.8 Zemmouri earthquake (Algeria) from InSAR time series, *Geophys. Res. Lett.*, *39*, L10307, doi:10.1029/2012GL051344.

1. Introduction

[2] Understanding the crustal deformation and earthquake cycle requires the analysis of postseismic deformation, a transient response of the lithosphere to the stress changes caused by moderate to large earthquakes. The 21 May 2003 Zemmouri earthquake and related coseismic rupture (Mw 6.8) in the Tell Atlas of northern Algeria is a motivating case study of postseismic deformation associated with a thrust faulting event. This seismic event is the largest earthquake of

the last decade that can be studied with space geodesy in the Tell Atlas fold and thrust belt. Most of seismic and geodetic studies suggest a N60°–65° trending fault rupture, dipping 40° to 50° SE and located offshore about 8–13 km from the coastline [Delouis *et al.*, 2004; Meghraoui *et al.*, 2004; Ayadi *et al.*, 2008; Mahsas *et al.*, 2008; Belabbes *et al.*, 2009].

[3] Following the 2003 Zemmouri earthquake, the study of continuous GPS (CGPS) measurements at 6 benchmarks gave evidence of <1 cm/yr postseismic deformation during 2.5 years [Mahsas *et al.*, 2008]. The CGPS data can be best explained with shallow slip patches (<7.5-km-depth) with up to 30 cm afterslip, equivalent to an earthquake with moment magnitude of Mw 6.3. In this paper, to obtain a better picture of the postseismic surface deformation during 7 years, we use Small Baseline InSAR (SBI) technique with Envisat SAR data acquired by the European Space Agency. The mean velocity field deduced from the SBI reveals surface deformation of both tectonic and non-tectonic origin. We model the ground deformation along the coastal region with afterslip on the coseismic fault, and discuss the coseismic/postseismic deformation and the role of poro-elastic/visco-elastic deformation.

2. Seismotectonic Setting

[4] The 21 May 2003 Zemmouri earthquake (Mw 6.8) occurred in the Tell Atlas of northern Algeria that results from the 5–6 mm/yr present day rate of convergence between Africa and Eurasia [Nocquet and Calais, 2004]. The region is the source of frequent large and moderate seismic events mostly with thrust fault mechanisms in agreement with the regional tectonics [Morel and Meghraoui, 1996]. In north-central Algeria, the dominant active tectonic structures are NE-SW to E-W trending fold and thrust system including the Blida thrusts, Mitidja Basin and Sahel anticline (Figure 1) [Maouche *et al.*, 2011]. The 2003 earthquake ruptured ~15-km-wide crust, and caused 55-km-long coastline uplift. The coseismic uplift was ~0.5 m along the coastline, reaching a maximum 0.75 m east of Boumerdes and minimum near Cap Djenet [Meghraoui *et al.*, 2004]. Taking into account the size of coseismic slip, the investigation of postseismic deformation using satellite geodesy became suitable.

3. InSAR Data Processing and Analysis

[5] We use the Multi-temporal SBI technique of the software package StaMPS (see details of processing procedure in Hooper [2008]) using the ROI-PAC [Rosen *et al.*, 2004] for focusing the raw ASAR images, and the DORIS [Kampes and Usai, 1999] for calculating the interferograms with 90-m SRTM data. The technique minimizes the perpendicular, temporal and Doppler baselines for maximizing

¹Department of Geology, Istanbul Technical University, Istanbul, Turkey.

²Institut de Physique du Globe, CNRS-UMR 7516, Strasbourg, France.

³Division of Physical Sciences and Engineering, King Abdullah University of Science and Technology, Thuwal, Saudi Arabia.

⁴FSTGAT, Université des Sciences et Techniques Houari Boumediene, Algiers, Algeria.

⁵Agence Nationale des Ressources Hydrauliques, Blida, Algeria.

Corresponding author: E. Cetin, Institut de Physique du Globe, CNRS-UMR 7516, 5, rue René Descartes, F-67084 Strasbourg CEDEX, France. (e.cetin@unistra.fr)

Copyright 2012 by the American Geophysical Union. 0094-8276/12/2012GL051344

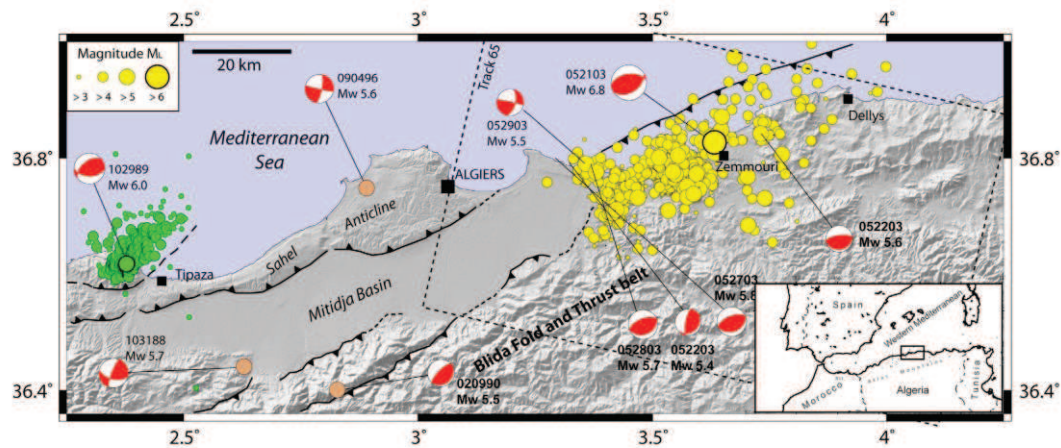


Figure 1. Tectonics and seismicity of the Zemmouri-Boumerdes region shown with SRTM shaded topography. Focal mechanisms are from Global CMT project. Two destructive earthquakes and related aftershocks (Mont Chenoua-Tipasa 1989 and Zemmouri 2003, green and yellow circles, respectively) limit the Mitidja-Algiers active zone (black lines are thrust faults [Maouche et al., 2011]). Dashed box is the Envisat image frame (Track 65). Black box in inset map shows the study region.

the correlation of generated interferograms and increasing the number of observable ground points [Berardino et al., 2002].

[6] A map of cumulative Line of Sight (LOS) displacements between 12-July-2003 and 18-September-2010 is obtained from a mean LOS velocity field calculated from about 86,000 coherent pixels identified in 31 descending ENVISAT images covering the earthquake region (Figure 2a). The map reveals range increase largely in three regions reaching 12 mm/yr in the Mitidja basin, 3.5 mm/yr around Boumerdes, and 2 mm/yr around Cap Djenet (Figures 2a and 2b). Range increase in the descending imaging geometry can be due to either ground subsidence or westerly horizontal ground motion. While the high rate of range increase in the Mitidja basin SW of Cap Matifou can be attributed to subsidence due to excess ground water extraction in Holocene fine-grained alluvial deposits [Mimouni, 2010], those observed in the earthquake coastal region are likely due to both horizontal and vertical displacements associated with the postseismic deformation, the basements of these regions being mainly formed by solid rocks (e.g., granitic and volcanic units). Although the range increase in Boumerdes area is consistent with the CGPS measurements showing both subsidence and northwestward horizontal slip, the CGPS results with large component of uplift and range decrease in Cap Djenet (CDJP) [Mahsas et al., 2008] contradicts with the InSAR range increase results. As for the coseismic uplift, the postseismic ground deformation in Boumerdes and Cap Djenet must result from crustal deformation; this inference may be supported by the logarithmic decay in InSAR time series (Figure 2b). The correlation between InSAR time series and water level piezometric changes due to seasonal water level fluctuation and ground water extraction (Figure 2b) [Mimouni, 2010] supports the evidence for subsidence in the Mitidja basin.

[7] Although much smaller, the sense of postseismic range change (i.e., increase) in the Zemmouri-Boumerdes and Cap Djenet is remarkably opposite to that observed (i.e., decrease)

during the coseismic deformation [see Belabbès et al., 2009]. This can be explained by shallow afterslip below or above the area of coseismic slip on the fault surface since it produces both NW directed horizontal motion and subsidence. Hence, we obtain the range increase, consistent with the shallow afterslip model proposed by Mahsas et al. [2008]. Afterslip on fault sections of coseismic slip would give rise to uplift and range decrease, similarly to the coseismic motion. Considering the coseismic fault rupture parameters and satellite imaging geometry, the LOS velocity field largely depends on vertical movement as InSAR in this case can detect only 20–25% of NW horizontal displacements and about 90% of the vertical displacements.

4. Modeling Geodetic Data

[8] We investigate how a model of afterslip can explain the InSAR LOS velocity field and CGPS measurements of Mahsas et al. [2008]. Our inverse modeling is based on the boundary element software, Poly3Dinv [Maerten et al., 2005] that predicts surface displacements due to dislocations on triangular faults buried in a linear elastic and homogeneous half-space with a damped least square minimization. The curved model fault dipping $\sim 45^\circ$ towards the south and trending $N60^\circ-65^\circ E$ along the coast is deduced from coseismic SAR, GPS data, and coastal uplift measurements (Figure 2a) [Belabbès et al., 2009]. The fault surface is discretized into triangular elements from surface down to the 20-km-depth. The distribution of reverse slip on triangular elements was then inverted with the scale-dependent smoothing operator of Poly3Dinv to avoid unphysical oscillatory slip, using the cumulative LOS change along the shoreline and re-estimated horizontal GPS displacements during ~ 7 years. We use time series provided by Mahsas et al. [2008] to recalculate horizontal GPS velocities taking into account the total displacements recorded in between the acquisition of the first Envisat image in July 2003, and the end of CGPS measurements in October 2005. Here, the GPS displacement rate for the next

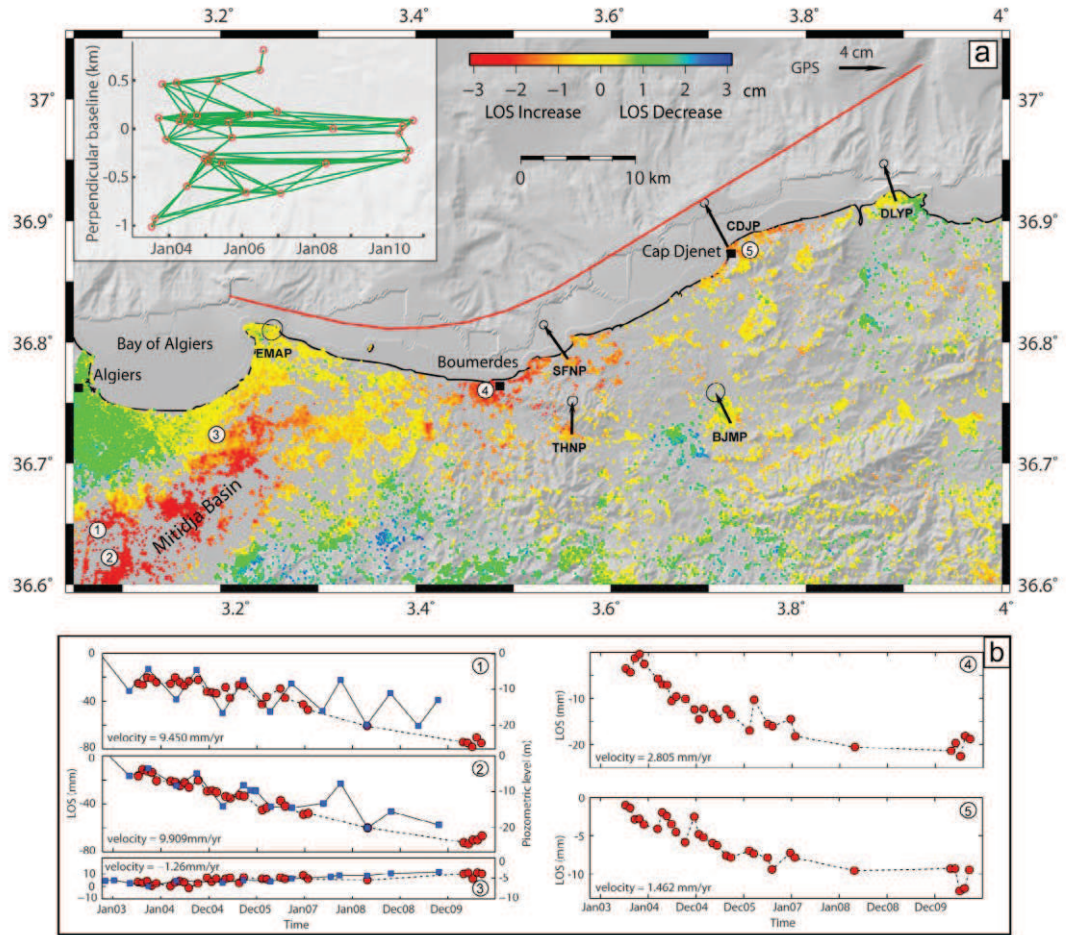


Figure 2. (a) Seven-year postseismic cumulative LOS range change following the 2003 Zemmouri earthquake calculated from 31 descending Envisat images on Track 65. Movements away from the satellite are shown with yellow to red colors and, those towards the satellite with yellow to blue. The black arrows with 95% confidence ellipses are 2.5-year cumulative postseismic GPS displacements from *Mahsas et al.* [2008]. Red line is the trace of the modeled fault on the sea floor. Numbers show the locations of time series plotted in Figure 2b. Inset is the baseline plot showing the interferogram pairs (green lines) between radar images (red circles). (b) Time series of InSAR data (red circles) and groundwater table measurements (blue squares [Mimouni, 2010]) in the study area. Note the strong correlation between water level fluctuations and InSAR phase changes in the Mitidja basin (plots 1 to 3). Postseismic deformation in the earthquake region (plot 4 and 5) is manifested by logarithmic decay in the InSAR time series.

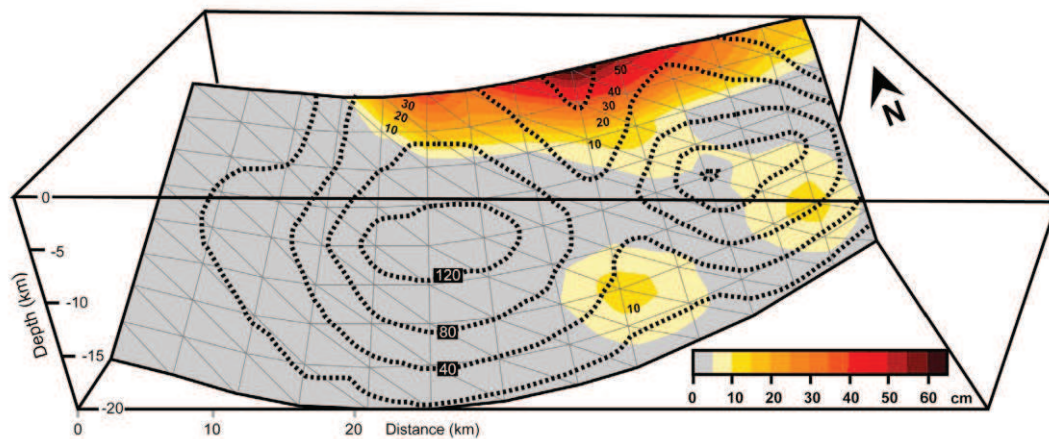


Figure 3. Color-coded postseismic afterslip distribution on the Zemmouri earthquake rupture. Black dashed lines show the coseismic slip distribution inferred by *Belabbes et al.* [2009]. The afterslip distribution inverted from InSAR and GPS data shows two patches of maximum slip (40 to 65 cm) along the upper sections of the fault (<5-km-depth) complementing the coseismic slip at deeper fault sections.

five years till the acquisition of the last Envisat image in September 2010 is assumed to be linear. We then run several inversions weighting the GPS and LOS data equally with 0 (rough) to 1 (smooth) smoothing factor to explore its effects on the location, magnitude of slip and misfit. Although the fit improves almost linearly for LOS data with decreasing smoothing factor and roughness (Figure 4b inset), at a certain point GPS data exhibit a higher misfit as the slip localizes further reaching 2 m maximum. The preferred model of slip distribution shown in Figure 3 is obtained with an optimum 0.4 smoothing factor for both data sets with 0.57 cm RMS misfit. As for all other models with different smoothing factors, the preferred model predicts up to 65 cm shallow afterslip localized mostly between 5-km-depth and surface. The weakly pronounced afterslip is distributed on two patches above the lobes of high coseismic slip. The coseismic slip deficit at the uppermost sections of the fault appears to be filled by the postseismic afterslip, indicating a complementary slip distribution also observed in other large earthquakes [*Reilinger et al.*, 2000]. The resolution tests shown in Figure S1 in the auxiliary material indicates that the InSAR data have an adequate resolution in constraining the shallow slip on the fault.¹ As illustrated in Figure 4, the fit between the model and InSAR data can be reasonably accepted. In contrast, the GPS fit in the south and east is poor and requires deeper slip on fault although the model predicts the overall northward displacements observed by GPS. The discrepancy between the modeled and observed GPS velocities and the InSAR data is probably partly due to much faster decays of the afterslip on the deeper sections of the fault. The estimated moment released for 7 years (2003–2010) is 4.1×10^{18} Nm ($M_w = 6.34$), ~28% higher than that estimated during the first 2.5 years [*Mahsas et al.*, 2008]. The cumulative postseismic moment release during 7 years may range between 15 to 25% of the coseismic

moment release estimated from seismology and geodesy [*Delouis et al.*, 2004; *Belabbes et al.*, 2009].

5. Discussion and Conclusion

[9] Postseismic deformation associated with the Zemmouri earthquake from 2003 to 2010 is documented using Envisat data combined with 2.5-year GPS data. The broad spatial coverage and seven years of high-resolution SBI data provide a powerful constraint on the characteristics of postseismic deformation. The results reveal two lobes of relatively higher rate of surface deformation with 3.5 to 2 mm/yr LOS displacement in Boumerdes and Cap Djenet, respectively, as opposed to the coseismic uplift. Elastic dislocation modeling shows that these lobes can be adequately explained by shallow (<5 km) afterslip with up to 0.65 m displacement above the coseismic slip with 4.1×10^{18} Nm ($M_w = 6.34$) cumulative moment release. The coseismic and postseismic slip distributions are shown to be complementary implying that both types of surface deformation with the same fault model suggest well-constrained fault rupture parameters. The large amount of afterslip gives rise to additional static stress transfer onto the neighboring faults and affects previous Coulomb stress modeling [*Lin et al.*, 2011]. This also changes our perception of the seismic cycle characterization and suggests longer recurrence intervals for large earthquakes in the Algiers region.

[10] Three mechanisms are widely used to explain the postseismic deformation of numerous large and moderate earthquakes: (1) afterslip on the coseismic rupture plane [*Smith and Wyss*, 1968], (2) visco-elastic relaxation in the lower crust/upper mantle [*Pollitz et al.*, 2000], and (3) poro-elastic rebound [*Peltzer et al.*, 1998]. While in similar cases only one mechanism is claimed to have operated [*Freed*, 2007], in other examples several mechanisms are thought to contribute to postseismic deformation [*Hearn et al.*, 2009]. Following the 2003 Zemmouri thrust earthquake, the after-slip distribution is well constrained and appears to be the

¹Auxiliary materials are available in the HTML. doi:10.1029/2012GL051344.

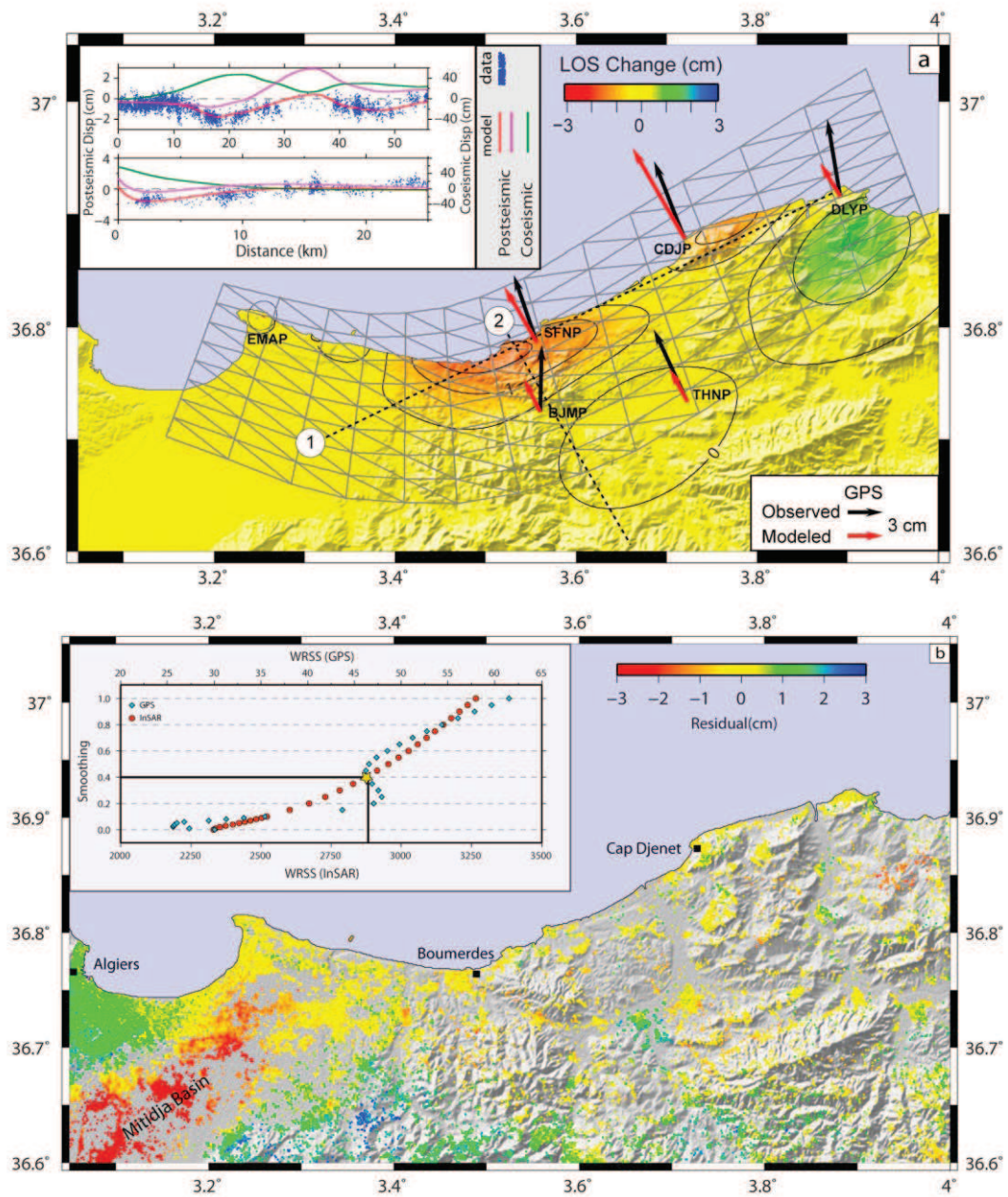


Figure 4. (a) Model of 7-year cumulative LOS surface deformation and GPS displacements predicted by the modeled slip distribution shown in Figure 3. The fault rupture projected to the surface is illustrated by the triangulated network; parallel and perpendicular profiles to the fault are located by number 1 and 2. Inset shows LOS change of modeled (red lines) and observed (blue dots) postseismic surface deformation, together with coseismic model (green lines [Belabbes *et al.*, 2009]). Pink lines show vertical component of the LOS change predicted by the model. (b) Residual LOS velocity field. Inset shows the trade-off between misfit (weighted residual sum of squares) and the smoothing factor in the InSAR and GPS data inversion. An optimum solution can be obtained with a 0.4 smoothing factor.

most significant mechanism of the postseismic deformation mostly at shallow depths. Part of the postseismic deformation can be due to poro-elastic and/or visco-elastic relaxation in the lithosphere (Figures S2a and S2b). Postseismic deformation of the Chi-Chi thrust earthquake (Mw 7.7) obtained from GPS measurements over a 15-month period are better explained by afterslip than viscoelastic relaxation [Hsu et al., 2007]. In the Zemmouri earthquake, the visco-elastic relaxation model [Mahsas et al., 2008] predicts the subsidence observed in the InSAR results. The model however fails to explain the far field horizontal motions observed with GPS and the two-lobe pattern observed by SBI. The visco-elastic contribution to the observed surface deformation remains unclear (Figure S2a). On the other hand, the poro-elastic rebound is a fairly rapid response [Riva et al., 2007], and its contribution is likely to be small since the first SAR image was taken ~6 weeks after the earthquake (Figure S2b).

[11] **Acknowledgments.** This work was performed thanks to the ESA grant for ENVISAT images through the CIP-2532 project. Esra Cetin benefited from the EGIIDE-Eiffel grant (721450B) during the completion of this work. We are thankful to A. Hooper for providing access to StaMPS software tools and to Samir Belabbes and Noel Gourmelen for discussions. We thank Tim Wright and an anonymous reviewer for improving a previous version of the paper.

[12] The Editor thanks Tim Wright and an anonymous reviewer for assisting with the evaluation of this paper.

References

- Ayadi, A., C. Dorbath, F. Ousadou, S. Maouche, M. Chikh, M. Bounif, and M. Meghraoui (2008), Zemmouri earthquake rupture zone (Mw 6.8, Algeria): Aftershocks sequence relocation and 3D velocity model, *J. Geophys. Res.*, *113*, B09301, doi:10.1029/2007JB005257.
- Belabbes, S., C. Wicks, Z. Cakir, and M. Meghraoui (2009), Rupture parameters of the 2003 Zemmouri (Mw 6.8), Algeria, earthquake from joint inversion of interferometric synthetic aperture radar, coastal uplift, and GPS, *J. Geophys. Res.*, *114*, B03406, doi:10.1029/2008JB005912.
- Berardino, P., G. Fornaro, R. Lanari, and E. Sansosti (2002), A new algorithm for surface deformation monitoring based on small baseline differential SAR interferograms, *IEEE Trans. Geosci. Remote Sens.*, *40*, 2375–2383, doi:10.1109/TGRS.2002.803792.
- Delouis, B., M. Vallee, M. Meghraoui, E. Calais, S. Maouche, K. Lammali, A. Mahsas, P. Briole, F. Benhamouda, and K. Yelles (2004), Slip distribution of the 2003 Boumerdes-Zemmouri earthquake, Algeria, from teleseismic, GPS, and coastal uplift data, *Geophys. Res. Lett.*, *31*, L18607, doi:10.1029/2004GL020687.
- Freed, A. M. (2007), Afterslip (and only afterslip) following the 2004 Parkfield, California, earthquake, *Geophys. Res. Lett.*, *34*, L06312, doi:10.1029/2006GL029155.
- Hearn, E. H., S. McClusky, S. Ergintav, and R. E. Reilinger (2009), Izmit earthquake postseismic deformation and dynamics of the North Anatolian Fault Zone, *J. Geophys. Res.*, *114*, B08405, doi:10.1029/2008JB006026.
- Hooper, A. (2008), A multi-temporal InSAR method incorporating both persistent scatterer and small baseline approaches, *Geophys. Res. Lett.*, *35*, L16302, doi:10.1029/2008GL034654.
- Hsu, Y., P. Segall, S. Yu, L. Kuo, and C. Williams (2007), Temporal and spatial variations of post-seismic deformation following the 1999 Chi-Chi, Taiwan earthquake, *Geophys. J. Int.*, *169*, 367–379, doi:10.1111/j.1365-246X.2006.03310.x.
- Kampes, B., and S. Usai (1999), Doris: The Delft Object-oriented Radar Interferometric software, paper presented at ITC 2nd ORS Symposium, Int. Inst. for Geoinf. Sci. and Earth Obs., Enschede, Netherlands.
- Lin, J., R. Stein, M. Meghraoui, S. Toda, A. Ayadi, C. Dorbath, and S. Belabbes (2011), Stress transfer among an echelon and opposing thrusts and tear faults: Triggering caused by the 2003 Mw = 6.9 Zemmouri, Algeria, earthquake, *J. Geophys. Res.*, *116*, B03305, doi:10.1029/2010JB007654.
- Maerten, F., P. Resor, D. Pollard, and L. Maerten (2005), Inverting for slip on three dimensional fault surfaces using angular dislocations, *Bull. Seismol. Soc. Am.*, *95*(5), 1654–1665, doi:10.1785/0120030181.
- Mahsas, A., K. Lammali, K. Yelles, E. Calais, A. Freed, and P. Briole (2008), Shallow afterslip following the 2003 May 21, Mw = 6.9 Boumerdes earthquake, Algeria, *Geophys. J. Int.*, *172*, 155–166, doi:10.1111/j.1365-246X.2007.03594.x.
- Maouche, S., M. Meghraoui, C. Morhange, S. Belabbes, Y. Bouhadad, and H. Haddoum (2011), Active coastal thrusting and folding, and uplift rate of the Sahel Anticline and Zemmouri earthquake area (Tell Atlas, Algeria), *Tectonophysics*, *509*, 69–80, doi:10.1016/j.tecto.2011.06.003.
- Meghraoui, M., S. Maouche, B. Chema, Z. Cakir, A. Aoudia, A. Harbi, P. Alasset, A. Ayadi, Y. Bouhadad, and F. Benhamouda (2004), Coastal uplift and thrust faulting associated with the Mw = 6.8 Zemmouri (Algeria) earthquake of 21 May, 2003, *Geophys. Res. Lett.*, *31*, L19605, doi:10.1029/2004GL020466.
- Mimouni, O. (2010), Pollutions des eaux de la région d'Alger, leurs impacts sur l'environnement et les risques majeurs, report, Univ. des Sci. et Tech. Houari Boumediene, Algiers.
- Morel, J. L., and M. Meghraoui (1996), Goringe-Alboran-Tell tectonic zone: A transpression system along the Africa-Eurasia plate boundary, *Geology*, *24*, 755–758, doi:10.1130/0091-7613(1996)024<0755:GATTZA>2.3.CO;2.
- Nocquet, J. M., and E. Calais (2004), Geodetic measurements of crustal deformation in the western Mediterranean and Europe, *Pure Appl. Geophys.*, *161*, 661–681, doi:10.1007/s00024-003-2468-z.
- Peltzer, G., P. Rosen, F. Rogez, and K. Hudnut (1998), Poro-elastic rebound along the Landers 1992 earthquake surface rupture, *J. Geophys. Res.*, *103*(B12), 30,131–30,145, doi:10.1029/98JB02302.
- Pollitz, F. F., G. Peltzer, and R. Bürgmann (2000), Mobility of continental mantle: Evidence from postseismic geodetic observations following the 1992 Landers earthquake, *J. Geophys. Res.*, *105*, 8035–8054, doi:10.1029/1999JB900380.
- Reilinger, R. E., et al. (2000), Coseismic and postseismic fault slip for the 17 August 1999, M = 7.5, Izmit, Turkey earthquake, *Science*, *289*(5484), 1519–1524, doi:10.1126/science.289.5484.1519.
- Riva, R. E. M., A. Borghi, A. Aoudia, R. Barzaghi, R. Sabadini, and G. F. Panza (2007), Viscoelastic relaxation and long-lasting after-slip following the 1997 Umbria-Marche (central Italy) earthquakes, *Geophys. J. Int.*, *169*, 534–546, doi:10.1111/j.1365-246X.2007.03315.x.
- Rosen, P., S. Hensley, G. Peltzer, and M. Simons (2004), Updated repeat orbit interferometry package released, *Eos Trans. AGU*, *85*(5), 47, doi:10.1029/2004EO050004.
- Smith, S. W., and M. Wyss (1968), Displacement on the San Andreas fault subsequent to the 1966 Parkfield earthquake, *Bull. Seismol. Soc. Am.*, *58*(6), 1955–1973.

APPENDIX D

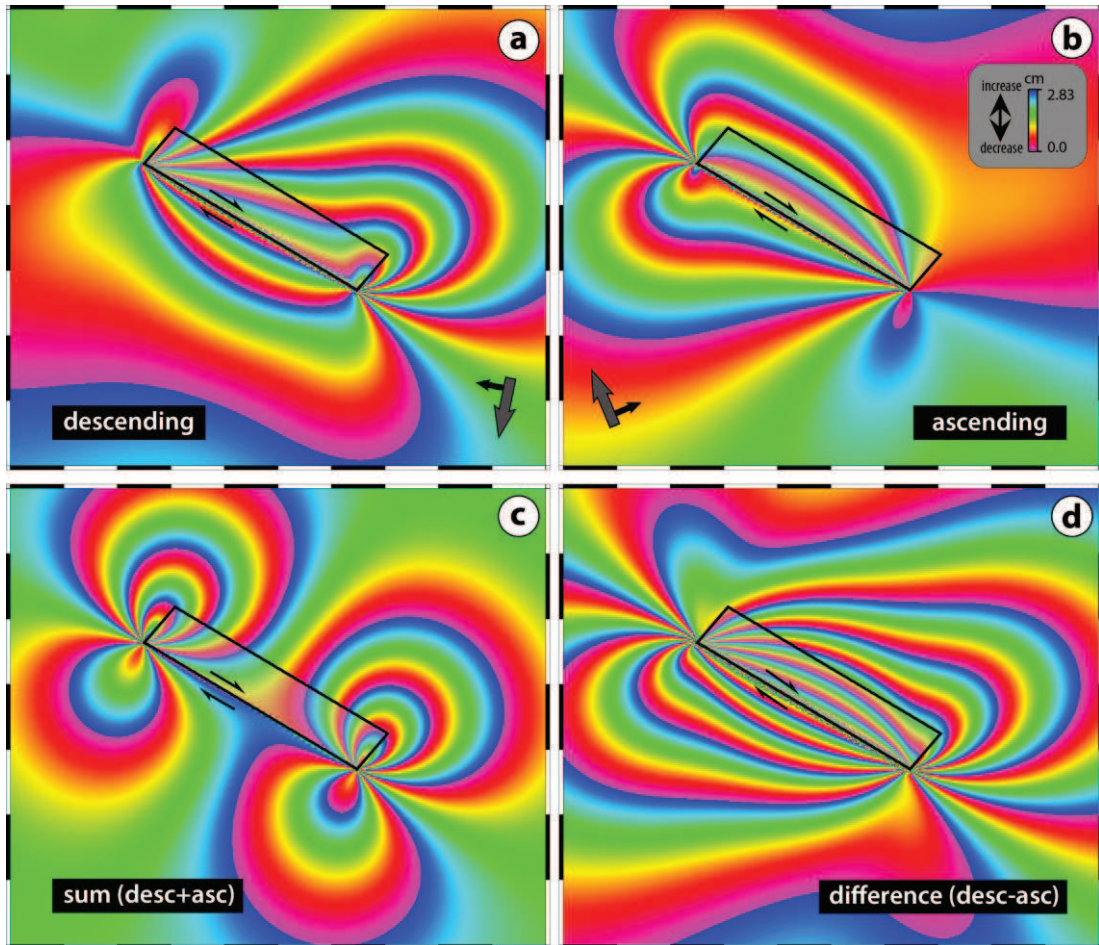


Figure D.1 : (a-b) Since InSAR measures surface change in 1-D (i.e. between surface and the radar) the surface deformation due to a right-lateral strike-slip fault on the ground will be recorded differently from ascending and descending orbits. The model fault used in the figure trends approximately NE-SW and has a dip of about 80° to the NE. The uniform slip observed on the fault surface is 50 cm. (c) The sum of the two phases of ascending and descending interferograms is largely vertical motion, and (d) the difference between two phases (descending minus ascending) is approximately east-west motion.

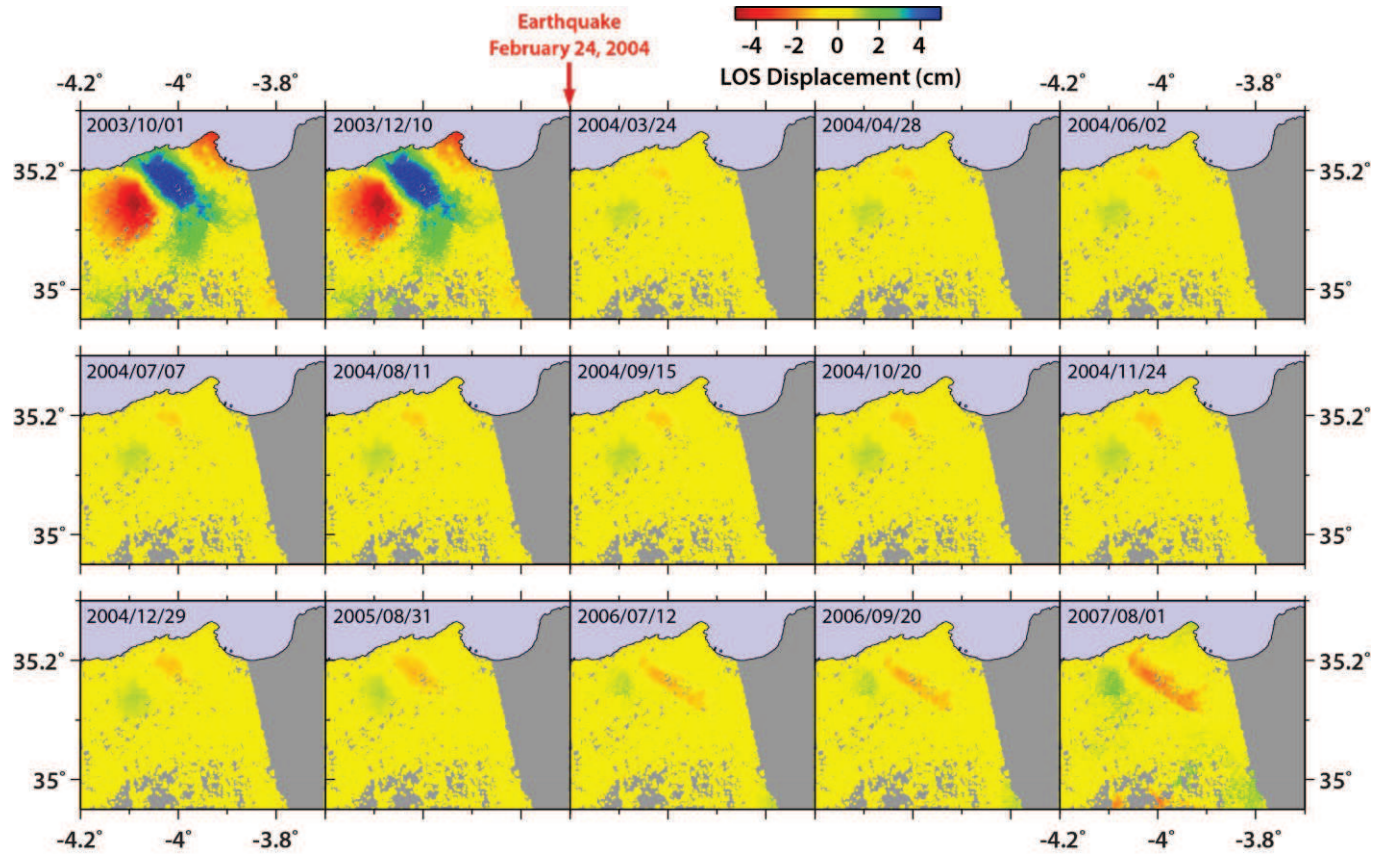


Figure D.2 : Time series of ascending LOS for Al Hoceima region between 2003 and 2007. Each image represents the incremental displacement towards the satellite since the time of the previous image, relative to pixels in the northwest corner.

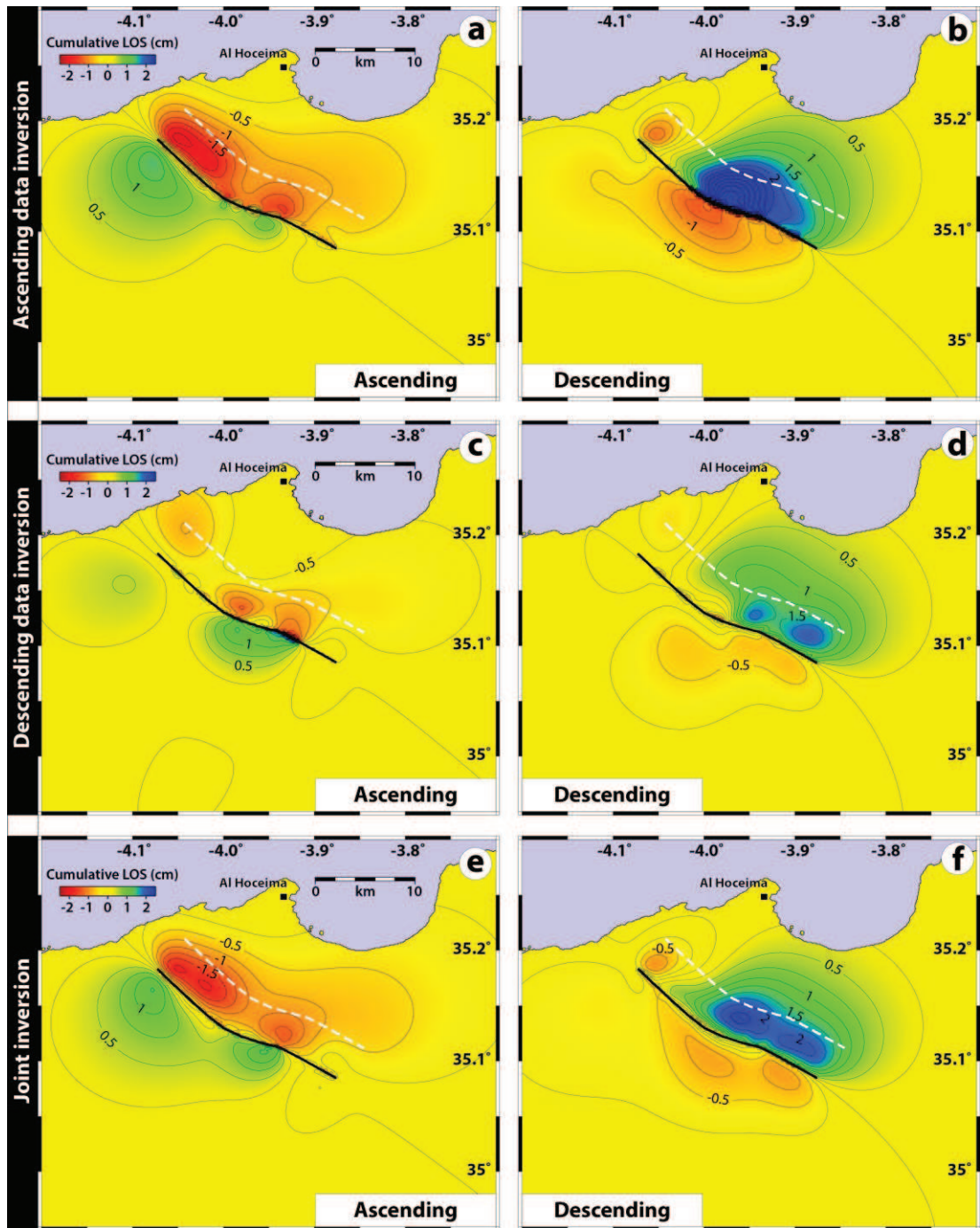


Figure D.3 : Model of 3.3-year cumulative LOS postseismic surface deformation predicted by the modeled slip distribution shown in Figure 4.11. Black lines show the top of the modeled fault. White dashed lines show the bottom of the modeled fault.

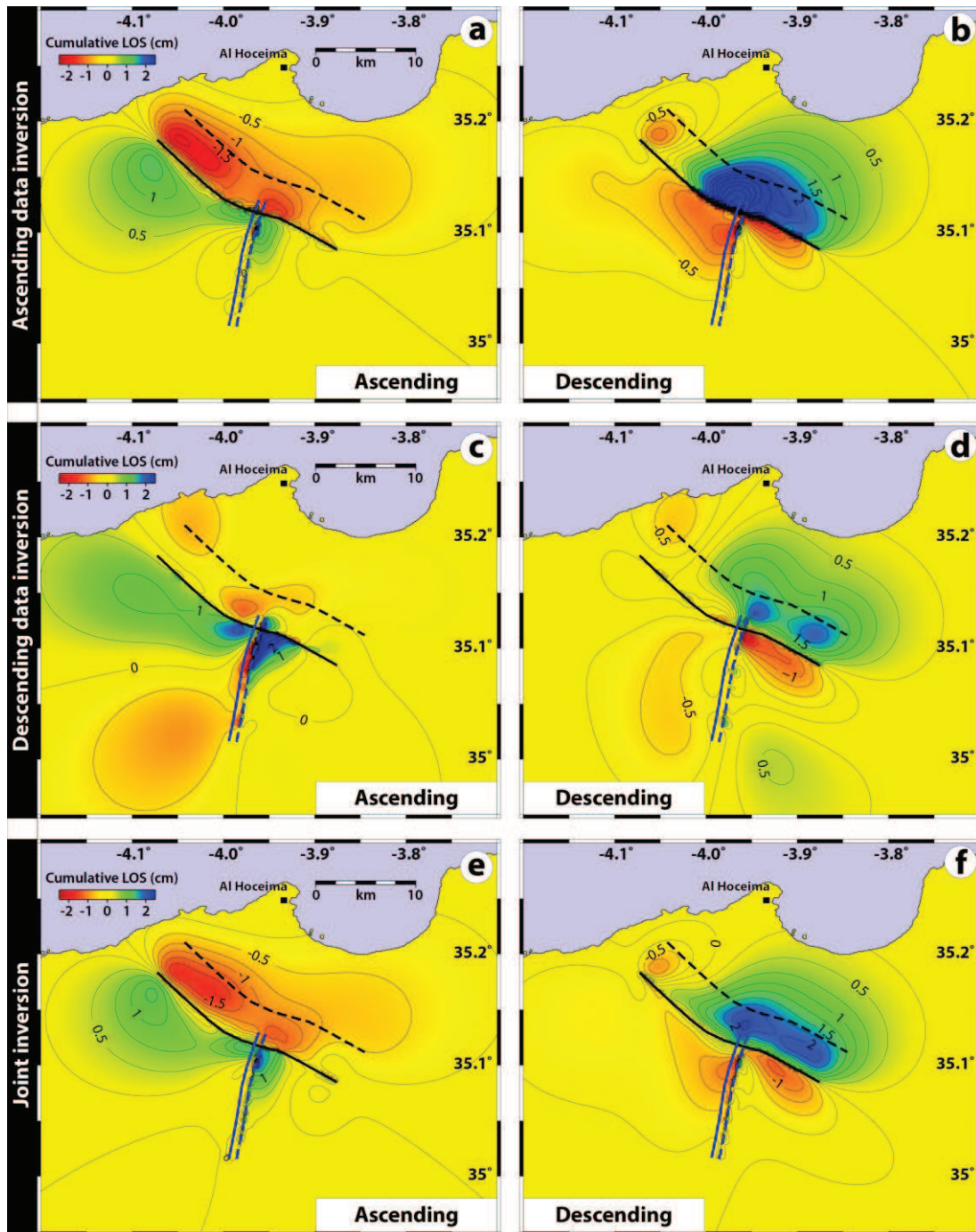


Figure D.4 : Model of 3.3-year cumulative LOS postseismic surface deformation predicted by the two fault rupture inversions according to aftershocks distribution. Black line shows the main modeled fault. Blue line indicates the fault branch obtained using aftershocks distribution.

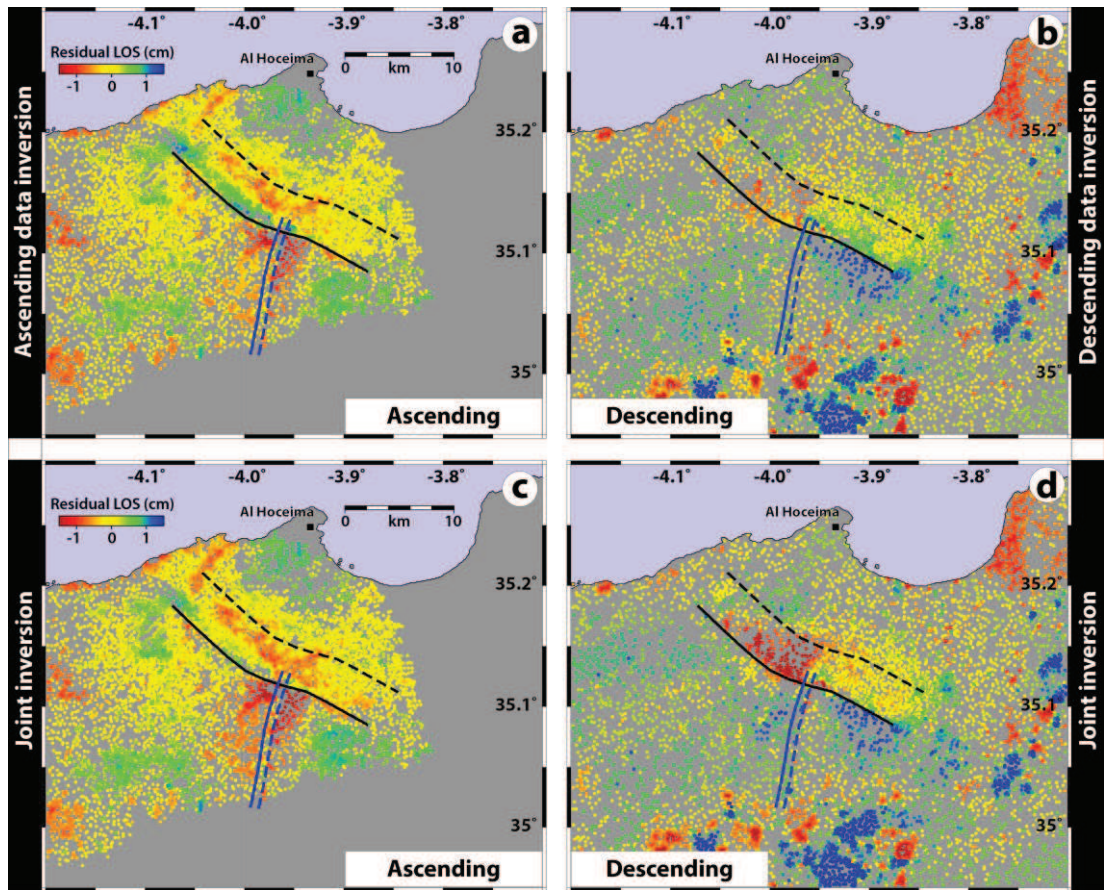


Figure D.5 : Residual maps obtained after subtracting the synthetic InSAR data (Figure D.3) from the observed data (shown in Figure 4.10). Residuals after inversion of **(a)** the ascending and **(b)** the descending data alone, and **(c, d)** jointly with a lower weighting for the descending data. Black line shows the main coseismic model fault, and blue line is the secondary fault branch.

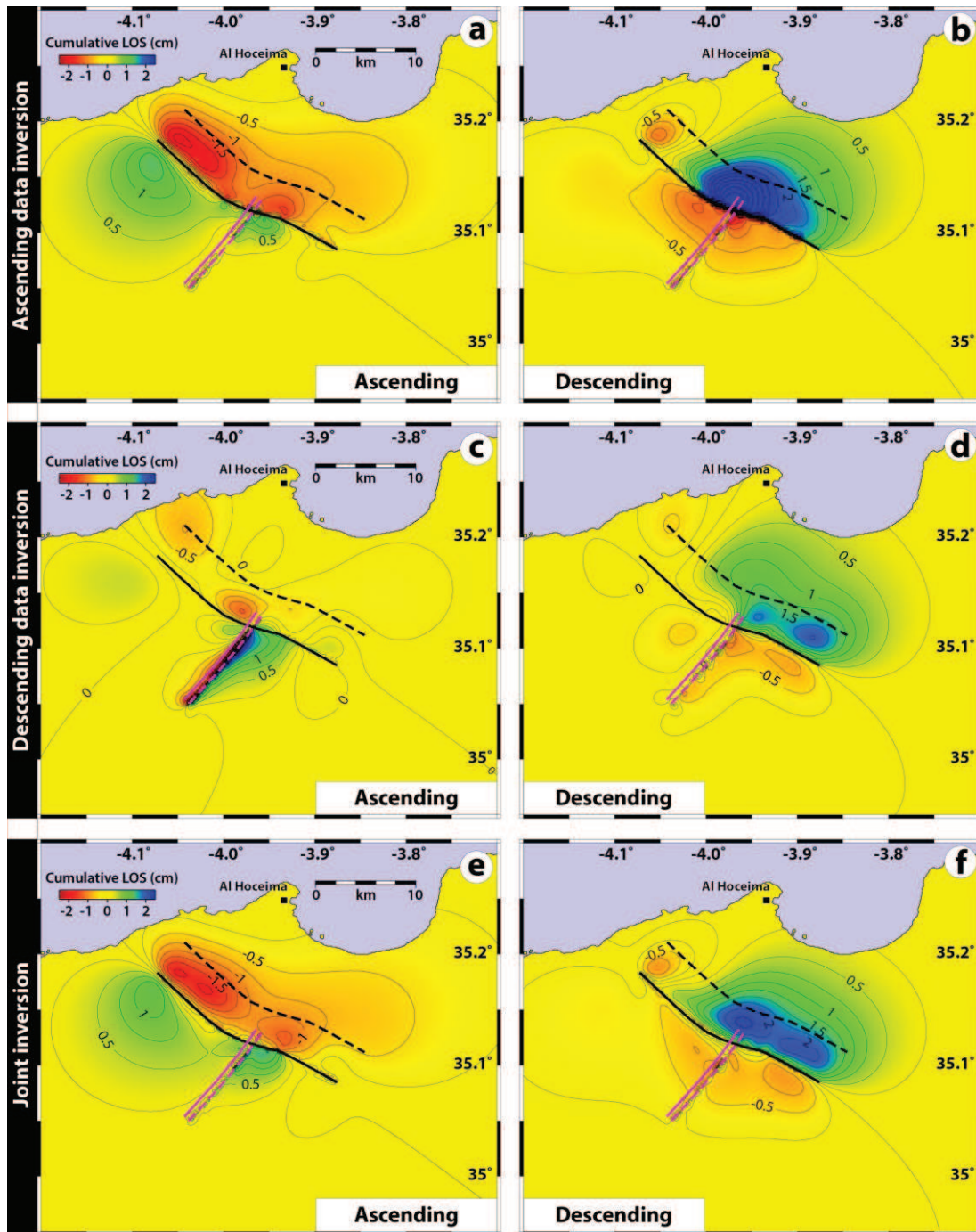


Figure D.6 : Model of 3.3-year cumulative LOS postseismic surface deformation predicted by the two fault rupture inversions according to PS LOS change in the southern section of the fault. Black line shows the main modeled fault. Pink line indicates the fault branch obtained using PS LOS displacement fields.

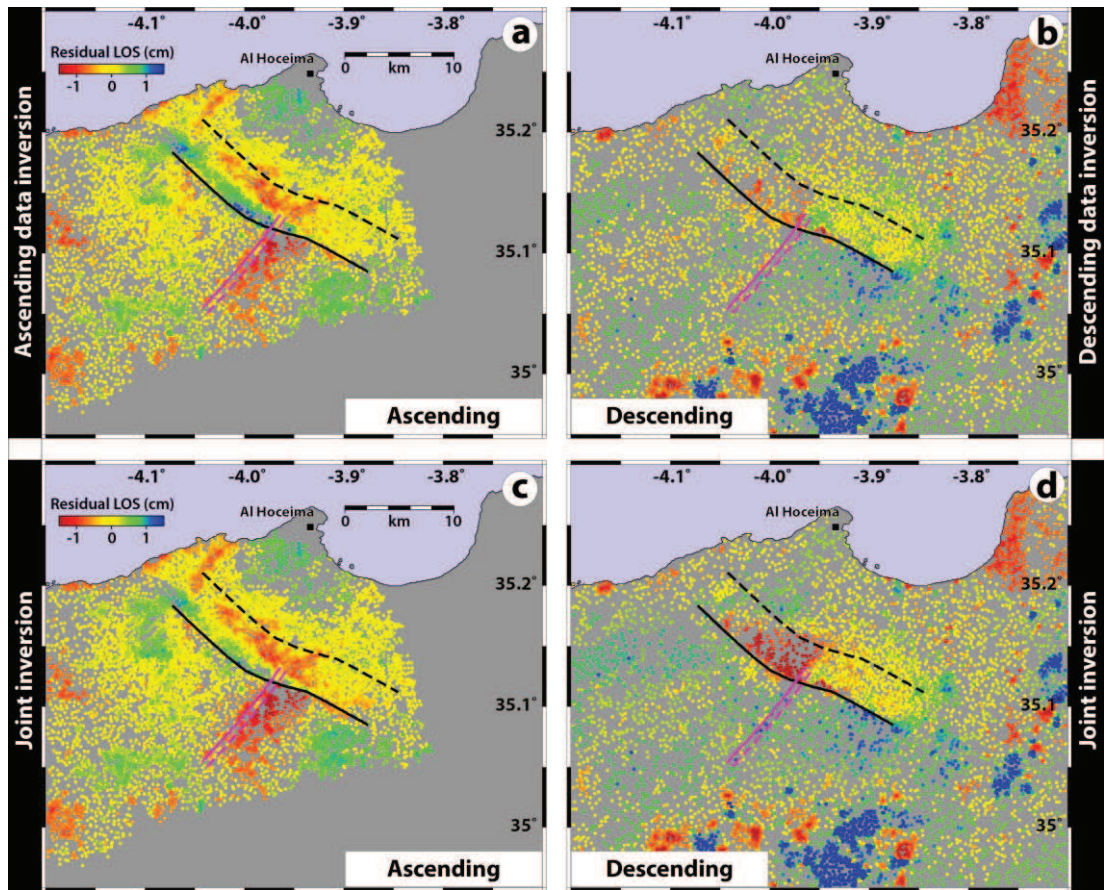


Figure D.7 : Residual maps obtained after subtracting the synthetic InSAR data (Figure D.5) from the observed data (shown in Figure 4.10). Residuals after inversion of **(a)** the ascending and **(b)** the descending data alone, and **(c, d)** jointly with a lower weighting for the descending data. Black line shows the main coseismic model fault, and pink line is the secondary fault branch.

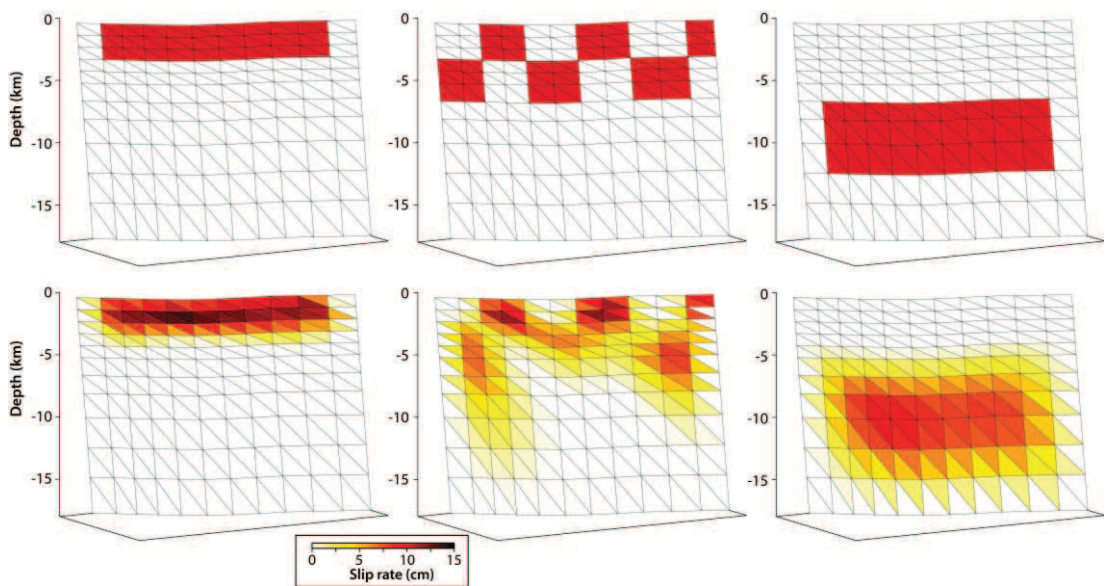


Figure D.8 : Resolution test using checker-box approach with 0.10 m slip at different depths for each cell.

APPENDIX E

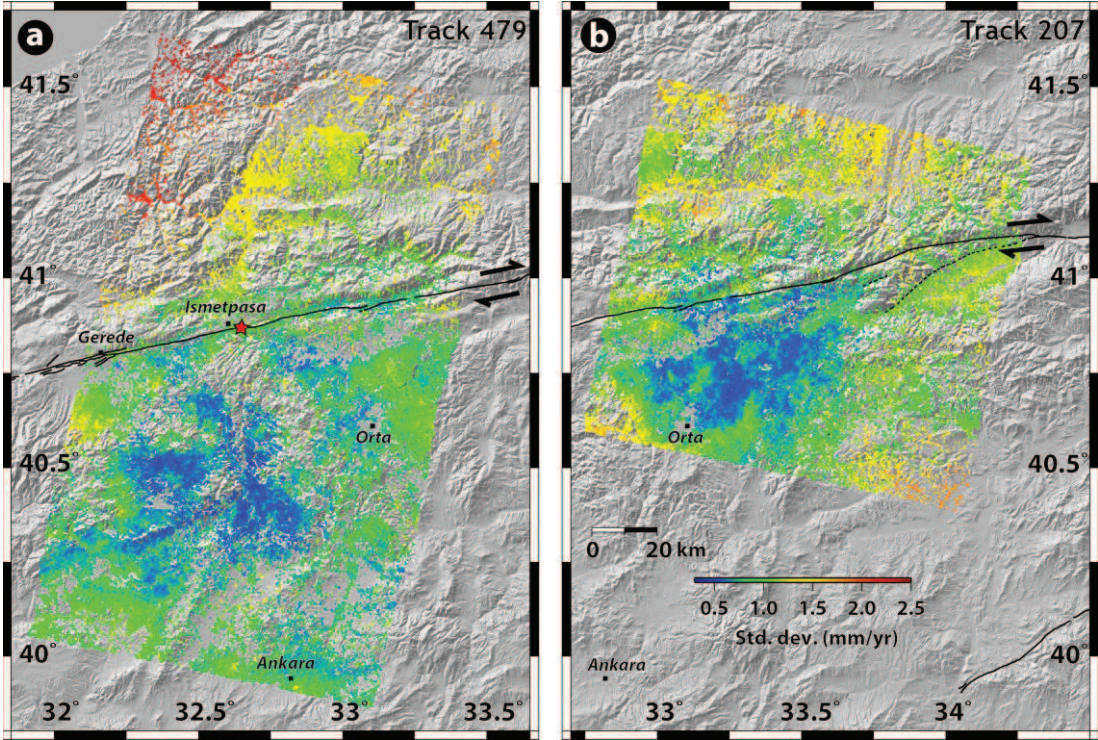


Figure E.1 : Velocity standard deviation maps calculated by StaMPS using bootstrapping.

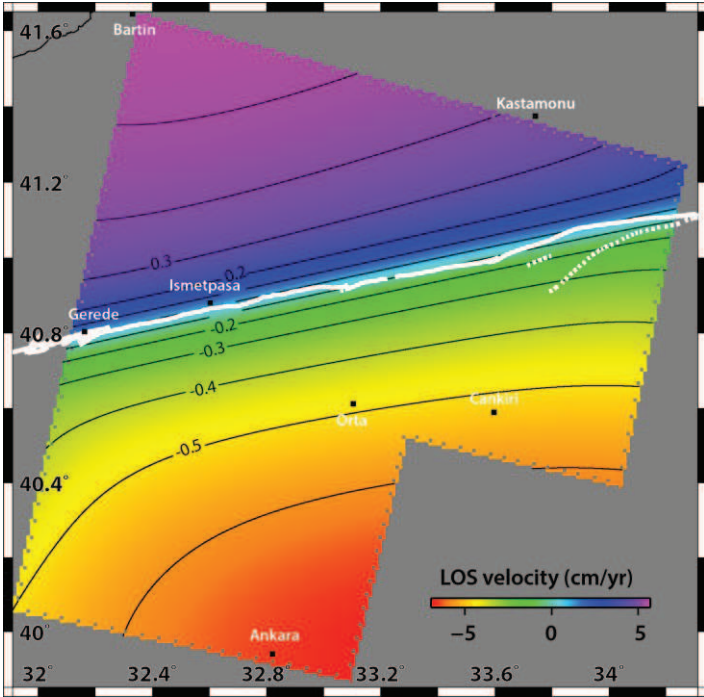


Figure E.2 : Variable interseismic slip model using multiple fault patches to flatten the far field velocity field.

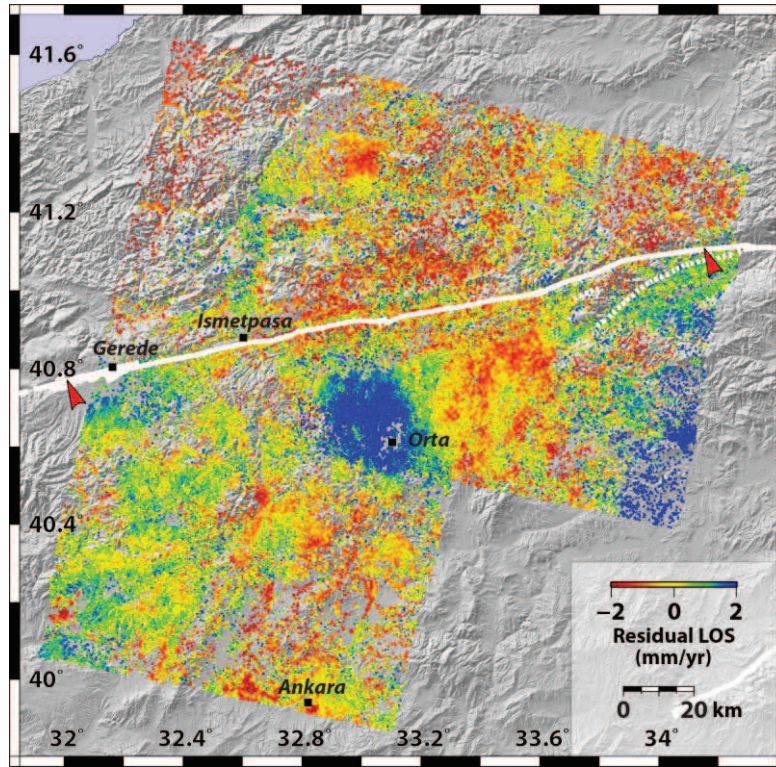


Figure E.3 : Residual LOS velocity field.

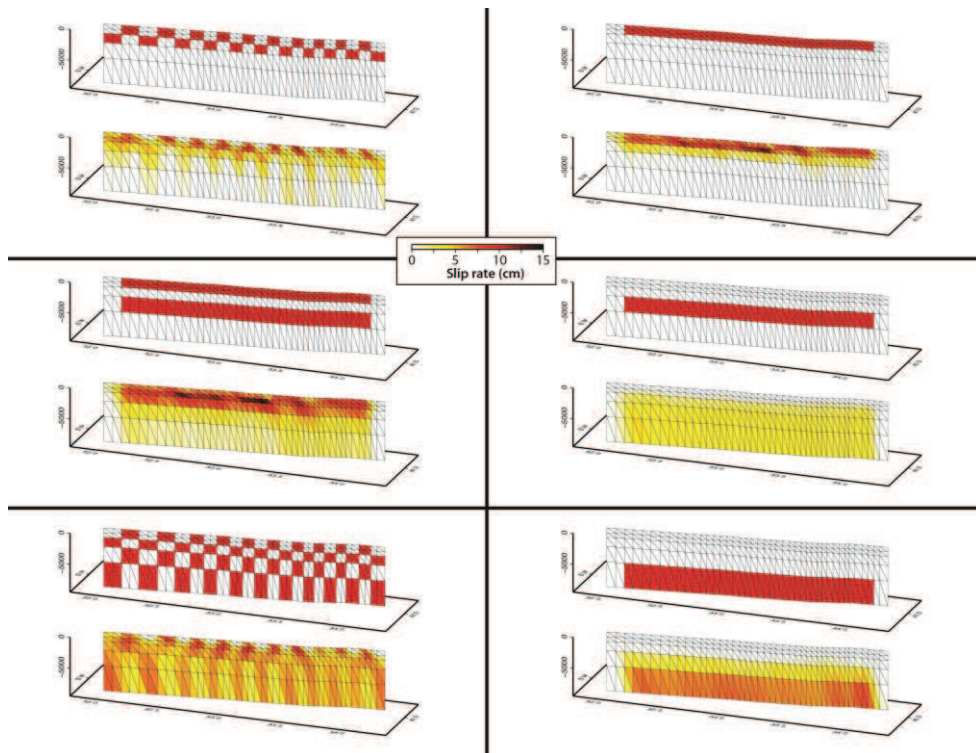


Figure E.4 : Resolution test using checker-box approach with 0.10 m slip at different depths for each cell.



RESEARCH ARTICLE

10.1002/2014GC005307

Key Points:

- The 3-D aseismic slip distribution on the Ismetpaşa segment revealed by modeling
- Creeping section considerably longer than those estimated by previous studies
- Fault creep can be correlated with geology at shallow depths along the NAF

Supporting Information:

- Readme
- Figures S1–S4

Correspondence to:

E. Cetin,
esra.cetin@itu.edu.tr

Citation:

Cetin, E., Z. Cakir, M. Meghraoui, S. Ergintav, and A. M. Akoglu (2014), Extent and distribution of aseismic slip on the Ismetpaşa segment of the North Anatolian Fault (Turkey) from Persistent Scatterer InSAR, *Geochem. Geophys. Geosyst.*, 15, 2883–2894, doi:10.1002/2014GC005307.

Received 20 FEB 2014

Accepted 23 JUN 2014

Accepted article online 25 JUN 2014

Published online 22 JUL 2014

Extent and distribution of aseismic slip on the Ismetpaşa segment of the North Anatolian Fault (Turkey) from Persistent Scatterer InSAR

Esra Cetin^{1,2}, Ziyadin Cakir¹, Mustapha Meghraoui², Semih Ergintav³, and Ahmet M. Akoglu⁴

¹Department of Geology, Istanbul Technical University, Istanbul, Turkey, ²EOST-UMR 7516, Institut de Physique du Globe de Strasbourg, Strasbourg, France, ³Department of Geodesy, Kandilli Observatory and Earthquake Research Institute, Bogaziçi University, Istanbul, Turkey, ⁴Division of Physical Sciences and Engineering, King Abdullah University of Science and Technology, Thuwal, Saudi Arabia

Abstract We use the Persistent Scatterer InSAR (PSI) technique with elastic dislocation models and geology along the creeping section of the North Anatolian Fault (NAF) at Ismetpaşa, to map and deduce the velocity field and the aseismic slip distribution. Revealing the spatiotemporal nature of the creep helped us associate the creep with potential lithological controls, hence providing a new perspective to better understand the underlying causes and mechanisms. The PSI analysis of Envisat ASAR images between 2003 and 2010 reveals a clear picture of surface creep along the fault and a new interseismic velocity field transitioning gradually between the creeping and the locked fault sections. The creep rate is found to fluctuate along a 100 km long section of the fault in a manner similar to that along the Hayward fault, reaching a maximum of $\sim 20 \pm 2$ mm/yr, close to the far field plate velocity ($\sim 25 \pm 1.5$ mm/yr). At Ismetpaşa, it is in the range of 8 ± 2 mm/yr, consistent with the previous geodetic observations. The creeping section appears to extend 30 km further east than those previously reported. Modeling of the PSI data reveals a heterogeneous creep distribution at depth with two main patches confined mostly to the uppermost 5 km portion of the seismogenic crust, releasing annually 6.2×10^{16} Nm ($M_w = 5.1$) geodetic moment. Our analysis combined with previous studies suggests that creep might have commenced as postseismic deformation following the 1944 earthquake and has evolved to stable fault creep with time. There is a correlation between aseismic surface creep and the geology along the fault as it is in major part associated to rocks with low frictional strength such as the andesitic-basaltic, limestone, and serpentine bodies within the fault zone.

1. Introduction

Understanding the mechanics of major active faults is important for reliable seismic hazard evaluations and better understanding of the earthquake physics [Carpenter *et al.*, 2011]. Although the majority of active faults may be locked, accumulating strain over a long period of time (e.g., up to 300 years along a single segment of the North Anatolian Fault [Barka, 1996]) and releasing it abruptly during moderate-to-large earthquakes ($M_w > 6$), some faults slip freely, accumulating little or no strain and generating no significant earthquakes [Thatcher, 1979; Burford and Harsh, 1980]. Faults that exhibit surface creep can appear to be locked at shallow or midcrustal depths, but nevertheless episodically produce moderate earthquakes. Examples of such partially locked faults include the Hayward fault [Savage and Lisowski, 1993; Schmidt *et al.*, 2005], the Superstition Hills fault [Bilham, 1989; Wei *et al.*, 2009], the Longitudinal Valley fault [Champenois *et al.*, 2012; Thomas *et al.*, 2014], and the Ismetpaşa segment of the North Anatolian Fault [Ambraseys, 1970; Cakir *et al.*, 2005]. Knowledge of the extent and rate of aseismic creep on the fault plane is therefore critical for reliable assessment of seismic hazard as it effectively reduces the fault surface area capable of rupture in earthquakes. Its spatiotemporal variation along faults has also important implications for forecasting the timing, locations, and potential sizes of future earthquakes and for understanding the fault behavior [Bürgmann *et al.*, 2000].

The Ismetpaşa creeping segment was ruptured by the 1944 Bolu-Gerede ($M = 7.3$) and 1951 Kurşunlu ($M = 6.9$) earthquakes, part of the westward migrating earthquake sequence of the NAF during the twentieth century (Figure 1) [Barka and Kadinsky-Cade, 1988; Barka, 1996; Stein *et al.*, 1997]. Based on the railway maintenance reports, Ambraseys [1970] estimated a rapid right-lateral surface creep of 50 mm/yr following

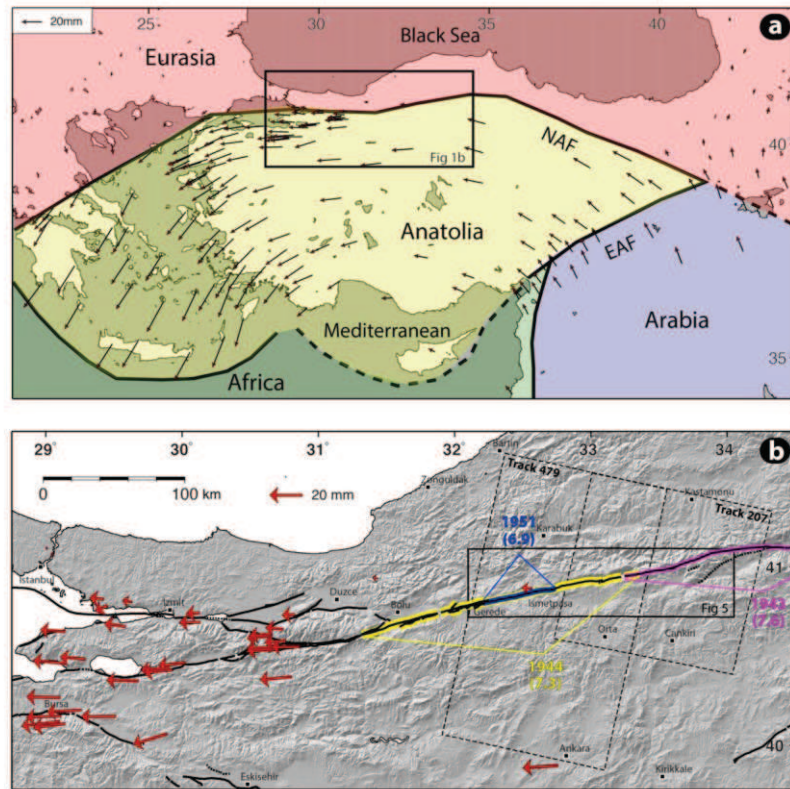


Figure 1. (a) Tectonic map of Turkey and surrounding regions with GPS vectors in a Eurasia fixed reference frame [Reilinger et al., 2006]. Rectangle shows the location of Figure 1b. (b) Shaded SRTM topography map along the North Anatolian Fault zone in northwestern Turkey with the recent rupture segments of large earthquakes [Barka and Kadinsky-Cade, 1988; Şaroglu et al., 1992]. The dashed rectangles are the Envisat image frames with track numbers used in this study.

the 1944 earthquake until the 1951 event. The spatiotemporal evolution of the surface creep at Işmetpaşa remained, however, unknown until the mid-2000s despite its discovery in the late sixties [Ambraseys, 1970]. Offset measurements on the walls of the railway station at Işmetpaşa town suggested that the creep rate had decreased to 20 mm/yr between 1957 and 1969 [Ambraseys, 1970]. A microgeodetic network installed across the fault at Işmetpaşa in 1972, added with other geodetic measurements (LIDAR and InSAR) along the creeping segment, shows an exponential or logarithmic decrease of creep rate reaching a steady slip rate of about 9 mm/yr over the last decade [Aytun, 1982; Eren, 1984; Deniz et al., 1993; Cakir et al., 2005; Kutoglu and Akcin, 2006; Kutoglu et al., 2008; Kutoglu et al., 2010; Karabacak et al., 2011; Ozener et al., 2012; Kaneko et al., 2013]. Using the conventional InSAR method, Cakir et al. [2005] identified, for the first time, a 70 km long lateral extent of the creeping section, roughly confirmed later on by Kaneko et al. [2013] using stacking of independent InSAR data.

In this study we present an interseismic velocity field mapped using the Persistent Scatterer InSAR (PSI) time series technique [Ferretti et al., 2001; Hooper et al., 2004] between 2003 and 2010 on two overlapping descending tracks of Envisat ASAR (C-band) satellite covering the NAF between 32.1°E and 34.3°E (Figure 1). We use the surface velocity field and provide for the first time a model of aseismic slip distribution on the fault using elastic half-space dislocations. Finally, we discuss the mechanism of aseismic creep, its

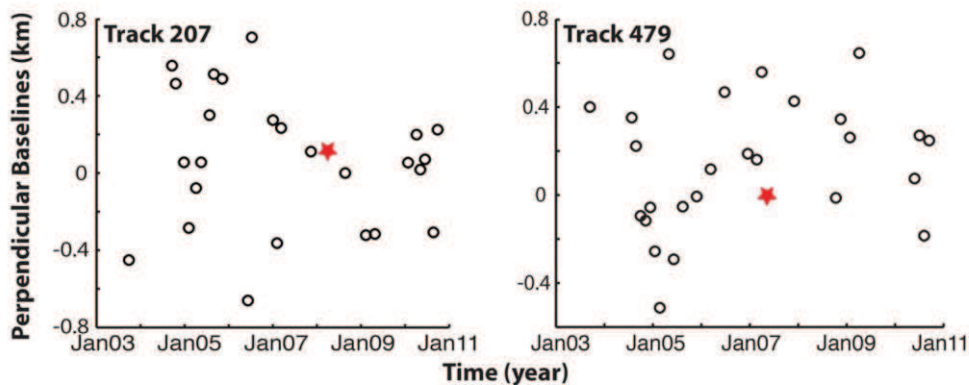


Figure 2. Baseline versus time plot of synthetic aperture radar orbits from two Envisat tracks used to calculate the deformation field and the time series. Empty circles denote the SAR images with stars indicating the master orbits chosen for the PSI analyses.

initiation, and the potential causes for its along-strike variation on the basis of creep rate variation and lithology along the fault.

2. InSAR Observations

The PSI method is an advanced multitemporal InSAR technique, capable of simultaneous processing of multiple SAR acquisitions in time, which will increase the number of locations where a subtle deformation signal can be extracted by reducing the associated errors [Ferretti *et al.*, 2001]. It has been successfully used to reveal slow surface creep along the Longitudinal Valley (Eastern Taiwan) [Champanois *et al.*, 2012] and Izmit (Turkey) faults [Cakir *et al.*, 2012]. Such advanced techniques are able to reduce the effects of noise and signal decorrelation due to atmospheric effects, digital elevation model (DEM) errors, and orbital inaccuracies [Hooper, 2008]. Compared to conventional InSAR, the PSI analysis generates time series of ground deformations for individual targets using multitemporal stacks of synthetic aperture radar (SAR) images with regard to these targets that have a constant echo over the time are called persistent scatterers (PS) [Ferretti *et al.*, 2000; Hooper *et al.*, 2004; Kampes, 2005; Motagh *et al.*, 2007; Cigna *et al.*, 2011; Peyret *et al.*, 2011; Dehghani *et al.*, 2013]. There are various PSI approaches to detect the PS pixels and estimate the ground deformation signal [Ferretti *et al.*, 2001; Hooper *et al.*, 2007; Ketelaar, 2008]. In comparison, PS selection algorithms and deformation estimation methods are different in between these approaches. In this study, we present interseismic velocity fields obtained from PSI analysis with a single master network using the StaMPS (Stanford Method for PS) software package that takes the advantage of spatial correlation between pixels and does not use any temporal deformation model in the PS identification step [Hooper, 2008; Dehghani *et al.*, 2013]. The PS pixels are successfully detected through the phase analysis in a series of iterations even though their amplitude is low. The StaMPS uses ROI_PAC software [Rosen *et al.*, 2004] for focusing the raw images and DORIS software [Kampes and Usai, 1999] for calculating interferograms with the SRTM 90 m DEM data [Farr *et al.*, 2007] for removal of the topographic phase contribution. Orbital errors are estimated and removed from the mean line-of-sight (LOS) velocity field with a best fit bilinear ramp. Potential unwrapping errors in each interferogram were checked visually as recommended by Hooper [2008]. Velocity standard deviation maps, calculated by StaMPS using bootstrapping, reach a maximum of 2.4 mm/yr for two individual overlapping tracks (Figure S1, supporting information). The detailed processing procedure can be found in Hooper [2008].

2.1. Surface Velocity Field

We have analyzed 55 Envisat ASAR images on two descending and overlapping tracks (T479 and T207; Figure 1b) between 2003 and 2010 (Figure 2). Images acquired on 6 May 2007 on T479 and 8 August

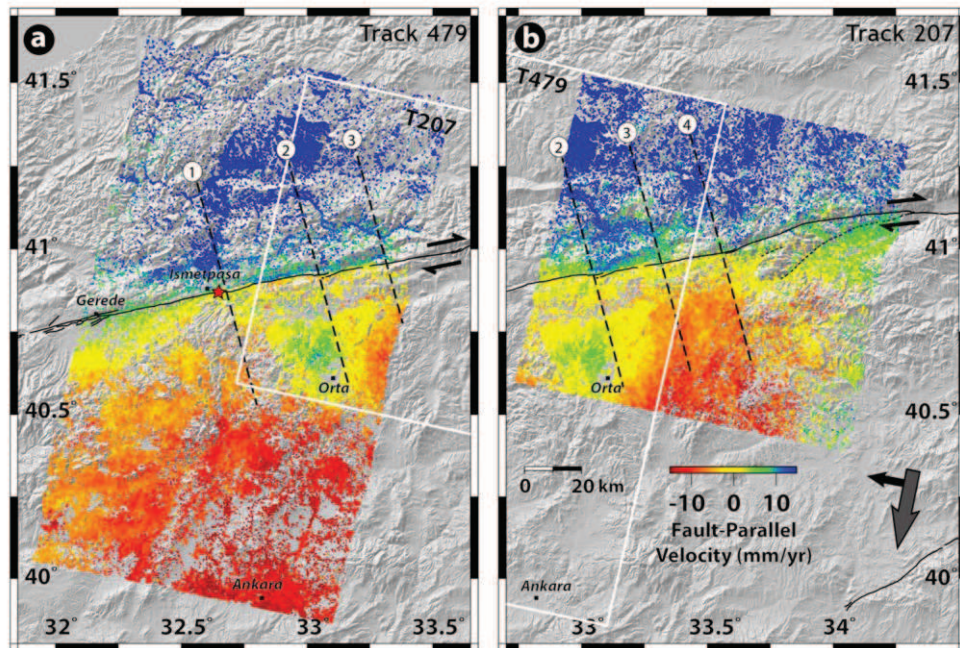


Figure 3. Velocity field in the region of Ismetpaşa deduced from PSI time series. (a, b) Fault-parallel horizontal velocity field (identical color scale for both tracks) between 2003 and 2010 on a SRTM shaded relief image with known active faults (black lines). The gray and black arrows to the bottom right corner show the satellite flight direction (descending) and the line-of-sight direction (right looking), respectively. Movements away from the satellite are shown with warm colors and toward the satellite are shown with cool colors, which are consistent with the right-lateral sense of motion of the NAF. Thick dashed lines with numbers are locations of profiles as shown in Figure 4. Red star shows the location of the PSI and GPS time series plotted in Figure 7. White boxes show the neighboring Envisat track used in this study.

2008 on T207 are chosen as the master scenes of all the interferometric pairs in each track to minimize the spatial and temporal decorrelation and atmospheric effects. A mean radar line-of-sight (LOS) velocity field for each track is obtained and then projected to fault-parallel horizontal velocities assuming that the radar LOS displacements are due to purely horizontal motion on a N76°E trending strike-slip fault, parallel to the strike of the Ismetpaşa segment taking into account the local incidence angles that vary across the range. The fault-parallel velocity field shown in Figure 3 reveals very clearly the surface creep as well as the interseismic strain accumulation across the NAF. Warm colors (i.e., negative velocities) on the southern side of the fault indicate motion away from the satellite (i.e., westward) and cool colors (i.e., positive velocities) on the northern side of the fault indicate motion toward the satellite (i.e., eastward), consistent with a right-lateral sense of plate motion across the NAF. Surface creep is characterized by steep fault-parallel velocity gradients and by a sharp color contrast across the fault trace along a distance of more than 100 km (Figure 3). In contrast, locked segments are clearly shown by gradual changes in the velocity field across the fault, particularly between Gerede and Ismetpaşa. Besides, to the south of the NAF the interseismic signal is strongly disturbed by a circular deformation pattern attributed to the postseismic displacements after the 6 June 2000 Orta earthquake [Taymaz et al., 2007; Cakir and Akoglu, 2008].

Fault-parallel velocities along four different profiles are shown in Figure 4 together with best fit models for creeping and locked faults obtained with elastic dislocations. The velocity profiles of locked faults (at 15 km depth) show a classic arctangent shape predicted by elastic screw dislocations across a strike-slip fault [Savage and Burford, 1973]. Conversely, the steps in the velocity profiles at the fault indicate surface creep. The shape and height of these steps are controlled by the locking depth and creep rate; abrupt vertical changes

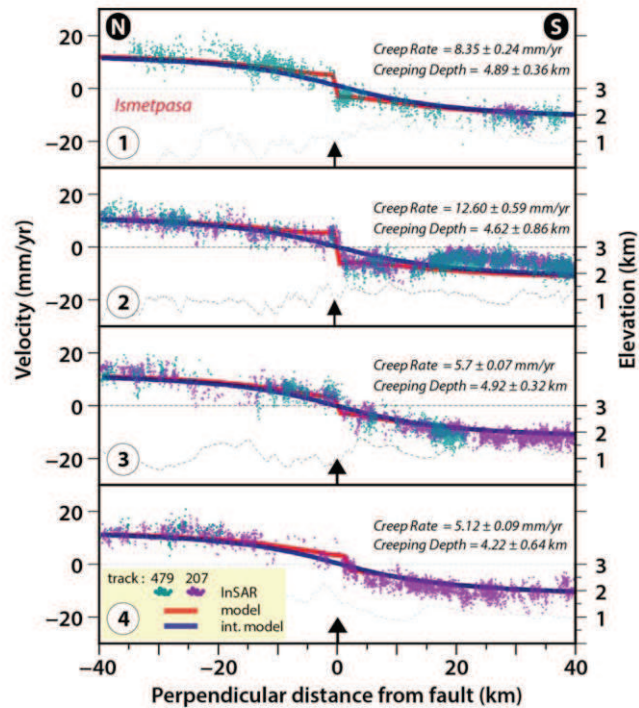


Figure 4. Observed and modeled fault-parallel velocity profiles perpendicular to the fault. Red curves show the best fitting model to PSI data with the creep rate and depth given above. The blue curves represent an interseismic model for a locked fault at 15 km of depth. Dashed line represents the topographic elevation along the profiles. Arrows indicate the mapped active fault location. Profile-1 crosses the location of the offset wall and the geodetic network that have been used to measure the creep rate at Ismetpasa over the last 40 years.

indicating creep reaching to the surface, and gradual changes showing deeper locking depths. It is worthwhile noting that fault-parallel velocities in Figure 4 do not correlate with topography.

2.2. Estimation of Creep Rate and Extent

In order to determine the surface creep rate and its variations along the fault, we first subtract from the velocity field the interseismic model as explained in the modeling section below. Subsequently, profiles of residual velocities perpendicular to the fault are extracted at every ~1 km along the fault. Along 3 km on each side of the fault, we find a best fitting line to the profiles and compute the creep rate as an offset of the intercepts of these two lines at the fault trace (Figure 5) [Burford and Harsh, 1980]. Using standard

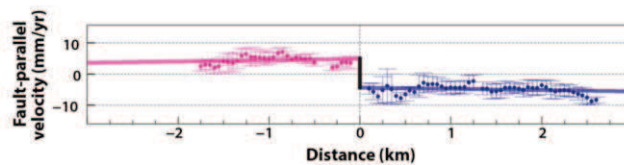


Figure 5. Estimation procedure for the creep rate using best fitting lines to InSAR velocity profiles that extend for 3 km on both sides of the fault (pink and blue colors). Creep rate is calculated from the offset of the two lines at the fault trace (e.g., the length of black line).

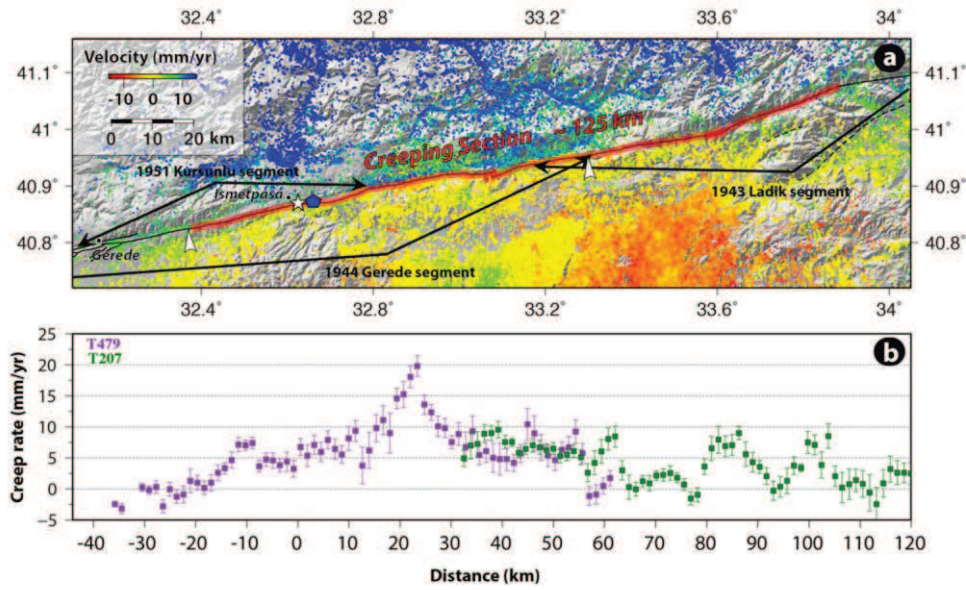


Figure 6. Rate and extent of aseismic surface creep along the Ismetpaşa section of the North Anatolian Fault. (a) A mosaicked map of fault-parallel horizontal velocity field on SAR image tracks T479 and T207. Red line shows the creeping section of the NAF and the blue pentagon indicates the location of the micro-GPS network. White star represents the location of the wall where creep was discovered by Ambraseys [1970]. White arrows show the extents previously found by Cakir *et al.*, [2005] and Kaneko *et al.*, [2013]. (b) Creep rates with error bars along the fault are estimated from the InSAR velocities on track T479 (pink color) and track T207 (green color).

deviations of PS pixels predicted by StaMPS, weighted means are calculated at every 50 m using a bin width of 100 m along these fault perpendicular profiles. The error bars of creep rates for individual profiles are estimated from the root-mean-square residuals of the curve fitting using weighted means. The results reveal a ~120 km long creeping section with a creep rate varying in an oscillating manner along the fault and reaching a maximum of 20 ± 2 mm/yr around 20 km east of Ismetpaşa (Figure 6). At its eastern end, it overlaps with the western part of the 1943, and the eastern part of the 1944 and 1951 earthquake ruptures (Figure 6a). Note that despite some discrepancies, creep rate estimates from two different InSAR data sets

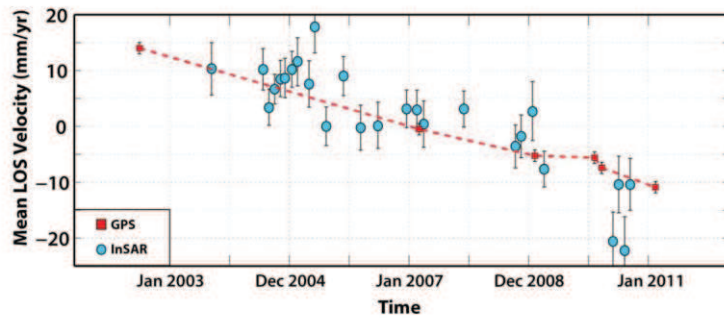


Figure 7. Time series of line-of-sight InSAR (blue circles) and GPS (red squares) velocities (blue pentagon shown in Figure 6) [Ozener *et al.*, 2012]. The LOS velocities represent the mean of all pixels in a circle of ~600 m diameter to the north and south of the fault around the GPS network. The general trend and decay of creeping rate from InSAR time series are in good agreement with GPS time series.

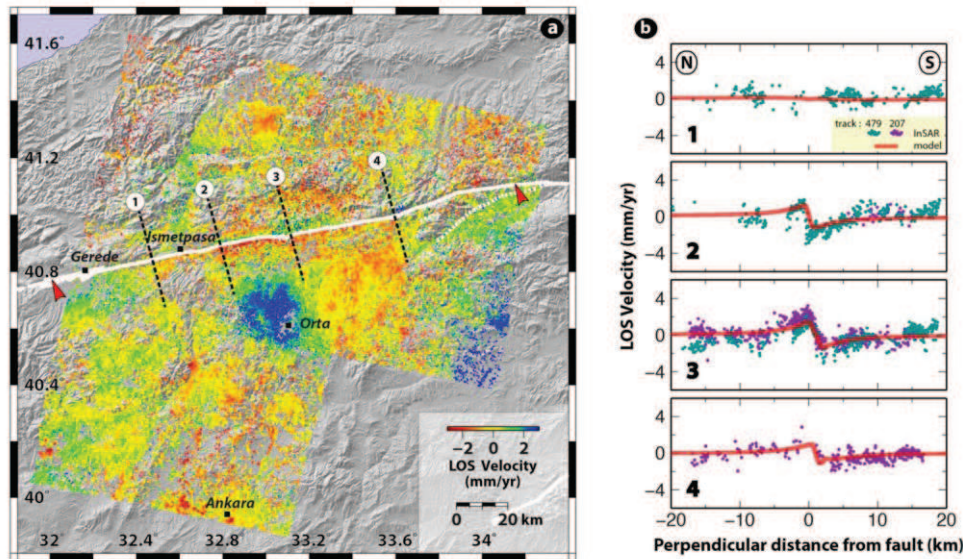


Figure 8. Modeling of aseismic slip distribution. (a) Residual LOS velocities, obtained by the removal of the long-term signal due to interseismic loading and unwrapping, atmospheric, and orbital errors, are used to model the aseismic slip on the fault. The blue circular anomaly located around the town of Orta is most likely due to the postseismic deformation of the 6 June 2000 Orta earthquake ($M_w = 6.0$). Red arrows on the fault (white lines) indicate the tips of the modeled fault shown in Figure 9. Dashed lines show the profiles in Figure 8b. (b) Observed (green and purple points) and modeled residual velocities (red lines) along the profiles perpendicular to the fault.

in the central section of the fault are overall in good agreement. The creep rate is 8 ± 2 mm/yr at Ismetpaşa, consistent with most previous studies [Deniz *et al.*, 1993; Cakir *et al.*, 2005; Karabacak *et al.*, 2011; Ozener *et al.*, 2012; Kaneko *et al.*, 2013]. The InSAR LOS time series are in good agreement with LOS-projected GPS time series at Ismetpaşa [Ozener *et al.*, 2012] and show linear decays with time (Figure 7).

3. Modeling

To estimate the aseismic slip distribution on the Ismetpaşa segment, we model the LOS displacements using the Poly3Dinv software [Maerten *et al.*, 2005] that uses the boundary element approach. To infer the aseismic slip distribution on the fault, we first model and remove from the LOS velocity field the long-wavelength signal due to the interseismic strain assuming that the regional deformation due to the secular loading arises from buried displacement below the NAF. To model this secular loading, we use the far field (>20 km away from the fault) LOS velocity field data (with the Orta earthquake region being masked). We invert for a right-lateral sense of slip on a single fault patch buried below 10 km to infinity (900 km) and obtain ~ 25 mm/yr of interseismic slip rate. However, the model does not entirely account for the long-wavelength signal in the velocity field, implying the presence of unwrapping and unmodeled atmospheric errors, and orbital residuals in the data. We therefore obtain a variable interseismic slip model using multiple fault patches (12 triangles) to flatten the far field velocity field required for modeling the distribution of shallow creep on the fault (Figure S2, supporting information). We subtract this inverted interseismic model from the LOS velocity field and obtain a residual LOS velocity field that is considered as a creep signal in vicinity of the fault (Figure 8). The residual LOS velocities show a sharp color contrast across the fault that can also be seen in the profiles shown in Figure 8b. Some of the remaining velocities, which are on the corner of the tracks with ± 2 – 3 mm/yr, in the velocity field are, however, most probably due to atmospheric artifacts or unmodeled orbital errors but these do not affect offset at fault. In addition, the postseismic surface deformation associated with the 2000 Orta earthquake [Cakir and Akoglu, 2008] becomes more prominent and appears as circular area of range decrease ~ 30 km across anomaly with a blue color.

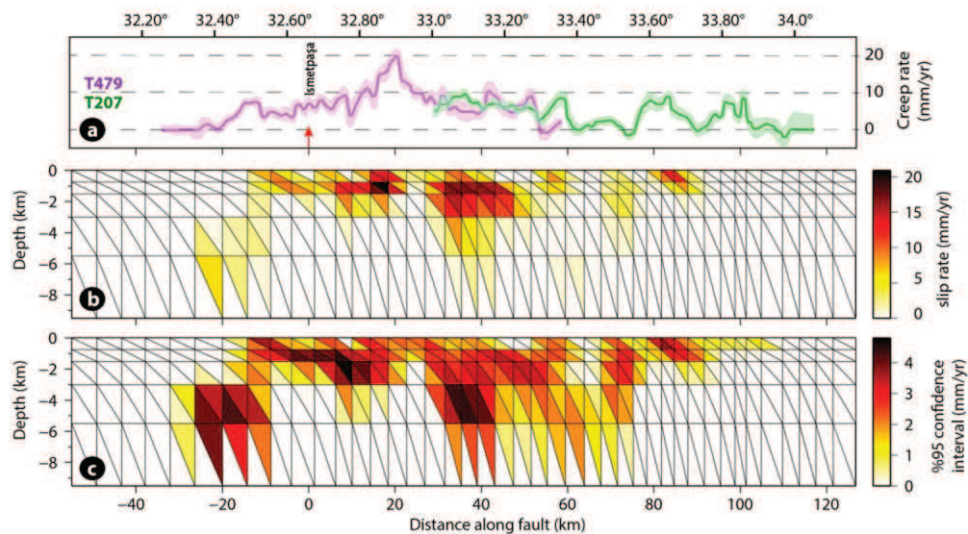


Figure 9. (a) Variation of surface creep rate along the fault; (b) depth distribution of the variable aseismic slip on the Işmetpaşa creeping segment. Red arrow indicates the position of the geodetic network located 3.5 km east of the train station near Hamamlı village at Işmetpaşa. Slip is heterogeneously distributed along the fault and confined mostly to uppermost 5 km of the seismogenic crust with a maximum slip of $\sim 20 \pm 2$ mm/yr 20 km west of Işmetpaşa. (c) Uncertainty of the slip distribution with depth obtained from inversions of 200 InSAR data sets perturbed with synthetic noise.

To model the creep on the fault surface, we formed a vertical fault from surface to a depth of 10 km, using quadrangles of about 5 km long along the fault strike. The width of the quadrangles increases from 1 to 3 km in the downdip direction (Figures 8 and 9). To evaluate the uncertainty of slip distribution, we first estimate a 1-D covariance function for each data set by radially averaging a 2-D autocorrelation function calculated using the power spectrum of the data in the far field where there are no orbital ramps or deformation signal due to aseismic creep [Hanssen, 2001]. We then fit a colored noise model [Lennon, 2000] to the 1-D covariance function. Using the procedures in Fukushima *et al.* [2003], for each data set on the two tracks we construct 200 simulations of spatially correlated random noise that matches the colored noise model. We use them to perturb each of our original data sets [Funning *et al.*, 2005] which are then inverted for pure right-lateral strike slip (locked on the fault edges, except at its top) using a scale-dependent umbrella-smoothing operator to avoid any unphysical oscillatory slip distribution. A smoothing factor of 0.5 is used since lower values predict slip rates much higher than the interseismic slip rates estimated from the GPS measurements (24.2 ± 0.2 mm/yr) by Reilinger *et al.* [2006] and from InSAR (25 ± 1.5 mm/yr) in this study. After calculating the mean slip, we estimate %95 confidence intervals from its distribution on each triangular patch. The results show a shallow creeping depth (mostly above 5 km) and an intermittent slip distribution with a highest rate of 20 ± 2 mm/yr on several patches along the fault, similar to that inferred along the Hayward fault [Schmidt *et al.*, 2005] (Figure 9). Although the surface creep deduced from offsets of best fitting lines correlates to some extent with the creep inferred with Poly3Dinv modeling at depth, the largest patch located ~ 40 km east of Işmetpaşa is not obvious in the surface creep rate curves. Figure 8b illustrates that the model explains the LOS data reasonably well (~ 1.25 mm/yr RMS; Figure S3, supporting information). As expected, checker-box tests show that slip resolution decreases with increasing depth, but as shown in Figure S4 (supporting information) the InSAR data have an adequate resolution in constraining the shallow slip (< 5 km) on the fault.

4. Discussion

The mechanical behavior of active fault zones can vary from continuous aseismic creep to sudden rupture during earthquakes, and the same fault zone may evolve either laterally or at depth from seismic to

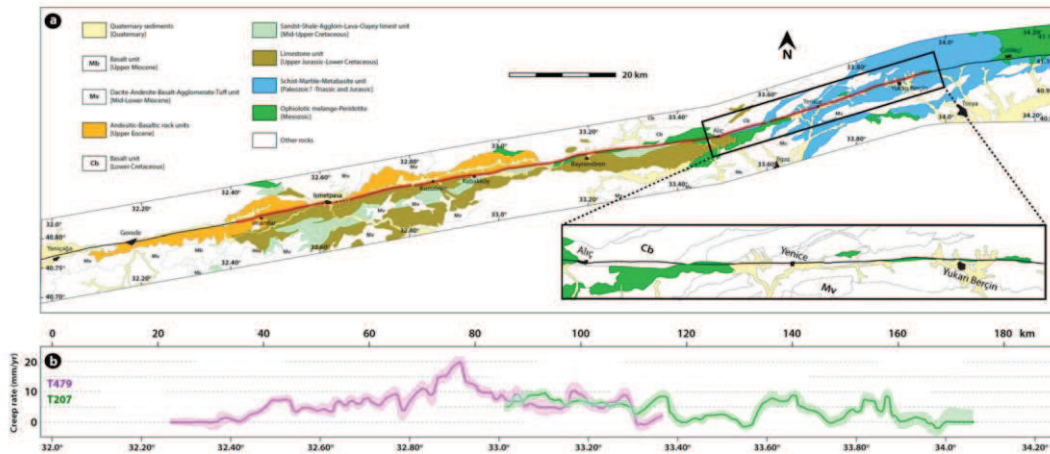


Figure 10. (a) Geology map of the study region simplified from *Herece and Akay* [2003] with surface creep rates along the North Anatolian Fault obtained in this study. Geological units presumably involved in creeping are shown in colors and the others are labeled in white with abbreviations. Black and red lines represent the active fault and the creeping segment, respectively. The eastern end of the creeping section can be clearly seen in the inset rectangle. (b) Creep rates and error ranges for two individual tracks are indicated in purple and green colors as in Figure 6.

aseismic deformation [Freed, 2007; Gratier et al., 2013]. It is therefore important to determine whether this transition is geologically and tectonically controlled since some types of rocks are more prone to seismic failure while the others are more likely to exhibit aseismic creep [Gratier et al., 2013]. If the fault zone rocks are weaker than the surrounding rocks and do not heal after the rupture, they may exhibit stable sliding friction behavior, so called velocity-strengthening conditions [Carpenter et al., 2011]. Inherited tectonic structures, the presence of weak rocks or the thickness of the gouge zone may control the distribution of surface creep. Serpentine [Allen, 1968] and clay rich lithology [Warr and Cox, 2001] have long been identified as zones of structural characteristics with phyllosilicate foliations resulting into fault weakening [Colletini et al., 2009]. Similarly, calcareous rocks with phyllosilicates are able to creep in the upper crust by pressure solution [Gratier et al., 2013].

Analysis of geological maps reveals that the aseismic surface creep can be, to some extent, correlated with the geology along the North Anatolian Fault (Figure 10). The major surface creep in the shallow depths of the western part of the creeping segment, overlapping with 1944 earthquake rupture is correlated with the Upper Jurassic-Lower Cretaceous limestone unit, probably due to pressure solution. In the eastern part of the creeping segment, which overlaps with the 1943 earthquake rupture, aseismic slip is possibly related to the serpentinite bodies marked in the geology map as Mesozoic ophiolitic mélangé along the fault zone (Figure 10a). There appears to be no correlation, however, between the variation of creep rate and surface lithology along the fault (Figure 10).

The downward circulation of meteoric fluids may also contribute to the creep in the weaker upper crust as shown by the numerous hot springs along the Alpine active fault zone in New Zealand [Allis and Shi, 1995], and in particular in the western and central western segments of the North Anatolian Fault zone. In fact, Paleozoic metamorphic rocks, along with Mesozoic limestone and flysch, comprise the basement rocks in the geothermal fields along the North Anatolian Fault zone [Erisen et al., 1996]. Therefore, both the geology and the downward circulation of meteoric fluids might have a control on the aseismic slip of the Ismetpaşa segment.

Although it is not known whether or not the fault was creeping before the 1944 earthquake, postseismic measurements at Ismetpaşa reveals an exponential decay in creep rate that appears to have graded into a steady state slip over the last decades or so (Figure 11). This suggests that aseismic slip may continue for decades, and plausibly during the entire earthquake cycle (~200–300 years). Change in the creep rate with

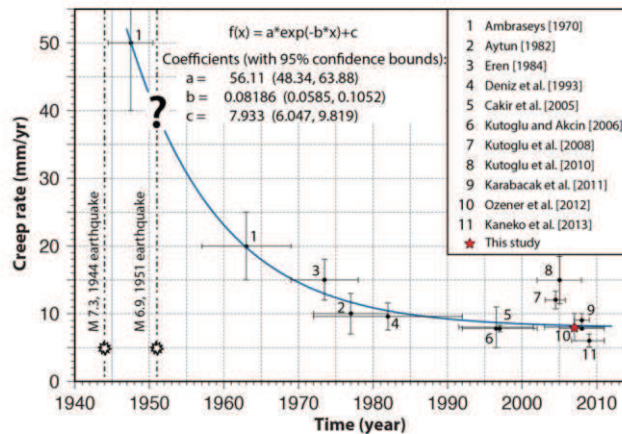


Figure 11. Time history of surface creep at Ismetpaşa as reported by various studies following the 1944 earthquake [after Cakir et al., 2005]. Horizontal and vertical bars are the time window and error range of measurements, respectively. The question mark corresponds to the unknown effect of the 1951 earthquake on creep rate. Curve shows the fit of the exponential relaxation function to the change of the creep rate with time [Savage et al., 2005].

time is fitted to an exponential relaxation function that suggests Newtonian behavior of creep in a ductile shear zone [Savage et al., 2005]. Using fully dynamic models of earthquake creep, Kaneko et al. [2013] inferred that the friction behavior of Ismetpaşa creeping segment is velocity strengthening at shallow depths, changing to velocity weakening at 3–6 km depth. Our models suggest that these properties may vary in space along the fault.

5. Conclusions

We have studied the spatial distribution of aseismic creep on the Ismetpaşa segment of the NAF using Envisat ASAR data between 2003 and 2010. The surface velocity field obtained with the PSI technique provides a tighter constraint on the characteristics of surface creep compared to conventional InSAR techniques. The results reveal a surface creep rate of 8 ± 2 mm/yr at Ismetpaşa which reaches a maximum of 20 ± 2 mm/yr 20 km to the east. Aseismic slip releases every year a moment of 6.2×10^{16} Nm, which is equivalent of an earthquake of $M_w = 5.1$. It implies that a significant portion of the fault is locked and accumulates interseismic strain to be released coseismically as demonstrated with the 1943, 1944, and 1951 earthquakes. High creep rates coincide mostly with the 1951 and eastern part of the 1944 earthquake ruptures. Measurements over the last 60 years show that creep on the Ismetpaşa segment has graded with time into a steady state rate after the 1944 and/or 1951 earthquakes (Figure 11), suggesting that it was probably triggered as post-seismic afterslip following the 1944 earthquake as was found with the surface deformation following the 1999 Izmit earthquake [Cakir et al., 2012].

Three-dimensional elastic dislocation modeling suggests that surface creep occurs along a 100 km long section since the easternmost 20 km creeping section estimated with best fitting linear approximations (Figure 6b) is not detected with the 3-D elastic dislocation modeling (Figure 9) probably due to high level of noise in this section. The creeping section extends at least 30 km further east compared to the previous studies [Cakir et al., 2005; Kaneko et al., 2013]. Modeling results indicate a shallow creeping depth, mostly less than 5 km, in good agreement with the velocity-strengthening at shallow depths deduced from dynamic models by Kaneko et al. [2013] and elastic dislocation models by Cakir et al. [2005]. Thus, the Ismetpaşa segment appears to be locked with a higher stressing rate at the lower seismogenic crust, which is able to generate strain release during moderate-large earthquakes such as those that occurred in the 1943, 1944, and 1951

earthquakes. An analysis of the geological structures suggests that aseismic slip along the Ismetpaşa creep segment is mainly controlled by the limestone and serpentine bodies.

Acknowledgments

InSAR data were copyrighted and obtained through the category-1 project AQTR-2436 of the European Space Agency and the Geohazard Superites program. SAR images were processed at the TUBITAK ULAKBIM High Performance and Grid Computing Centre of Turkey. Financial support is from TUBITAK project 107Y281. This is part of the dissertation of Esra Cetin who is supported by the French Embassy (in Turkey) Bourse Etudes scholarship program (778343D and 797216D) and by the TUBITAK-BIDEB 22148 scholarship program during the completion of this work. Most of the figures in this paper were generated using the public domain Generic Mapping Tools (GMT) software [Wessel and Smith, 1998]. We thank Tim Wright and anonymous reviewer for constructive comments that greatly improved this manuscript.

References

- Allen, C. R. (1968), The tectonic environments of seismically active and inactive areas along the San Andreas fault system, *Stanford Univ. Publ. Geol. Sci.*, **11**, 70–80.
- Allis, R. G., and Y. Shi (1995), New insights to temperature and pressure beneath the central Southern Alps, New Zealand, *N. Z. J. Geol. Geophys.*, **38**, 585–592.
- Ambraseys, N. N. (1970), Some characteristic features of the Anatolian fault zone, *Tectonophysics*, **9**, 143–165.
- Aytun, A. (1982), Creep measurements in the Ismetpaşa region of the North Anatolian Fault Zone, in *Multidisciplinary Approach to Earthquake Prediction*, edited by A. M. Isikara and A. Vogel, vol. 2, pp. 279–292, Friedr. Vieweg & Sohn, Braunschweig, Germany.
- Barka, A. A. (1996), Slip distribution along the North Anatolian fault associated with the large earthquakes of the period 1939–1967, *Bull. Seismol. Soc. Am.*, **86**, 1238–1254.
- Barka, A. A., and K. Kadinsky-Cade (1988), Strike-slip fault geometry in Turkey and its influence on earthquake activity, *Tectonics*, **7**(3), 663–684.
- Billham, R. (1989), Surface slip subsequent to the 24 November 1987 Superstition Hills, California, earthquake monitored by digital creepmeters, *Bull. Seismol. Soc. Am.*, **79**, 424–450.
- Burford, R. O., and P. W. Harsh (1980), Slip on the San Andreas fault in central California from alignment array surveys, *Bull. Seismol. Soc. Am.*, **70**, 1223–1261.
- Bürgmann, R., D. Schmidt, R. Nadeau, M. d'Allesio, E. Fielding, D. Manaker, T. McEvilly, and M. H. Murray (2000), Earthquake potential along the northern Hayward fault, *Science*, **289**, 1178–1182.
- Cakir, Z., and A. M. Akoglu (2008), Synthetic aperture radar interferometry observations of the M = 6.0 Orta earthquake of 6 June 2000 (NW Turkey): Reactivation of a listric fault, *Geochem. Geophys. Geosyst.*, **9**, Q08009, doi:10.1029/2008GC002031.
- Cakir, Z., A. M. Akoglu, S. Belabbes, S. Ergintav, and M. Meghraoui (2005), Creeping along the Ismetpaşa section of the North Anatolian Fault (Western Turkey): Rate and extent from InSAR, *Earth Planet. Sci. Lett.*, **238**, 225–234.
- Cakir, Z., S. Ergintav, H. Ozener, U. Dogan, A. M. Akoglu, M. Meghraoui, and R. Reilinger (2012), Onset of aseismic creep on major strike-slip faults, *Geology*, **40**(12), 1115–1118.
- Carpenter, B. M., C. Marone, and D. M. Saffer (2011), Weakness of the San Andreas Fault revealed by samples from the active fault zone, *Nat. Geosci.*, **4**, 251–254.
- Champanois, J., B. Fruneau, E. Pathier, B. Deffontaine, K.-C. Lin, and J.-C. Hu (2012), Monitoring of active tectonic deformations in the Longitudinal Valley (Eastern Taiwan) using Persistent Scatterer InSAR method with ALOS PALSAR data, *Earth Planet. Sci. Lett.*, **337**–**338**, 144–155.
- Cigna, F., B. Osmanoglu, E. Cabral-Cano, T. H. Dixon, J. A. Avila-Olivera, V. H. Garduno-Monroy, C. DeMets, and S. Wdowinski (2011), Monitoring land subsidence and its induced geological hazard with synthetic aperture radar interferometry: A case study in Morelia, Mexico, *Remote Sens. Environ.*, **117**, 146–161.
- Collettini, C., A. Niemeijer, C. Viti, and C. Marone (2009), Fault zone fabric and fault weakness, *Nature*, **462**, 907–910.
- Dehghani, M., A. Hooper, R. Hanssen, M. J. V. Zojé, S. Saatchi, and I. Entezam (2013), Hybrid conventional and persistent scatterer SAR interferometry for land subsidence monitoring in Tehran Basin, Iran, *ISPRS J. Photogramm. Remote Sens.*, **79**, 157–170.
- Deniz, R., A. Aksoy, D. Yalin, H. Seeger, and O. Hirsch (1993), Determination of crustal movement in Turkey by terrestrial geodetic methods, *J. Geodyn.*, **18**, 13–22.
- Eren, K. (1984), Strain analysis along the North Anatolian fault by using geodetic surveys, *Bull. Geod.*, **58**, 137–149.
- Erisen, B., I. Akkus, N. Uygur, and A. Kocak (1996), *Türkiye Jeotermal Enerjileri*, Gen. Dir. of Miner. Res. and Explor., Ankara.
- Farr, T. G., et al. (2007), The shuttle radar topography mission, *Rev. Geophys.*, **45**, RG2004, doi:10.1029/2005RG000183.
- Ferretti, A., C. Prati, and F. Rocca (2000), Nonlinear subsidence rate estimation using permanent scatterers in differential SAR interferometry, *IEEE Trans. Geosci. Remote Sens.*, **38**, 2202–2212.
- Ferretti, A., C. Prati, and F. Rocca (2001), Permanent scatterers in SAR interferometry, *IEEE Trans. Geosci. Remote Sens.*, **39**, 8–20.
- Freed, A. M. (2007), Afterslip (and only afterslip) following the 2004 Parkfield, California, earthquake, *Geophys. Res. Lett.*, **34**, L06312, doi:10.1029/2006GL029155.
- Fukushima, Y., O. Nishizawa, H. Sato, and M. Ohtake (2003), Laboratory study on scattering characteristics in rock samples, *Bull. Seismol. Soc. Am.*, **93**, 253–263.
- Funing, G. J., B. Parsons, and T. J. Wright (2005), Surface displacements and source parameters of the 2003 Bam (Iran) earthquake from Envisat advanced synthetic aperture radar imagery, *J. Geophys. Res.*, **110**, B09406, doi:10.1029/2004JB003338.
- Gratier, J.-P., F. Thouvenot, L. Jenatton, A. Tourette, M.-L. Doan, and F. Renard (2013), Geological control of the partitioning between seismic and aseismic sliding behaviours in active faults: Evidence from the Western Alps, France, *Tectonophysics*, **600**, 226–242.
- Hanssen, R. F. (2001), *Radar Interferometry: Data Interpretation and Error Analysis*, vol. 2, Springer, N. Y.
- Herece, E., and E. Akay (2003), *Atlas of North Anatolian Fault, Spec. Publ. Ser. 2*, Gen. Dir. of Miner. Res. and Explor., Ankara.
- Hooper, A. (2008), A multi-temporal InSAR method incorporating both persistent scatterer and small baseline approaches, *Geophys. Res. Lett.*, **35**, L16302, doi:10.1029/2008GL034654.
- Hooper, A., H. Zebker, P. Segall, and B. Kampes (2004), A new method for measuring deformation on volcanoes and other natural terrains using InSAR persistent scatterers, *Geophys. Res. Lett.*, **31**, L23611, doi:10.1029/2004GL021737.
- Hooper, A., P. Segall, and A. Zebker (2007), Persistent scatterer interferometric synthetic aperture radar for crustal deformation analysis, with application to Volcan Alcedo, Galapagos, *J. Geophys. Res.*, **112**, B07407, doi:10.1029/2006JB004763.
- Kampes, B. M. (2005), *Displacement Parameter Estimation Using Permanent Scatterer Interferometry*, Ph.D. thesis, Delft Univ. of Technol., Delft, Netherlands.
- Kampes, B. M., and S. Usai (1999), Doris: The delft object-oriented radar interferometric software, paper presented at ITC 2nd ORS Symposium, Int. Inst. of Geoinf. Sci. and Earth Obs., Enchede, Netherlands.
- Kaneko, Y., Y. Fialko, D. T. Sandwell, X. Tong, and M. Furuya (2013), Interseismic deformation and creep along the central section of the North Anatolian fault (Turkey): InSAR observations and implications for rate-and-state friction properties, *J. Geophys. Res.*, **118**, 316–331, doi:10.1029/2012JB009661.
- Karabacak, V., E. Altunel, and Z. Cakir (2011), Monitoring aseismic creep along the North Anatolian Fault (Turkey) using ground-based LIDAR, *Earth Planet. Sci. Lett.*, **304**, 64–70.

- Ketelaar, K. (2008), Satellite radar interferometry, subsidence monitoring techniques, PhD thesis, Delft Univ. of Technol. Delft, Netherlands.
- Kutoglu, H. S., and H. Akcin (2006), Determination of 30-year Creep on the Ismetpaşa segment of the North Anatolian Fault using an old geodetic network, *Earth Planets Space*, *58*, 937–942.
- Kutoglu, H. S., H. Akcin, H. Kemalder, and K. S. Gormus (2008), Triggered creep rate on the Ismetpaşa segment of the North Anatolian Fault, *Nat. Hazards Earth Syst. Sci.*, *8*, 1369–1373.
- Kutoglu, H. S., H. Akcin, O. Gundogdu, K. S. Gormus, and E. Koksal (2010), Relaxation on the Ismetpaşa segment of the North Anatolian Fault after Golcuk $M_w = 7.4$ and Duzce $M_w = 7.2$ shocks, *Nat. Hazards Earth Syst. Sci.*, *10*, 2653–2657.
- Lennon, J. J. (2000), Red-shifts and red herrings in geographical ecology, *Ecography*, *23*, 101–113.
- Maerten, F., P. Resor, D. Pollard, and L. Maerten (2005), Inverting for slip on three dimensional fault surfaces using angular dislocations, *Bull. Seismol. Soc. Am.*, *95*(5), 1654–1665.
- Motagh, M., J. Hoffmann, B. Kampes, M. Baes, and J. Zschau (2007), Strain accumulation across the Gazikoy-Saros segment of the North Anatolian Fault inferred from persistent scatterer interferometry and GPS measurements, *Earth Planet. Sci. Lett.*, *255*, 432–444.
- Ozener, H., A. Dogru, and B. Turgut (2012), Quantifying aseismic creep on the Ismetpaşa segment of the North Anatolian Fault Zone (Turkey) by 6 years of GPS observations, *J. Geodyn.*, *67*(7), 72–77.
- Peyret, M., S. Dominguez, R. Cattin, J. Champenois, M. Leroy, and A. Zajac (2011), Present-day interseismic surface deformation along the Longitudinal Valley, eastern Taiwan, from a PS-InSAR analysis of the ERS satellite archives, *J. Geophys. Res.*, *116*, B03402, doi:10.1029/2010JB007898.
- Reilinger, R. E., et al. (2006), GPS constraints on continental deformation in the Africa-Arabia-Eurasia continental collision zone and implications for the dynamics of plate interactions, *J. Geophys. Res.*, *111*, B05411, doi:10.1029/2005JB004051.
- Rosen, P., S. Hensly, G. Peltzer, and M. Simons (2004), Updated repeat orbit interferometry package released, *Eos Trans. AGU*, *85*(5), 47.
- Şaroğlu, F., Ö. Emre, and I. Kuşçu (1992), *Active Fault Map of Turkey*, Gen. Dir. of Miner. Res. and Explor., Ankara.
- Savage, J. C., and R. O. Burford (1973), Geodetic determination of relative plate motion in central California, *J. Geophys. Res.*, *78*, 832–845.
- Savage, J. C., and M. Lisowski (1993), Inferred depth of creep on the Hayward fault, central California, *J. Geophys. Res.*, *98*, 787–793.
- Savage, J. C., J. L. Svarc, and S.-B. Yu (2005), Postseismic relaxation and transient creep, *J. Geophys. Res.*, *110*, B11402, doi:10.1029/2005JB003687.
- Schmidt, D. A., R. Bürgmann, R. M. Nadeau, and M. A. d'Alessio (2005), Distribution of aseismic slip-rate on the Hayward fault inferred from seismic and geodetic data, *J. Geophys. Res.*, *110*, B08406, doi:10.1029/2004JB003397.
- Stein, R. S., A. Barka, and J. H. Dieterich (1997), Progressive failure on the North Anatolian fault since 1939 by earthquake stress triggering, *Geophys. J. Int.*, *128*, 594–604.
- Taymaz, T., T. J. Wright, S. Yolsal, O. Tan, E. Fielding, and G. Seyitoglu (2007), Source characteristics of the 6 June 2000 Orta, Cankiri (central Turkey) earthquake: A synthesis of seismological, geological and geodetic (InSAR) observations, and internal deformation of the Anatolian plate, *Geol. Soc. Spec. Publ.*, *291*, 259–290.
- Thatcher, W. (1979), Systematic inversion of geodetic data in central California, *J. Geophys. Res.*, *84*, 2283–2297.
- Thomas, M. Y., J. P. Avouac, J. Champenois, J. C. Lee, and L. C. Kuo (2014), Spatio-temporal evolution of seismic and aseismic slip on the Longitudinal Valley Fault, Taiwan, *J. Geophys. Res.*, *119*, doi:10.1002/2013JB010603, in press.
- Warr, L. N., and S. Cox (2001), Clay mineral transformations and weakening mechanisms along the Alpine fault, New Zealand, *Geol. Soc. Spec. Publ.*, *186*, 85–101.
- Wei, M., D. Sandwell, and Y. Fialko (2009), A silent $M_{4.8}$ event of October 3–6, 2006, on the Superstition Hills Fault, Southern California, *J. Geophys. Res.*, *114*, B07402, doi:10.1029/2008JB006135.
- Wessel, P., and W. H. F. Smith (1998), New improved version of Generic Mapping Tools released, *Eos Trans. AGU*, *79*(47), 579.

CURRICULUM VITAE

Name Surname: Esra ÇETİN

Place and Date of Birth: Çan 06/01/1985

E-Mail: cetines@itu.edu.tr

EDUCATION:

B.Sc.: Istanbul Technical University, Department of Geological Eng., 2008

M.Sc.: Istanbul Technical University, Eurasia Institute of Earth Sciences, Earth System Science, 2010

PROFESSIONAL EXPERIENCES AND REWARDS:

February – December 2010: Teaching Assistant, Department of the General Geology, Muğla University (Field geological mapping, petrography, surveying)

December 2010 – currently: Teaching Assistant, Department of the General Geology Istanbul Technical University

September 2011 – July 2012: Eiffel scholarships grantholder from French Government - EGIDE, Strasbourg, France

February 2013 – June 2013: “Bourses de doctorat en co-tutelle” provided by the French Embassy

November 2013 – March 2014: “Bourses de doctorat en co-tutelle” provided by the French Embassy

November 2013 – June 2014: TUBITAK-BIDEB 2214/B scholarship program

PUBLICATIONS, PRESENTATIONS AND PATENTS ON THE THESIS:

- **Cetin, E.,** M. Meghraoui, Z. Cakir, A.M. Akoglu, O. Mimouni, and M. Chebbah (2012), Seven years of postseismic deformation following the 2003 Mw=6.8 Zemmouri earthquake (Algeria) from InSAR Time Series, *Geophysical Research Letters*, 39, L10307, doi:10.1029/2012GL051344.
- **Cetin, E.,** Z. Cakir, M. Meghraoui, S. Ergintav, A.M. Akoglu (2014), Extent and distribution of aseismic slip on the Ismetpaşa segment of the North Anatolian Fault (Turkey) from Persistent Scatterer InSAR, *Geochem. Geophys. Geosyst.*, 15, doi:10.1002/2014GC005307.
- **Cetin, E.,** Z. Cakir, M. Meghraoui, A.M. Akoglu, P.J. Gonzalez, Coseismic and postseismic deformation associated with the Mw=6.4 February 24, 2004 Al Hoceima earthquake (Morocco) from InSAR (in preparation).

Analysis and Modeling of Crustal Deformation using InSAR Time Series Along Selected Active Faults within the Africa-Eurasia Convergence Zone

Résumé

Les travaux de cette thèse de Doctorat ont été menés dans le cadre de l'accord en co-tutelle entre l'Université de Strasbourg (EOST) et Istanbul Technical University (Dept. of Geology), avec l'octroi d'une bourse d'étude annuelle de l'Ambassade de France à Ankara, une bourse d'excellence EIFFEL de 10 mois, et un support financier de 8 mois de « TUBITAK 2214B - joint Ph.D. ».

La zone de convergence de plaques Afrique – Eurasie comporte des failles capables de générer de forts séismes destructeurs. L'objectif de cette thèse est une meilleure compréhension du comportement de ces failles, et du cycle sismique associé, par l'analyse des déformations co-, post- et inter-sismiques enregistrées en surface, dans la zone de convergence. Une attention particulière est portée aux déformations lentes et à leur part dans le cycle sismique, mesurées en surface et analysées à l'aide des techniques InSAR (Synthetic Aperture Radar Interferometry), et modélisées par les méthodes de la dislocation élastique.

Résumé en anglais

This Ph.D. thesis is conducted in the frame of the “co-tutelle” scholarship (EOST-ITU) provided by French Embassy in Ankara. In addition, a 10-month scholarship « Bourse excellence Eiffel », and 8-month scholarship « TUBITAK 2214B - joint Ph.D. » were other sources of support for the preparation of this thesis.

The convergence between African and Eurasian plates is at the origin of active tectonic structures that generate large and destructive earthquakes. This thesis aims to improve our understanding of fault behavior and the earthquake cycle by analyzing surface deformation along selected active faults during the periods of co-, post-and inter-seismic deformation within the Africa-Eurasia convergence zone. In this context, slow deformation observed at the surface and associated with the earthquake cycle is analyzed using Synthetic Aperture Radar Interferometry (InSAR) time series technique, and modeled with elastic dislocation methods.